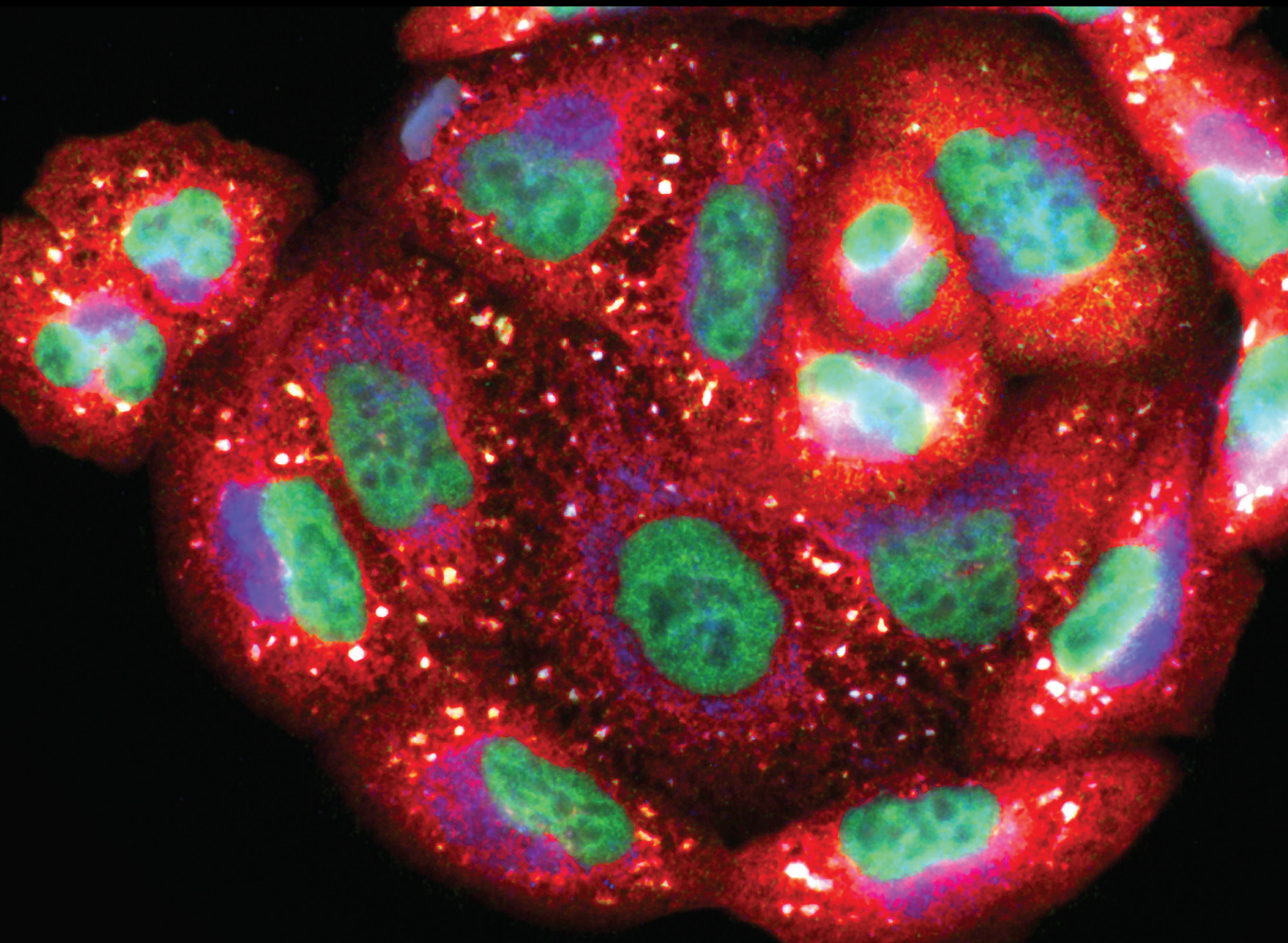


Diagnostics and Mechanisms of Nanomaterials and Oxidative Stress in Cancer, Inflammatory, and Cardiovascular Disease

Lead Guest Editor: Daoud Ali

Guest Editors: Madhukar Saxena and Khuram Ahmad





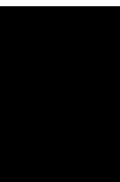
**Diagnostics and Mechanisms of Nanomaterials
and Oxidative Stress in Cancer, Inflammatory,
and Cardiovascular Disease**

Oxidative Medicine and Cellular Longevity

**Diagnostics and Mechanisms of
Nanomaterials and Oxidative Stress
in Cancer, Inflammatory, and
Cardiovascular Disease**

Lead Guest Editor: Daoud Ali

Guest Editors: Madhukar Saxena and Khuram
Ahmad



Copyright © 2020 Hindawi Limited. All rights reserved.

This is a special issue published in "Oxidative Medicine and Cellular Longevity" All articles are open access articles distributed under the Creative Commons Attribution License, which permits unrestricted use, distribution, and reproduction in any medium, provided the original work is properly cited.

Chief Editor

Jeannette Vasquez-Vivar, USA

Associate Editors

Amjad Islam Aqib, Pakistan
Angel Catalá , Argentina
Cinzia Domenicotti , Italy
Janusz Gebicki , Australia
Aldrin V. Gomes , USA
Vladimir Jakovljevic , Serbia
Thomas Kietzmann , Finland
Juan C. Mayo , Spain
Ryuichi Morishita , Japan
Claudia Penna , Italy
Sachchida Nand Rai , India
Paola Rizzo , Italy
Mithun Sinha , USA
Daniele Vergara , Italy
Victor M. Victor , Spain

Academic Editors

Ammar AL-Farga , Saudi Arabia
Mohd Adnan , Saudi Arabia
Ivanov Alexander , Russia
Fabio Altieri , Italy
Daniel Dias Rufino Arcanjo , Brazil
Peter Backx, Canada
Amira Badr , Egypt
Damian Bailey, United Kingdom
Rengasamy Balakrishnan , Republic of Korea
Jiaolin Bao, China
Ji C. Bihl , USA
Hareram Birla, India
Abdelhakim Bouyahya, Morocco
Ralf Braun , Austria
Laura Bravo , Spain
Matt Brody , USA
Amadou Camara , USA
Marcio Carochio , Portugal
Peter Celec , Slovakia
Giselle Cerchiaro , Brazil
Arpita Chatterjee , USA
Shao-Yu Chen , USA
Yujie Chen, China
Deepak Chhangani , USA
Ferdinando Chiaradonna , Italy

Zhao Zhong Chong, USA
Fabio Ciccarone, Italy
Alin Ciobica , Romania
Ana Cipak Gasparovic , Croatia
Giuseppe Cirillo , Italy
Maria R. Ciriolo , Italy
Massimo Collino , Italy
Manuela Corte-Real , Portugal
Manuela Curcio, Italy
Domenico D'Arca , Italy
Francesca Danesi , Italy
Claudio De Lucia , USA
Damião De Sousa , Brazil
Enrico Desideri, Italy
Francesca Diomede , Italy
Raul Dominguez-Perles, Spain
Joël R. Drevet , France
Grégory Durand , France
Alessandra Durazzo , Italy
Javier Egea , Spain
Pablo A. Evelson , Argentina
Mohd Farhan, USA
Ioannis G. Fatouros , Greece
Gianna Ferretti , Italy
Swaran J. S. Flora , India
Maurizio Forte , Italy
Teresa I. Fortoul, Mexico
Anna Fracassi , USA
Rodrigo Franco , USA
Juan Gambini , Spain
Gerardo García-Rivas , Mexico
Husam Ghanim, USA
Jayeeta Ghose , USA
Rajeshwary Ghosh , USA
Lucia Gimeno-Mallench, Spain
Anna M. Giudetti , Italy
Daniela Giustarini , Italy
José Rodrigo Godoy, USA
Saeid Golbidi , Canada
Guohua Gong , China
Tilman Grune, Germany
Solomon Habtemariam , United Kingdom
Eva-Maria Hanschmann , Germany
Md Saquib Hasnain , India
Md Hassan , India

Tim Hofer , Norway
John D. Horowitz, Australia
Silvana Hrelia , Italy
Dragan Hrnčić, Serbia
Zebo Huang , China
Zhao Huang , China
Tarique Hussain , Pakistan
Stephan Immenschuh , Germany
Norsharina Ismail, Malaysia
Franco J. L. , Brazil
Sedat Kacar , USA
Andleeb Khan , Saudi Arabia
Kum Kum Khanna, Australia
Neelam Khaper , Canada
Ramoji Kosuru , USA
Demetrios Kouretas , Greece
Andrey V. Kozlov , Austria
Chan-Yen Kuo, Taiwan
Gaocai Li , China
Guoping Li , USA
Jin-Long Li , China
Qiangqiang Li , China
Xin-Feng Li , China
Jialiang Liang , China
Adam Lightfoot, United Kingdom
Christopher Horst Lillig , Germany
Paloma B. Liton , USA
Ana Lloret , Spain
Lorenzo Loffredo , Italy
Camilo López-Alarcón , Chile
Daniel Lopez-Malo , Spain
Massimo Lucarini , Italy
Hai-Chun Ma, China
Nageswara Madamanchi , USA
Kenneth Maiese , USA
Marco Malaguti , Italy
Steven McAnulty, USA
Antonio Desmond McCarthy , Argentina
Sonia Medina-Escudero , Spain
Pedro Mena , Italy
V́ctor M. Mendoza-Núñez , Mexico
Lidija Milkovic , Croatia
Alexandra Miller, USA
Sara Missaglia , Italy

Premysl Mladenka , Czech Republic
Sandra Moreno , Italy
Trevor A. Mori , Australia
Fabiana Morroni , Italy
Ange Mouithys-Mickalad, Belgium
Iordanis Mourouzis , Greece
Ryoji Nagai , Japan
Amit Kumar Nayak , India
Abderrahim Nemmar , United Arab Emirates
Xing Niu , China
Cristina Nocella, Italy
Susana Novella , Spain
Hassan Obied , Australia
Pál Pacher, USA
Pasquale Pagliaro , Italy
Dilipkumar Pal , India
Valentina Pallottini , Italy
Swapnil Pandey , USA
Mayur Parmar , USA
Vassilis Paschalis , Greece
Keshav Raj Paudel, Australia
Ilaria Peluso , Italy
Tiziana Persichini , Italy
Shazib Pervaiz , Singapore
Abdul Rehman Phull, Republic of Korea
Vincent Pialoux , France
Alessandro Poggi , Italy
Zsolt Radak , Hungary
Dario C. Ramirez , Argentina
Erika Ramos-Tovar , Mexico
Sid D. Ray , USA
Muneeb Rehman , Saudi Arabia
Hamid Reza Rezvani , France
Alessandra Ricelli, Italy
Francisco J. Romero , Spain
Joan Roselló-Catafau, Spain
Subhadeep Roy , India
Josep V. Rubert , The Netherlands
Sumbal Saba , Brazil
Kunihiro Sakuma, Japan
Gabriele Saretzki , United Kingdom
Luciano Saso , Italy
Nadja Schroder , Brazil

Anwen Shao , China
Iman Sherif, Egypt
Salah A Sheweita, Saudi Arabia
Xiaolei Shi, China
Manjari Singh, India
Giulia Sita , Italy
Ramachandran Srinivasan , India
Adrian Sturza , Romania
Kuo-hui Su , United Kingdom
Eisa Tahmasbpour Marzouni , Iran
Hailiang Tang, China
Carla Tatone , Italy
Shane Thomas , Australia
Carlo Gabriele Tocchetti , Italy
Angela Trovato Salinaro, Italy
Rosa Tundis , Italy
Kai Wang , China
Min-qi Wang , China
Natalie Ward , Australia
Grzegorz Wegrzyn, Poland
Philip Wenzel , Germany
Guangzhen Wu , China
Jianbo Xiao , Spain
Qiongming Xu , China
Liang-Jun Yan , USA
Guillermo Zalba , Spain
Jia Zhang , China
Junmin Zhang , China
Junli Zhao , USA
Chen-he Zhou , China
Yong Zhou , China
Mario Zoratti , Italy


Contents

Butterbur (*Petasites hybridus*) Extract Ameliorates Hepatic Damage Induced by Ovalbumin in Mice

Rana M. Alhusayan , Badr Abdullah Aldahmash , Doaa M. El-Nagar , Ahmad Rady , Khalid Elfakki Ibrahim , and Saad Alkahtani 


Research Article (9 pages), Article ID 3178214, Volume 2020 (2020)

Green-Synthesized Silver Nanoparticles Induced Apoptotic Cell Death in MCF-7 Breast Cancer Cells by Generating Reactive Oxygen Species and Activating Caspase 3 and 9 Enzyme Activities

Ikram Ullah , Ali Talha Khalil, Muhammad Ali, Javed Iqbal, Waqar Ali, Saud Alarifi, and Zabta Khan Shinwari



Research Article (14 pages), Article ID 1215395, Volume 2020 (2020)

Isokotomolide A from *Cinnamomum kotoense* Induce Melanoma Autophagy and Apoptosis *In Vivo* and *In Vitro*

Jian Li, Chung-Yi Chen, Jyun Yin Huang, Lin Wang, Zixuan Xu, Wenyi Kang, Miao-Hsia Lin, and Hui-Min David Wang 




Research Article (16 pages), Article ID 3425147, Volume 2020 (2020)

***In Vitro* Studies on the Immunomodulatory Effects of *Pulicaria crispa* Extract on Human THP-1 Monocytes**

Tarfa Albrahim, Moonerah M. Alnasser, Mashaal R. Al-Anazi, Muneera D. AlKahtani, Saad Alkahtani , and Ahmed A. Al-Qahtani 



Research Article (14 pages), Article ID 7574606, Volume 2020 (2020)

A Novel Oral Astaxanthin Nanoemulsion from *Haematococcus pluvialis* Induces Apoptosis in Lung Metastatic Melanoma

Hsing-Yu Haung, Yi-Chen Wang, Ying-Chen Cheng, Wenyi Kang , Shang-Hsiu Hu, Dengyong Liu , Chaogeng Xiao, and Hui-Min David Wang 





Research Article (13 pages), Article ID 2647670, Volume 2020 (2020)

Genetic Polymorphism of the Nrf2 Promoter Region (rs35652124) Is Associated with the Risk of Diabetic Foot Ulcers

Rajan Teena , Umapathy Dhamodharan, Daoud Ali, Kesavan Rajesh, and Kunka Mohanram Ramkumar 


Clinical Study (9 pages), Article ID 9825028, Volume 2020 (2020)

Investigation of Cytotoxicity Apoptotic and Inflammatory Responses of Biosynthesized Zinc Oxide Nanoparticles from *Ocimum sanctum* Linn in Human Skin Keratinocyte (Hacat) and Human Lung Epithelial (A549) Cells

Bader Almutairi, Gadah Albahser , Rafa Almeer , Nouf M. Alyami, Hanouf Almukhlafi, Khadijah N. Yaseen, Saad Alkahtani , and Saud Alarifi 




Research Article (9 pages), Article ID 1835475, Volume 2020 (2020)

Exploration of Cadmium Dioxide Nanoparticles on Bioaccumulation, Oxidative Stress, and Carcinogenic Potential in *Oreochromis mossambicus* L.

Monera A. Al-Abdan, May N. Bin-Jumah, and Saud Alarifi 

Research Article (11 pages), Article ID 5407159, Volume 2020 (2020)

Crystal Growth and Kinetic Behaviour of *Pseudoalteromonas espejiana* Assisted Biosynthesized Gold Nanoparticles

Rashmi Gupta, Gourav Kumar, Sabya Sachi Das, Saad Alkahtani , Abdullah Alkahtane, Badr Aldahmash, Saud Alarifi , Bader Almutairi, Gadah Albasher , Amit Kumar Nayak, and Md Saquib Hasnain 

Research Article (12 pages), Article ID 6501294, Volume 2020 (2020)

Research Article

Butterbur (*Petasites hybridus*) Extract Ameliorates Hepatic Damage Induced by Ovalbumin in Mice

Rana M. Alhusayan ¹, Badr Abdullah Aldahmash ¹, Doaa M. El-Nagar ^{1,2},
Ahmad Rady ¹, Khalid Elfakki Ibrahim ¹, and Saad Alkahtani ¹

¹Department of Zoology, College of Science, King Saud University, P.O. Box 2455, Riyadh 11451, Saudi Arabia

²Department of Zoology, Faculty of Women for Science, Arts and Education, Ain Shams University, Cairo, Egypt

Correspondence should be addressed to Badr Abdullah Aldahmash; baldhmash@ksu.edu.sa

Received 24 July 2020; Accepted 7 December 2020; Published 15 December 2020

Academic Editor: Madhukar Saxena

Copyright © 2020 Rana M. Alhusayan et al. This is an open access article distributed under the Creative Commons Attribution License, which permits unrestricted use, distribution, and reproduction in any medium, provided the original work is properly cited.

The liver is the most vital organ that could be influenced by inducers of hypersensitivity such as ovalbumin. The current study was carried out to explore the effects of butterbur (*Petasites hybridus*) extract on the ovalbumin-induced liver hypersensitivity in Swiss albino male mice. Animals were divided into 4 groups, 1st group served as a control group, 2nd group treated with daily oral administration of 75 mg/kg of butterbur extract, 3rd group received single oral dose 100 mg/kg of ovalbumin to induce hypersensitivity, and 4th group treated with oral administration of butterbur extract one-day post to the hypersensitivity induction. Ovalbumin induces a significant increase in the activity of liver enzymes and MDA and decreased the activity of CAT after the ovalbumin treatment. Histopathological investigations revealed marked pathological alterations in liver tissues in the form of hyaline degeneration and fibrosis. Additionally, heavy immune response indicated by immunostaining of MDA and TNF- α could be observed. In contrast, posttreatment with butterbur extract after hypersensitivity induction resulted in a significant decrease of liver enzymes and oxidative stress and reduced the inflammation and fibrosis of liver tissues. These results suggest that butterbur extract is considered as anti-inflammatory and antioxidant therapeutic herb for hypersensitivity treatment of liver.

1. Introduction

The liver is the largest organ in the mammalian body that plays a main role in proteins, lipids, and carbohydrate metabolism [1]. Additionally, it plays a vital role to remove bacteria, viruses, and exogenous antigens from the systemic circulation. However, the liver might be subjected to injury associated with its role [2–5]. On the other hand, ovalbumin is known to induce asthma by causing chronic airway inflammation manifested by infiltration of neutrophils, eosinophils, and lymphocytes into bronchial lumen with increasing of reactive nitrogen and reactive oxygen species (ROS) levels. Inflammation and ROS production might induce liver injury, as well as lung damage ([6, 7]; Abdsmall et al., 2018).

Nowadays, herbal remedies attract growing interest as an alternative of chemical therapy, because of their potential role in reducing pathological changes and oxidative stress

([8–10]; [11]). *Petasites hybridus* or butterbur is considered one of the best remedies in treating asthma, cough, plague, and fever [12–14]. The main active constituents of butterbur are petasin and isopetasin [15]. Both are responsible for the inhibition of leukotriene synthesis and consequently, inflammation. Therefore, it had been suggested that *butterbur* is able to effectively treat urinary disorders, obstructive bronchitis, and bile obstruction, as well as liver and intestinal disorders [16, 17]. In this study, we illustrate the potential effect of *butterbur* extract to reduce the ovalbumin-induced inflammation and liver damages in albino mice.

2. Materials and Methods

2.1. Animals. Male mice of the Swiss albino strain aged 12 weeks and weighing 25 ± 5 g were used for the experiment. The animals were acclimated to $22(\pm 1)$ °C and maintained

under conditions of 12 h periods of light and dark, with free access to clean water and commercial mice food. The animals were housed in polypropylene cages inside a well-ventilated room. The experiments were approved by the board of studies, College of Science, King Saud University, Riyadh, Saudi Arabia. The animals which were used in this study were maintained and used by following the local and international guidelines for the use and care of laboratory animals.

2.2. Chemicals. Ovalbumin (cat # 02230) was purchased from LOBA CHEMIE, Colaba, Mumbai, Maharashtra 400005, India. Butterbur extract powder (*Petasites hybridus*) was from Swanson Health Products Company, 075 40th Ave S, Fargo, ND 58104, USA.

2.3. Experimental Design. Mice were distributed into four experimental groups each containing 10 mice. Animals were randomly divided into 4 groups, 1st group served as the control group, 2nd group treated with daily oral administration of 75 mg/kg of butterbur extract [18], 3rd group received single oral dose 100 mg/kg of ovalbumin to induce hypersensitivity [19], and 4th group treated with oral administration of butterbur extract one-day post to the hypersensitivity induction. Oral gavage was used for the administration of each of the medication. The experiment lasted for 45 days. At the end of the 45 days, the animals were sacrificed, and the blood was collected without anticoagulant and centrifuged at 3000 rpm for 15 minutes to separate the sera and stored at -80°C until used. Livers were collected, cut, and fixed in 10% neutral buffered formalin.

2.4. Liver Index. At the end of the experimental period, each mouse was weighed; livers were removed and weighed. Liver index was calculated by dividing the weight of liver by the body weight and then multiplying by 100 [20].

2.5. Biochemical Analysis. Sera were used for the estimation of ALT, AST, creatinine, and BUN according to Pratt and Kaplan [21].

2.6. Catalase (CAT). Catalase activity in liver homogenate was assayed by the method according to [22]. The assay depends on the ability of the enzyme to inhibit phenazinemethosulphate-mediated reduction of nitro blue tetrazolium dye and measured at 560 nm (Bio-systems, BTS-350, Spain). The concentration of produced CAT has been expressed as nanomole per gram.

2.7. Lipid Peroxidation (MDA). Lipid peroxidation in liver homogenate was determined according to the method of [23]. It determined by the absorbance at 535 nm (Bio-systems, BTS-350, Spain). The concentration of produced MDA has been expressed as nanomole per gram.

2.8. Histopathological Analysis. Livers were collected and cut into small pieces and fixed in 10% neutral buffered formalin. Following fixation, specimens were dehydrated, embedded in wax, and then sectioned into 5 μ m thickness sections. Staining was performed using hematoxylin/eosin and Masson's trichrome as described elsewhere [24]. Sections were examined under light microscope, and images were taken at 400x.

2.9. Immunohistochemical Analysis. The sections were prepared and mounted on electrostatic slides. Sections were deparaffinized in xylene and rehydrated in descending concentration of ethanol and finally in distilled water. Sections were heated in citrate buffer (pH = 6) within microwave for 5 minutes and washed with PBS buffer for 5 minutes. Sections were incubated in peroxidase blocking solution for 10 minutes and incubated overnight at 4°C in diluted primary antibodies (1 : 1000) anti-malondialdehyde (ab194225, Abcam) and anti-TNF- α antibody (ab1793, Abcam). Sections were rinsed with PBS buffer 3 times each for 5 minutes and incubated with biotinylated goat anti-mouse (ab128976) for 30 minutes at room temperature, followed by incubation in avidin-biotin complex for 30 min. The sections were then rinsed 3 times with PBS each for 5 minutes and incubated in DAB solution for 10 minutes. After that, Mayer's hematoxylin was added. Finally, the sections were dehydrated using ascending concentrations of ethanol and cleared with two washes of xylene. Sections were mounted, and images were taken at 400x. Images were analyzed using the Fiji software to calculate the optical density using the formula $OD = \log (\max \text{ intensity} / \text{mean intensity})$, where the max intensity = 255 for 8-bit images.

2.10. Statistical Analysis. One-way ANOVA was carried out, and the statistical comparisons among the groups were performed with Duncan's test using a statistical package program (SPSS version 16.0). Data = mean \pm standard error of mean and p values <0.05 were considered significant.

3. Results

3.1. Posttreatment with Butterbur Extract Decreases the Liver Index of Ovalbumin-Treated Mice. To investigate the effect of butterbur extract on the ovalbumin-induced liver abnormalities in mice, liver index has been calculated. As shown in (Figure 1(a)), we could observe an insignificant decrease in liver index in butterbur-treated animals in comparison to the untreated controls. In contrast, ovalbumin-treated animal showed an increase in liver index in comparison to the control animals. However, posttreatment with butterbur (75 mg/kg) insignificantly decreases the liver index of the ovalbumin-treated animals.

3.2. Butterbur Extract Improves Liver Function of Ovalbumin-Treated Mice. Liver function in mice was assessed by measuring the level of liver enzymes (ALT and AST) in treated mice and control group. The group that received butterbur extract showed insignificant changes compared to the control group in all tested animals. In contrast, ovalbumin administration induced a significant increase of ALT and AST activities (Figures 1(b) and 1(c), respectively), whereas, posttreatment with butterbur seems to rescue the liver toxicity induced by ovalbumin. Indeed, ALT and AST activities dropped significantly compared to ovalbumin-treated mice as shown in Figures 1(b) and 1(c), respectively.

3.3. Butterbur Extract Lowers the Ovalbumin-Induced Oxidative Stress in Mice Liver. We further investigated the effect of butterbur extract on the ovalbumin-treated mice.

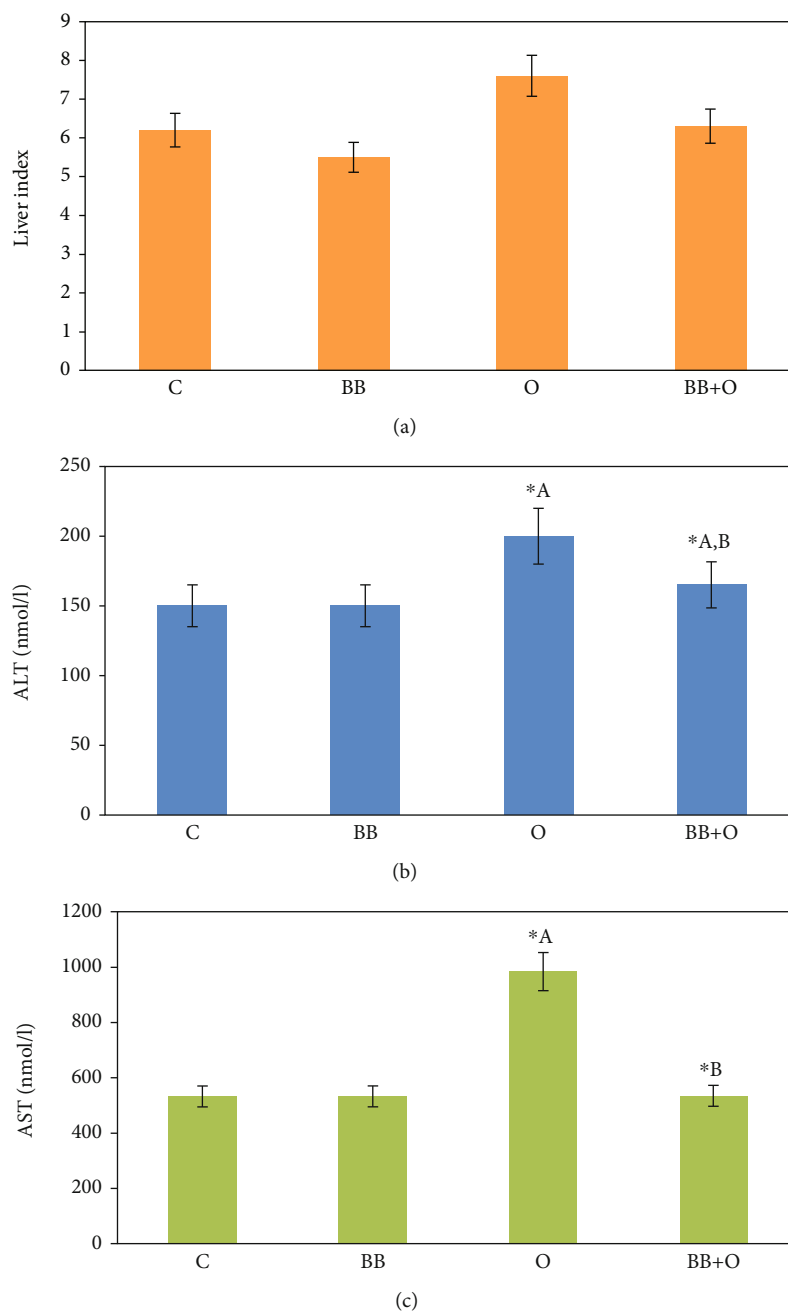


FIGURE 1: Effects on liver index and liver functions. (a) Histogram of liver index showing a significant increase of the group treated with 100 mg/kg ovalbumin compared to the control group and a significant decrease in the posttreated group with 75 mg/kg of butterbur extract. (b, c) Ovalbumin (100 mg/kg) induces a significant increase of ALT and AST activities of treated mice, respectively, compared to the control mice. Posttreatment with butterbur extract (75 mg/ml) induces a significant decrease of both activities. Data = mean \pm the standard error of mean. *^aSignificant compared to the control group. *^bSignificant compared to the ovalbumin group. $p \leq 0.05$.

The oxidative stress level was detected by measuring the known oxidative stress markers CAT and MDA in liver homogenate. The results are shown in Figure 2. Mice livers treated with butterbur extract displayed an insignificant change in CAT and MDA activities compared to the untreated control group. In contrast, we measured a significant decrease of CAT activity, as well as a significant increase of MDA activity in ovalbumin-treated mice compared to the untreated control group, whereas posttreatment

of butterbur extract resulted in an insignificant increase of CAT activity and a significant decrease of MDA activity compared to ovalbumin-treated group that referred to the effective role of butterbur extract to lower the oxidative stress induced by ovalbumin.

3.4. Butterbur Extract Posttreatment Improves the Pathological Abnormalities Induced by Ovalbumin Treatment in Mice Liver. We further explored the effect of butterbur extract on

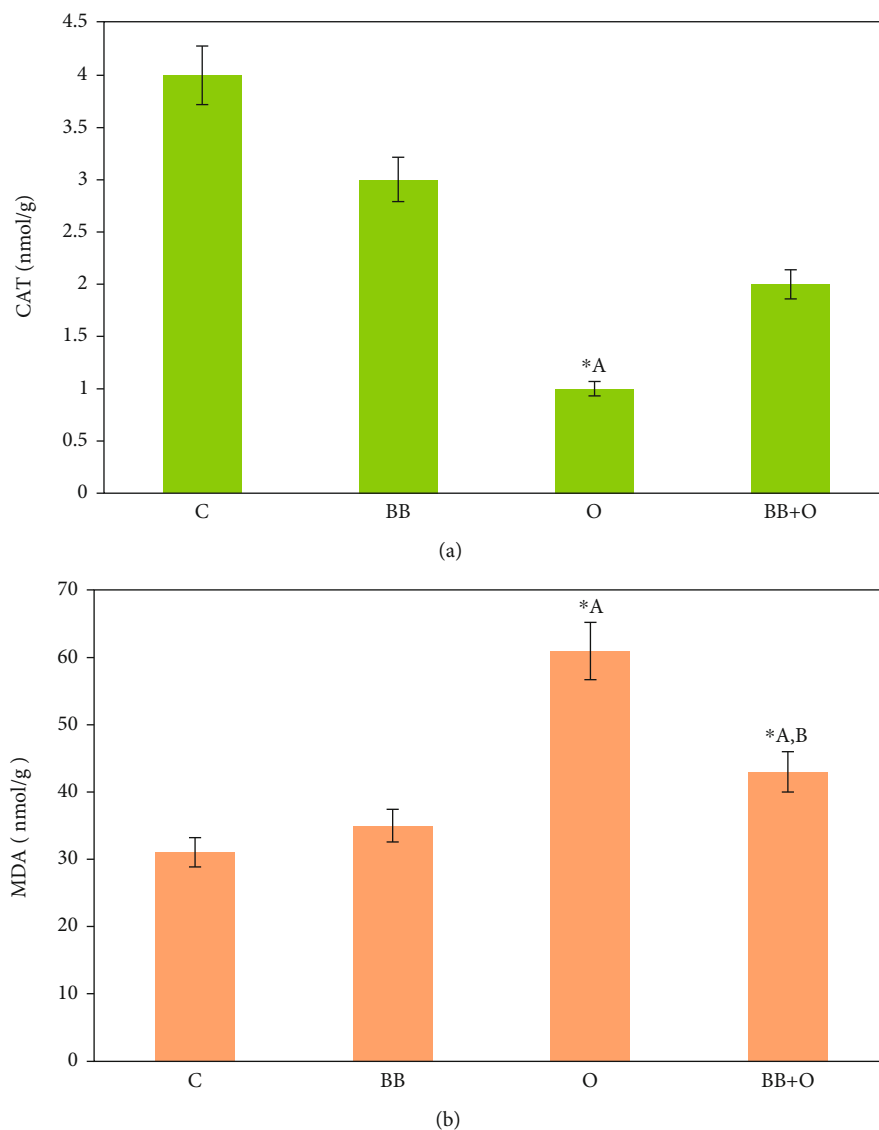


FIGURE 2: Butterbur extract lowers oxidative stress induced by the ovalbumin in mice liver. Histograms of oxidative stress activity. (a) Ovalbumin treatment (100 mg/kg) shows a significant decrease of CAT activity compared to control and an insignificant increase in the posttreated mice group with 75 mg/kg of butterbur extract. (b) Ovalbumin treatment (100 mg/kg) reveals a significant increase of MDA activity compared to the control group. Posttreatment with butterbur extract (75 mg/kg) displays a significant decrease of MDA activity. Data = mean \pm the standard error of mean. ^{*A}Significant compared to the control group. ^{*B}Significant compared to the ovalbumin group. $p \leq 0.05$.

the ovalbumin-induced toxicity using histochemical analysis of treated and nontreated liver sections. As shown in (Figure 3(a)), control liver section exhibited normal liver tissue that consisted of central vein surrounded by network of hepatocytes separated from each other by blood sinusoids with Kupffer cells. Similar results could be obtained in butterbur-treated animals. However, activation of Kupffer cells could be observed here (Figure 3(b)). In contrast, liver section of mice treated with ovalbumin exhibited marked pathological abnormalities, manifested by accumulation of large infiltration cells and giant macrophages. Furthermore, hyaline degeneration, fibrosis, and necrotic foci could be also observed (Figure 3(c)). In contrast, posttreatment with

butterbur extract revealed healthy hepatocytes with some Kupffer cell activation and a few numbers of scattered inflammatory cells (Figure 3(d)).

On the other side, Masson's trichrome-stained liver sections revealed no collagenous fiber depositions in both control and mice group treated with butterbur extract (Figures 3(e) and 3(f)), whereas the liver section treated with ovalbumin displayed heavy incidence of collagenous fiber depositions between hyaline-degenerated hepatocytes and around the vein (Figure 3(g)). Posttreatment of butterbur extract showed less depositions of collagenous fibers surrounding the vein and a few numbers of inflammatory cells (Figure 3(h)).

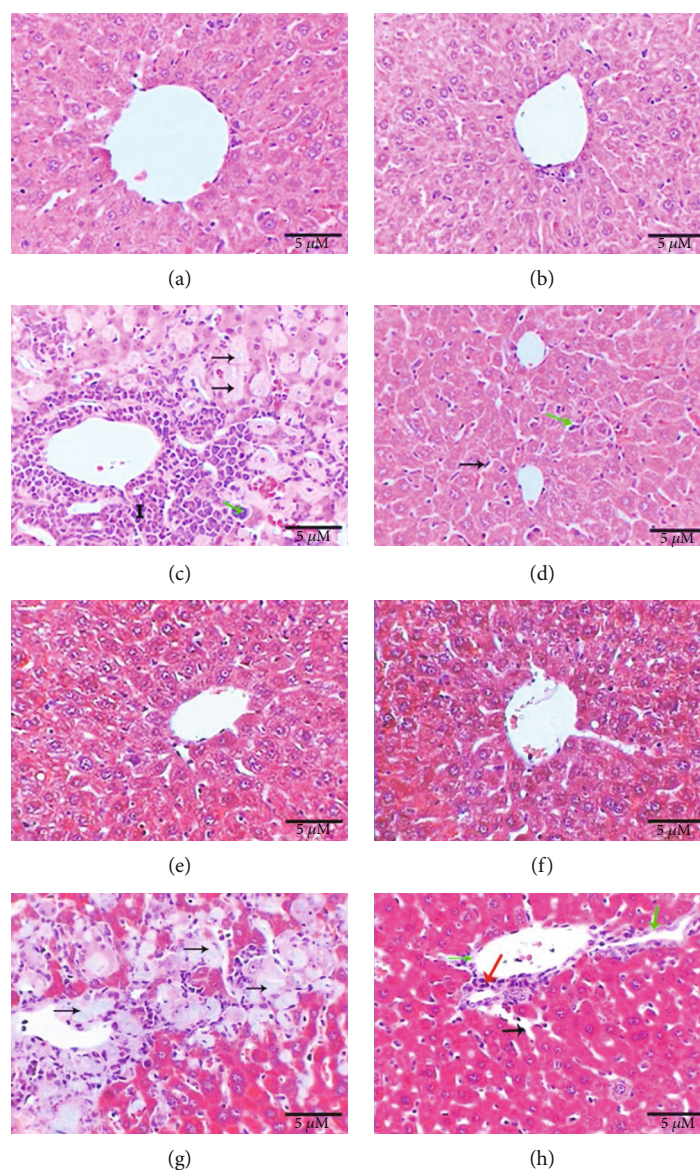


FIGURE 3: Posttreatment with butterbur extract reduces the pathological singe induces after ovalbumin treatment. Photomicrographs of liver showing (a) normal control liver; (b) normal structure of liver in the group treated with butterbur extract (75 mg/kg); (c) liver of the group treated with (100 mg/kg) ovalbumin shows great aggregations of inflammatory cells (labelled I), giant macrophage (green arrow), and hyaline degeneration (black arrows); (d) liver of the group posttreated with butterbur extract shows healthy hepatocytes, activation of Kupffer cells (black arrow), and inflammatory cells (green arrows) (H&E-400x scale 10 μ m); (e) no fibrosis in control liver; (f) no collagenous fibers in the liver of the group treated with butterbur; (g) liver of the group treated with ovalbumin (100 mg/kg) reveals depositions of collagenous fibers surrounded the vein and in between hyaline-degenerated hepatocytes (black arrows); (h) liver of the group posttreated with butterbur extract (75 mg/kg) displays less depositions of collagenous fibers (green arrows), inflammatory cells (red arrows), and activation of Kupffer cells (black arrows) (M.Tr.-400x; scale bar = 10 μ m).

3.5. Butterbur Extract Posttreatment Lowers the Ovalbumin-Induced Oxidative Stress and Inflammation in Mice Liver. As shown in Figures 4(a) and 4(b), control group and butterbur-treated groups showed no immune response against MDA and TNF- α antibodies, whereas the group treated with ovalbumin revealed strong immune response manifested by intense brown spots against MDA (Figure 4(c)) and also against TNF- α . Interestingly, the last spots were mainly concentrated in leukocytes (Figure 4(g)). In addition to a signif-

icant increase of optical density compared to the control group (Figure 5), butterbur extract posttreatment resulted in a weak immune response against MDA (Figure 4(d)) and TNF- α (Figure 4(h)). Furthermore, optical density revealed a significant decrease compared to the ovalbumin-treated group (Figure 5).

Collectively, our results suggest a positive effect of butterbur extract on the reduction of oxidative stress and inflammation induced by ovalbumin.

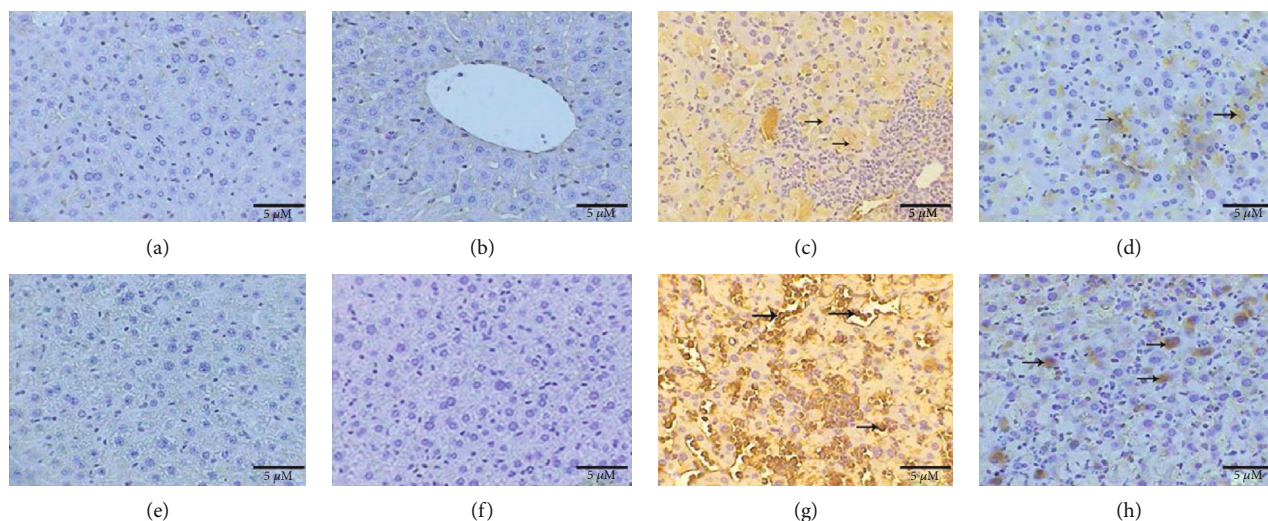


FIGURE 4: Posttreatment with butterbur extract reduces MDA and TNF- α in ovalbumin-treated liver. Photomicrographs of liver sections stained immunohistochemically (a) no immune response against MDA in the control group, (b) no immune response in the group treated with butterbur extract (75 mg/kg), (c) intense immune response against MDA (arrows) in ovalbumin-treated group, (d) weak immune response against MDA in the group posttreated with butterbur extract to ovalbumin, (e) no immune response against TNF- α in the control group, (f) no immune response in the group treated with butterbur extract, (g) strong immune reactivity against TNF- α in the group treated with ovalbumin, and (h) weak immune reactivity against TNF- α in the group posttreated with butterbur extract to ovalbumin (ABC-method 400x; scale bar = 10 μ m).

4. Discussion

Ovalbumin has been reported to develop hypersensitivity in lung tissues indicated by peribronchial and perivascular cell inflammation composed principally of eosinophils and lymphocytes [25]. Additionally, ovalbumin induces hypersecretion of mucus in treated animals, which considers the prominent histopathological features of ovalbumin-induced hypersensitivity [26]. Furthermore, it is considered as a potent allergen that causes activation of allergic mediators such as mast cells, inflammatory cytokines, eosinophils, and histamine, which have been recognized to play a key role in inflammatory reactions against ovalbumin upon exposure [27, 28]. To our knowledge, the induction of hypersensitivity through ovalbumin in the liver has not been reported. Therefore, the biochemical and pathological changes in the liver after ovalbumin treatment had been highlighted for the first time in this study. The ovalbumin treatment exhibited high levels of liver enzymes due to severe degeneration of hepatocytes, besides accumulation of large aggregations of inflammatory cells and macrophages, in addition to the induction of hyaline degeneration, necrosis, and fibrosis.

Some studies have indicated that allergens in general lead to autoimmune inflammation in the liver such as granulocytic and lymphocytic cell inflammation, granulomas, necrosis, and fibrosis [6, 29, 30]. Indeed, the present study illustrated that ovalbumin induced hypersensitivity in the form of heavy oxidative stress in treated mice. This hypersensitivity is manifested by the high level of MDA activity and the significant decrease of CAT activity in liver homogenate. Additionally, the immunohistochemistry study showed high incidence of MDA in the liver tissue and strong immune reactivity against TNF- α .

Butterbur is a herbaceous plant, belonging to the *Asteraceae*, that has been used in folk medicine in Asia and America for therapeutic of many illnesses such as fever, respiratory diseases, spasms, and pain. Beside many other compounds included in butterbur, two major compounds (petasin and isopetasin) are suggested to be responsible for the pharmacological effects of butterbur [31, 32]. The extracts from butterbur are used to treat a variety of ailments including spasms of the urogenital and digestive tracts, asthma, migraines, and allergic rhinitis [33–35]. The current study pointed out that butterbur extract is a potent inhibitor of hypersensitivity induced by ovalbumin. This finding had been suggested depending on the decrease of hypersensitivity-related liver enzymes in response to butterbur extract treatment. Catalase is an important liver enzyme that is dealing with oxidative stress and reactive oxygen species. Ovalbumin reduced the activity of CAT in treated mice; however, posttreatment with butterbur extract reinduces the CAT activity. The activity of CAT in addition to decreasing of MDA and increasing of CAT activities that changed due to ovalbumin administration that coincided with findings of other study demonstrated that butterbur extract could enhance the biochemical and oxidative stress which changes by kainic acid [36]. It was reported that the intense antioxidant effect of butterbur extract might be attributed to the impact incidence of polyphenols, glycosides, and some flavonoids as patuletin. On the other hand, the presence of furofuran lignan called petasignolide seemed to have powerful antioxidant effect that exerts an effort to ameliorate the hepatocellular damage by reducing oxidative stress [37]. Moreover, treatment with butterbur extract after hypersensitivity induction resulted in attenuation of pathological signs resulted from hypersensitivity as inflammation,

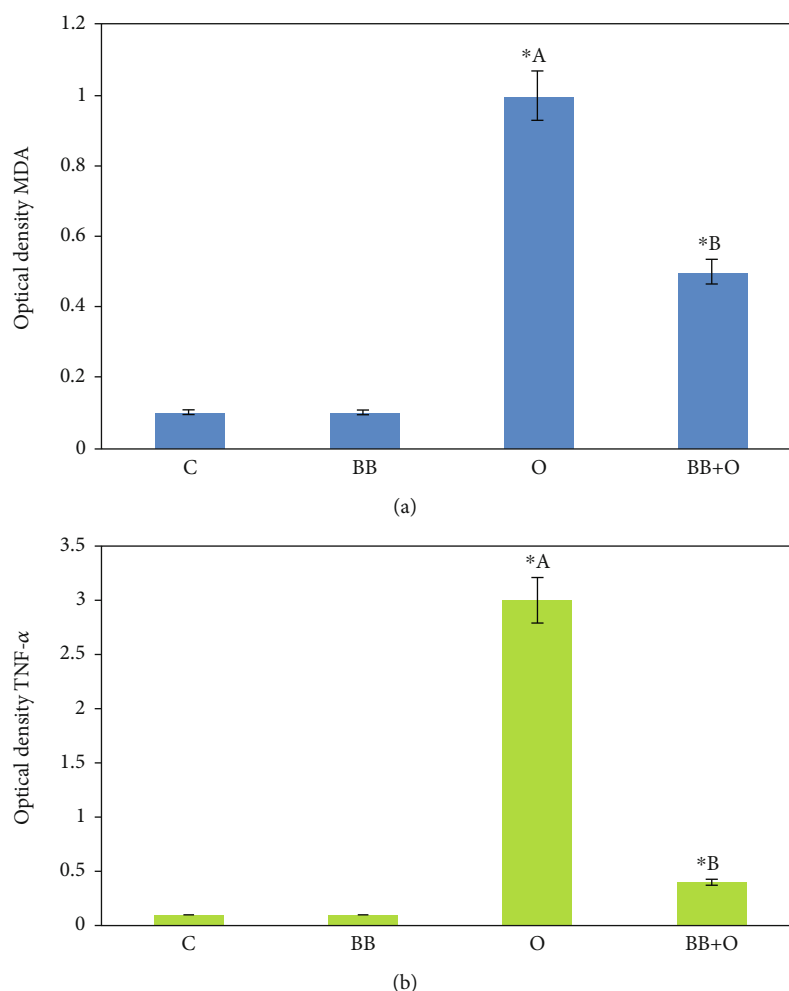


FIGURE 5: Histograms of optical density of immunohistochemistry staining. (a) Optical density of images stained against MDA shows a significant increase in the group treated with 100 mg/kg of ovalbumin and a significant decrease in the posttreated group with 75 mg/kg of butterbur extract. (b) Optical density of images stained against TNF- α shows a significant increase in the group treated with 100 mg/kg of ovalbumin and a significant decrease in the posttreated group with 75 mg/kg of butterbur extract. Data = mean \pm the standard error of mean. *^aSignificant compared to the control group. *^bSignificant compared to the ovalbumin group. $p \leq 0.05$.

degeneration, and fibrosis that agreed with previous studies which clarified that petasin and isoptasin of butterbur could exert anti-inflammatory actions via inhibition of leukotriene synthesis and cyclooxygenases [12]. Furthermore, decreasing of oxidative stress and inflammation in the liver tissue was clarified by immunohistochemistry. Altogether, our study suggests the effectiveness of butterbur extract in the treatment of ovalbumin-induced hypersensitivity in mice liver.

5. Conclusion

Present finding suggests that butterbur extract is considered as an anti-inflammatory and an antioxidant therapeutic herb for hypersensitivity treatment of liver.

Data Availability

The data generated or analyzed in this article are online publicly available without request.

Conflicts of Interest

The authors declare no conflicts of interest.

Acknowledgments

The authors extend their appreciation to King Saud University, Riyadh, Saudi Arabia, for funding the work through Researchers Support Project (RSP-2020/214).

References

- [1] E. G. Giannini, R. Testa, and V. Savarino, "Liver enzyme alteration: a guide for clinicians," *Canadian Medical Association journal*, vol. 172, no. 3, pp. 367–379, 2005.
- [2] P. Kubes and C. Jenne, "Immune responses in the liver," *Annual Review of Immunology*, vol. 36, no. 1, pp. 247–277, 2018.

- [3] P. E. Marques, A. G. Oliveira, R. V. Pereira et al., "Hepatic DNA deposition drives drug-induced liver injury and inflammation in mice," *Hepatology*, vol. 61, no. 1, pp. 348–360, 2015.
- [4] H. Niknahad, R. Heidari, R. Firuzi et al., "Concurrent inflammation augments antimalarial drugs-induced liver injury in rats," *Advanced pharmaceutical bulletin*, vol. 6, no. 4, pp. 617–625, 2016.
- [5] G. Tiegs, "Cellular and cytokine-mediated mechanisms of inflammation and its modulation in immune-mediated liver injury," *Zeitschrift für Gastroenterologie*, vol. 45, no. 1, pp. 63–70, 2007.
- [6] V. Bulani, K. Biyani, R. Kale et al., "Inhibitory effect of Calotropis gigantea extract on ovalbumin-induced airway inflammation and arachidonic acid induced inflammation in a murine model of asthma," *International Journal of Current Research in Biology and Medicine*, vol. 1, pp. 19–25, 2011.
- [7] S. G. Kim, E. Lee, N. Y. Park et al., "Britanin attenuates ovalbumin-induced airway inflammation in a murine asthma model," *Archives of Pharmacal Research*, vol. 39, no. 7, pp. 1006–1012, 2016.
- [8] G. Albasher, R. Almeer, F. O. Al-Otibi, N. Al-Kubaisi, and A. M. Mahmoud, "Ameliorative effect of Beta vulgaris root extract on chlorpyrifos-induced oxidative stress, inflammation and liver injury in rats," *Biomolecules*, vol. 2019, pp. 1–9, 2019.
- [9] D. F. Mansour, H. M. I. Abdallah, B. M. M. Ibrahim, R. R. Hegazy, R. S. E. Esmail, and L. O. Abdel-Salam, "The carcinogenic agent diethylnitrosamine induces early oxidative stress, inflammation and proliferation in rat liver, stomach and colon: protective effect of ginger extract," *Asian Pacific Journal of Cancer Prevention*, vol. 20, no. 8, pp. 2551–2561, 2019.
- [10] M. Tiwari, U. N. Dwivedi, and P. Kakkar, "Tinospora cordifolia extract modulates COX-2, iNOS, ICAM-1, pro-inflammatory cytokines and redox status in murine model of asthma," *Journal of ethnopharmacology*, vol. 153, no. 2, pp. 326–337, 2014.
- [11] R. C. Toledo, L. F. Brito, M. M. Caetano et al., "Acute treatment with Mangifera indica L. leaf extract attenuates liver inflammation in rats fed a cafeteria diet," *Food & Function*, vol. 10, no. 8, pp. 4861–4867, 2019.
- [12] H. C. Diener, F. G. Freitag, and U. Danesch, "Safety profile of a special butterbur extract from Petasites hybridus in migraine prevention with emphasis on the liver," *Cephalalgia Reports*, vol. 1, p. 251581631875930, 2018.
- [13] M. Giles, C. Ulbricht, K. Khalsa, C. Kirkwood, C. Park, and E. Basch, "Butterbur: an evidence-based systematic review by the natural standard research collaboration," *Journal of herbal pharmacotherapy*, vol. 5, pp. 119–143, 2005.
- [14] D. K. Lee, R. D. Gray, F. M. Robb, S. Fujihara, and B. J. Lipworth, "A placebo-controlled evaluation of butterbur and fexofenadine on objective and subjective outcomes in perennial allergic rhinitis," *Clinical and experimental allergy*, vol. 34, no. 4, pp. 646–649, 2004.
- [15] M. Sheykhzade, S. Smajilovic, A. Issa, S. Haunso, S. B. Christensen, and J. Tfelt-Hansen, "S-petasin and butterbur lactones dilate vessels through blockage of voltage gated calcium channels and block DNA synthesis," *European Journal of Pharmacology*, vol. 593, no. 1-3, pp. 79–86, 2008.
- [16] S. Benemei, F. De Logu, S. L. Puma et al., "The anti-migraine component of butterbur extracts, isopetasin, desensitizes peptidergic nociceptors by acting on TRPA1 cation channel," *British journal of pharmacology*, vol. 174, no. 17, pp. 2897–2911, 2017.
- [17] F. M. Robb, D. K. C. Lee, K. Haggart, and B. J. Lipworth, "Butterbur, an herbal remedy, confers complementary anti-inflammatory activity in asthmatic patients receiving inhaled corticosteroids," *Journal of Allergy and Clinical Immunology*, vol. 13, 2, Supplement, p. S36, 2004.
- [18] C. Ulbricht, E. Basch, W. Weissner, and D. Hackman, "An evidence-based systematic review of herb and supplement interactions by the Natural Standard Research Collaboration," *Expert Opinion on Drug Safety*, vol. 5, no. 5, pp. 719–728, 2006.
- [19] L. Zhou and Y. Hu, "Immunological effect of different doses of all-trans retinoic acid on ovalbumin allergic mice," *Zhonghua er ke za zhi= Chinese journal of pediatrics*, vol. 52, no. 9, pp. 667–672, 2014.
- [20] B. Aldahmash, D. El-Nagar, and K. Ibrahim, "Attenuation of hepatotoxicity and oxidative stress in diabetes STZ-induced type 1 by biotin in Swiss albino mice," *Saudi Journal of Biological Sciences*, vol. 23, no. 2, pp. 311–317, 2016.
- [21] D. Pratt and M. Kaplan, "Evaluation of abnormal liver-enzyme results in asymptomatic patients," *The New England journal of medicine*, vol. 342, no. 17, pp. 1266–1271, 2000.
- [22] H. Aebi, "Catalase *in vitro*: B. isolation, purification, characterization, and assay of antioxygenic enzymes," *Methods in Enzymology*, vol. 105, pp. 121–126, 1984.
- [23] H. Ohkawa, N. Ohishi, and K. Yagi, "Assay for lipid peroxides in animal tissues by thiobarbituric acid reaction," *Analytical Biochemistry*, vol. 95, no. 2, pp. 351–358, 1979.
- [24] T. Martinello, F. Pascoli, G. Caporale, A. Perazzi, I. Iacopetti, and M. Patrino, "Might the Masson trichrome stain be considered a useful method for categorizing experimental tendon lesions?," *Histology and histopathology*, vol. 30, article 11601, 2015.
- [25] D. Shoseyov, H. Bibi, S. Offer et al., "Treatment of ovalbumin-induced experimental allergic bronchitis in rats by inhaled inhibitor of secretory phospholipase A(2)," *Thorax*, vol. 60, no. 9, pp. 747–753, 2005.
- [26] N. S. S. Shamshuddin and Z. R. Mohd, "Gelum honey attenuates ovalbumin-induced airway inflammation in a mice model of allergic asthma," *Journal of traditional and complementary medicine*, vol. 8, no. 1, pp. 39–45, 2018.
- [27] T. Ogawa, S. Miura, Y. Tsuzuki et al., "Chronic allergy to dietary ovalbumin induces lymphocyte migration to rat small intestinal mucosa that is inhibited by MAdCAM-1," *American Journal of Physiology-Gastrointestinal and Liver Physiology*, vol. 286, no. 5, pp. G702–G710, 2004.
- [28] H. Zemmouri, O. Sekiou, S. Ammar et al., "Urtica dioica attenuates ovalbumin-induced inflammation and lipid peroxidation of lung tissues in rat asthma model," *Pharmaceutical Biology*, vol. 55, no. 1, pp. 1561–1568, 2017.
- [29] W. H. Kim, H. J. An, J. Y. Kim et al., "Beneficial effects of melittin on ovalbumin-induced atopic dermatitis in mouse," *Scientific Reports*, vol. 7, no. 1, article 17679, 2017.
- [30] H. You, S. Chen, L. Mao et al., "The adjuvant effect induced by di-(2-ethylhexyl) phthalate (DEHP) is mediated through oxidative stress in a mouse model of asthma," *Food and Chemical Toxicology*, vol. 71, pp. 272–281, 2014.
- [31] W. C. Ko, C. B. Lei, Y. L. Lin, and C. F. Chen, "Mechanisms of relaxant action of S-petasin and S-isopetasin, sesquiterpenes of Petasites formosanus, in isolated guinea pig trachea," *Planta Medica*, vol. 67, no. 3, pp. 224–229, 2001.
- [32] O. A. Thomet, U. N. Wiesmann, K. Blaser, and H. U. Simon, "Differential inhibition of inflammatory effector functions by

- petasin, isopetasin and neopetasin in human eosinophils," *Clinical and experimental allergy*, vol. 8, pp. 1310–1320, 2001.
- [33] U. Danesch, "Petasites hybridus (butterbur root) extract in the treatment of asthma - an open trial," *Alternative Medicine Review*, vol. 9, no. 1, pp. 54–62, 2004.
- [34] R. Lipton, H. Göbel, K. Einhäupl, K. Wilks, and A. Mauskop, "Petasites hybridus root (butterbur) is an effective preventive treatment for migraine," *Neurology*, vol. 63, no. 12, pp. 2240–2244, 2004.
- [35] A. Wilson, K. Haggart, E. Sims, and B. Lipworth, "Effects of fexofenadine and desloratadine on subjective and objective measures of nasal congestion in seasonal allergic rhinitis," *Clinical and experimental allergy*, vol. 32, no. 10, pp. 1504–1509, 2002.
- [36] S. Oh, D. E. Sok, and M. Kim, "Neuroprotective effects of butterbur and rough aster against kainic acid-induced oxidative stress in mice," *Journal of medicinal food*, vol. 8, no. 2, pp. 169–176, 2005.
- [37] C. H. Park, M. Y. Kim, D. E. Sok, J. H. Kim, J. H. Lee, and M. R. Kim, "Butterbur (*Petasites japonicus* Max.) extract improves lipid profiles and antioxidant activities in monosodium L-glutamate-challenged mice," *Journal of medicinal food*, vol. 13, no. 5, pp. 1216–1223, 2010.

Research Article

Green-Synthesized Silver Nanoparticles Induced Apoptotic Cell Death in MCF-7 Breast Cancer Cells by Generating Reactive Oxygen Species and Activating Caspase 3 and 9 Enzyme Activities

Ikram Ullah ^{1,2}, Ali Talha Khalil,³ Muhammad Ali,¹ Javed Iqbal,⁴ Waqar Ali,⁵ Saud Alarifi,⁶ and Zabta Khan Shinwari^{1,7}

¹Department of Biotechnology, Quaid-i-Azam University, Islamabad 45320, Pakistan

²Qarshi Herb Research Centre, Qarshi Industries Pvt. Ltd., Hattar-Haripur, Pakistan

³Department of Pathology, Medical Technology Institution, Lady Reading Hospital, Peshawar, Pakistan

⁴Department of Plant Sciences, Quaid-i-Azam University, Islamabad 45320, Pakistan

⁵Department of Biotechnology, University of Malakand, Chakdara, Lower Dir, Pakistan

⁶Department of Zoology, College of Science, King Saud University, P.O. Box 2455, Riyadh 11451, Saudi Arabia

⁷Pakistan Academy of Sciences, Islamabad, Pakistan

Correspondence should be addressed to Ikram Ullah; ikrambiotech@gmail.com

Received 30 July 2020; Revised 25 August 2020; Accepted 26 August 2020; Published 6 October 2020

Academic Editor: Madhukar Saxena

Copyright © 2020 Ikram Ullah et al. This is an open access article distributed under the Creative Commons Attribution License, which permits unrestricted use, distribution, and reproduction in any medium, provided the original work is properly cited.

Silver nanoparticles are among the most significant diagnostic and therapeutic agents in the field of nanomedicines. In the current study, the green chemistry approach was made to optimize a cost-effective synthesis protocol for silver nanoparticles from the aqueous extract of the important anticancer plant *Fagonia indica*. We investigated the anticancer potential and possible involvement of AgNPs in apoptosis. The biosynthesized AgNPs are stable (zeta potential, -16.3 mV) and spherical with a crystal size range from 10 to 60 nm. The MTT cell viability assay shows concentration-dependent inhibition of the growth of Michigan Cancer Foundation-7 (MCF-7) cells (IC_{50} , 12.35 μ g/mL). In addition, the fluorescent microscopic analysis shows activation of caspases 3 and 9 by AgNPs that cause morphological changes (AO/EB assay) in the cell membrane and cause nuclear condensation (DAPI assay) that eventually lead to apoptotic cell death (Annexin V/PI assay). It was also observed that AgNPs generate reactive oxygen species (ROS) that modulate oxidative stress in MCF-7 cells. This is the first study that reports the synthesis of a silver nanoparticle mediated by *Fagonia indica* extract and evaluation of the cellular and molecular mechanism of apoptosis.

1. Introduction

Cancer of the breast is the most important cause of mortalities in women all over the globe. Various chemotherapeutic treatments can be applied for its treatment. However, they are costly and accompanied by frightening side effects. In addition, cells in breast cancer are becoming resistant to the various available chemotherapies [1]. Therefore, it is mandatory to search for alternative treatment options that are efficient, cost-effective, and biocompatible. Recently, metal and

metal oxide nanoparticles have developed as a stimulating area of research because of their widespread applications [2–8]. Nanobiotechnology has noteworthy applications in biomedical sciences as a field aiding therapeutics and diagnostics [9–11]. Recently, AgNPs have been comprehensively researched because of their interesting physical, biochemical, and therapeutic properties [12, 13].

Numerous chemical and physical methods are adopted for the synthesis of AgNPs [14]. Although these methods are effective, they come with some shortcomings. The chem-

ical and physical methods require high energy resources and generate toxic by-products and hazardous wastes [5, 15]. Recent researches indicate the presence of noxious chemicals with the chemically synthesized nanoparticles making them relatively unfavourable for biomedical applications [16]. To overcome the issue of energy balance and toxic by-products, complete green methods are used for the synthesis of AgNPs. Therefore, a paradigm shift is observed towards the biological synthesis of AgNPs. Many biological assets like plants, microbes, algae, and yeasts are used to synthesize nanoparticles [17]. However, due to their ample availability, low cost and a rich source of bio-reducing agents, plants, and plant products are the most frequently used approach for the synthesis of nanoparticles [18, 19]. Biosynthesis is beneficial over other methods because of its low cost, rapidity, single step synthesis, high yield, and biocompatibility [20]. Furthermore, the size can be controlled easily by adjusting the salt concentrations, pH, and temperature.

The interface of medicinal plants, nanoparticles, and cancer is an exciting horizon for the search of alternative and cheap chemotherapeutics. Herein, we optimized a complete green protocol for the phytosynthesis of AgNPs via aqueous extracts of the medicinally important plant *Fagonia indica*. Indigenous knowledge reveals potential anticancer properties of *Fagonia indica*. It is used in making herbal tea. Recent research also indicated the significant anticancer potential of *Fagonia* against MCF-7 cells [21]. Hitherto, the biological synthesis of AgNPs has been reported by researchers [13, 22, 23]; however, to date, no reports are available to study the anticancer mechanism of the phytosynthesized AgNPs mediated by the aqueous extract of *Fagonia indica*. This novel study describes the biosynthesis of AgNPs and investigates their cellular and molecular mechanisms of apoptosis caused by the *Fagonia* extract-mediated AgNPs. Earlier studies show various biological properties of biogenic AgNPs, such as antimicrobial [24–28], anticancerous [29–31], anti-angiogenic, antiparasitic [32, 33], cytotoxic [34–37], and antitumor [38, 39]. AgNPs have differential effects in the killing of cancer cells. Sanpui and his coworkers demonstrated that AgNPs induced apoptosis by affecting the membrane integrity and normal cellular functions [40]. Vasanth and his colleagues reported apoptosis in human cervical cells by treatment with AgNPs [29].

Chemotherapy and combinational chemotherapy are still the common methods for the treatment of breast cancer [41]. However, due to their potential disadvantages, it is imperative to look for alternative and effective treatments. The current study was intended to synthesize silver nanoparticles by a simple and ecofriendly process using medicinal flora. Furthermore, the phytosynthesized AgNPs were studied for their anticancer activities in MCF-7 breast cancer cells while their anticancer mechanism is unveiled using different mechanistic assays.

2. Materials and Methods

2.1. Optimization of AgNP Biosynthesis. The stock solution of *Fagonia indica* aqueous extract (5 mg/mL) and AgNO₃ (1 M)

was prepared in distilled water. AgNO₃ (extra pure, Merck) was diluted into 1, 2, 4, and 8 mM solutions. The extract and AgNO₃ solution were mixed in the ratio of 1:2, 1:4, 1:8, and 1:10. The reaction mixtures were kept at room temperature and at 50, 60, 70, 80, and 90°C in the dark. The time-dependent data were taken at an interval of 10, 20, 40, 60, 90, and 120 min and 3, 4, and 5 hrs. The solution was stirred for 4 hours, and a color change was observed. For characterization, the mixture was centrifuged for 20 min at 13,000 rpm to get the pellet. The pellet was washed three times to remove any unbound plant compounds with distilled water by repeated centrifugation. Finally, the pellet was freeze-dried and lyophilized. The powder AgNPs obtained were further processed for characterization.

2.2. Characterization of AgNPs. UV-vis (JASCO, V-530) with a resolution of 1 nm in the range of 300 to 600 nm was used to observe the reduction of Ag⁺ ions in a colloidal solution. The zeta potential and hydrodynamic size were calculated using a Zetasizer (Malvern Instruments Ltd., U.K.). The crystalline nature and size of the nanoparticles were confirmed through X-ray diffraction analysis (X-ray diffractometer, Bruker D8 Advance) equipped with 40 kV/30 Ma X-ray, $2\theta/\theta$ scanning mode, CuK α radiation ($\lambda = 1.5418 \text{ \AA}$) and a fixed monochromator in the range of 20–80 degrees. The Scherrer approximation ($D = k\lambda/\beta \cos \theta$) was used to calculate the average size of the nanoparticles. FT-IR was carried out at Shimadzu (Shimadzu Corporation) to investigate the type of functional groups involved in the reduction and capping of nanoscale silver. The samples for electron microscopy were gold coated (JEOL, Model No. JFC-1600), and images were obtained by scanning electron microscope (ZEISS EVO-MA 10, Oberkochen, Germany).

2.3. Cell Culture. Dulbecco's modified Eagle's medium (DMEM) pH = 7.2 to which 10% FBS was supplemented was used to culture breast cancer MCF-7 cells. The media were also added with gentamicin (100 U/mL) to prevent any cross contamination. A humidified incubator with 5% CO₂ was used to incubate cells. The cell population (80–90%) was harvested using trypsin then washed in PBS and used for further experiments.

2.4. Cell Viability Assays. The previously described protocol of MTT cytotoxicity assessment with slight modifications was used to investigate the viability of cells [42]. Cancer cells were grown to a density of 2×10^4 cells/well for 24 hours and then exposed to different test concentrations of AgNPs for 24 hours. After, PBS with added 5.0 mg/mL MTT was introduced at the rate of 10 μ L into each well and incubated for another 4 hours. The introduction of MTT led to the formation of formazan crystals inside the live cells. DMSO (100 μ L) was introduced for dissolving the formazan crystals, and the readings were taken at 570 nm using a microplate ELISA reader (BioTek).

2.5. Morphological Study with Fluorescence Microscopy. AgNP-treated MCF-7 cells were investigated by AO/EB fluorescence staining techniques for determination of apoptosis [43]. Briefly, six-well plates were used to culture MCF-7 cells

to a density of 1×10^5 cells per well for 24 hours. Cells were then exposed to the already calculated inhibitory concentration (IC_{50}) for 24 hrs. Unexposed cells to AgNPs were taken as the control. A mixture of the AO/EB dyes ($20 \mu\text{L}$) was prepared by mixing the two dyes prepared initially at $100 \mu\text{g}/\text{mL}$ in PBS each. After staining the treated and control samples, these cells were monitored and imaged by fluorescence microscope (Olympus) with excitation (488 nm) and emission (520 nm).

2.6. Observation of Chromatin Changes. 4,6-Diamidino-2-phenylindole (DAPI) staining assay was used to further examine the alterations of chromatin which is an integral part of the process of apoptosis [44]. The fluorescent dye DAPI was intended for the staining of nuclear DNA in cells which have undergone the process of apoptosis. Briefly, cells (MCF-7) were grown to the density of 1×10^6 cells/well and introduced to the 24-well plates in the log phase followed by 24 h incubation. Afterwards, the IC_{50} concentrations of photosynthesized AgNPs were applied, and the culture was kept for up to 24 hours. After the treatment, 1x PBS was used to wash the cells which were fixed with $50 \mu\text{L}$ of water and methanol mixed together in 1:1. $100 \mu\text{L}$ of the $1 \mu\text{g}/\text{mL}$ of the DAPI dye was used for staining followed by incubation at 37°C for 30 minutes in the dark. $20 \mu\text{L}$ of PBS:glycerin (1:1) was introduced to remove the excess dye. Changes in chromatin were observed under inverted fluorescence microscope (40x). Apoptotic cells were expressed in percentage calculated as

$$\% \text{apoptotic cells} = \left(\frac{\text{amount of apoptotic nuclei}}{\text{amount of all cells}} \right) \times 100 \quad (1)$$

2.7. Cell Apoptosis Assay. The quantification of the extent of apoptosis was performed by using Annexin V-FITC/PI double staining assay [45]. Only the IC_{50} concentration of AgNPs was considered for the treatment. Briefly, washing was carried out with PBS for the collected cells at least two times, and then staining was carried out with PI and Annexin V-FITC. Flow cytometry (Millipore Corporation, Billerica, MA, USA) was performed. Number of live cells, necrotic cells, late apoptotic cells, and early apoptotic cells were distinguished by direct counting of the cells.

2.8. Quantification of Caspase 3 and 9 Activities. Caspase 3 and 9 assay kits (Caspase-Glo[®] 3 and 9 reagents, Promega) were used to quantify caspase activities. Briefly, 50,000 MCF-7 cells/well were seeded in a 96-well plate. The cells were incubated in a 5% CO_2 humidified incubator at 37°C for 24 hours. The 96-well plates containing AgNP-treated and AgNP-untreated control cells were then allowed to equilibrate at room temperature. $100 \mu\text{L}$ of Caspase-Glo[®] 3 or 9 reagent was added to each well of a 96-well plate (test well and control) containing $100 \mu\text{L}$ of culture medium. The plate was covered and the content mixed for 30 seconds at 500 rpm. The optical density was measured (ELISA reader, BioTek) at 405 nm after incubation of the plate at room temperature for 30 min.

2.9. ROS Assay in MCF-7 Cells. Dichlorofluorescein diacetate (DCFDA) probes were used to investigate the intracellular ROS production [46]. Briefly, the MCF-7 cells were seeded in 12-well plates for 24 hours and then treated with the IC_{50} concentration of AgNPs for 24 h. Trypsin EDTA was used to detach the cells. The cells were washed with PBS and resuspended in $200 \mu\text{L}$ PBS containing a 10 mM DCFH-DA fluorescent probe. The reaction mixture was incubated for 30 minutes at 37°C . The extent of ROS generated was measured through a fluorescent spectrophotometer.

2.10. Data Analysis. Cytotoxicity of the nanoparticles was expressed as the concentration ($\mu\text{g}/\text{mL}$) inhibiting the growth of 50% cells (IC_{50}). Data was analyzed through MS Excel 2019, and IC_{50} was estimated through TableCurve 2D software. The graphs were prepared with OriginPro 8.1 and GraphPad.

3. Results and Discussions

3.1. Biosynthesis. Biosynthesis of AgNPs using the green route has been optimized using the extract of *Fagonia indica*. Biological synthesis is considered the most adequate method compared to the physical and chemical means. Hitherto, while being effective, these physical and chemical synthesis methods are accompanied by certain disadvantages like cost, energy demands, and generation of toxic hazardous waste streams [15, 47]. Furthermore, in some reports, it was indicated that some toxic chemicals could remain adhered with the nanoparticles synthesized from chemical means which could not be used in biomedical applications [16, 48]. Therefore, biomodulated synthesis of AgNPs is preferred. *Fagonia indica* is a very important medicinal plant, and its therapeutic potential is well documented. Recent reports suggested the significant anticancer potential for the *Fagonia* species under in vitro conditions [49]. The medicinal potential of *Fagonia* is attributed to the novel phenolic and flavonoid chemical components, and these phytochemicals play the role of chelation and stabilize the nanoparticles in their biosynthesis. Although the biogenic synthesis of Ag nanoparticles has been reported successfully via plants, biosynthesis using medicinal plants with anticancer potential is rare. A mechanism proposed for the biosynthesis has been suggested in Figure 1.

3.2. UV-Vis Spectrophotometry. Biomodulated synthesis of AgNPs was optimized using different parameters. These parameters include optimization by (a) precursor concentration, (b) extract concentration, (c) temperature, and (d) time. As the aqueous extracts were added to the precursor solution, a color change was observed which indicates a successful reduction process. Figure 2 indicates the variation in color from light brown to darkish brown which can be attributed to the enhancement in the bioreduction process.

Aqueous extract-mediated reduction of AgNO_3 in AgNPs was monitored using a spectrophotometer in the UV-visible range. The surface plasmon resonance was found

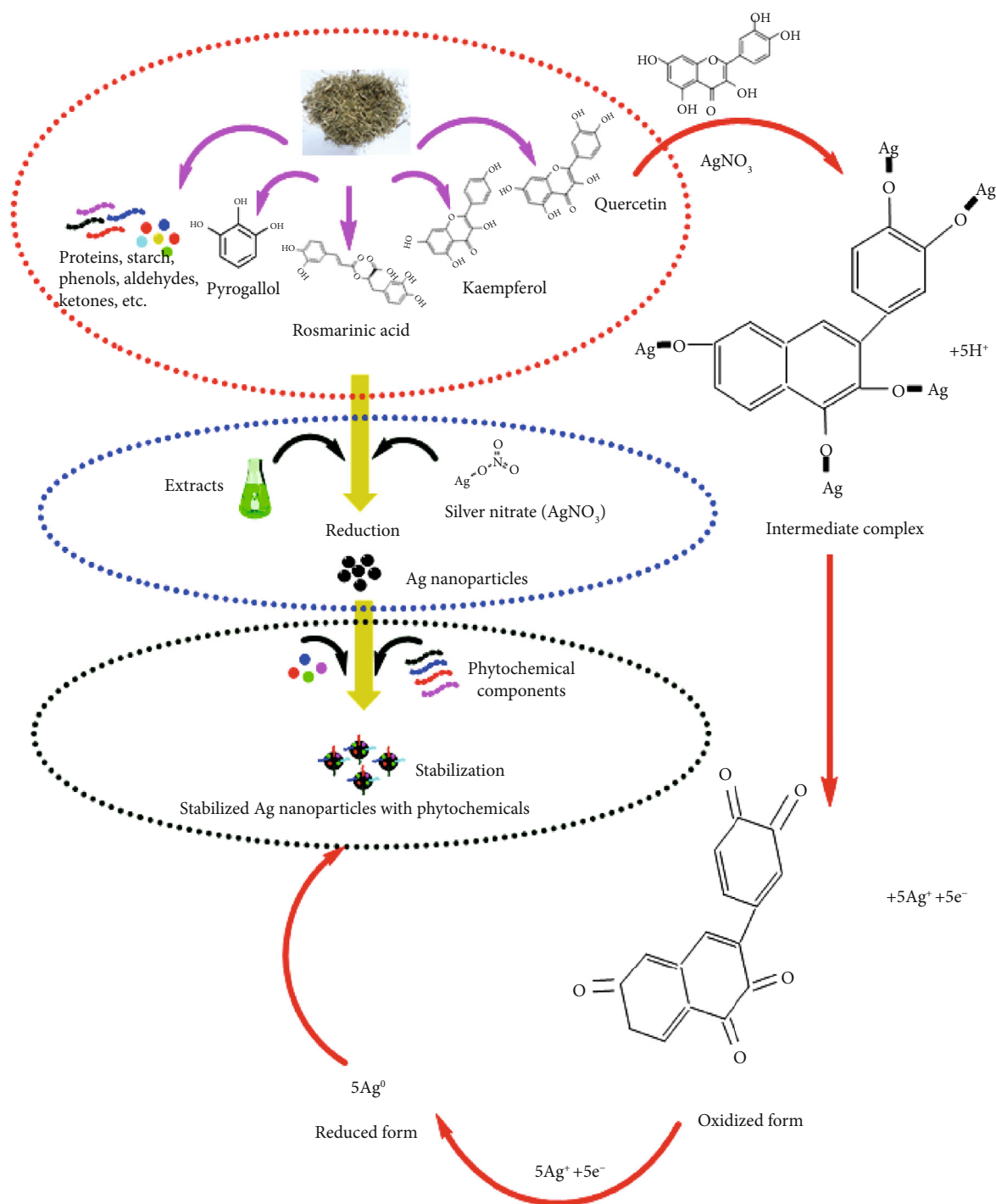


FIGURE 1: Proposed mechanism of silver ion reduction by plant metabolite into silver nanoparticles.

to be ~430 nm. Results of the various optimization parameters are presented in Figures 3(a)–3(d). The concentration of 1 mM AgNO₃ was found to be effective and yielded silver nanoparticles, while at higher concentrations, the biosynthesis was insignificant as indicated in Figure 3(a). Therefore, the concentration of 1 mM was processed for the further optimization experiments. Figure 3(b) suggests the variation in concentrations of plant extracts by keeping the concentration of the precursor as 1 mM as indicated in

Figure 3(b). Temperature-dependent biosynthesis was performed by applying a varying degree of temperature with a difference of 5°C between the ranges of 40°C to 60°C. It can be observed that below 50°C, there was no formation of AgNPs. Ag nanoparticle formation was indicated at 55°C and 60°C. The temperature of 60°C was considered as the optimum temperature for biomodulated AgNP synthesis. Furthermore, the formation of AgNPs was monitored relative to time. Time-based optimization was

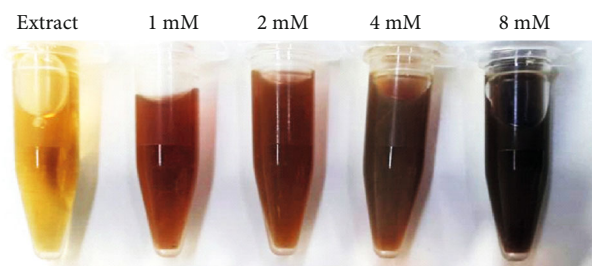


FIGURE 2: Variation in color intensity of green silver nanoparticles mediated at different AgNO_3 concentrations by leaf extracts combined at the ratio of 1 to 10 (extract : AgNO_3).

carried out from 0 hr to 2 hrs. It was investigated that the biosynthesis was increased relative to the increase in the time period. Biosynthesis was maximum after the duration of 2 hrs as deduced from Figure 3(d). Already optimized parameters were used to carry out the biosynthesis. The results of our study using UV-vis spectroscopy are consistent with the earlier study reported using diverse plant extracts [50–54].

3.3. X-Ray Diffraction (XRD). XRD analysis was used to examine the crystallinity level of silver nanoparticles. Figure 4 demonstrates the XRD pattern of biosynthesized AgNPs. The obtained Bragg peaks were found to be consistent with crystallographic reflections from 111 (35.68°), 200 (51.62°), 220 (65.86°), and 311 (77.95°) that corresponds to the JCPDS pattern 04-0783. Average size was calculated as 12.09 nm using the Debye-Scherrer approximation [55]; the results accord with previous results reported by Ullah et al. [56], Prakash et al. [57], and Ajitha et al. [58].

3.4. Dynamic Light Scattering (DLS) Analysis. The size distribution was further studied using the dynamic light scattering technique. An average hydrodynamic particle size was calculated as 23.68 nm with a polydispersity index near 1. Our result agrees with the particle size of 27 to 32 nm obtained by Kotakadi et al. [59] using the leaf extract of *Catharanthus roseus*. Anandalakshmi and coworkers reported a hydrodynamic size of 150 nm with a diameter of 74 nm [60]. Zeta potential value is an indicator of the stability of the nanoparticle which was calculated as -16.3 mV (Figure 5). The zeta potential is the electric potential resulting from the distribution of charges which indirectly determine the stability of nanoparticles in colloidal suspension [61]. Our results are consistent with the earlier data reported by many research groups [9, 62].

3.5. Scanning Electron Microscopy (SEM). SEM micrograph is indicated in Figure 6. The figure shows polydispersed nanoparticles with low agglomeration. The shape of the nanoparticles was observed to be spherical (73.37 at the 200 nm scale). Remya et al. obtained nanoscale silver with a size range of 25–51 nm using *Cassia fistula* flower extract [63]. The same type of results was reported in *Acalypha*

indica- and *Syzygium alternifolium*-mediated syntheses of AgNPs [24, 64].

3.6. Cytotoxicity. 3-(4,5-Dimethylthiazol-2-Yl)-2,5-diphenyl-tetrazolium bromide (MTT) cell viability assay was used to determine the cytotoxicity of the extract and AgNPs in MCF-7 cells. The percent growth inhibition of the MCF-7 cells at different doses (5, 10, 20, 25, 50, 100 and 200 $\mu\text{g}/\text{mL}$) was compared to that of untreated cells. Figure 7(a) shows a concentration-dependent growth inhibition of *in vitro* cultured breast cancer cells. The IC_{50} value was calculated as 12.35 $\mu\text{g}/\text{mL}$ for AgNP-treated cells and 25.09 $\mu\text{g}/\text{mL}$ for extract-treated cells. This 50% cytotoxic concentration was used for further experiments in this study. Earlier studies report the same type of results studying the effect of green-synthesized AgNPs in MCF-7 cells [22, 65, 66].

3.7. Acridine Orange-Ethidium Bromide (AO/EB) Fluorescent Assay. The AO/EB fluorescence microscopic staining assay was used to observe the morphological changes in MCF-7 cells. AO/EB staining differentiates between apoptotic and normal cells. Figure 8 shows the control untreated, extract, and AgNP-treated cells at 12.35 $\mu\text{g}/\text{mL}$ (AgNPs) and 25.09 $\mu\text{g}/\text{mL}$ (extract) concentrations after 24 hours. The figure shows that the control cells did not change and the cell remains green after staining, whereas the color of the treated cells changed (orange), indicating the apoptotic cells. Moreover, the treated cells show membrane blebbing, shrinkage, and nuclear fragmentation. The same type of membrane changes was observed in MCF-7-treated cells of *Morinda pubescens*-synthesized silver nanoparticles [67], *Teucrium stocksianum* extract-mediated AgNPs [23], *Syzygium aromaticum* extract-mediated AgNPs [22, 68], and *Solanum trilobatum* fruit extract silver nanoparticles [69].

3.8. Nuclear Morphology. The outcome of AgNPs on nuclear changes was observed using the DAPI staining assay. Figure 8 indicates significant changes in the morphology of the chromatin nuclear material after DAPI staining of AgNP and extract-treated cells for 24 hours compared to the untreated control. It can be observed that the control cells have normal rounded nuclei with normal blue color, whereas the treated cells have a bright color, abnormal nuclei, and condensed chromatin with irregular cell structure. These results are consistent with Ciftci et al. [70]. Our results coincide with the previous studies on the influence of green-synthesized AgNPs and plant alkaloids on apoptosis in MCF-7 cells [22, 71, 72]. The apoptosis was further confirmed with Annexin V/PI flow cytometric assay.

3.9. Annexin V/Propidium Iodide Apoptosis Detection Assay. To further confirm apoptosis, Annexin V/PI staining assay was used. The assay demonstrated the apoptosis in cancer cells exposed to AgNPs (12.35 $\mu\text{g}/\text{mL}$) and extract (25.09 $\mu\text{g}/\text{mL}$) for 24 hours. Figure 9 shows that untreated cells did not display any significant apoptosis, whereas extract and AgNP-treated cells become apoptotic after 24

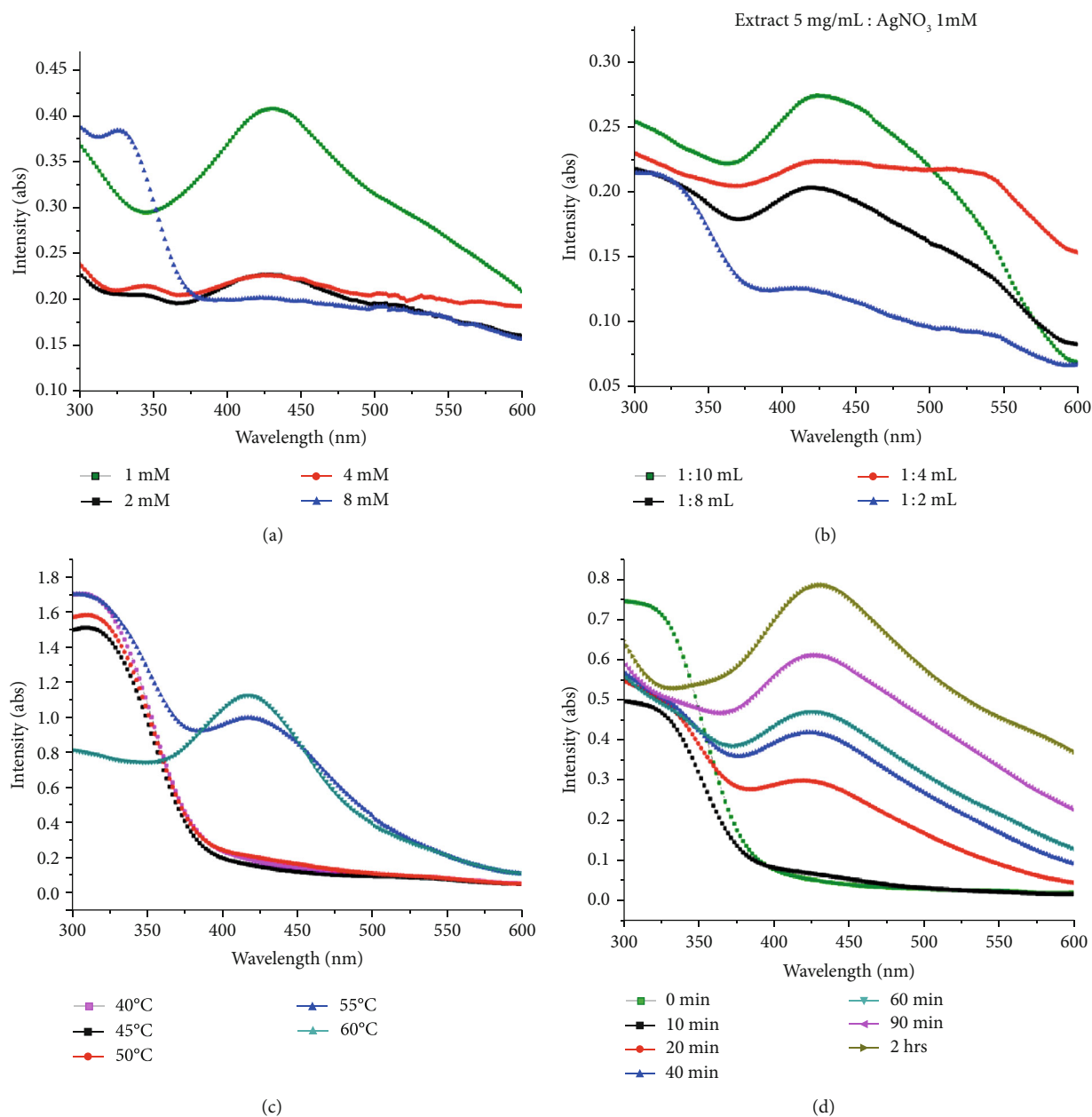


FIGURE 3: Optimization of different parameters for bioinspired synthesis of silver nanoparticles. UV-vis spectrum of AgNPs mediated by leaf aqueous extracts of *Fagonia indica*: (a) effect of AgNO_3 concentration, (b) effect of extract and AgNO_3 (1 mM) ratios on the synthesis of green nanoparticles, (c) effect of temperature, and (d) duration of time for synthesis of silver nanoparticles at different time intervals.

hours with early apoptotic cell populations of 43.05% and an apoptotic population of 23.62%. Changes in the population of viable cells indicate that the cell becomes apoptotic due to AgNP-inducing antitumor activities. Similarly, Sriram and colleagues studied the anticancer effects of AgNPs in a tumor model and observed a decrease in the tumor volume [38]. Furthermore, silver nanoparticles induce various biochemical pathways that are involved in the enhanced anticancer activities in MCF-7 cells (Figure 10). Liang et al. [73] and Venugopal et al. [68] observed that green-synthesized silver nanoparticles conjugated with hyaluronic acid-induced apoptosis in cells via

autophagy, mitochondrial dysfunction, arrest of the cell cycle, and causing lipid peroxidation.

3.10. Caspase 3 and 9 Activities. Apoptosis is the course of programmed cellular death that manifests disassembling of the intracellular components while avoiding harm and inflammation of surrounding cells [74]. Caspases are involved in the regulation of inflammatory responses and cell death [75]. Functionally, caspases have two main types, i.e., effector (caspases 3, 6, and 7) and initiator (caspases 2, 8, 9, and 10) caspases [76, 77]. Apoptosis is initiated by the interaction of caspase 3 with

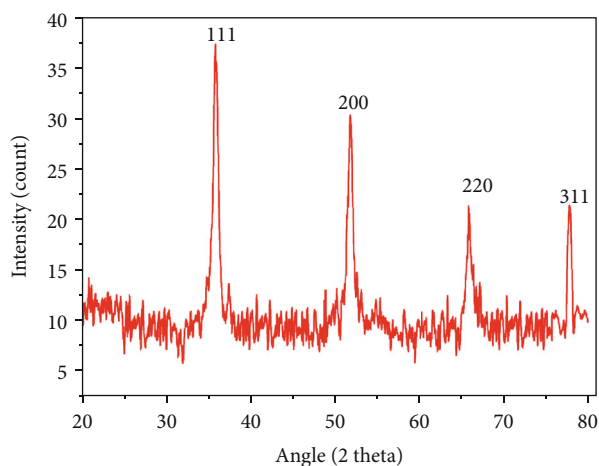


FIGURE 4: X-ray diffraction (XRD) pattern of green-synthesized AgNPs showing Bragg reflection at angle 2 theta.

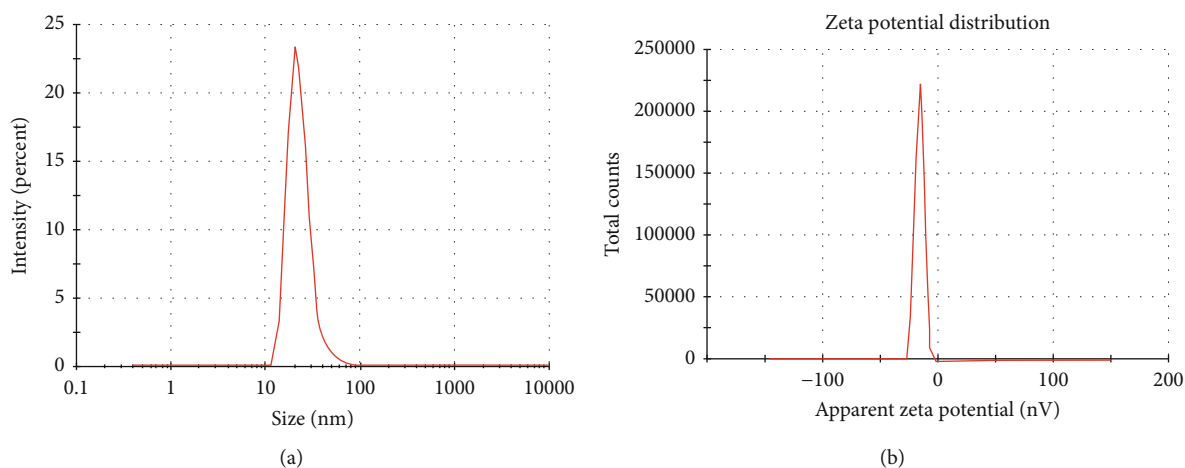


FIGURE 5: DLS analysis of green-synthesized nanoparticles in (a) zeta size and (b) zeta potential.

caspses 8 and 9. This signal interaction also displays no return in the apoptotic pathway [78]. The apoptosis was further authenticated by measuring the level of the caspase 3 and 9 production in AgNP and extract-treated MCF-7 cells over the untreated control group. Caspses 3 and 9 are the terminal phase inducer of program cell death in cancer cells when activated by external stimuli. The caspase 3 and 9 activities were twofold enhanced in cells exposed to AgNPs and extract compared to control (untreated) cells (Figure 11). The results are consistent with that of Kikuchi et al. [79, 80]. Morphological changes in the membrane and nucleus suggest the possible role of silver nanoparticles in inducing apoptosis in cancer cells [22]. During apoptosis, a series of initiator caspses, e.g., caspase 9, and executioner caspses, e.g., caspase 3, are expressed as an inactive zymogen in the cytoplasm that helps in the program cell death [81, 82]. AgNPs activate these caspses 3 and 9 and some other reactive oxygen species that cause DNA damage, endoplasmic reticulum stress, misfolding of proteins, and apoptosis as

shown in Figure 10. It has been reported that on activation, caspase 3 cleaves and translocates caspase-activated DNase (CAD) that results in DNA fragmentation. DNA fragmentation by endonuclease activity is considered as a prominent event in the apoptosis which occurs in the early stages [83]. The same type of observation was made by Arora et al. studying the effect of AgNPs on cellular responses [84].

3.11. Measurement of ROS (Reactive Oxygen Species). The oxidative pressure made by the free radical produced in response to the external stimuli is the premier cause of apoptosis in cancer cells. Previous research indicates that AgNPs cause oxidative stress and suppress the function of tumor suppressor genes, reduce mitochondrial potential, and induce lipid peroxidation that results in cell apoptosis [85]. A possible mechanism by which apoptosis is manifested by AgNPs is shown in Figure 10. The production of ROS was estimated after treating MCF-7 cells with extract (25.09 $\mu\text{g}/\text{mL}$) and AgNPs (12.35 $\mu\text{g}/\text{mL}$).

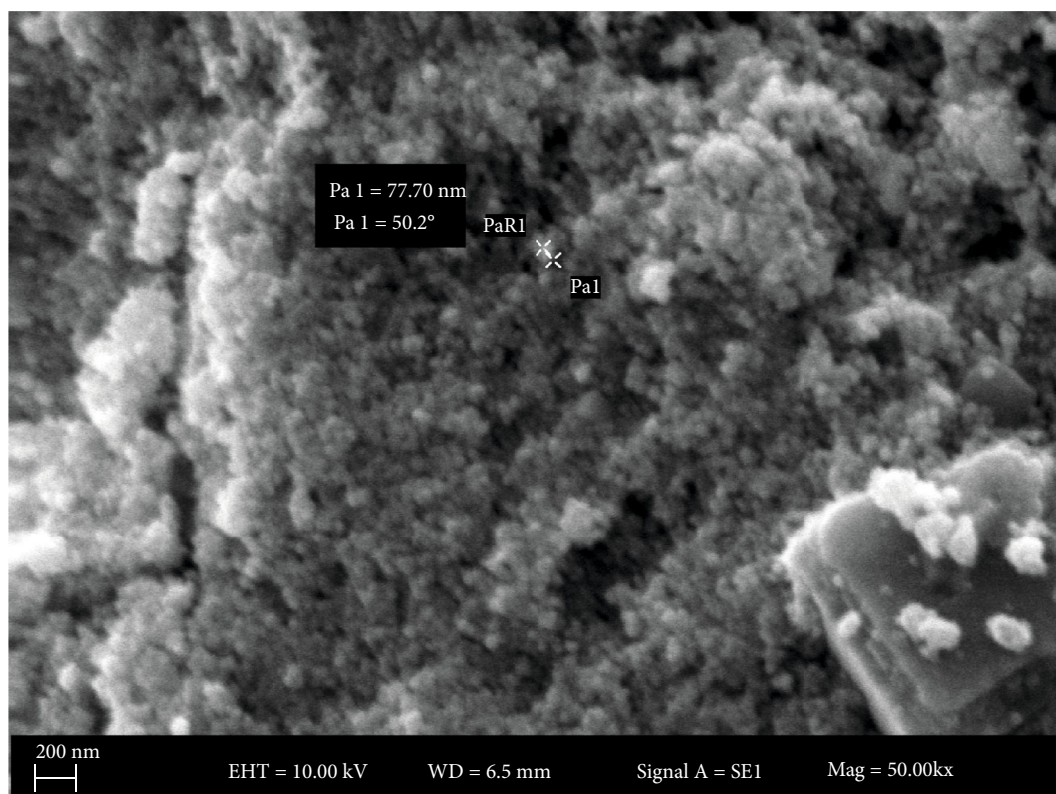


FIGURE 6: Morphology of AgNPs. SEM micrograph at the scale of 200 nm shows spherical nanoparticles.

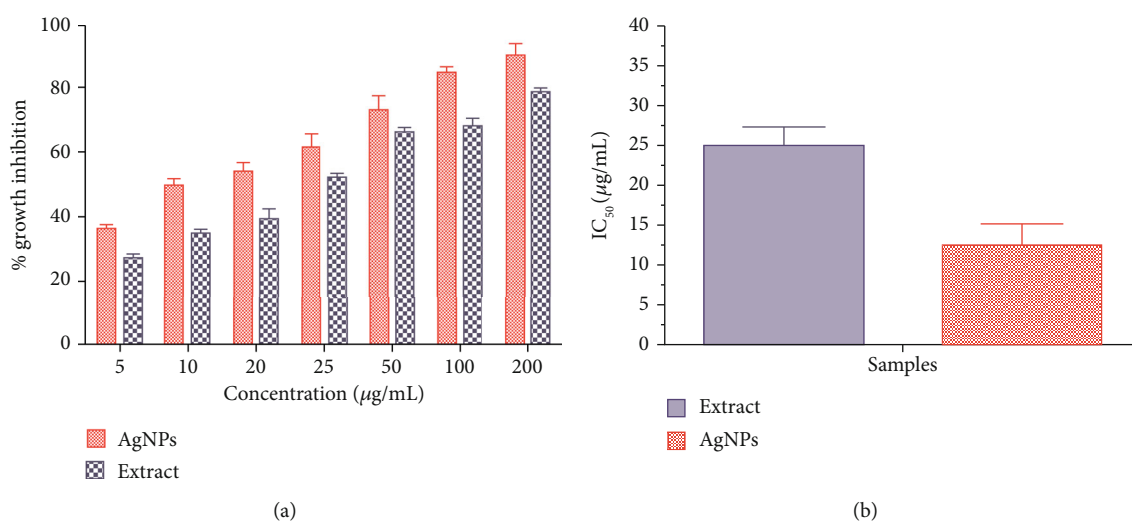


FIGURE 7: Cytotoxicity of extract and AgNPs in MCF-7 cells. Values are the average \pm standard deviation of three experiments conducted in duplicates: (a) percent growth inhibition; (b) IC_{50} concentration.

The estimation of ROS equivalent to H_2O_2 (μM) was evaluated compared to the control untreated cell with a different time interval. Figure 12 demonstrates the quantification of ROS in AgNP- and extract-exposed cells related to the control cells. However, AgNPs were more efficient in the production of ROS as compared to extract-treated cells. This may be due to the effect

wherein the plant extract has the ability to scavenge some free radicals. The production of ROS was maximum after 16 hours, and it turned to decrease gradually. The effect of ROS on cellular events depends on the concentrations and duration of treatment. A typical response of cellular events during stress condition is the cell cycle arrest at the G_0 phase, mitochondrial dysfunction, and apoptosis

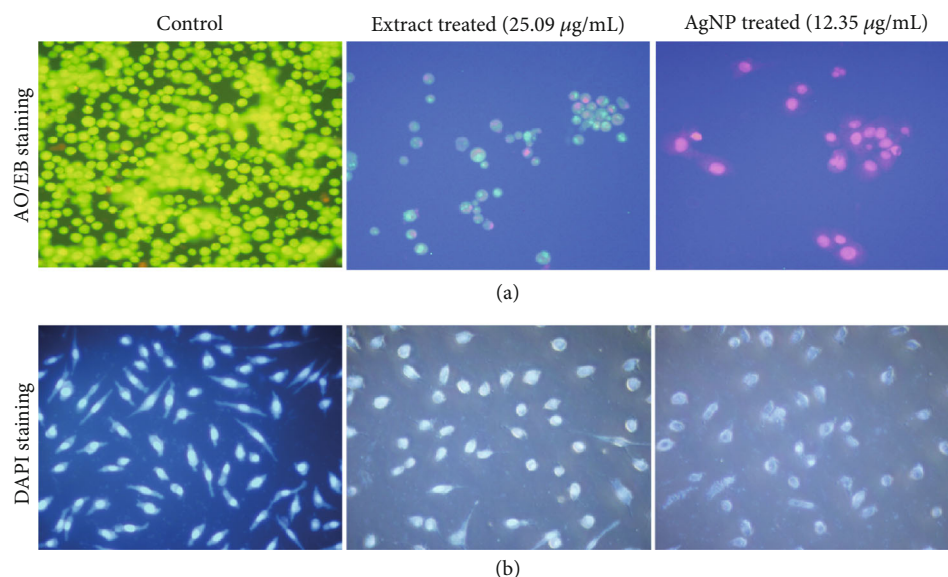


FIGURE 8: Morphological observation of MCF-7 cells treated with extract and AgNPs. (a) Acridine orange-ethidium bromide (AO/EB) staining. Green indicates viable cells, and reddish/orange staining of the cells indicates apoptotic cells. (b) Morphological changes in the nuclei of MCF-7 cells after treatment with extract and AgNPs induced apoptosis. The changes were observed with DAPI nuclear staining of the treated cells.

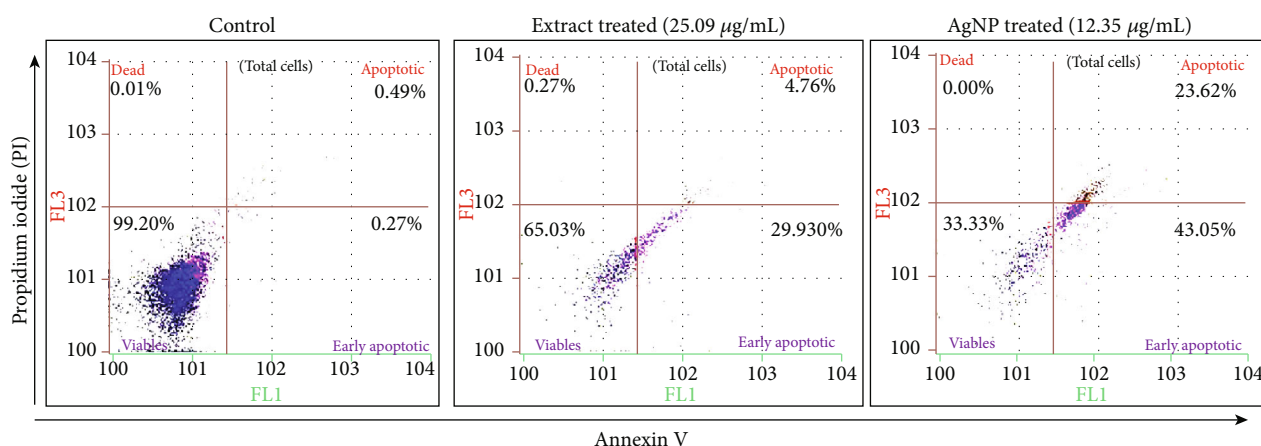


FIGURE 9: Flow cytometry analysis of MCF-7 cells by double-labelling with Annexin V and PI dyes. The figure shows the early apoptotic, late apoptotic, live, and dead cells given in each quadrant of the untreated growth control cell compared to AgNP-treated cells.

[86]. The level of ROS-triggering agents is proposed to be used as a therapeutic agent that can selectively kill cancer cells [69, 87]. We observed that the level of ROS generated by AgNPs is on a time-dependent manner. Hsin and colleagues reported that AgNPs generate ROS (reactive oxygen species) in the NIH3T3 cell and induce mitochondria-dependent apoptosis by activating the JNP pathway [88]. ROS are free radicals generated by the biological system for their normal cell functions. The abnormal level of ROS results in the malfunction of cellular components that cause damage to DNA, lipid peroxidation, arresting cell cycle caspase activation, and apoptosis [89].

4. Conclusion

In this study, we report a one-step biosynthesis of eco-friendly and stable AgNPs from *Fagonia indica* leaf extract at an optimum condition of 1 mM AgNO₃ when combined with 5 mg/mL extract in a ratio of 1:10 (extract to AgNO₃) at 60°C for 2 hours. Furthermore, controlled size nanoparticles (10-60 nm) were obtained that were confirmed by XRD, DLS, and SEM analyses. The *Fagonia indica* extract and AgNPs induced anticancer activity in a concentration-dependent manner. The NPs and extract induce membrane permeability, nuclear condensation in an apoptotic manner due to activation of caspases, and

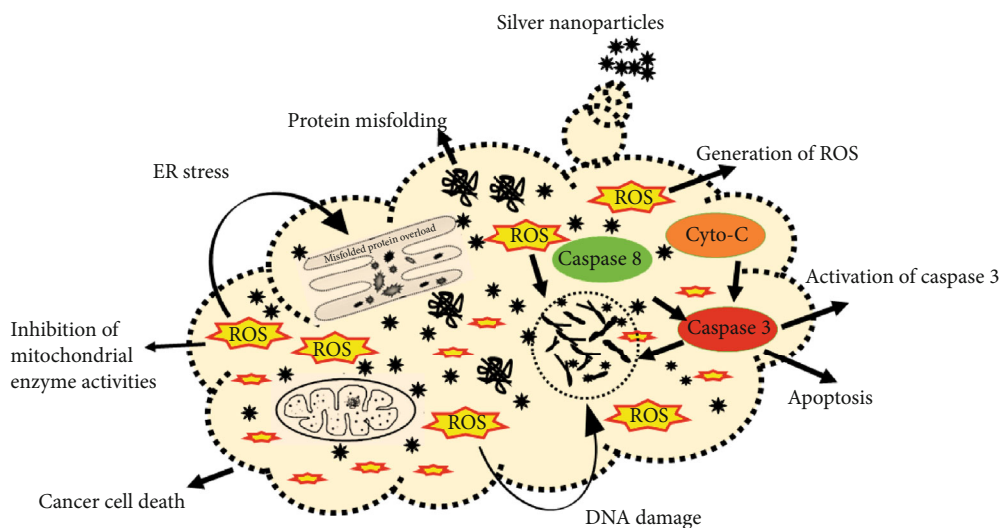


FIGURE 10: Proposed mechanism of apoptosis induced by caspases and reactive oxygen species.

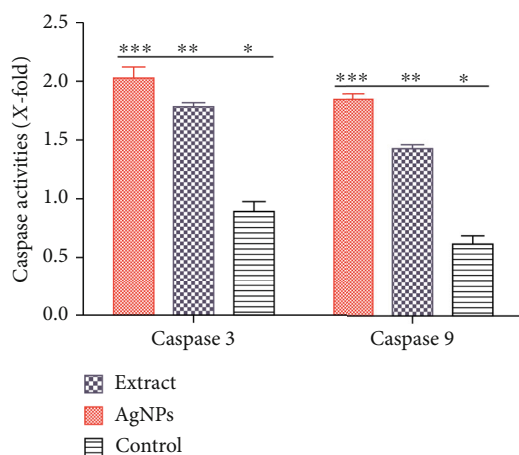


FIGURE 11: Quantification of caspase 3 and caspase 9 activity in MCF-7 cells exposed to 12.35 $\mu\text{g}/\text{mL}$ AgNPs and 25.09 $\mu\text{g}/\text{mL}$ extract.

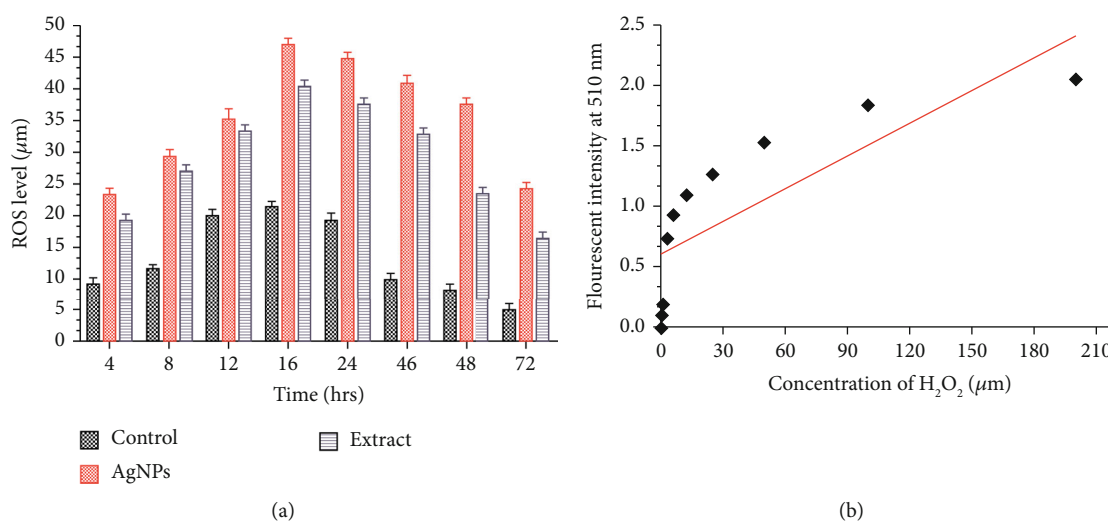


FIGURE 12: Effects of extract and AgNP exposition on ROS generation in MCF-7 cells. (a) Extent of H_2O_2 generation at different time intervals in MCF-7 cells stained with a DCFDH fluorescent probe. (b) Standard curve of H_2O_2 .

generation of reactive oxygen species. Furthermore, these nanoparticles have the potential for the future development of the anticancer drug.

Data Availability

The data analyzed and mentioned in the text are all included in the manuscript and available to the reader.

Conflicts of Interest

The authors declare that they have no conflict of interest.

Acknowledgments

This work was funded by the Researchers Supporting Project number RSP-2020/27, King Saud University, Riyadh, Saudi Arabia.

References

- [1] V. Özmen, "Breast cancer in the world and Turkey," *Journal of Breast Health*, vol. 4, pp. 7–12, 2008.
- [2] A. T. Khalil, M. Ovais, I. Ullah et al., "Sageretia thea (Osbeck.) mediated synthesis of zinc oxide nanoparticles and its biological applications," *Nanomedicine*, vol. 12, no. 15, pp. 1767–1789, 2017.
- [3] A. T. Khalil, M. Ovais, I. Ullah et al., "Sageretia thea (Osbeck.) modulated biosynthesis of NiO nanoparticles and their in vitro pharmacognostic, antioxidant and cytotoxic potential," *Artificial Cells, Nanomedicine, and Biotechnology*, vol. 46, no. 4, pp. 838–852, 2018.
- [4] A. T. Khalil, M. Ovais, I. Ullah, M. Ali, Z. K. Shinwari, and M. Maaza, "Biosynthesis of iron oxide (Fe₂O₃) nanoparticles via aqueous extracts of Sageretia thea (Osbeck.) and their pharmacognostic properties," *Green Chemistry Letters and Reviews*, vol. 10, no. 4, pp. 186–201, 2017.
- [5] F. T. Thema, E. Manikandan, M. S. Dhlamini, and M. Maaza, "Green synthesis of ZnO nanoparticles via Agathosma betulina natural extract," *Materials Letters*, vol. 161, pp. 124–127, 2015.
- [6] F. T. Thema, E. Manikandan, A. Gurib-Fakim, and M. Maaza, "Single phase Bunsenite NiO nanoparticles green synthesis by Agathosma betulina natural extract," *Journal of Alloys and Compounds*, vol. 657, pp. 655–661, 2016.
- [7] S. Vasantharaj, N. Sripriya, M. Shanmugavel, E. Manikandan, A. Gnanamani, and P. Senthilkumar, "Surface active gold nanoparticles biosynthesis by new approach for bionanocatalytic activity," *Journal of Photochemistry and Photobiology B: Biology*, vol. 179, pp. 119–125, 2018.
- [8] M. Anbuvaran, M. Ramesh, E. Manikandan, and R. Srinivasan, "Vitex negundo leaf extract mediated synthesis of ZnO nanoparticles and its antibacterial and photocatalytic activities," *Asian Journal of Nanoscience and Materials*, vol. 2, pp. 99–110, 2019.
- [9] S. Mukherjee, D. Chowdhury, R. Kotcherlakota et al., "Potential theranostics application of bio-synthesized silver nanoparticles (4-in-1 system)," *Theranostics*, vol. 4, no. 3, pp. 316–335, 2014.
- [10] S. Mukherjee, V. B. S. Prashanthi, P. R. Bangal, B. Sreedhar, and C. R. Patra, "Potential therapeutic and diagnostic applications of one-step in situ biosynthesized gold nanoconjugates (2-in-1 system) in cancer treatment," *RSC Advances*, vol. 3, no. 7, pp. 2318–2329, 2013.
- [11] Q. Li, S. Mahendra, D. Y. Lyon et al., "Antimicrobial nanomaterials for water disinfection and microbial control: potential applications and implications," *Water Research*, vol. 42, no. 18, pp. 4591–4602, 2008.
- [12] S. Dehghanizade, J. Arasteh, and A. Mirzaie, "Green synthesis of silver nanoparticles using Anthemis atrapatana extract: characterization and in vitro biological activities," *Artificial Cells, Nanomedicine, and Biotechnology*, vol. 46, no. 1, pp. 160–168, 2018.
- [13] H. E. A. Mohamed, S. Afridi, A. T. Khalil et al., "Biosynthesis of silver nanoparticles from Hyphaene thebaica fruits and their in vitro pharmacognostic potential," *Materials Research Express*, vol. 6, no. 10, p. 1050c9, 2019.
- [14] S. Iravani, H. Korbekandi, S. Mirmohammadi, and B. Zolfaghari, "Synthesis of silver nanoparticles: chemical, physical and biological methods," *Research in pharmaceutical sciences*, vol. 9, p. 385, 2014.
- [15] A. Diallo, B. D. Ngom, E. Park, and M. Maaza, "Green synthesis of ZnO nanoparticles by Aspalathus linearis: structural & optical properties," *Journal of Alloys and Compounds*, vol. 646, pp. 425–430, 2015.
- [16] A. K. Zak, W. H. B. A. M. Razali, and M. Darroudi, "Synthesis and characterization of a narrow size distribution of zinc oxide nanoparticles," *International Journal of Nanomedicine*, vol. 6, p. 1399, 2011.
- [17] M. K. Swamy, K. M. Sudipta, K. Jayanta, and S. Balasubramanya, "The green synthesis, characterization, and evaluation of the biological activities of silver nanoparticles synthesized from Leptadenia reticulata leaf extract," *Applied Nanoscience*, vol. 5, no. 1, pp. 73–81, 2015.
- [18] J. Y. Song and B. S. Kim, "Rapid biological synthesis of silver nanoparticles using plant leaf extracts," *Bioprocess and Biosystems Engineering*, vol. 32, no. 1, pp. 79–84, 2009.
- [19] F. Erci, R. Cakir-Koc, and I. Isildak, "Green synthesis of silver nanoparticles using Thymbra spicata L. var. spicata (zahter) aqueous leaf extract and evaluation of their morphology-dependent antibacterial and cytotoxic activity," *Artificial cells, nanomedicine, and biotechnology*, vol. 46, no. sup1, pp. 150–158, 2018.
- [20] H. Singh, J. Du, and T.-H. Yi, "Green and rapid synthesis of silver nanoparticles using Borago officinalis leaf extract: anticancer and antibacterial activities," *Artificial Cells, Nanomedicine, and Biotechnology*, vol. 45, no. 7, pp. 1310–1316, 2016.
- [21] M. Lam, A. R. Carmichael, and H. R. Griffiths, "An aqueous extract of Fagonia cretica induces DNA damage, cell cycle arrest and apoptosis in breast cancer cells via FOXO3a and p53 expression," *Plo S one*, vol. 7, no. 6, article e40152, 2012.
- [22] K. Venugopal, H. A. Rather, K. Rajagopal et al., "Synthesis of silver nanoparticles (Ag NPs) for anticancer activities (MCF 7 breast and A549 lung cell lines) of the crude extract of Syzygium aromaticum," *Journal of Photochemistry and Photobiology B: Biology*, vol. 167, pp. 282–289, 2017.
- [23] I. Ullah, E. Ş. Abamor, M. Bağırova, Z. K. Shinwari, and A. M. Allahverdiyev, "Biomimetic production, characterisation, in vitro cytotoxic and anticancer assessment of aqueous extract-mediated AgNPs of Teucrium stocksianum Boiss," *IET Nanobiotechnology*, vol. 12, no. 3, pp. 270–276, 2018.

- [24] P. Yugandhar and N. Savithamma, "Biosynthesis, characterization and antimicrobial studies of green synthesized silver nanoparticles from fruit extract of *Syzygium alternifolium* (Wt.) Walp. An endemic, endangered medicinal tree taxon," *Applied Nanoscience*, vol. 6, no. 2, pp. 223–233, 2016.
- [25] Y. Rout, S. Behera, A. K. Ojha, and P. Nayak, "Green synthesis of silver nanoparticles using *Ocimum sanctum* (Tulashi) and study of their antibacterial and antifungal activities," *Journal of Microbiology and Antimicrobials*, vol. 4, no. 6, pp. 103–109, 2012.
- [26] A. Petica, S. Gavriliu, M. Lungu, N. Buruntea, and C. Panzaru, "Colloidal silver solutions with antimicrobial properties," *Materials Science and Engineering: B*, vol. 152, no. 1-3, pp. 22–27, 2008.
- [27] H. Padalia, P. Moteriya, and S. Chanda, "Green synthesis of silver nanoparticles from marigold flower and its synergistic antimicrobial potential," *Arabian Journal of Chemistry*, vol. 8, no. 5, pp. 732–741, 2015.
- [28] R. Janthima, A. Khamhaengpol, and S. Siri, "Egg extract of apple snail for eco-friendly synthesis of silver nanoparticles and their antibacterial activity," *Artificial Cells, Nanomedicine, and Biotechnology*, vol. 46, no. 2, pp. 361–367, 2017.
- [29] K. Vasanth, K. Ilango, R. MohanKumar, A. Agrawal, and G. P. Dubey, "Anticancer activity of *Moringa oleifera* mediated silver nanoparticles on human cervical carcinoma cells by apoptosis induction," *Colloids and Surfaces B: Biointerfaces*, vol. 117, pp. 354–359, 2014.
- [30] D. Raghunandan, B. Ravishankar, G. Sharanbasava et al., "Anti-cancer studies of noble metal nanoparticles synthesized using different plant extracts," *Cancer Nanotechnology*, vol. 2, no. 1-6, pp. 57–65, 2011.
- [31] A. M. Shawkey, M. A. Rabeh, A. K. Abdulall, and A. O. Abdelatif, "Green nanotechnology: anticancer activity of silver nanoparticles using *Citrullus colocynthis* aqueous extracts," *Advances in Life Science and Technology*, vol. 13, pp. 60–70, 2013.
- [32] H. Saad, M. I. Soliman, A. M. Azzam, and B. Mostafa, "Antiparasitic activity of silver and copper oxide nanoparticles against *Entamoeba histolytica* and *Cryptosporidium parvum* cysts," *Journal of the Egyptian Society of Parasitology*, vol. 45, no. 3, pp. 593–602, 2015.
- [33] A. M. Allahverdiyev, E. S. Abamor, M. Bagirova et al., "Antileishmanial effect of silver nanoparticles and their enhanced antiparasitic activity under ultraviolet light," *International Journal of Nanomedicine*, vol. 6, pp. 2705–2714, 2011.
- [34] S. Yadegari-Dehkordi, H. R. Sadeghi, N. Attaran-Kakhki, M. Shokouhi, and A. Sazgarnia, "Silver nanoparticles increase cytotoxicity induced by intermediate frequency low voltages," *Electromagnetic Biology and Medicine*, vol. 34, pp. 317–321, 2014.
- [35] T. Y. Suman, S. R. R. Rajasree, A. Kanchana, and S. B. Elizabeth, "Biosynthesis, characterization and cytotoxic effect of plant mediated silver nanoparticles using *Morinda citrifolia* root extract," *Colloids and Surfaces B: Biointerfaces*, vol. 106, pp. 74–78, 2013.
- [36] B. Kulandaivelu and K. M. Gothandam, "Cytotoxic effect on cancerous cell lines by biologically synthesized silver nanoparticles," *Brazilian Archives of Biology and Technology*, vol. 59, 2016.
- [37] E.-J. Park, J. Yi, Y. Kim, K. Choi, and K. Park, "Silver nanoparticles induce cytotoxicity by a Trojan-horse type mechanism," *Toxicology In Vitro*, vol. 24, no. 3, pp. 872–878, 2010.
- [38] M. I. Sriram, S. B. M. Kanth, K. Kalishwaralal, and S. Gurunathan, "Antitumor activity of silver nanoparticles in Dalton's lymphoma ascites tumor model," *International Journal of Nanomedicine*, vol. 5, p. 753, 2010.
- [39] E. Z. Gomma, "Antimicrobial, antioxidant and antitumor activities of silver nanoparticles synthesized by *Allium cepa* extract: a green approach," *Journal of Genetic Engineering and Biotechnology*, vol. 15, no. 1, pp. 49–57, 2017.
- [40] P. Sanpui, A. Chattopadhyay, and S. S. Ghosh, "Induction of apoptosis in cancer cells at low silver nanoparticle concentrations using chitosan nanocarrier," *ACS Applied Materials & Interfaces*, vol. 3, no. 2, pp. 218–228, 2011.
- [41] H. Ozer, J. O. Armitage, C. L. Bennett et al., "2000 update of recommendations for the use of hematopoietic colony-stimulating factors: evidence-based, clinical practice guidelines," *Journal of Clinical Oncology*, vol. 18, no. 20, pp. 3558–3585, 2000.
- [42] J. C. Stockert, A. Blázquez-Castro, M. Cañete, R. W. Horobin, and Á. Villanueva, "MTT assay for cell viability: intracellular localization of the formazan product is in lipid droplets," *Acta Histochemica*, vol. 114, no. 8, pp. 785–796, 2012.
- [43] S. Kasibhatla, G. P. Amarante-Mendes, D. Finucane, T. Brunner, E. Bossy-Wetzel, and D. R. Green, "Acridine orange/ethidium bromide (AO/EB) staining to detect apoptosis," *Cold Spring Harbor Protocols*, vol. 2006, no. 21, 2006.
- [44] S. Machana, N. Weerapreeyakul, S. Barusruks, K. Thumanu, and W. Tanthanuch, "Synergistic anticancer effect of the extracts from *Polyalthia evecta* caused apoptosis in human hepatoma (HepG2) cells," *Asian Pacific Journal of Tropical Biomedicine*, vol. 2, no. 8, pp. 589–596, 2012.
- [45] A. M. Rieger, K. L. Nelson, J. D. Konowalchuk, and D. R. Barreda, "Modified annexin V/propidium iodide apoptosis assay for accurate assessment of cell death," *Journal of visualized experiments*, vol. 50, article e2597, 2011.
- [46] X. Wang and M. G. Roper, "Measurement of DCF fluorescence as a measure of reactive oxygen species in murine islets of Langerhans," *Analytical Methods*, vol. 6, no. 9, pp. 3019–3024, 2014.
- [47] M. Ovais, A. T. Khalil, A. Raza et al., "Green synthesis of silver nanoparticles via plant extracts: beginning a new era in cancer theranostics," *Nanomedicine*, vol. 11, no. 23, pp. 3157–3177, 2016.
- [48] M. Darroudi, Z. Sabouri, R. Kazemi Oskuee, A. Khorsand Zak, H. Kargar, and M. H. N. Abd Hamid, "Green chemistry approach for the synthesis of ZnO nanopowders and their cytotoxic effects," *Ceramics International*, vol. 40, no. 3, pp. 4827–4831, 2014.
- [49] D. Puri and A. Bhandari, "Fagonia: a potential medicinal desert plant," *Journal of Nepal Pharmaceutical Association*, vol. 27, no. 1, pp. 28–33, 2015.
- [50] P. Balashanmugam and K. P. Thangavelu, "Biosynthesis characterization of silver nanoparticles using *Cassia roxburghii* DC. aqueous extract, and coated on cotton cloth for effective antibacterial activity," *International Journal of Nanomedicine*, vol. 10, p. 87, 2015.
- [51] Z. Zaheer, "Silver nanoparticles to self-assembled films: green synthesis and characterization," *Colloids and Surfaces B: Biointerfaces*, vol. 90, pp. 48–52, 2012.
- [52] S. Gurunathan, J.-K. Jeong, J. W. Han, X.-F. Zhang, J. H. Park, and J.-H. Kim, "Multidimensional effects of biologically synthesized silver nanoparticles in *Helicobacter pylori*,

- Helicobacter felis, and human lung (L132) and lung carcinoma A549 cells,” *Nanoscale Research Letters*, vol. 10, no. 1, p. 35, 2015.
- [53] G. Sharma, A. Sharma, M. Kurian, R. Bhavesh, J. Nam, and S. Lee, “Green synthesis of silver nanoparticle using *Myristica fragrans* (nutmeg) seed extract and its biological activity,” *Digest Journal of Nanomaterials & Biostructures (DJNB)*, vol. 9, 2014.
- [54] H. E. A. Mohamed, S. Afridi, A. T. Khalil et al., “Phytosynthesis of BiVO₄ nanorods using *Hyphaene thebaica* for diverse biomedical applications,” *AMB Express*, vol. 9, no. 1, pp. 200–214, 2019.
- [55] S. P. Dubey, M. Lahtinen, and M. Sillanpää, “Tansy fruit mediated greener synthesis of silver and gold nanoparticles,” *Process Biochemistry*, vol. 45, no. 7, pp. 1065–1071, 2010.
- [56] I. Ullah, Z. K. Shinwari, and K. ATJPJB, “Investigation of the cytotoxic and antileishmanial effects of *Fagonia indica* L. extract and extract mediated silver nanoparticles (AgNPs),” *Pakistan Journal of Botany*, vol. 49, pp. 1561–1568, 2017.
- [57] P. Prakash, P. Gnanaprakasam, R. Emmanuel, S. Arokiyaraj, and M. Saravanan, “Green synthesis of silver nanoparticles from leaf extract of *Mimusops elengi*, Linn. for enhanced antibacterial activity against multi drug resistant clinical isolates,” *Colloids and Surfaces B: Biointerfaces*, vol. 108, pp. 255–259, 2013.
- [58] B. Ajitha, Y. Ashok Kumar Reddy, and P. S. Reddy, “Biogenic nano-scale silver particles by *Tephrosia purpurea* leaf extract and their inborn antimicrobial activity,” *Spectrochimica Acta Part A: Molecular and Biomolecular Spectroscopy*, vol. 121, pp. 164–172, 2014.
- [59] V. S. Kotakadi, Y. S. Rao, S. A. Gaddam, T. N. V. K. V. Prasad, A. V. Reddy, and D. V. R. S. Gopal, “Simple and rapid biosynthesis of stable silver nanoparticles using dried leaves of *Catharanthus roseus*, Linn. G. Donn and its anti microbial activity,” *Colloids and Surfaces B: Biointerfaces*, vol. 105, pp. 194–198, 2013.
- [60] K. Anandalakshmi, J. Venugobal, and V. Ramasamy, “Characterization of silver nanoparticles by green synthesis method using *Petalium murex* leaf extract and their antibacterial activity,” *Applied Nanoscience*, vol. 6, no. 3, pp. 399–408, 2016.
- [61] B. J. Kirby and E. F. Hasselbrink, “Zeta potential of microfluidic substrates: I. Theory, experimental techniques, and effects on separations,” *ELECTROPHORESIS*, vol. 25, no. 2, pp. 187–202, 2004.
- [62] K. Jyoti, M. Baunthiyal, and A. Singh, “Characterization of silver nanoparticles synthesized using *Urtica dioica* Linn. leaves and their synergistic effects with antibiotics,” *Journal of Radiation Research and Applied Sciences*, vol. 9, no. 3, pp. 217–227, 2019.
- [63] R. R. Remya, S. R. R. Rajasree, L. Aranganathan, and T. Y. Suman, “An investigation on cytotoxic effect of bioactive AgNPs synthesized using *Cassia fistula* flower extract on breast cancer cell MCF-7,” *Biotechnology Reports*, vol. 8, pp. 110–115, 2015.
- [64] C. Krishnaraj, R. Ramachandran, K. Mohan, and P. T. Kalaiichelvan, “Optimization for rapid synthesis of silver nanoparticles and its effect on phytopathogenic fungi,” *Spectrochimica Acta Part A: Molecular and Biomolecular Spectroscopy*, vol. 93, pp. 95–99, 2012.
- [65] R. Vivek, R. Thangam, K. Muthuchelian, P. Gunasekaran, K. Kaveri, and S. Kannan, “Green biosynthesis of silver nanoparticles from *Annona squamosa* leaf extract and its in vitro cytotoxic effect on MCF-7 cells,” *Process Biochemistry*, vol. 47, no. 12, pp. 2405–2410, 2012.
- [66] S. A. Sadat Shandiz, M. Shafiee Ardestani, D. Shahbazzadeh et al., “Novel imatinib-loaded silver nanoparticles for enhanced apoptosis of human breast cancer MCF-7 cells,” *Artificial cells, nanomedicine, and biotechnology*, vol. 45, no. 6, pp. 1082–1091, 2017.
- [67] L. Inbathamizh, T. M. Ponnu, and E. J. Mary, “In vitro evaluation of antioxidant and anticancer potential of *Morinda pubescens* synthesized silver nanoparticles,” *Journal of Pharmacy Research*, vol. 6, no. 1, pp. 32–38, 2013.
- [68] K. Venugopal, H. Ahmad, E. Manikandan et al., “The impact of anticancer activity upon *Beta vulgaris* extract mediated biosynthesized silver nanoparticles (Ag-NPs) against human breast (MCF-7), lung (A549) and pharynx (Hep-2) cancer cell lines,” *Journal of Photochemistry and Photobiology B: Biology*, vol. 173, pp. 99–107, 2017.
- [69] M. Ramar, B. Manikandan, P. N. Marimuthu et al., “Synthesis of silver nanoparticles using *Solanum trilobatum* fruits extract and its antibacterial, cytotoxic activity against human breast cancer cell line MCF 7,” *Spectrochimica Acta Part A: Molecular and Biomolecular Spectroscopy*, vol. 140, pp. 223–228, 2015.
- [70] H. Ciftci, M. TÜRK, U. TAMER, S. Karahan, and Y. Menemen, “Silver nanoparticles: cytotoxic, apoptotic, and necrotic effects on MCF-7 cells,” *Turkish Journal of Biology*, vol. 37, pp. 573–581, 2013.
- [71] S. S. Bhattacharyya, S. K. Mandal, R. Biswas et al., “In vitro studies demonstrate anticancer activity of an alkaloid of the plant *Gelsemium sempervirens*,” *Experimental Biology and Medicine*, vol. 233, no. 12, pp. 1591–1601, 2008.
- [72] V. Kathiravan, S. Ravi, and S. Ashokkumar, “Synthesis of silver nanoparticles from *Melia dubia* leaf extract and their in vitro anticancer activity,” *Spectrochimica Acta Part A: Molecular and Biomolecular Spectroscopy*, vol. 130, pp. 116–121, 2014.
- [73] J. Liang, F. Zeng, M. Zhang et al., “Green synthesis of hyaluronic acid-based silver nanoparticles and their enhanced delivery to CD44+ cancer cells,” *RSC Advances*, vol. 5, no. 54, pp. 43733–43740, 2015.
- [74] D. R. McIlwain, T. Berger, and T. W. Mak, “Caspase functions in cell death and disease,” *Cold Spring Harbor Perspectives in Biology*, vol. 5, p. a008656, 2013.
- [75] Y. Shi, “Mechanisms of caspase activation and inhibition during apoptosis,” *Molecular Cell*, vol. 9, no. 3, pp. 459–470, 2002.
- [76] K. M. Boatright, M. Renatus, F. L. Scott et al., “A unified model for apical caspase activation,” *Molecular Cell*, vol. 11, no. 2, pp. 529–541, 2003.
- [77] S. J. Riedl and Y. Shi, “Molecular mechanisms of caspase regulation during apoptosis,” *Nature Reviews Molecular Cell Biology*, vol. 5, no. 11, pp. 897–907, 2004.
- [78] G. M. Cohen, “Caspases: the executioners of apoptosis,” *Biochemical Journal*, vol. 326, no. 1, pp. 1–16, 1997.
- [79] M. Kikuchi, S. Kuroki, M. Kayama, S. Sakaguchi, K.-K. Lee, and S. Yonehara, “Protease activity of procaspase-8 is essential for cell survival by inhibiting both apoptotic and nonapoptotic cell death dependent on receptor-interacting protein kinase 1 (RIP1) and RIP3,” *Journal of Biological Chemistry*, vol. 287, no. 49, pp. 41165–41173, 2012.
- [80] B. C. G. Selvi, J. Madhavan, and A. Santhanam, “Cytotoxic effect of silver nanoparticles synthesized from *Padina tetrastratica* on breast cancer cell line,” *Advances in Natural*

- Sciences: Nanoscience and Nanotechnology*, vol. 7, p. 035015, 2016.
- [81] H. Nakajima, J. Magae, M. Tsuruga et al., "Induction of mitochondria-dependent apoptosis through the inhibition of mevalonate pathway in human breast cancer cells by YM529, a new third generation bisphosphonate," *Cancer Letters*, vol. 253, no. 1, pp. 89–96, 2007.
- [82] J. Ma, di Zhao, H. Lu, W. Huang, and D. Yu, "Apoptosis signal-regulating kinase 1 (ASK1) activation is involved in silver nanoparticles induced apoptosis of A549 lung cancer cell line," *Journal of Biomedical Nanotechnology*, vol. 13, no. 3, pp. 349–354, 2017.
- [83] A. H. Wyllie, "Glucocorticoid-induced thymocyte apoptosis is associated with endogenous endonuclease activation," *Nature*, vol. 284, no. 5756, pp. 555–556, 1980.
- [84] S. Arora, J. Jain, J. M. Rajwade, and K. M. Paknikar, "Cellular responses induced by silver nanoparticles: in vitro studies," *Toxicology Letters*, vol. 179, no. 2, pp. 93–100, 2008.
- [85] A. Nel, T. Xia, L. Mädler, and N. Li, "Toxic potential of materials at the nanolevel," *science*, vol. 311, no. 5761, pp. 622–627, 2006.
- [86] H. Li, J. Chen, C. Xiong, H. Wei, C. Yin, and J. Ruan, "Apoptosis induction by the total flavonoids from *Arachniodes exilis* in HepG2 cells through reactive oxygen species-mediated mitochondrial dysfunction involving MAPK activation," *Evidence-based Complementary and Alternative Medicine*, vol. 2014, 11 pages, 2014.
- [87] N. Lampiasi, A. Azzolina, N. D'Alessandro et al., "Antitumor effects of dehydroxymethylepoxyquinomicin, a novel nuclear factor- κ B inhibitor, in human liver cancer cells are mediated through a reactive oxygen species-dependent mechanism," *Molecular Pharmacology*, vol. 76, no. 2, pp. 290–300, 2009.
- [88] Y.-H. Hsin, C.-F. Chen, S. Huang, T.-S. Shih, P.-S. Lai, and P. J. Chueh, "The apoptotic effect of nanosilver is mediated by a ROS- and JNK-dependent mechanism involving the mitochondrial pathway in NIH3T3 cells," *Toxicology Letters*, vol. 179, no. 3, pp. 130–139, 2008.
- [89] H. J. Forman and M. Torres, "Reactive oxygen species and cell signaling," *American Journal of Respiratory and Critical Care Medicine*, vol. 166, supplement_1, pp. S4–S8, 2002.

Research Article

Isokotomolide A from *Cinnamomum kotoense* Induce Melanoma Autophagy and Apoptosis *In Vivo* and *In Vitro*

Jian Li,¹ Chung-Yi Chen,² Jyun Yin Huang,³ Lin Wang,⁴ Zixuan Xu,¹ Wenyi Kang,⁵ Miao-Hsia Lin,⁶ and Hui-Min David Wang^{1,3,7,8} 

¹College of Food and Biological Engineering, Jimei University, Xiamen 361021, China

²Department of Nutrition and Health Science, School of Medical and Health Sciences, Fooyin University, Kaohsiung 831, Taiwan

³Graduate Institute of Biomedical Engineering, National Chung Hsing University, Taichung 402, Taiwan

⁴College of Chemistry & Pharmacy, Northwest A&F University, Yangling, Shaanxi 712100, China

⁵Joint International Research Laboratory of Food & Medicine Resource Function, Henan Province, Henan University, Kaifeng 475004, China

⁶Graduate Institute of Microbiology, College of Medicine National Taiwan University, Taipei 100, Taiwan

⁷Graduate Institute of Medicine, College of Medicine, Kaohsiung Medical University, Kaohsiung 807, Taiwan

⁸Department of Medical Laboratory Science and Biotechnology, China Medical University, Taichung City 404, Taiwan

Correspondence should be addressed to Hui-Min David Wang; davidw@dragon.nchu.edu.tw

Received 22 June 2020; Revised 24 August 2020; Accepted 11 September 2020; Published 27 September 2020

Academic Editor: Daoud Ali

Copyright © 2020 Jian Li et al. This is an open access article distributed under the Creative Commons Attribution License, which permits unrestricted use, distribution, and reproduction in any medium, provided the original work is properly cited.

Melanoma is an aggressive cancer with high lethality. In order to find new anticancer agents, isokotomolide A (Iso A) and secokotomolide A (Sec A) isolated from *Cinnamomum kotoense* were identified to be potential bioactive agents against human melanoma but without strong antioxidative properties. Cell proliferation assay displayed Iso A and Sec A treated in the normal human skin cells showed high viabilities. It also verified that two of them possess strong antimelanoma effect in concentration-dependent manners, especially on B16F10, A2058, MeWo, and A375 cells. Wound healing assay presented their excellent antimigratory effects. Through 3-N,3-N,6-N,6-N-Tetramethylacridine-3,6-diamine (acridine orange, AO) staining and Western blot, the autophagy induced by treatment was confirmed, including autophagy-related proteins (Atgs). By using annexin V-FITC/PI double-stain, the apoptosis was confirmed, and both components also triggered the cell cycle arrest and DNA damage. We demonstrated the correlations between the mitogen-activated protein kinase (MAPK) pathway and antimelanoma, such as caspase cascade activations. To further evaluate *in vivo* experiments, the inhibition of tumor cell growth was verified through the histopathological staining in a xenograft model. In this study, it was confirmed that Iso A and Sec A can encourage melanoma cell death via early autophagy and late apoptosis processes.

1. Introduction

Skin cancer is one of the most aggressive malignant tumors, which especially occurs in people with light skin. The primary reason of skin cancer is the overexposure to ultraviolet (UV) radiation [1]. Chemical mutagens, genetic susceptibility, human papillomavirus, and tobacco consumption can also lead to skin cancer. In addition, the utilization of immunosuppressive drugs such as azathioprine and cyclosporine A has been reported to result in the occurrence of skin cancer [2]. There are three skin cancers: squamous cell carcinoma

(SCC), basal cell carcinoma (BCC), and malignant melanoma. BCC grows slowly and can damage the surrounding tissue, but it does not have the ability to spread to other areas. SCC is a kind of abnormal cell cancer with uncontrolled growth arising from the squamous cells. It can occur in all areas of the body and are the most common in the areas exposed to sunlight. SCC possesses the ability of metastasis and can harm other areas of the body. BCC and SCC are defined as nonmelanoma skin cancer (NMSC) [3]. Malignant melanoma is highly aggressive which develops from the pigment-containing cells known as melanocytes. Melanoma

can spread rapidly through the whole body of the patient, and thus causes a very low survival rate [4].

The most effective method to prevent skin cancer is avoiding exposure to UV radiation and using sunscreen. If the skin cancer occurs, in the initial stage, it can be curable by surgical elimination, while in the advanced stage, it is usually treated by immunotherapy and chemotherapy [5]. The classical pharmacotherapy employed for the treatment of skin cancers usually includes 5-fluorouracil, imiquimod, diclofenac, and ingenol mebutate. In recent years, the phytochemicals such as quercetin, epigallocatechin-3-gallate, resveratrol, and curcumin have been applied in the melanoma treatment [6–8].

The mitogen-activated protein kinase (MAPK) cascade activation is the center of various signaling pathways. It plays an important role in receiving the membrane receptors to convert and transmit signals into the nucleus. There are three different pathways of MAPKs, i.e., the extracellular-signal-regulated kinase (ERK), c-Jun N-terminal kinase (JNK), and p38 MAPK. The JNK pathway is known to regulate the cell growth and death, however, the mechanism of how the JNK/MAPK signaling pathway inhibits the melanoma has not been fully clarified. This study was aimed at figuring out the naturally occurring chemotherapeutic agent and evaluated their cytotoxicity on melanoma. *Cinnamomum kotoense* Kanehira is a kind of Lauraceae evergreen small tree, which is native to Lanyu Island, a small island of southeast Taiwan. The bark is used as medicine to prevent colds, pain, bleeding, and so on. It is also rich in cinnamon oil to be the main component as cinnamaldehyde and exudes fragrance to clean air. Iso A and Sec A were constituents isolated from the leaves of *Cinnamomum kotoense* (Figure 1). A previous study had shown that Iso A was an agent capable of inducing human nonsmall lung cancer apoptosis [9]. Iso A and Sec A also exhibited cytotoxicity on Hela cells [10]. In this study, a hypothesis was proposed that both components were potential elements against the melanoma cells to investigate the possible antimelanoma mechanism. We investigated the effects of Iso A and Sec A on the suppressions in cellular proliferation, cell cycle arrest, cell migration, and the activations of autophagy and apoptosis pathways, and *in vivo* examinations.

2. Materials and Methods

2.1. Materials and Reagents. Vitamin C, ethylene diamine tetraacetic acid (EDTA), butyl hydroxy anisid (BHA), trichloroacetic acid, potassium ferricyanide, FeCl_3 , $\text{FeCl}_2 \cdot 4\text{H}_2\text{O}$, 3-(4,5-Dimethylthiazol-2-yl)-2,5-diphenyltetrazolium bromide (MTT), dimethyl sulfoxide (DMSO), Dulbecco's modified Eagle's medium (DMEM), fetal bovine serum (FBS), Trpsin-0.5%EDTA, and phosphate-buffered saline (PBS). Antibodies against β -actin, cleaved caspase 3, 9, and peroxidase-conjugated anti-rabbit IgG secondary antibody were purchased from cell signaling (Beverly, MA, USA). Antibodies of B-cell lymphoma 2 (Bcl-2), JNK, Beclin-1 (Atg-6), Atg 5, 10, and 16 were purchased from ABGENT Co. (San Diego, CA, USA). Peroxidase-conjugated anti-mouse IgG secondary antibody was purchased from Pierce

(Rockford, IL, USA). All the other chemicals and reagents were purchased from Sigma Chemical (St. Louis, MO, USA).

2.2. Extraction and Isolation of Compounds. The air-dried leaves of *Cinnamomum kotoense* (11.0 kg) were extracted with MeOH (80 L \times 6) at room temperature, and the MeOH extract (201.2 g) was obtained upon the concentration under reduced pressure [9]. The MeOH extract, suspended in H_2O (1 L), was partitioned with CHCl_3 to give fractions soluble in CHCl_3 and H_2O . The CHCl_3 -soluble fraction was chromatographed over silica gel using *n*-hexane-EtOAc-acetone as an eluent to produce five fractions. Part of fraction 1 was subjected to Si gel chromatography by eluting with *n*-hexane-EtOAc, and then enriched with EtOAc to furnish 10 fractions. Fraction 1-1 was resubjected to Si gel chromatography, eluting with *n*-hexane-EtOAc, and enriched gradually with EtOAc to obtain five other fractions. Fraction 1-1-2 eluted with *n*-hexane-EtOAc was further separated using silica gel column chromatography and preparative thin-layer chromatography (TLC), giving Sec A (327 mg). Part of fraction 2 was subjected to Si gel chromatography by eluting with *n*-hexane-EtOAc and enriched with EtOAc to furnish six fractions. Fraction 2-3 was resubjected to Si gel chromatography, eluting with *n*-hexane-EtOAc, and enriching gradually with EtOAc to obtain four fractions [11]. Fraction 2-3-2 eluted with *n*-hexane-EtOAc was further separated with silica gel column chromatography and preparative TLC (*n*-hexane-EtOAc; and gave Iso A).

2.3. 1, 1-Diphenyl-2-Picrylhydrazyl (DPPH) Radical Scavenging Activity. DPPH is an unstable radical and has a strong absorbance at 517 nm, when DPPH is reduced by an antioxidant or combined with another free radical, its absorbance will be reduced or even disappear [11]. Thus, DPPH is applied to examine the antioxidant activity by detecting radical scavenging capability. Briefly, added 1.0 μL accurate concentration (10, 50, 100, and 200 μM) of Iso A or Sec A to 99 μL DPPH (60 μM). In addition, the positive control was vitamin C, because of its excellent antioxidant activity. We detected the absorbance value at 517 nm; the radical scavenging capability (percentage) was calculated by formula as follows:

$$\text{Radical scavenging activity(\%)} = \frac{(A_{\text{control}} - A_{\text{sample}})}{A_{\text{control}}} \times 100\% \quad (1)$$

2.4. Metal Chelating Activity. Metal ion is one of the causes for the lipid peroxidation, especially ferrous ion which is prooxidant. This assay is based on the complexes of ferrous ions and ferrozine have a color reaction at 562 nm, and the lower absorbance means the better metal chelating activity [12]. 1.0 μL various dosages (10, 50, 100, and 200 μM) of Iso A or Sec A were added into 10 μL $\text{FeCl}_2 \cdot 4\text{H}_2\text{O}$ (2.0 mM) to mix with 20 μL ferrozine (5.0 mM), and EDTA acted as a positive control. The absorbance of the mixture was observed at 562 nm. The chelating power activity was calculated as Equation (1):

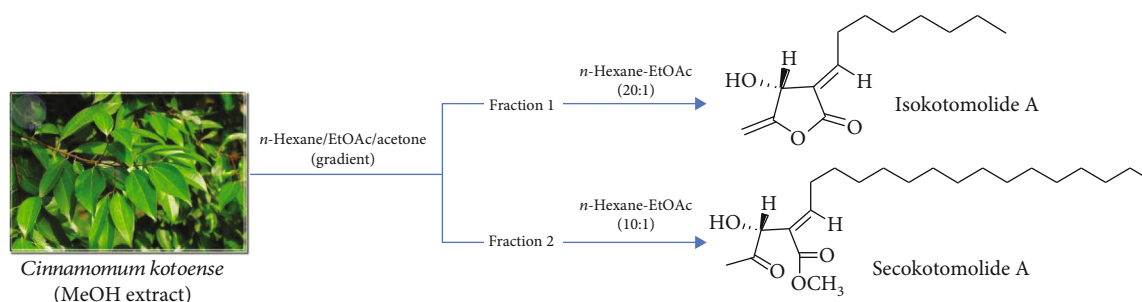


FIGURE 1: The purification and chemical structures of Iso A and Sec A.

2.5. Reducing Power. We used the reduce power assay to test the reductive ability of Iso A and Sec A. Briefly, 85 μL , 0.2 M phosphate buffer (pH 4.4), 2.5 μL $\text{K}_3\text{Fe}(\text{CN})_6$ (20%), and various suitable concentrations of samples were mixed together at 50°C for 20 min. After that, 160 μL of trichloroacetic acid (TCA) (10%) was added to the mixture with the centrifugation at 3,000 rpm for 10 min to collect the supernatant for the optical absorbance measurement at 700 nm. Butyl hydroxyl anisid (BHA) was viewed as a positive control. A higher absorbance value means a better reductive activity [13].

2.6. Cell Cultures. Hs68, HaCaT, B16F10, MeWo, A2058, and A375 cell lines were purchased from the Bioresource Collection and Research Center (BCRC, Hsinchu, Taiwan). Six cells were kept in a cell culture dish at 37°C and 5% CO_2 in DMEM supplemented with 10% FBS, 100 U/mL of penicillin, 100 mg/mL of streptomycin, and 0.25 $\mu\text{g}/\text{mL}$ of amphotericin B [10]. DMSO was dissolved stock solutions of Iso A and Sec A (both at 1.0 M), and the tested concentrations were prepared by diluting with free medium, and the final DMSO concentration was less than 1.0% to avoid from unexpected biochemical reactions.

2.7. Cell Proliferation Assay. The cell proliferation effects of Iso A and Sec A on normal and melanoma cells were tested by MTT assay [14]. This method was based on the property that mitochondrial succinate dehydrogenase from living cells made MTT reduced to water-insoluble blue-violet crystal formazan and deposited in the cells, and dead cells without this function. Briefly, 1×10^4 cells were seeded in a 96-well microplate. After 24 h, discarded the medium, cells were treated with various concentrations (10, 25, 50, and 100 μM) of Iso A and Sec A or vehicle control in a final volume of 100 μL culture medium. The experimental doses were accorded to our previous tests. After cultured within 37°C, 5% CO_2 incubator for 24 h, we replaced the medium with 100 μL fresh broth contained 0.5 mg/mL MTT. The plate was kept in a 37°C incubator for 2 h. We discarded the medium to add 100 μL DMSO dissolving the purple formazan crystals and gently shook the plate in darkness for 10 min. The optical absorbance values (A) were measured at 595 nm (BioTek, WA, USA). Cell viabilities were calcu-

lated according to the formula as follows:

$$\text{Cell viability (\%)} = \frac{(A_{\text{sample}} - A_{\text{blank}})}{(A_{\text{control}} - A_{\text{blank}})} \times 100\%. \quad (2)$$

2.8. Autophagic Vacuoles Detection by Acridine Orange Staining. B16F10 cells were chosen for the further homologous study to seed in a 6-well dish at a density of 1×10^5 , after 24 h, treated with various concentrations of Iso A and Sec A for 24 h, washed cells twice with PBS, and then incubated with serum-free medium contained 5 $\mu\text{g}/\text{mL}$ acridine orange (AO, Molecular Probes, Eugene, Oregon, USA) at room temperature for 15 min [15]. We used an inverted fluorescence microscope to obtain the AO fluorescence images. AVO was stained with red color, and the nucleus DNA and cytosolic RNA were stained with green color.

2.9. Annexin V-FITC/PI Binding Assay to Analyze Apoptosis. To further confirm the apoptosis of Iso A and Sec A-treated malignant melanoma B16F10 cells, annexin V-fluorescein isothiocyanate (FITC)/propidium iodide (PI) double-staining was performed (Biovision, annexin V-FITC apoptosis kit) [16]. 1×10^5 cells were kept in a 6-well dish and were treated with tested Iso A and Sec A concentrations (10, 25, 50, and 100 μM) or vehicle control in a total volume of 100 μL culture medium for 24 h. We collected the medium, washing twice with PBS to trypsinize the adherent cells. The centrifugation at 1,000 rpm at 4°C for 10 min was set to collect cells and label with annexin V-FITC/PI. The incubation was in darkness for 15 min, and the samples were analyzed by a flow cytometry (Millipore guava easyCyte HT, MA, USA).

2.10. DNA Damage and Cell Cycle Analysis. To identify the phase distribution of cellular DNA, cell cycle analysis was performed as described [17]. B16F10 cells were cultured at a density of 1×10^5 cells in a 6-well dish, and then monolayer cells were treated with various concentrations (10, 25, 50, and 100 μM) of Iso A, Sec A, or vehicle control for 24 h. Collected adherent and floating cells and washed once with precooled PBS, then fixed cells with precooled 70% ethanol overnight at 4°C. After centrifugation at 1,200 rpm for 3 min, wash the cell pellets once with precooled PBS, centrifuged again, and then stained cells with 100 $\mu\text{g}/\text{mL}$ RNase and 50 $\mu\text{g}/\text{mL}$ PI in PBS buffer, and incubated in darkness at room

temperature for 30 min. The DNA contents of PI-stained cells were analyzed by flow cytometry.

2.11. Western Blot Analysis. 1×10^6 B16F10 cells were treated with Iso A, Sec A, or vehicle control for 24 h. Cells were harvested and lysed with lysis buffer (Thermo Scientific Pierce RIPA Buffer) to extract cellular proteins. The lysates were centrifuged at 1,200 rpm for 30 min, and the protein concentrations were measured with the bicinchoninic acid (BCA) protein assay kit (Pierce, Rockford, IL, USA). Sodium dodecyl sulfate-polyacrylamide gel electrophoresis (SDS-PAGE) was performed to separate the same amounts of proteins and then electrotransferred the proteins on gel to a polyvinylidene fluoride (PVDF) membrane (PALL Life Science, Ann Arbor, MI, USA). The membrane was blocked with a blocking buffer (Pierce TOOLSPEED PLUS Blocking Reagent) and washed with TBST (Tris-buffered saline, with Tween-20, pH 8.0). The membrane was incubated with the corresponding primary antibody, shaking at 4°C overnight, washed three times with TBST and blocked again, and then incubated with secondary antibody against the corresponding primary antibody for 90 min. The signal was visualized by enhanced chemiluminescence (ECL) detection with West Femto Maximum Sensitivity Substrate kit (SuperSignal, Rockford, IL, USA) [12].

2.12. RNA Isolation and Extraction. The RNA was isolated and extracted by Trizol RNA isolation reagent, which could resolve cell lysates and separate RNA, DNA, and proteins. First, 1 mL Trizol reagent was increased to each and move to the 1.5 mL microtube at room temperature for 5 min. Then, 200 μ L BCP per mL of Trizol reagent was added and mixed intensely [18]. After incubation for 2 min, the samples were centrifuged at $14,000 \times g$ for 20 min. The sample homogenates formed three phases, from which the aqueous phase on the top of the homogenate was move to a new Eppendorf tube. To precipitate RNA, an equal volume of isopropanol was blended. The mixture was centrifuged at $13,000 \times g$ for 15 min, and the supernatant liquid was divided. The RNA pellet was washed with 1 mL of 75% ethanol to get rid of the residual salts. In the end, the mixture was centrifuged at $13,000 g$ for 5 min, and the RNA pellet was dehydrated and dissolved with 50 μ L diethylpyrocarbonate- (DEPC-) treated water. The concentration and quality of the RNA extracts were determined by BioTek (Lionheart Technologies, Inc.)

2.13. Quantitative Real-Time Polymerase Chain Reaction (qRT-PCR). qRT-PCR is a method detected for evaluating gene expression level by measuring the cDNA products after each cycle of PCR increase. For qRT-PCR, a reactive mixture with SYBR Green Master Mix (Qiagen, Valencia, CA, USA) templates and primers was used [4]. All qRT-PCR reactions were finished by a StepOnePlus™ System. The reactions were carried out according to the following program: cDNA templates were initiated at 95°C, annealed at 65°C, and elongated at 70°C, and all steps were repeated with 40 cycles of enlargement. At the end of the annealing stage of the experiments, fluorescence acquisition was started to determine. The

designed forward and reverse primers from 5' to 3' used in this experiment are shown in (Table S1).

2.14. Cell Migration Assay. The population of cellular migratory inhibition effect was examined by wound healing assay as described [15] and performed with minor modification. In brief, 5×10^5 cells were seeded in 6-well plates and grown to complete confluence. We created a clear wound area on a monolayer culture with a 200 μ L plastic pipette tip to wash once with PBS and then treated with the samples. Afterward, we used a microscope taking photos at time intervals of 0, 6, 12, and 24 h to check the wound closure. The cell movement and migration through the wound area were calculated by the free software, ImageJ.

2.15. Animal Material. In this study, the application of animals complied with the guiding principles in the care and use of animals of the American physiology society was approved by the National Chung Hsing University Use Committee (IACUC: 106-111, Figure S1). BALB/c nude female mice (4-5 weeks) were purchased from BioLASCO Experimental Animal Center (Taiwan Co., Ltd) [19, 20]. The mice were housed in plexiglass cages in a temperature-controlled room ($22 \pm 1^\circ\text{C}$), on a 12 h/12 h light/dark schedule, and with free access to food and water (fed a standard laboratory diet). After one week, 18 mice were randomly divided into 3 groups ($n = 6$, each group): Group A, vehicle blank control; Group B, B16F10 only; and Group C, B16F10 with Iso A treatment.

2.16. Xenograft Tumor Assay. The performance of xenograft tumor assay was described previously with minor modifications. In brief, BALB/c nu/nu female mice were housed, and the *in vivo* experiments were performed at the animal center. Mice were implanted subcutaneously with 1×10^7 of B16F10 homologous cells in 0.1 mL PBS injected subcutaneously in each mouse [19]. Mice were treated four times a week with a subcutaneous injection of Iso A (200 mg/kg) until sacrifice at day 35. The diameters of xenograft tumor were measured at 4 days intervals with Vernier calipers and calculated as $(\text{length} \times \text{width}^2)/2$ in mm^3 .

2.17. Histopathological Analyses of Xenografted Tumor. The fresh tumor tissues were made in paraffin, cut into 3 mm thick chunks, set in plastic cassettes, and immersed in 10% neutral buffered formalin for 7 days. Staining of sectioned paraffin-embedded tumor tissue with Hematoxylin and Eosin (H&E). This stain is visible for tissue processing, embedding, and sectioning. The range of Iso A-treatment shrunk the tumor weight and volume was evaluated, and the assessment of mitotic cell division in the xenografted tumor fragments was also observed via H&E images [20].

2.18. Statistical Analysis. Statistical data were shown as mean \pm standard deviation (SD) values, and Student's test was applied to determine the difference between the control vehicle and experimental groups, * $p < 0.05$ versus control; ** $p < 0.01$ versus control.

3. Results

3.1. Antioxidant Activity of Iso A and Sec A. Since melanomas occur on the skin and most of them are caused by UV exposure, the impacts of oxidative stresses on melanoma have attracted researchers' attentions. Antioxidants are thought to prevent UV-induced oxidative stress and DNA damage, and previous studies have shown that antioxidant intakes can prevent melanoma developments. Therefore, the antioxidant activities of Iso A and Sec A were evaluated (Table 1). At testing concentrations, two constituents did not show good antioxidant activities, and thus it was speculated that both components did not suppress melanoma proliferation by antioxidative properties.

3.2. Antiproliferative Effects of Iso A and Sec A. This work was aimed at finding the potential agents with antimelanoma effects, and a good leading compound should also be safe enough for normal cells. Thus, the effectivenesses of two components was evaluated on the proliferation of normal human skin cells including fibroblast Hs68 cell line and keratinocyte HaCaT cell line. Figure 2(a) showed the results from MTT assay of 24 h treatment at the concentrations of 0 (a vehicle control), 10, 25, 50, and 100 μM , respectively. All experimental concentrations were at less than 1.0% DMSO. Iso A presented no cytotoxicity on fibroblasts and minor cytotoxicity on keratinocytes at high concentrations. Sec A demonstrated a slight cytotoxic effect on keratinocytes and fibroblast cells at concentrations of 10 and 25 μM , respectively, but at the concentrations of 50 and 100 μM , Sec A influenced the survival of fibroblasts. IC_{50} (the half-maximal inhibitory concentration) is the quantitative value of the potency on Iso A or Sec A in the suppression to the specific cellular viability. To evaluate the effects of two compounds on malignant melanomas, the MTT method was also applied on B16F10, MeWo, A2058, and A375 cells (Figure 2(b)). Four melanoma cells were treated with concentrations from 0 to 100 μM for 24 h, respectively. The cell proliferation of melanoma cells was inhibited by both compounds in concentration-dependent manners, and the treatments illustrated excellent anticancer effects, especially on B16F10, A2058, and MeWo cells. At the concentrations of 50 and 100 μM , we observed that more than half of the cells were dead. According to these findings, we chose B16F10 as our testing cell line at 25 and 100 μM for the further studies.

3.3. The Formation of Autophagic Vacuoles (AVO) in Iso A and Sec A-Treated B16F10 Cells. To identify if Iso A and Sec A treatments will induce autophagic cell death in B16F10 cells, AO staining was performed. AO is a lysosomotropic metachromatic fluorescent dye and can be used to analyze the lysosomal membrane permeability status. During the autophagy process, autophagosome fuses with lysosome to produce autolysosome, phagolysosome, and autophagolysosome. B16F10 cells were incubated with Iso A and Sec A and then labeled with AO to visualize the acidic vesicular organelles (AVOs) of acidic autophagolysosome. The cell nuclei DNA and cytosol RNA were stained with green color,

and AVOs were observed in red color (Figure 2(c)). There was an obvious enhancement of red fluorescence, which indicated that testing samples can induce autophagy on the melanoma cells. In addition, the number of cells was also significantly reduced at high concentrations, pointing out the excellent cytotoxicity in dose-dependent manners.

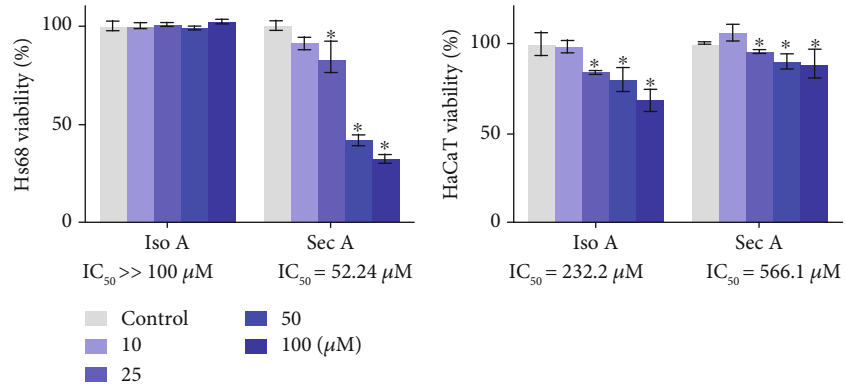
3.4. Iso A and Sec A Cause Apoptotic Cell Death on B16F10 Cells. The two-dimensional flow cytometry was employed to evaluate the cytotoxic effects of Iso A and Sec A. In the early apoptotic cells, cell membrane surface damage occurs, and the phospholipidine serine (PS) on the inner surface can be reversed to the outer membrane of the cell. Annexin V is a phospholipid-binding protein with a high affinity for phosphatidylserine and was applied to detect the early cell apoptosis. Propidium iodide (PI) is a nucleic acid dye and was used to label the late apoptotic cells and dead cells. The flow cytometry presented annexin V-FITC staining in x -axis and PI staining in y -axis. Briefly, the left lower quadrant means living cells, and the right lower and right upper quadrants mean early and late apoptotic cells, respectively. In addition, the left upper quadrant refers to necrotic cells. B16F10 cells were cultured with various concentrations of Iso A and Sec A or a vehicle control for 24 h (Figure 3(a)). The treated cells presented obvious apoptosis compared with the vehicle control. Iso A caused significant apoptotic cell death at the concentration of 50 and 100 μM , and the percentage of late apoptosis cells in the group treated with 50 μM Iso A was increased to $64.07 \pm 0.97\%$ and the group treated with 100 μM was increased to $91.51 \pm 0.30\%$, compared with $5.26 \pm 0.28\%$ of the control. Sec A presented a concentration-dependent manner to trigger apoptosis mechanism as Iso A to suppress melanoma growth. The group treated with 100 μM Sec A induced $46.76 \pm 3.49\%$ cells to enter late apoptosis, compared with $6.03 \pm 0.78\%$ of the vehicle control group.

3.5. Iso A and Sec A Induce DNA Damage and Cell Cycle Arrest. The cellular DNA content and cell cycle were tested after the treatments at various concentrations of Iso A and Sec A for 24 h. B16F10 cells were harvested and washed once with PBS, fixed by precooled 70% ethanol overnight, stained by PI, and analyzed by the flow cytometry. The accumulation of the G0/G1 population is usually thought as a biomarker of DNA damage and an occurrence of apoptosis [21]. As shown in Figure 3(b), after exposure to Iso A for 24 h, the G0/G1 accumulation arose obviously, and the G2/M profile decreased. To compare with $48.20 \pm 1.3\%$ on the shape in G0/G1 phase of vehicle control, the treated groups were increased to $48.27 \pm 0.2\%$, $58.30 \pm 0.4\%$, $73.50 \pm 0.1\%$, and $55.77 \pm 0.9\%$ at the concentrations of 10, 25, and 50 μM , respectively. At 100 μM , alive B16F10 cells were too few to be examined precisely. Sec A induced DNA damage to arise the G0/G1 accumulation which was similar to Iso A performance. We compared with the value of $47.4 \pm 0.6\%$ in G0/G1 accumulation in the control group; Sec A treatment elevated the other group values to $50.77 \pm 0.6\%$, $58.95 \pm 0.2\%$, and $70.30 \pm 0.8\%$ in sequence at 10, 25, and 50 μM . For the same reason, at high dose, B16F10 surface structure and

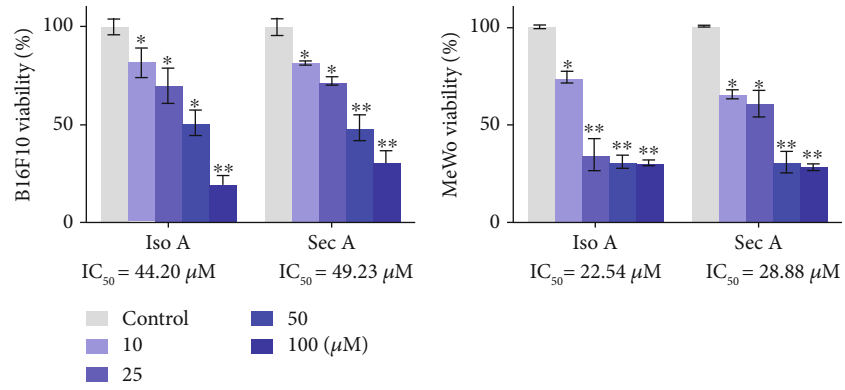
TABLE 1: The antioxidant activity assays of Iso A and Sec A.

Compounds (μM)	DPPH radical scavenging ability (%)				Metal chelating activity (%)				Reducing power (OD_{700})			
	10	50	100	200	10	50	100	200	10	50	100	200
Iso A	≤ 5.0	≤ 5.0	≤ 10.0	≤ 15.0	≤ 5.0	≤ 5.0	≤ 10.0	≤ 15.0	0.099 ± 0.003	0.099 ± 0.004	0.103 ± 0.002	0.127 ± 0.003
Sec A	≤ 5.0	≤ 5.0	≤ 10.0	19.98 ± 1.62	≤ 5.0	≤ 5.0	≤ 10.0	≤ 15.0	0.095 ± 0.003	0.101 ± 0.005	0.104 ± 0.003	0.114 ± 0.001
Vitamin C ^a	—	—	84.95 ± 1.86	—	—	—	—	—	—	—	—	—
EDTA ^b	—	—	—	—	—	—	92.66 ± 6.49	—	—	—	—	—
BHA ^c	—	—	—	—	—	—	—	—	—	—	0.736 ± 0.008	—

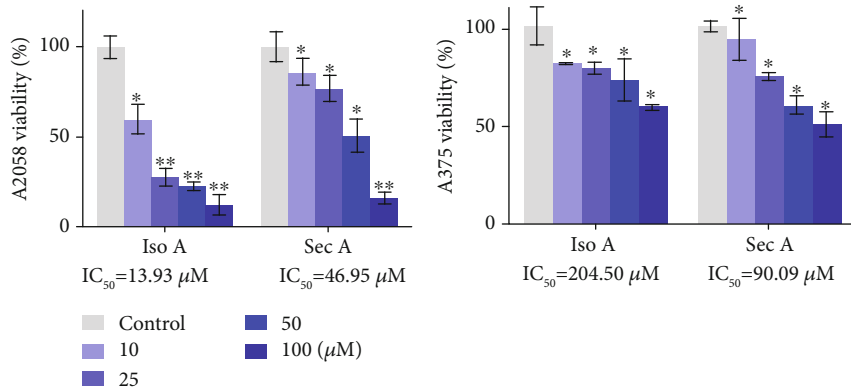
^aVitamin C was the positive control of DPPH radical scavenging capacity assay with concentration at $100 \mu\text{M}$; ^bEDTA was the positive control of metal chelating activity assay with concentration of at μM ; ^cBHA was the positive control of reducing power assay with concentration at $100 \mu\text{M}$.



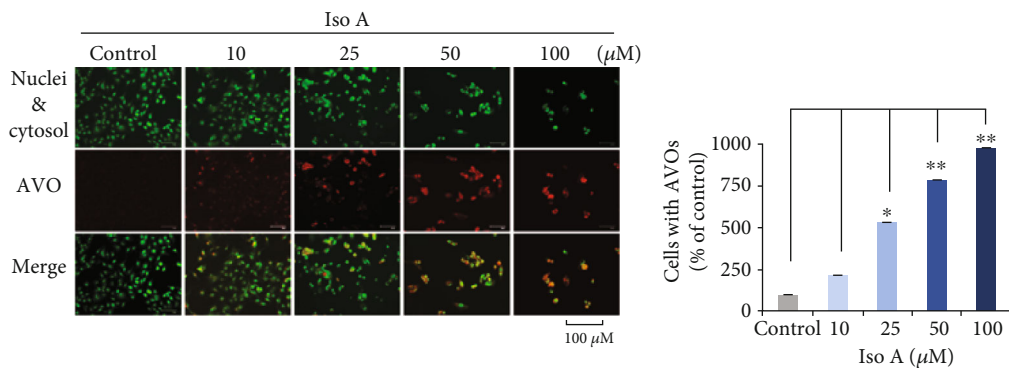
(a)



(b)



(c)



(d)

FIGURE 2: Continued.

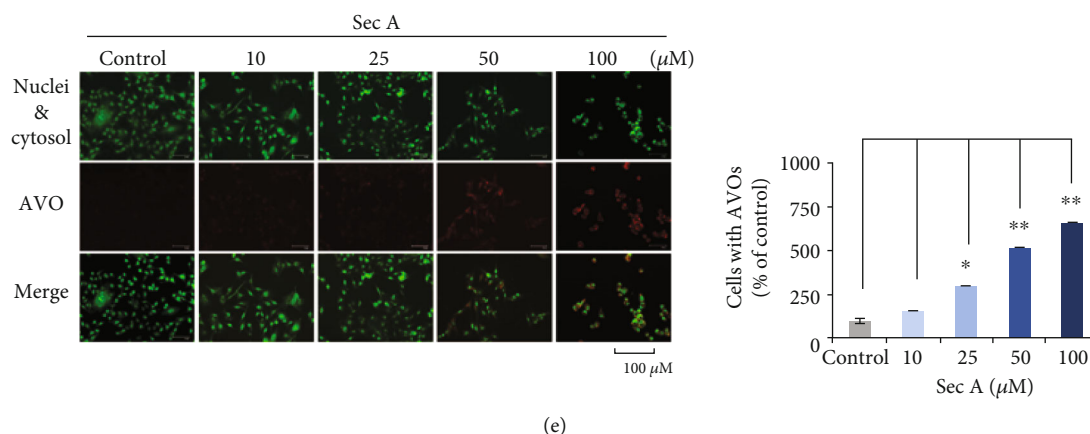


FIGURE 2: Effects of Iso A and Sec A on the normal and melanoma cells. (a) HaCaT and Hs68 proliferations after the treatments of Iso A and Sec A for 24 h. (b) Quantifications of B16F10, MeWo, A2058, and A375 cell growth inhibitions in the above conditions, respectively. (c) Fluorescent images of Iso A and Sec A-induced acidic autophagic AVOs. Cells were stained with AO to detect with a fluorescence microscopy. At least three photos were taken in various view versions, and one was chosen as an example to be demonstrated. The data represented mean values \pm SD of three independent experiments performed. * $p < 0.05$ and ** $p < 0.01$. $n = 3$.

DNA integrity were not good to be detected. In addition, the tumor cellular viability was decreased from 10 to 100 μM compared with the vehicle control group, which indirectly indicated the dose-dependent anticancer effects.

3.6. The Autophagy-Related mRNA and Protein Expressions. Since the AVO fluorescence enhancement after 24 h treatment was observed, quantitative real-time polymerase chain reaction (qRT-PCR) and Western blot analyses were conducted to further confirm the autophagy performance in Iso A and Sec A treated-B16F10 cells. In Figure 4(a), autophagic-related genes were examined, and we chose representative hallmarks to present this mechanism. Here, the transcriptional expressions involved in the programmed cell death signaling pathway were evaluated by the treatments of both experimental groups. It revealed that gene expressions of Atg 3, 6 (Beclin-1), and 12 were enhanced at a low dosage of 25 μM (early cell death phase) and decreased at 100 μM (late cell death phase). We also demonstrated typical autophagic-related proteins in Figure 4(b) after both compound treatments. Beclin-1, Atg 10, 16, and LC3B expressions were initially increased and then diminished at the concentrations of 25 and 100 μM , respectively, to show a consistent phenomenon with mRNA expressions. In addition, the expression level of Atg 5 was not upregulated drastically, but diminished significantly. The results presented that at the concentration of 25 μM , the expressions of mRNA and proteins were higher than that at 100 μM to point out in the early phase (lose dose), melanoma triggered a programmed cell death of autophagy.

3.7. Examining the Apoptotic-Related mRNA and Protein Expressions. Caspases are a family of cysteinyl aspartate-requiring proteases, which can be activated by proapoptotic stimuli. To additionally investigate the molecular mechanisms underlying the induced apoptosis in the cells, qRT-PCR analysis was focused on two panels of related genes in Figure 4(c). The tested concentrations were 0 (control, with

DMSO less than 1%, and PBS buffer), 25, and 100 μM for Iso A and Sec A-treated groups, respectively. There was a concentration-dependent extending manner on three genes in comparison to unstimulated counterparts, including caspase 9, Bax, and Bad. Western blot analysis was performed after 24 h treatment (Figure 4(d)). Here, the transcriptional expressions involved in the programmed cell death signaling pathway were evaluated of famous apoptotic proteins, JNK, Bcl-2, cyto c, cleavage caspase 9, and 3. Both data demonstrated that at the concentrations of 25 and 100 μM (in the late phase, high dosages), there were higher expressions of genes and proteins than the vehicle control group.

3.8. Cell Migration Inhibited by Iso A and Sec A. The cell migration usually plays a significant role in the maintenance of normal human physiology homeostasis. However, for cancer cells, the irregular proliferation of cell migration is usually responsible for the tumor metastasis. The potential migratory inhibition of B16F10 cells by Iso A and Sec A was evaluated by cellular wound healing assay as shown in Figure 5. After the treatments of 24 h, little cells migrated into the center zone between two dash lines of two experimental groups. The cell migration capacities were weakened, and it was concluded that our compounds inhibited the melanoma cellular movements in dose-dependent manners. At the concentrations of 50 and 100 μM , both compounds also had a cytotoxicity effect on B16F10 cells and influenced the survival of cells. At the concentrations of 10 and 25 μM , these compounds did not show strong cytotoxicity activities on cells, but the migration abilities were greatly inhibited compared with the vehicle control. This assay indicated that Iso A and Sec A possessed migration inhibitory potentials. Besides that, we will continue to examine the suppression abilities by using transwell assay in the coming future.

3.9. Histopathological and Immunohistochemical Analyses. After the above experimental studies and according to the regulations of 3R (Replacement, Reduction, and

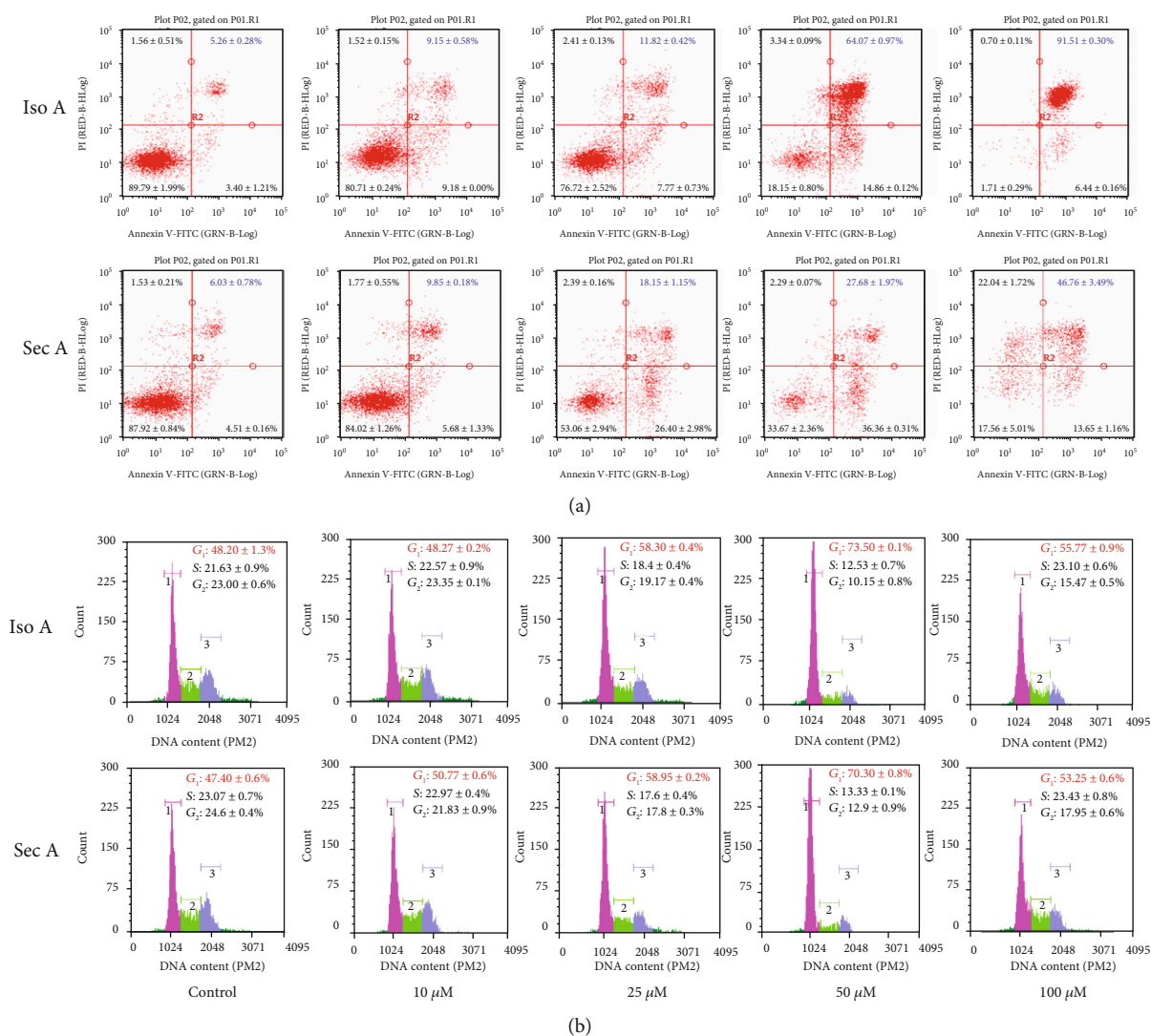


FIGURE 3: Cell apoptotic death and cycle distribution in B16F10 cells of Iso A and Sec A. (a, b) Iso A and Sec A induced cell apoptotic death. Apoptosis was analyzed by a flow cytometry after exposed to Iso A from 0 to 100 μM for 24 h and stained with annexin V/PI. (c, d) Effects of Iso A and Sec A on the cell cycle distribution in B16F10 cells. The cell cycle distribution in Iso A-induced B16F10 cells was determined by the flow cytometry. Cells were administered from 0 to 100 μM for 24 h. The data represented mean values \pm SD of three independent experiments performed. $n = 3$.

Refinement), we selected Iso A as our unique target compound to work *in vivo*. The xenograft assay showed that Iso A inhibited the melanoma B16F10 cell growth, and encouragingly, the dissected tumors were visibly smaller in the treatment groups compared to the vehicle group (Figure S2 and Figure 6(a)). We observed mice of the melanoma only group were all dead after four weeks without any therapeutic treatments; in the meantime, the other two group mice were alive with good exercise activity abilities and normal feeding properties. The data demonstrated that Iso A treatment effectively suppressed the tumor growth in the xenograft mice on tumor weight and tumor volume. Furthermore, H&E staining of the tumor tissues revealed abundant mitosis in the control group, whereas the number of mitosis-positive cells was significantly reduced in the sections from the Iso A treated mice (Figure 6(b)).

To further strengthen our research that Iso A induced autophagy and apoptosis promotes the inhibition of tumor growth in the *in vivo* examination, the immunohistochemical analyses revealed that the changes in autophagy and apoptosis were noteworthy in xenografted tumor tissues. Iso A treatment significantly increased the LC3B and cleavage caspase 3 expressions (Figure 6(c)). The quantification illustrated that the expression of cleavage caspase 3 was significantly higher than LC3B. Those results were consistent with our *in vitro* tests and indicated that Iso A induced the autophagy in the early stage and then triggered the cell death through apoptosis pathway.

4. Discussion

As a persuasive antimelanoma component, the agent should be harmless on normal cells and without side effects. Thus,

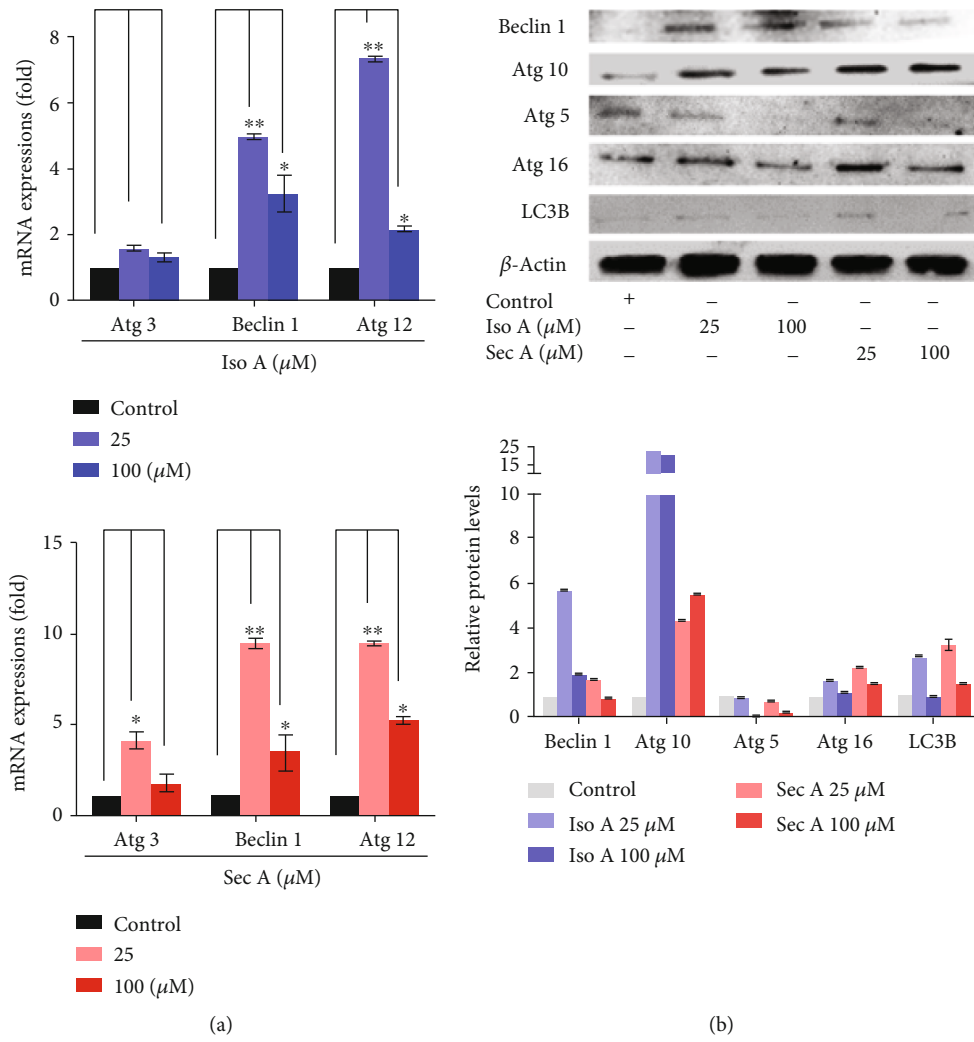


FIGURE 4: Continued.

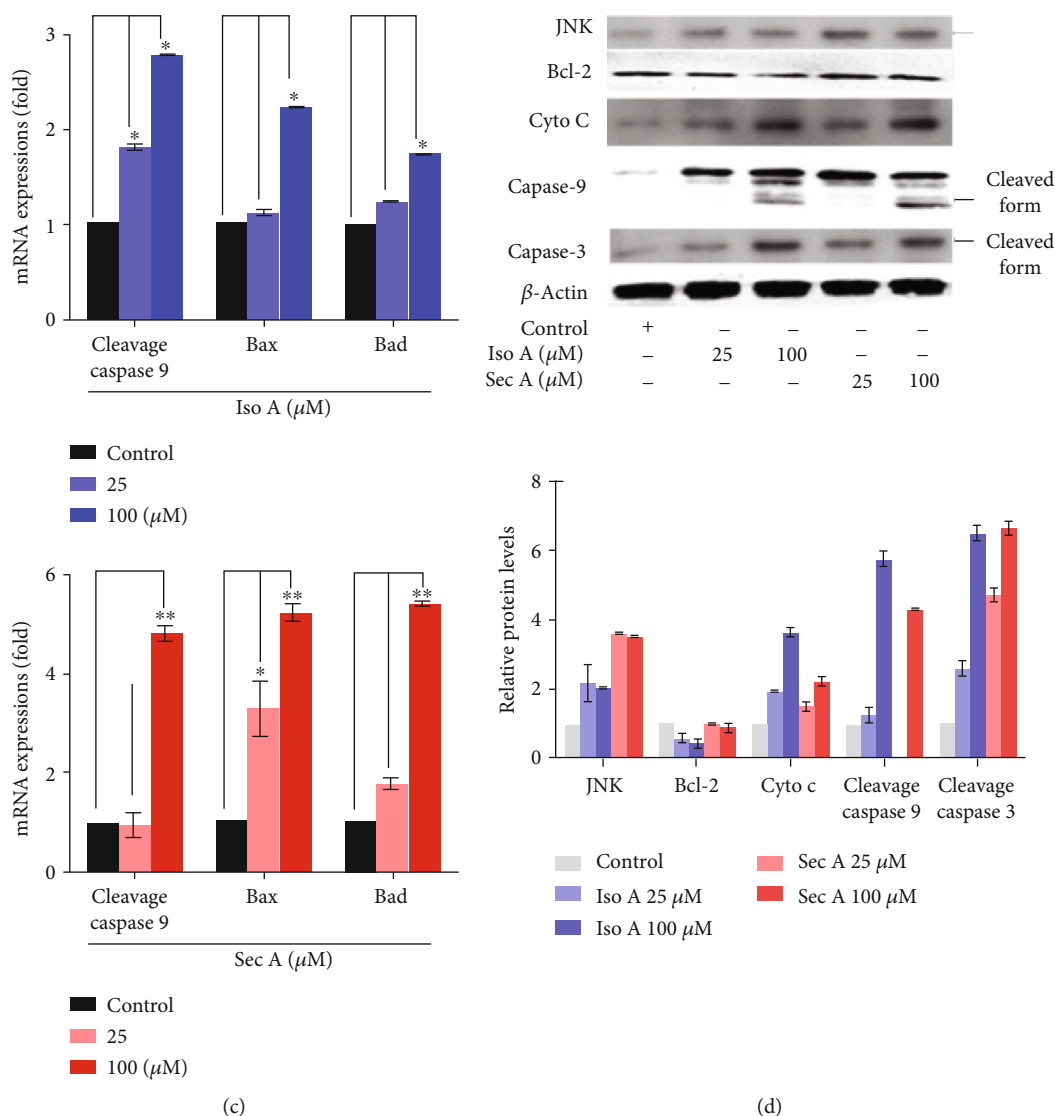


FIGURE 4: The autophagy and apoptosis-related mRNA and proteins induced by Iso A and Sec A in B16F10 cells. (a) Atg 3, 6, and 12 mRNA expression in B16F10 cells treated with different concentration (25 and 100 μM) was evaluated by the quantitative polymerase chain reaction and normalized to the GAPDH gene. (b) The autophagic-related proteins Beclin 1, Atg 10, 5, and 16 expressions. β -Actin was viewed as an internal control. (c) The mRNA expression of caspase 9, Bax, and Bad in B16F10 cells treated with different concentrations (25 and 100 μM) was evaluated by the quantitative polymerase chain reaction and normalized to the GAPDH gene. (d) The apoptosis-related proteins JNK, Bcl-2, Cytochrome c, Caspase 9, and 3 expressions in B16F10 cells with or without Iso A and Sec A treatment. β -Actin was viewed as an internal control. The data represented mean values \pm SD of three independent experiments performed. * $p < 0.05$ and ** $p < 0.01$. $n = 3$.

the cytotoxicity effect on normal skin cell growth is greatly important. Therefore, the cell viability assays were performed on the normal skin cells including fibroblasts and keratinocytes [22, 23]. Iso A and Sec A are pale yellowish liquid with the molecular formulas of $\text{C}_{13}\text{H}_{20}\text{O}_3$ and $\text{C}_{20}\text{H}_{36}\text{O}_4$, respectively. Iso A is a butanolide and Sec A is a secobutanolide. It was found that the Sec A inhibited the cell growth of both the melanoma and normal epidermal cells and HaCat keratinocytes cells because of the long-chain chemical structure. As shown in Figure 2(a), Iso A-treated normal cells presented high cell viabilities, thus Iso A may act as a potential anticancer agent. Sec A presented little cytotoxicity on keratinocytes and mild cytotoxicity at the concentrations of 10 and 25 μM

on the fibroblasts, and when the concentration increased to 50 and 100 μM , the cytotoxicity on the fibroblasts was also increased. Topical administration can also show good anti-melanoma effect and cause less damage to normal cells.

One of the major problems with cancer treatment is the abnormal fast proliferation and metastatic of tumor cells, which also leads to an increase in recurrence and mortality. In this study, to determine the cell proliferation inhibition effects of natural products on melanoma, four melanoma cells including B16F10, A2058, A375, and MeWo were treated with Iso A and Sec A from 0 to 100 μM for 24 h. As shown in Figures 2(b) and 2(c), our samples presented inhibitory activities on all four melanoma cells, and the

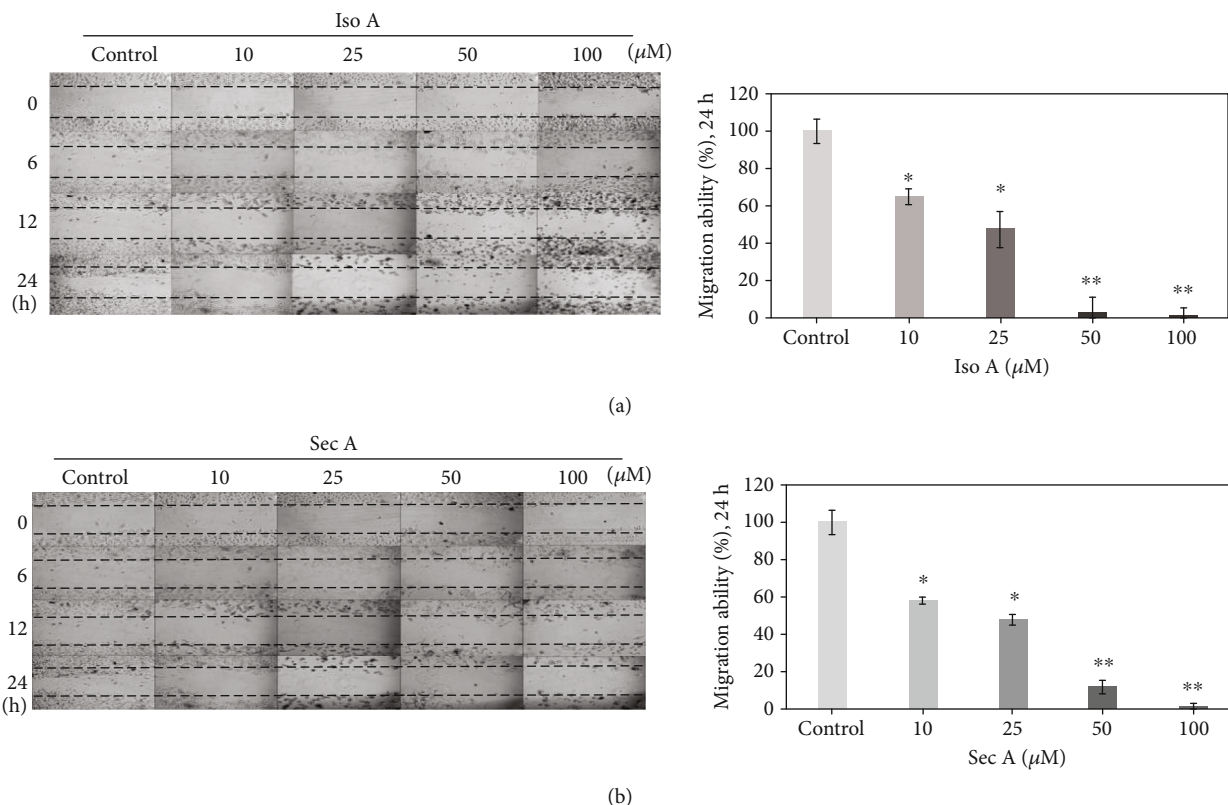


FIGURE 5: *In vitro* studies of migratory inhibition activities on B16F10 cells by Iso A and Sec A. The effects of migratory suppression were examined by wound healing assay after 24h treatment with 0, 10, 25, 50, and 100 μM , respectively. The migratory property was quantitatively measured by the software, ImageJ. The data represented mean values \pm SD of three independent experiments performed. * $p < 0.05$ and ** $p < 0.01$ (the vehicle group was compared as the control standard). $n = 3$.

cytotoxicity effects on B16F10, MeWo, and A2058 were relatively stronger. Previous studies have presented that the interaction between cancer cells and the extracellular matrix (ECM) plays an important role in the cell proliferation and migration [24]. Malignant melanoma is one of the most aggressive cancer, but the traditional treatment for metastatic melanoma is limited [25]. Chemotherapies such as fotemustine, dacarbazine, and temozolamide have been used for more than 35 years but are still ineffective in many ways [26]. Therefore, there is an urgent need to find new agents with antimigratory activity. In Figure 5, our results indicated that two compounds reduced the migratory ability of metastatic malignant melanoma cells. In high concentration treatment, the depression of cell migration might also contribute to the cell growth inhibition and cell death. Thus, it will be valuable to examine if Iso A and Sec A can modulate the ECM metabolism process to inhibit the metastasis and invasion of melanoma in the future work [27, 28]. In the coming future, we will continue to evaluate the migratory suppression via the transwell assay to reveal the detailed mechanism.

We further identified the roles of Atg caspase proteins in the autophagic and apoptotic cells induced by Iso A and Sec A in malignant melanoma B16F10 cells, and involved mRNA and proteins were examined. On the basis of the cell viability and cell migration assays, it was confirmed that both treatments induced the death of melanoma cells. There are three

major types of programmed cell death (PCD): apoptosis, autophagy, and necrosis [29]. In this study, the first two cell death mechanisms were focused on. Autophagy is a conserved catabolic process that digests cytoplasmic components within lysosomes, and it can be triggered by organelle damage, DNA damage, and cell starvation [30]. It is thought as a survival mechanism, which accelerates the degradation of damaged cytoplasmic contents and maintains the cellular homeostasis. However, excessive active autophagy can also lead to cell death. Through AO staining (Figures 2(d) and 2(e)), the performance of autophagy induced by the experimental treatment was initially confirmed, and Western blot analysis identified the autophagic cell death. Autophagy is regulated by a set of Atg proteins. Figures 4(a) and 4(b) revealed that two components enhanced the expressions of Atg 5, 10, 6, and 16 [29].

Among three PCD types, apoptosis is considered as the principal cell death pathway [31]. A series of assays were carried out to identify that the tumor cells are induced by autophagy in the early stage, and then apoptosis is induced by the treatments after the autophagy. Annexin V-FITC/PI double staining presented that in tested concentrations, the fraction ratio of late apoptosis cells which were in the right upper quadrant was significantly increased in dose-dependent manners (Figures 3(a) and 3(b)). With the purpose of blocking cell proliferation, controlling the cell cycle

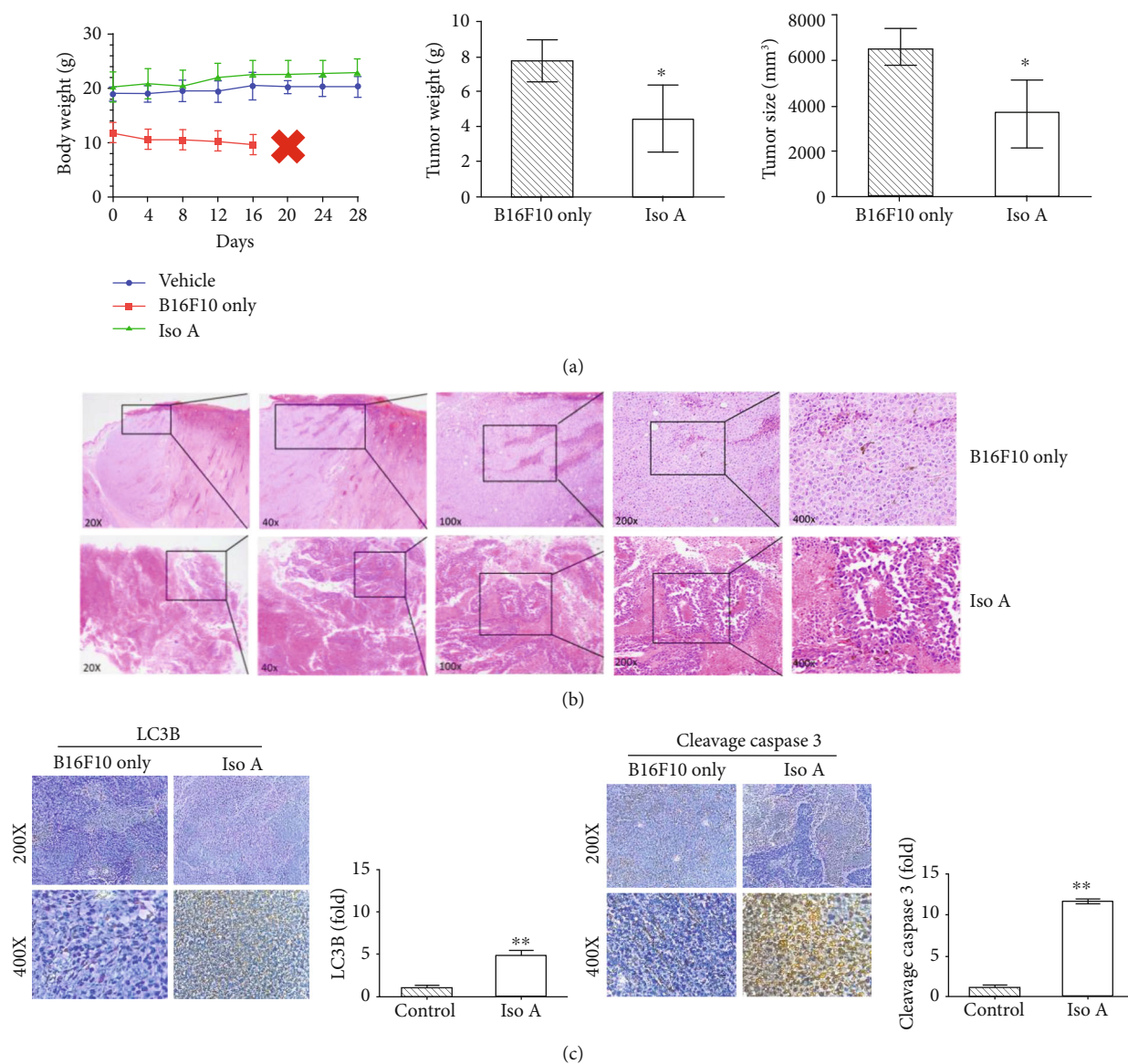


FIGURE 6: Animal test and histopathologic analysis of melanoma tumor inhibition (induced by B16F10 cells) treated with Iso A. $n = 6$. (a) Antitumor activity of Iso A in nude mice xenograft model. Mice morbidity-free survival efficacy, tumor weight, and tumor volume measurements were demonstrated after sacrifices. (b) H&E staining of tumor mass of BALB/c mice in the dorsal implant with xenograft B16F10 melanoma tumor cells of Iso A treatment. Smaller tumor mass and tumor cells expressed round to polygonal shapes with several characteristics, including melanin pigment, high mitosis, and central massive necrosis in the mouse. (c) Apoptotic protein LC3B expression and autophagic protein cleavage caspase 3 secretion in tissues treated with/without Iso A detected by immunohistochemistry. The data represented mean values \pm SD of three independent experiments performed. * $p < 0.05$ and ** $p < 0.01$.

presents a foremost regulatory mechanism [15]. The cell cycle analysis showed that two treatments stimulated DNA damage, arrested the cell cycle, and induced G2/M accumulation (Figures 6(d) and 6(e)). Caspases play a crucial role in the process of apoptotic cascade. Apoptosis can be triggered by internal or external factors, such as cytotoxic stress, DNA damage, and growth factor withdrawal [32]. In response to those proapoptotic stimuli, the outer membrane of mitochondrial will be damaged and lose the integrity, the permeabilization of mitochondrial will be increased, and the proapoptotic protein cytochrome c will be released to accelerate the caspase activation [33]. Western blot analysis

showed that both treatments triggered the release of cytochrome c, induced the activation of caspase 9, and then caspase 9 stimulated the downstream of caspase 3 (Figures 4(c) and 4(d)) [34]. JNK is an important branch of MAPK pathways, which plays a vital role in cell cycle, reproduction, apoptosis, cell stress, and other physiological and pathological processes. The results indicated that the MAPK signaling pathway might be the apoptosis reaction in those processes (Figure 7(b)). Bcl-2 is an antiapoptotic protein which can suppress the apoptosis. Previous studies have shown that Bcl-2 could inhibit autophagy by interacting with Bax/Bad and Beclin 1 [35]. The JNK-Bcl-2 pathway

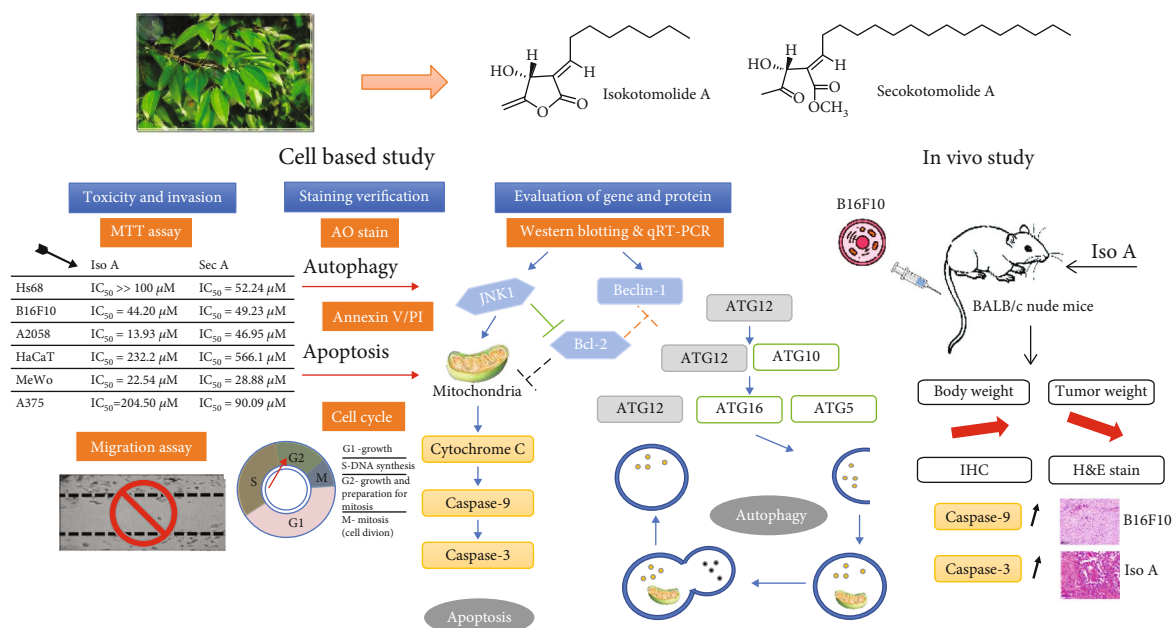


FIGURE 7: Proposed molecular mechanism diagram of *C. kotoense* components inhibit melanoma *in vitro* and *in vivo* signaling pathway.

activation can both trigger apoptosis and autophagy [36]. Because autophagy also plays a role in protecting the cells from death stimulus, the interaction between autophagy and apoptosis in Iso A and Sec A-treated cells should undergo advanced investigation.

In vivo research was followed to further boost the antitumor activities of our sample by xenografted BALB/c nude mice. This study demonstrated that Iso A has lower toxicity on normal human skin cells. The treatment via subcutaneous injection in xenografted nude mice resulted in a decrease of the tumor volume during the time course [37, 38]. Histopathological H&E staining of the tumor tissues demonstrated that there was abundant mitosis in the control group; however, the dorsal implant massive necrosis phenomenon was identified in the tumor sections treated with Iso A (Figures 6(b) and 6(c)). Smaller tumor mass and tumor cells expressed round to polygonal shapes with melanin pigment, advanced mitosis, and central massive necrosis within the xenografted mice. In summary, *in vitro* and *in vivo* examinations confirmed that Iso A and Sec A treatments inhibit the melanoma growth and metastasis effectively in Figure 7.

5. Conclusions

Based on the above results, we targeted Iso A and Sec A isolated from *Cinnamomum kotoense* from a variety of compounds screening with the purpose of melanoma therapy. Both Iso A and Sec A showed biofunctions that induced autophagy in the early stage and induced the cell death through apoptosis in human malignant melanoma and showed a little cytotoxicity on normal skin cells. Histopathological staining and immunohistochemical staining demonstrated that the tumor cell inhibited by Iso A. To our best knowledge, this is the first study of Iso A and Sec A to be potential natural herbal components for human melanoma

chemotherapy. Abbreviation within figures: Iso A: isokotomolide A; Sec A: secokotomolide A.

Data Availability

The datasets generated during and/or analysed during the current study are available from the corresponding author on reasonable request.

Conflicts of Interest

The authors declare no conflict of interest.

Authors' Contributions

Jian Li, Chung-Yi Chen, Jyun Yin Huang, Lin Wang, Zixuan Xu, Wenyi Kang, and Hui-Min David Wang performed the experiments and analyzed the data; Jian Li, Chung-Yi Chen, Lin Wang, Wenyi Kang, and Hui-Min David Wang contributed reagents/materials/analysis tools; Jian Li, Chung-Yi Chen, Jyun Yin Huang, Lin Wang, Zixuan Xu, Wenyi Kang, and Hui-Min David Wang wrote the paper. Jian Li and Chung-Yi Chen contributed equally to this work.

Acknowledgments

Jyun Yin Huang carried out his thesis research and contributed some results under the auspices of the Master Program in Graduate Institute of Biomedical Engineering, National Chung Hsing University. We also thank Miss Xiao Chung Li (School of Pharmacy, China Pharmaceutical University 211198, China) to assist the experiments. This work was supported by grants from the Ministry of Science and Technology, Taiwan (MOST 108-2221-E-005-044), and we also

thank the project of Natural Science Foundation of Fujian Province, China (Grant No. 2017J01636).

Supplementary Materials

Table S1: primers were used for qRT-PCR to analyze the apoptotic and antiapoptotic gene expressions. Figure S1: IACUC certificate of animal examinations (IACUC number: 106-111). Figure S2: antitumor activity of Iso A in the xenograft nude mice model via B16F10 melanoma cell model. (Supplementary Materials)

References

- [1] C.-Y. Chen, C.-C. Chiu, C.-P. Wu, Y.-T. Chou, and H.-M. Wang, "Enhancements of skin cell proliferations and migrations via 6-dehydrogingerdione," *Journal of Agricultural and Food Chemistry*, vol. 61, no. 6, pp. 1349–1356, 2013.
- [2] A. E. Coghill, L. G. Johnson, D. Berg, A. J. Resler, N. Leca, and M. M. Madeleine, "Immunosuppressive medications and squamous cell skin carcinoma: nested case-control study within the skin cancer after organ transplant (SCOT) cohort," *American Journal of Transplantation*, vol. 16, no. 2, pp. 565–573, 2016.
- [3] J. Wang, Y. Zhou, L. Ma et al., "CIAPIN1 targeted NHE1 and ERK1/2 to suppress NSCLC cells' metastasis and predicted good prognosis in NSCLC patients receiving pneumonectomy," *Oxidative Medicine and Cellular Longevity*, vol. 2019, Article ID 1970818, 15 pages, 2019.
- [4] L. C. Lin, C. Y. Chen, C. H. Kuo et al., "36H: A novel potent inhibitor for antimelanogenesis," *Oxidative Medicine and Cellular Longevity*, vol. 2018, Article ID 6354972, 12 pages, 2018.
- [5] S. Chummun and N. R. McLean, "Management of malignant skin cancers," *Surgery (Oxford)*, vol. 29, no. 10, pp. 529–533, 2011.
- [6] M. El-Kayal, M. Nasr, S. Elkheshen, and N. Mortada, "Colloidal (-)-epigallocatechin-3-gallate vesicular systems for prevention and treatment of skin cancer: a comprehensive experimental study with preclinical investigation," *European Journal of Pharmaceutical Sciences*, vol. 137, article 104972, 2019.
- [7] C. Caddeo, A. Nacher, A. Vassallo et al., "Effect of quercetin and resveratrol co-incorporated in liposomes against inflammatory/oxidative response associated with skin cancer," *International Journal of Pharmaceutics*, vol. 513, no. 1-2, pp. 153–163, 2016.
- [8] D. D'Arcangelo, C. Giampietri, M. Muscio, F. Scatozza, F. Facchiano, and A. Facchiano, "WIP1, BAG1, and PEX3 autophagy-related genes are relevant melanoma markers," *Oxidative medicine and cellular longevity*, vol. 2018, Article ID 1471682, 12 pages, 2018.
- [9] C.-Y. Chen, Y.-L. Hsu, Y.-Y. Chen, J.-Y. Hung, M.-S. Huang, and P.-L. Kuo, "Isokotomolide A, a new butanolide extracted from the leaves of *Cinnamomum kotoense*, arrests cell cycle progression and induces apoptosis through the induction of p53/p21 and the initiation of mitochondrial system in human non-small cell lung cancer A549 cells," *European Journal of Pharmacology*, vol. 574, no. 2-3, pp. 94–102, 2007.
- [10] C.-H. Chen, W.-L. Lo, Y.-C. Liu, and C.-Y. Chen, "Chemical and cytotoxic constituents from the leaves of *Cinnamomum kotoense*," *Journal of Natural Products*, vol. 69, no. 6, pp. 927–933, 2006.
- [11] C.-Y. Chen, K.-C. Cheng, A. Y. Chang, Y.-T. Lin, Y.-C. Hseu, and H.-M. Wang, "10-Shogaol, an antioxidant from *Zingiber officinale* for skin cell proliferation and migration enhancer," *International Journal of Molecular Sciences*, vol. 13, no. 2, pp. 1762–1777, 2012.
- [12] Y. Li, L. Wang, P. Wang et al., "Ginsenoside-Rg1 rescues stress-induced depression-like behaviors via suppression of oxidative stress and neural inflammation in rats," *Oxidative medicine and cellular longevity*, vol. 2020, Article ID 2325391, 15 pages, 2020.
- [13] Y.-T. Chen, C.-J. Kao, H.-Y. Huang et al., "Astaxanthin reduces MMP expressions, suppresses cancer cell migrations, and triggers apoptotic caspases of *in vitro* and *in vivo* models in melanoma," *Journal of Functional Foods*, vol. 31, pp. 20–31, 2017.
- [14] P.-H. Li, Y.-P. Chiu, C.-C. Shih et al., "Biofunctional activities of Equisetum *Ramosissimum* extract: protective effects against oxidation, melanoma, and melanogenesis," *Oxidative Medicine and Cellular Longevity*, vol. 2016, Article ID 2853543, 9 pages, 2016.
- [15] P.-F. Wu, C.-C. Chiu, C.-Y. Chen, and H.-M. D. Wang, "7-Hydroxydehydroneuciferine induces human melanoma death via triggering autophagy and apoptosis," *Experimental Dermatology*, vol. 24, no. 12, pp. 930–935, 2015.
- [16] H.-M. D. Wang, C.-C. Chen, P. Huynh, and J.-S. Chang, "Exploring the potential of using algae in cosmetics," *Biore-source Technology*, vol. 184, pp. 355–362, 2015.
- [17] H.-J. Zhong, L. Lu, K.-H. Leung et al., "An iridium(III)-based irreversible protein-protein interaction inhibitor of BRD4 as a potent anticancer agent," *Chemical Science*, vol. 6, no. 10, pp. 5400–5408, 2015.
- [18] M. Farrag, S. Abri, and N. D. Leipzig, "pH-dependent RNA isolation from cells encapsulated in chitosan-based biomaterials," *International Journal of Biological Macromolecules*, vol. 146, pp. 422–430, 2020.
- [19] L.-J. Liu, W. Wang, S.-Y. Huang et al., "Inhibition of the Ras/Raf interaction and repression of renal cancer xenografts *in vivo* by an enantiomeric iridium(III) metal-based compound," *Chemical Science*, vol. 8, no. 7, pp. 4756–4763, 2017.
- [20] D.-L. Ma, L.-J. Liu, K.-H. Leung et al., "Antagonizing STAT3 dimerization with a rhodium(III) complex," *Angewandte Chemie, International Edition*, vol. 53, no. 35, pp. 9178–9182, 2014.
- [21] H. M. Wang, C. C. Chiu, P. F. Wu, and C. Y. Chen, "Subamollide E from *Cinnamomum subavenium* induces sub-G1 cell cycle arrest and caspase-dependent apoptosis and reduces the migration ability of human melanoma cells," *Journal of Agricultural and Food Chemistry*, vol. 59, no. 15, pp. 8187–8192, 2011.
- [22] C.-C. Wang, S.-Y. Huang, S.-H. Huang et al., "A synthetic biological secondary metabolite, Lycogen™, produced and extracted from *Rhodobacter sphaeroides* WL-APD911 in an optimization scale-up strategy," *Food Science and Human Wellness*, vol. 6, no. 4, pp. 195–201, 2017.
- [23] P.-H. Li, L.-H. Liu, C.-C. Chang et al., "Silencing stem cell factor gene in fibroblasts to regulate paracrine factor productions and enhance c-kit expression in melanocytes on melanogenesis," *International Journal of Molecular Sciences*, vol. 19, no. 5, 2018.
- [24] M. Owyong, G. Efe, M. Owyong, A. J. Abbasi, V. Sitarama, and V. Plaks, "Overcoming barriers of age to enhance efficacy of

- cancer immunotherapy: the clout of the extracellular matrix,” *Frontiers in Cell and Development Biology*, vol. 6, 2018.
- [25] C. Rong, Z. Yun-Yan, L. Jia-Nan et al., “Ischemic postconditioning alleviates intestinal ischemia-reperfusion injury by enhancing autophagy and suppressing oxidative stress through the Akt/GSK-3 β /Nrf2 pathway in mice,” *Oxidative Medicine and Cellular Longevity*, vol. 2020, Article ID 6954764, 14 pages, 2020.
- [26] R. J. Davey, A. van der Westhuizen, and N. A. Bowden, “Metastatic melanoma treatment: combining old and new therapies,” *Critical Reviews in Oncology/Hematology*, vol. 98, pp. 242–253, 2016.
- [27] H.-Y. Chou, C. Lee, J.-L. Pan et al., “Enriched astaxanthin extract from *Haematococcus pluvialis* augments growth factor secretions to increase cell proliferation and induces MMP1 degradation to enhance collagen production in human dermal fibroblasts,” *International Journal of Molecular Sciences*, vol. 17, no. 6, 2016.
- [28] H. M. Wang, C. L. Kao, W. J. Li, H. T. Li, and C. Y. Chen, “Two new phenylalkanooids from the rhizomes of *Zingiber officinale*,” *Chemistry of Natural Compounds*, vol. 54, no. 1, pp. 7–9, 2018.
- [29] S. Shimizu, T. Yoshida, M. Tsujioka, and S. Arakawa, “Autophagic cell death and cancer,” *International Journal of Molecular Sciences*, vol. 15, no. 2, pp. 3145–3153, 2014.
- [30] B. Liu, Z. N. Oltvai, H. Bayır et al., “Quantitative assessment of cell fate decision between autophagy and apoptosis,” *Scientific Reports*, vol. 7, no. 1, article 17605, pp. 1–14, 2017.
- [31] Q. Chen, J. Kang, and C. Fu, “The independence of and associations among apoptosis, autophagy, and necrosis,” *Signal Transduction and Targeted Therapy*, vol. 3, no. 1, 2018.
- [32] C.-C. Tseng, Y.-J. Lin, W.-T. Liu et al., “Metabolic engineering probiotic yeast produces 3S, 3'S-astaxanthin 3'S-astaxanthin to inhibit B16F10 metastasis,” *Food and Chemical Toxicology*, vol. 135, pp. 110993–1111001, 2020.
- [33] L. Hu, Y. Zhang, W. Miao, and T. Cheng, “Reactive oxygen species and Nrf2: functional and transcriptional regulators of hematopoiesis,” *Oxidative Medicine and Cellular Longevity*, vol. 2019, Article ID 5153268, 11 pages, 2019.
- [34] G. Blandino, F. Valenti, A. Sacconi, and S. Di Agostino, “Wild type- and mutant p53 proteins in mitochondrial dysfunction: emerging insights in cancer disease,” *Seminars in Cell & Developmental Biology*, vol. 98, pp. 105–117, 2020.
- [35] Y. Chen, J.-Y. Huang, Y. Lin, I.-F. Lin, Y.-R. Lu, and L.-H. Liu, “Antioxidative and antimelanoma effects of various tea extracts via a green extraction method,” *Journal of Food Quality*, vol. 2018, Article ID 5156073, 6 pages, 2018.
- [36] J. Yang and S. Yao, “JNK-Bcl-2/Bcl-xL-Bax/Bak pathway mediates the crosstalk between matrine-induced autophagy and apoptosis via interplay with beclin 1,” *International Journal of Molecular Sciences*, vol. 16, no. 10, pp. 25744–25758, 2015.
- [37] C.-T. Chang, Y.-C. Hseu, V. Thiyagarajan et al., “Chalcone flavokawain B induces autophagic-cell death via reactive oxygen species-mediated signaling pathways in human gastric carcinoma and suppresses tumor growth in nude mice,” *Archives of Toxicology*, vol. 91, no. 10, pp. 3341–3364, 2017.
- [38] D. Denton, T. Xu, and S. Kumar, “Autophagy as a pro-death pathway,” *Immunology and Cell Biology*, vol. 93, no. 1, pp. 35–42, 2015.

Research Article

In Vitro Studies on the Immunomodulatory Effects of *Pulicaria crispa* Extract on Human THP-1 Monocytes

Tarfa Albrahim,¹ Moonerah M. Alnasser,² Mashaal R. Al-Anazi,³ Muneera D. ALKahtani,⁴ Saad Alkahtani ² and Ahmed A. Al-Qahtani ^{3,5}

¹College of Health and Rehabilitation Sciences, Department of Health Sciences, Clinical Nutrition, Princess Nourah Bint Abdulrahman University, Riyadh, Saudi Arabia

²Department of Zoology, College of Science, King Saud University, Riyadh, Saudi Arabia

³Department of Infection and Immunity, Research Center, King Faisal Specialist Hospital & Research Center, Riyadh, Saudi Arabia

⁴Department of Biology, College of Science, Princess Nourah bint Abdulrahman University, Riyadh, Saudi Arabia

⁵Department of Microbiology and Immunology, Alfaisal University, School of Medicine, Riyadh, Saudi Arabia

Correspondence should be addressed to Ahmed A. Al-Qahtani; aqahntani@kfshrc.edu.sa

Received 20 April 2020; Revised 29 June 2020; Accepted 21 July 2020; Published 26 September 2020

Guest Editor: Madhukar Saxena

Copyright © 2020 Tarfa Albrahim et al. This is an open access article distributed under the Creative Commons Attribution License, which permits unrestricted use, distribution, and reproduction in any medium, provided the original work is properly cited.

Background. *Pulicaria crispa* (*P. crispa*) is a plant from the Compositae family that exhibits antioxidant, anti-inflammatory, antibacterial, and cytotoxic activities. **Objective.** The current study aimed at investigating the immunomodulatory effects of *P. crispa* extract in lipopolysaccharide- (LPS-) stimulated human monocytic THP-1 cells. **Methods.** To induce macrophage differentiation, THP-1 cell lines were treated with phorbol-12-myristate 13-acetate, followed by exposure to LPS with or without 50 or 100 µg/ml of *P. crispa* extract. The following tests were employed to test the immunomodulatory effects of the extract: MTT assay, ELISA, Western blotting analysis, cell migration and phagocytosis assays, and Annexin V staining method. **Results.** Exposure to 100 µg/ml *P. crispa* extract significantly reduced THP-1 cell proliferation, migration, and phagocytosis (in LPS-stimulated cells, but not in unstimulated cells). Moreover, the extract alone significantly reduced the rate of THP-1 cell apoptosis, while it increased the rate of late apoptosis. Molecular investigations showed that treatment with *P. crispa* extract significantly upregulated the expression of ERK1, p-MAPK, P-P38, and Bcl2, while it significantly reduced the expression of ERK5, Bax, NF-κB, P-NF-κB, CCL1, CCL2, CCL5, CCL22, CXCL1, and CXCL10. **Conclusion.** *Pulicaria crispa* extract exhibited anti-inflammatory, antiproliferative, antimigratory, and antiphagocytic effects in LPS-stimulated THP-1 cells. Future studies should investigate these mechanisms in animal models with chronic inflammatory diseases.

1. Introduction

Macrophages (MΦs) are cells of the innate immune system that start differentiating in the human body in the second trimester of gestation. They are essential in maintaining immune homeostasis and play several roles in initiating and regulating the immune responses to foreign antigens [1]. Generally, MΦs were seen primarily as phagocytes that engulf bacteria and dying cells [2]; however, substantial recent evidence uncovered other functions executed by various surface and intracellular receptors of these cells. Such functions include regulation of bone remodeling [3], erythro-

poiesis [4], brain development [5], iron recycling [6], and tissue regeneration [7]. MΦs are classically divided into M1 and M2 cells: M1 MΦs which exhibit proinflammatory, bactericidal, and phagocytic activities and M2 cells which are involved in tissue regeneration and regulating the immune response via interleukin- (IL-) 10 secretion [8].

The role that MΦs play in inflammation is multifaceted [1]. Exposure to damage-associated molecular patterns (DAMPs), released from damaged cells, causes MΦs to secrete several cytokines including IL-1β, IL-6, tumor necrosis factor-α, and proinflammatory eicosanoids. These secreted molecules cause vasodilatation and edema, followed

by neutrophil recruitment [9]. Further, following phagocytosis and lysis of foreign organisms, MΦs present antigens from its surface major histocompatibility complex- (MHC-) II receptor molecules to allow T-helper cells to initiate adaptive immune response [10].

During resolution of the inflammation, some MΦs undergo apoptosis or convert from an initial proinflammatory (M1) phenotype to a healing proresolving (M2) phenotype consistent with plasticity of myeloid cells [11]. Examples of this behavior were observed in the muscles [12] and kidneys [13]. However, MΦs sometimes escape these destinies and become more active and with a longer lifespan [14]. The latter cells have been implicated in chronic inflammatory and autoimmune diseases [15].

Pulicaria crispera (also known as *Francoeuria crispera*) is a plant from the Compositae family that commonly grows in the Middle East countries, including Saudi Arabia and Egypt. Although it has been used in traditional medicine for a long time, it has become a topic of interest for medicinal research since the 1980s [16]. Previous studies have shown that *P. crispera* derivatives exert antioxidative [17], anti-inflammatory [18], and chemopreventive activities [19]. A phytochemical screening of *P. crispera* extract attributed these effects to the presence of coumarins, tannins, and flavonoids [18, 20].

The extracts of *P. crispera* have shown anti-inflammatory, as well as immunostimulatory effects. For example, several studies have shown antimicrobial effects for *P. crispera* extracts against Gram-negative bacteria [21–23], *Mycobacteria* [20, 21], *Candida albicans* [17], *Schistosoma mansoni* [24], *Leishmania* [25], and hepatitis B virus [26]. On the other hand, extracts from the *Pulicaria* species have been shown to inhibit neutrophil infiltration and alleviate oxidative stress. It was also postulated that it suppresses the generation of nitric oxide [27] and modulates the expression of intracellular adhesion molecule-1 (ICAM-1), tumor necrosis factor-(TNF-) α [18], and prostaglandin E2 [18]. Therefore, further study of their effects on the immune system, especially at the molecular level, will be particularly insightful.

Despite the benefits of the immune inflammatory response to foreign antigens, a dysregulated immune response can lead to a wide array of chronic inflammatory conditions [28]. Several *in vivo* and *in vitro* models have been proposed to study the anti-inflammatory and immunomodulatory effects of various phytochemicals and pharmaceutical compounds. Of these models, human leukemic THP-1 monocytes have attracted attention as a valid *in vitro* model to investigate the molecular mechanisms of inflammation [29–31]. For example, previous studies have used this model to evaluate the anti-inflammatory effects of several phytochemicals extracted from different organisms, including *Corydalis crispera*, *Corydalis dubia*, *Ajania nubigena*, *Meconopsis simplicifolia*, *Ocimum sanctum*, and *Uncaria tomentosa* [32–34].

Owing to the scarcity of molecular research regarding the immunomodulatory effects of *P. crispera* effects, the current study was performed to utilize human THP-1 cells as an *in vitro* model to test the effects of their exposure to lipopolysaccharide (LPS) and *P. crispera* extract.

2. Materials and Methods

2.1. *P. crispera* Extract. The preparation of the extract was described in detail elsewhere [26].

2.2. Growth and Maintenance of THP-1 Cells. The human monocytic THP-1 cells were cultured in RPMI media supplemented with 10% fetal bovine serum (FBS), 100 IU/ml penicillin, 100 μ g/ml streptomycin, and 3.7 g/l sodium bicarbonate. The cells were maintained in 37°C temperature and 5% CO₂.

2.3. Differentiation of THP-1 Cells into Macrophage-Like Cells. THP-1 cells (5×10^5) were incubated with 100 ng/ml of phorbol 12-myristate 13-acetate for 48 hours. The cells were then washed with RPMI 1640 serum-free medium to eliminate undifferentiated cells.

2.4. Treatment of MΦs with LPS and/or *P. crispera* Extract. Differentiated cells were treated with 100 ng/ml LPS, isolated from *Escherichia coli* O26:B6 bacteria (Sigma-Aldrich, St. Louis, MO, USA), alone, LPS + 50 μ g/ml or LPS + 100 μ g/ml of *P. crispera* extract. In some experiments, differentiated cells were treated with the extract alone (50 or 100 μ g/ml). The duration of the treatment was either 4 hours or 6 hours.

2.5. MTT Cell Proliferation Assay. The MTT assay kit (Abcam, Cambridge, MA, USA) was used following the manufacturer's instructions. The treated cells, at a density of 5×10^4 cells/well, were incubated with either 50 or 100 μ g/ml *P. crispera* extract for 1 to 8 days. After incubation with MTT reagent for three hours, the absorbance was read in the SpectraMax i3x Multi-Mode Microplate Reader (Molecular Devices, Sunnyvale, CA, USA) at 540 nm wavelength.

2.6. Expression Analysis by Real-Time Quantitative Reverse-Transcriptase Polymerase Chain Reaction (qRT-PCR). Total RNA was extracted from treated THP-1 cells using the QIAamp RNA Blood Mini Kit (Qiagen, Hilden, Germany) following the manufacturer's instructions, followed by a double-stranded cDNA synthesis using All-in-One cDNA Synthesis SuperMix (Biotool, Houston, TX, USA). The generated cDNA was used for real-time PCR experiments using target-specific primers and probes purchased from Applied Biosystems (Foster City, CA, USA). The mRNA expression levels of studied genes were normalized to GAPDH.

2.7. Enzyme-Linked Immunosorbent Assay (ELISA). Supernatants from treated cells were collected for quantitation of secreted proteins. The DuoSet® ELISA kit (R&D Systems, Minneapolis, MN, USA) was used to determine the quantities of IL-1 β , IL-8, CCL22, and CXCL10 following the manufacturer's instructions. Briefly, supernatants were added to wells precoated with protein-specific antibodies, incubated for 2 hours, washed three times with PBS, and incubated with Streptavidin-horseradish peroxidase (HRP) for 20 minutes. After washing, tetramethylbenzidine (TMB) substrate was added for 20 minutes, the reaction was stopped, and the color intensity was measured at wavelength 450 nm.

2.8. Western Blotting Analysis. The expression of ERK5, Bax, Bcl2, Cyclin-D1, ERK1, MEK1, NF- κ B, P-IKB- α , P-MAPK,

P-NF- κ B, and P-P38 in THP-1 cells was evaluated using the Western blotting analysis. The treated cells were lysed in the RIPA buffer, and the cellular proteins were separated on 12% SDS-polyacrylamide gel electrophoresis (PAGE). The proteins were then transferred to polyvinylidene difluoride (PVDF) membranes which were treated with 5% nonfat dry milk. The membranes were then probed with protein-specific primary antibodies overnight at 4°C, washed, and incubated with HRP-conjugated secondary antibodies. The reaction was detected by the addition of SuperSignal West Pico 16 Chemiluminescent substrate (Thermo Fisher Scientific, Waltham, MA). The bands were visualized on a GE Amersham Imager 600, and the proteins were quantified using the ImageJ software (National Institutes of Health, Bethesda, MD).

2.9. Cell Migration Assay. Cell migration was evaluated using the CytoSelect™ 24-Well Cell Migration Assay (Cell Biolabs, San Diego, CA, USA) following manufacturer's instructions. Briefly, treated cells were incubated in a serum-free RPMI in the upper chamber. The cells were allowed to migrate to the lower chamber filled with RPMI and FBS. The chamber was then incubated for 24 hours, and the migration capability was analyzed by reading the fluorescence of the GR dye at a wavelength of excitation/emission 480/520 nm.

2.10. Phagocytosis Assay. Treated THP-1 cells were incubated with Alexa Fluor 405-labeled Zymosan particles Molecular Probes (Carlsbad, CA, USA) for 1 hour in a serum-free RPMI medium at 37°C. Cells were washed three times with PBS to eliminate noninternalized fluorescent beads. The cells were analyzed by measuring the absorbance at OD of 405 nm.

2.11. Apoptosis Assay. Apoptosis was measured in treated cells by flow cytometry using Annexin V/propidium iodide double-staining as described before [35, 36], and the analysis was performed in FACScan equipped with the Cell Quest software (Becton Dickinson, Cockeysville, MD, USA).

2.12. Statistical Analysis. Data generated from the aforementioned assays were expressed as mean \pm standard error of mean and were presented in bar graphs with error bars. To compare the groups in, *t* test was used. A *p* value was considered significant if less than 0.05.

3. Results

3.1. The Effects of *Pulicaria crispa* Extract on THP-1 Cell Proliferation. To assess the effects of *P. crispa* extract on THP-1 cell proliferation, MTT assay was used by incubating the cells with 50 and 100 μ g/ml of the extract for 8 days. Analysis of the change in proliferation of the cells showed that while the vehicle control (DMSO) did not produce any significant difference in THP-1 cell proliferation in comparison to control monocytes, both concentrations of *P. crispa* extract significantly reduced the proliferation of the cells at each time point ($p = 0.01$) (Figure 1).

3.2. The Effects of *P. crispa* Extract on mRNA Expression in THP-1 Cells. To evaluate the mRNA expression of CCL2, CCL5, and TNF- α in THP-1 cells exposed to LPS or different

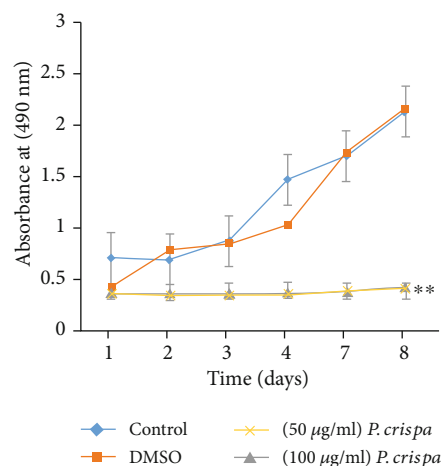


FIGURE 1: The effect of *P. crispa* extract on proliferation of THP-1 cells. The *y*-axis shows absorbance at 490 nm after incubation of cells treated with DMSO alone, 50 μ g/ml or 100 μ g/ml of *P. crispa* extract relative to untreated cells (control). ***p* value < 0.01 (treatment vs. control). Values represent the mean of three different experiments done in triplicate \pm SEM for each time point tested. Statistical analysis was performed using the *t* test.

concentrations of *P. crispa* extract, we used the qRT-PCR analysis. Exposure of cells to 100 ng/ml LPS at 4 and 6 hours significantly increased mRNA expression of CCL2 and CCL5 in a time-dependent manner ($p = 0.001$). However, treatment of LPS-exposed cells with *P. crispa* extract at 50 and 100 μ g/ml was associated with a significant decrease in CCL2 and CCL5 expression in comparison to LPS alone ($p = 0.001$) (Figures 2(a) and 2(b)). On the other hand, treatment of THP-1 cells with *P. crispa* extract alone resulted in a significant increase in mRNA expression of TNF- α at 4 and 6 hours ($p \leq 0.01$) (Figure 2(c)).

3.3. Protein Array Expression Analysis. Protein array was used to simultaneously detect expression of several proteins in treated cells. Comparison of control cells to cells treated with 100 ng/ml LPS showed significantly higher expression of ICAM1/CD54 ($p = 0.01$) and CCL2/MCP1 ($p = 0.03$), as well as significantly lower expression of IL1ra/IL1F3 ($p = 0.004$). However, no statistically significant differences were observed with regard to MIF, IL8, CCL1, MIP1a/MIP1b, CCL5/RANTES, and CXCL1/GROa (Figure 3(a)). In contrast, LPS-exposed cells treated with 100 μ g/ml *P. crispa* extract showed significant reductions with regard to CCL1 and CXCL1/GROa expression ($p < 0.05$). In addition, a significant increase in CCL5/RANTES, ICAM-1/CD54, and IL8 was observed. No significant differences were detected in the expression of MIF, IL1ra/IL1F3, and MIP-1a/MIP-1b (Figure 3(b)).

3.4. ELISA Assay Results. ELISA assay was used to confirm the results obtained by the protein array analysis. The supernatants of cultured cells were harvested after six hours of stimulation. The analysis of cells exposed to LPS only showed significant increase in the production of CCL22 ($p = 0.03$) and CXCL10 ($p = 0.001$) in comparison to control cells. On the other hand, LPS-exposed cells treated with *P. crispa*

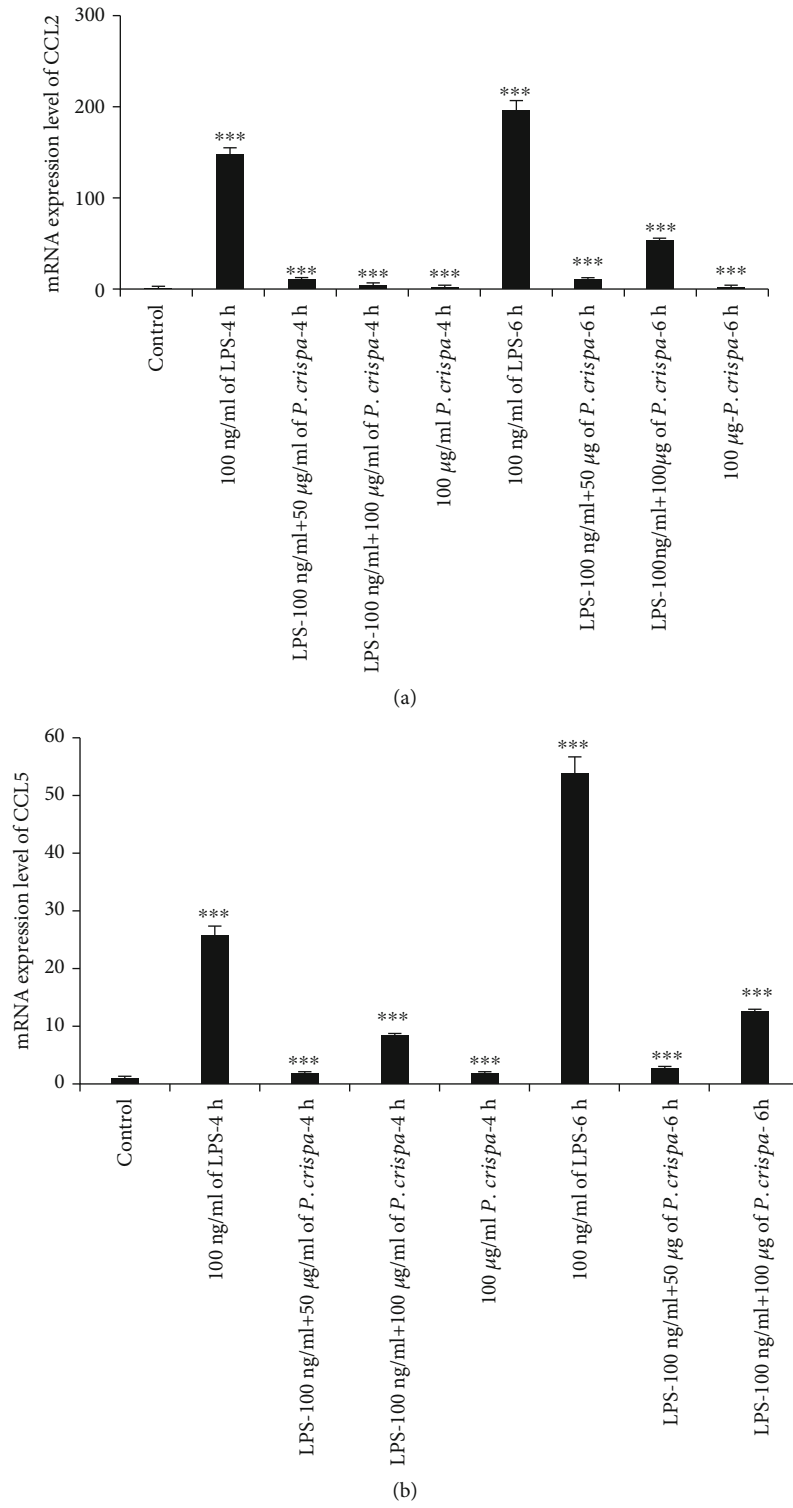


FIGURE 2: Continued.

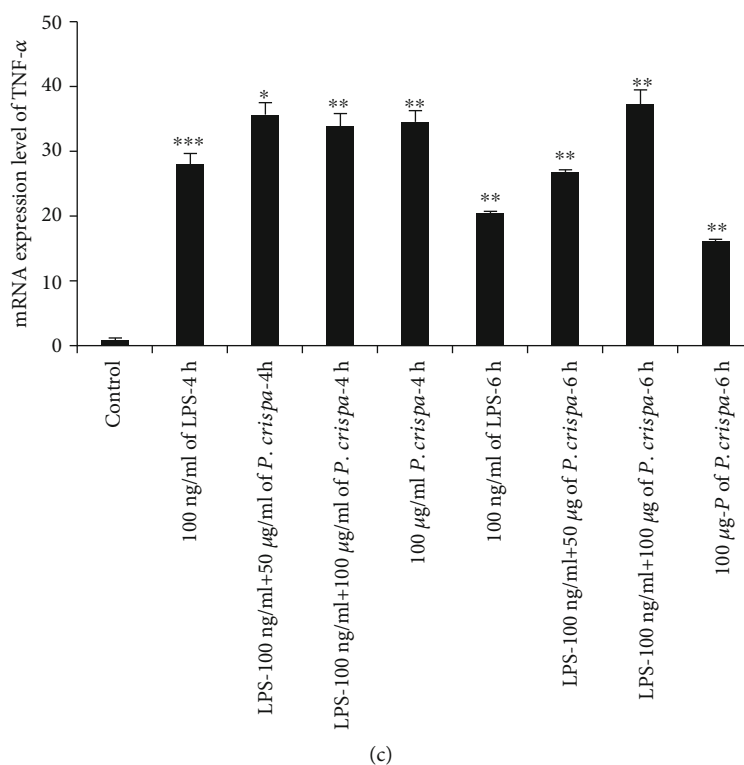


FIGURE 2: qRT-PCR analysis for the expression of (a) CCL2, (b) CCL5, and (c) TNF- α . The mRNA expression levels were normalized with GAPDH. Control cells were compared with LPS-treated cells. All other cells with different treatments were compared with LPS-treated cells. The data were expressed as mean \pm standard error done in triplicate for three independent experiments. Statistical significance was established using the *t* test. * <0.05 ; ** <0.01 ; *** <0.001 .

extract showed significant reduction in the production of CCL22 and CXCL10 ($p = 0.001$) (Figures 4(a) and 4(b)).

3.5. Western Blotting Analysis. The expression of 11 cell survival, apoptosis, and inflammatory proteins was measured through Western blotting analysis. In comparison to non-treated cells, LPS-exposed cells showed significant overexpression of ERK5, p-NF- κ B, and p-P38, as well as significant decreased expression of Bcl2, Bax, MEK1, ERK1, P-IKB- α , and NF- κ B. However, the expression of p-MAPK and Cyclin-D1 could not be detected in LPS-exposed cells (Figure 5). In contrast, LPS-exposed cells treated with 100 μ g/ml *P. crispa* extract showed significant downregulation of ERK5, Bax, P-IKB- α , and NF- κ B, as well as upregulation of Bcl2, ERK1, p-MAPK, and p-P38 in comparison to LPS only-treated cells. Of note, the expression of MEK1, P-NF- κ B, and Cyclin-D1 could not be detected in cells treated with LPS + *P. crispa* extract (Figure 5).

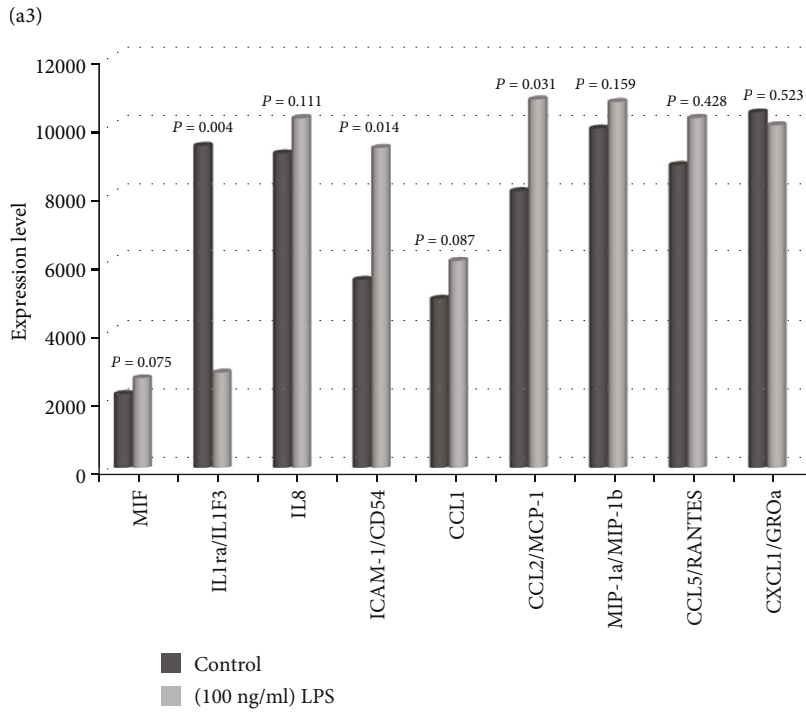
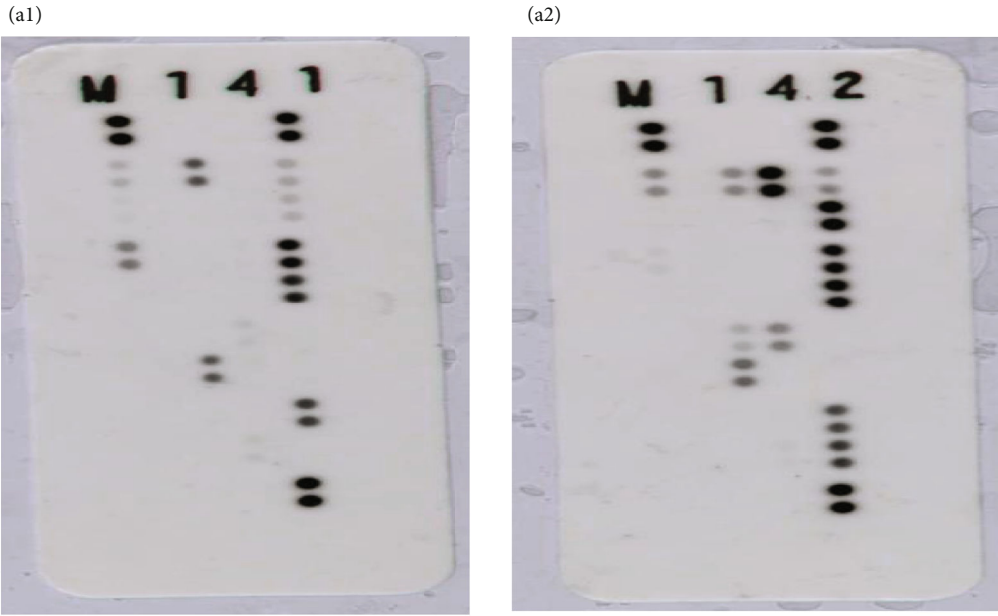
3.6. Cell Migration Assay. To assess the effect of *P. crispa* extract on the ability of THP-1 cell to respond to external stimuli, cell migration assay was used. The analysis showed that LPS-exposed cells were not significantly different from untreated control cells ($p = 0.279$). However, cells treated with *P. crispa* alone or in combination with LPS showed significantly reduced ($p < 0.0001$) cell migration capability in comparison to cells treated with LPS alone (Figure 6).

3.7. Phagocytosis Assay. The results of the phagocytosis assay showed that LPS-exposed THP-1 cells exhibited significantly less phagocytic activity than control untreated cells ($p < 0.0001$). Further, the addition of *P. crispa* extract to LPS-exposed cells reduced their phagocytic activity ($p < 0.0001$). However, THP-1 cells treated with *P. crispa* extract alone exhibited significantly higher phagocytic activity than cells treated with LPS alone ($p < 0.0001$) (Figure 7).

3.8. Flow Cytometry-Based Detection of Apoptosis. This assay was conducted using Annexin V/PI double-staining method. As shown in Figure 8 and Table 1, the majority (>90%) of monocyte cells and LPS-treated THP-1 cells remained viable with no statistically significant difference in both groups with regard to apoptotic and late apoptotic cells ($p = 0.77$). However, exposure of cells to *P. crispa* extract significantly decreased the number of apoptotic cells and increased the number of late apoptotic cells in comparison to control cells ($p = 0.15$). In comparison to LPS-treated cells, THP-1 cells treated with both LPS and *P. crispa* extract did not show significant differences in the percentage of apoptotic and late apoptotic cells ($p = 0.77$).

4. Discussion

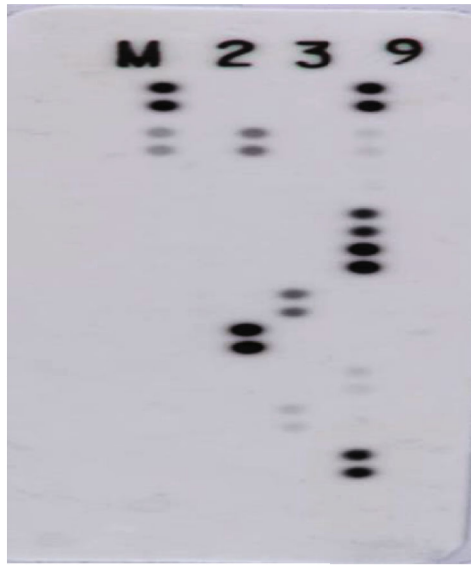
Persistent activation of M Φ s has been implicated in several chronic inflammatory and autoimmune diseases [37].



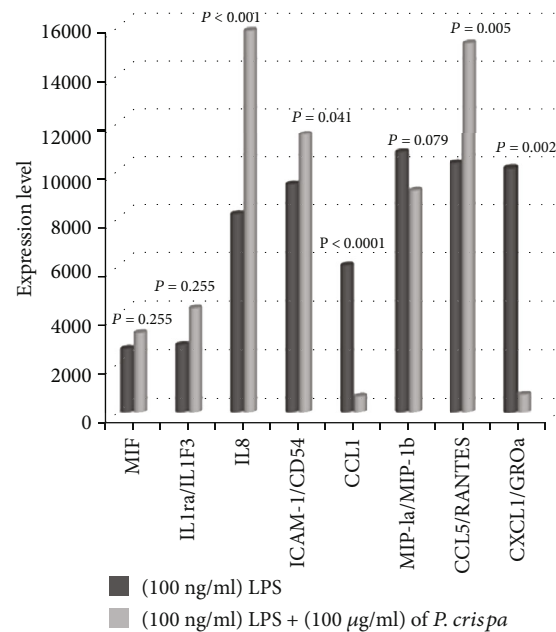
(a)

FIGURE 3: Continued.

(b1)



(b2)



(b)

FIGURE 3: Protein expression array analysis. (a) Control THP-1 cells (a1); cells treated with (100 ng/ml) of LPS (a2); histograms comparing the protein array expression results from controls and THP-1 cells treated 100 ng/ml of LPS (a3). (b) Cells treated with B2 B1 25 (100 ng/ml) of LPS + 100 µg/ml of *P. crispa* (b1); graphical representation of LPS-treated cells (shown in a2) compared with cells treated with LPS + *P. crispa* extract (b2). Statistical significance was established using the *t* test.

MΦs under prolonged stimulation secrete large quantities of proinflammatory and chemotactic molecules. These cells also become more resistant to apoptosis [38]. Here, we used an *in vitro* model (THP-1 human monocytes) to simulate activated macrophages during an inflammatory response.

To discuss our results, some physiological perspective is needed to be considered. Activated MΦs usually exhibit increased expression of molecules involved in proinflammatory signals such as NF-κB. This protein is essential in the pathway that increases the production of some interleukins,

such as IL-1, IL6, and TNF-α [39]. Furthermore, activated macrophages orchestrate the immune response by recruiting other cells into the inflammation area through chemotactic proteins, including CCL1, CCL2, CC5, CCL22, CXCL1, and CXCL10 [40]. Inside activated macrophages, the transcriptional program shifts in favor of prolonged survival, increased proliferation, and enhanced migration [41]. In this study, we further investigated these mechanisms and evaluated the role of *P. crispa* extract in modulating these functions in MΦs.

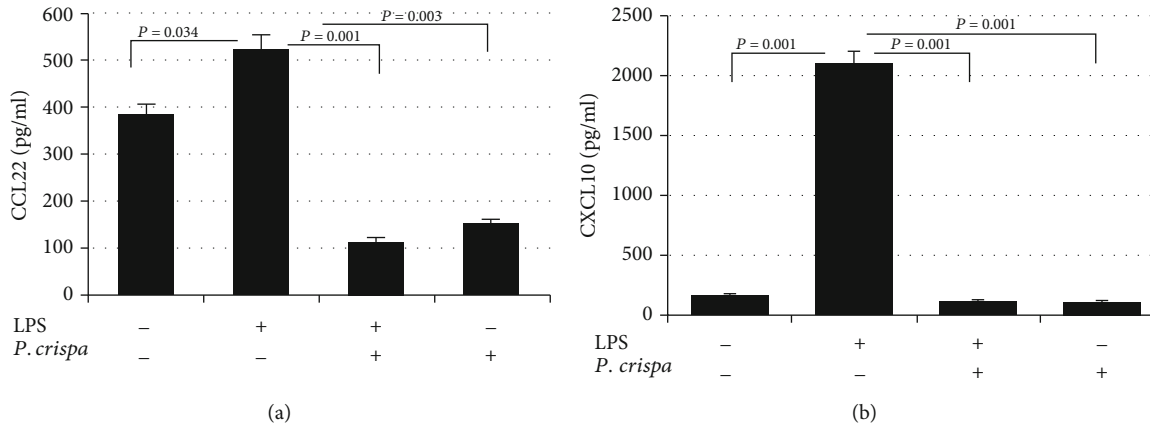


FIGURE 4: ELISA analysis of THP-1 cells after stimulation with LPS (100 ng/ml) with or without *P. crispa* extract (100 μ g/ml). The expressions of CCL22 (a) and CXCL10 (b) are detected. Culture supernatants were harvested 6 hours after stimulation and processed for ELISA. All samples were processed in triplicate for three independent experiments \pm SEM. Statistical significance was established using the *t* test.

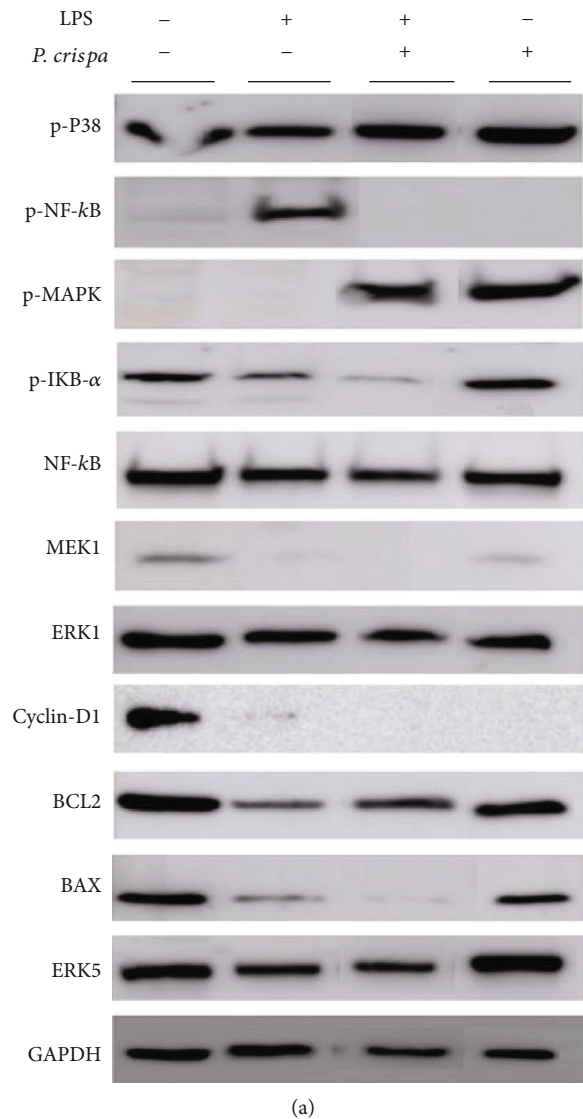


FIGURE 5: Continued.

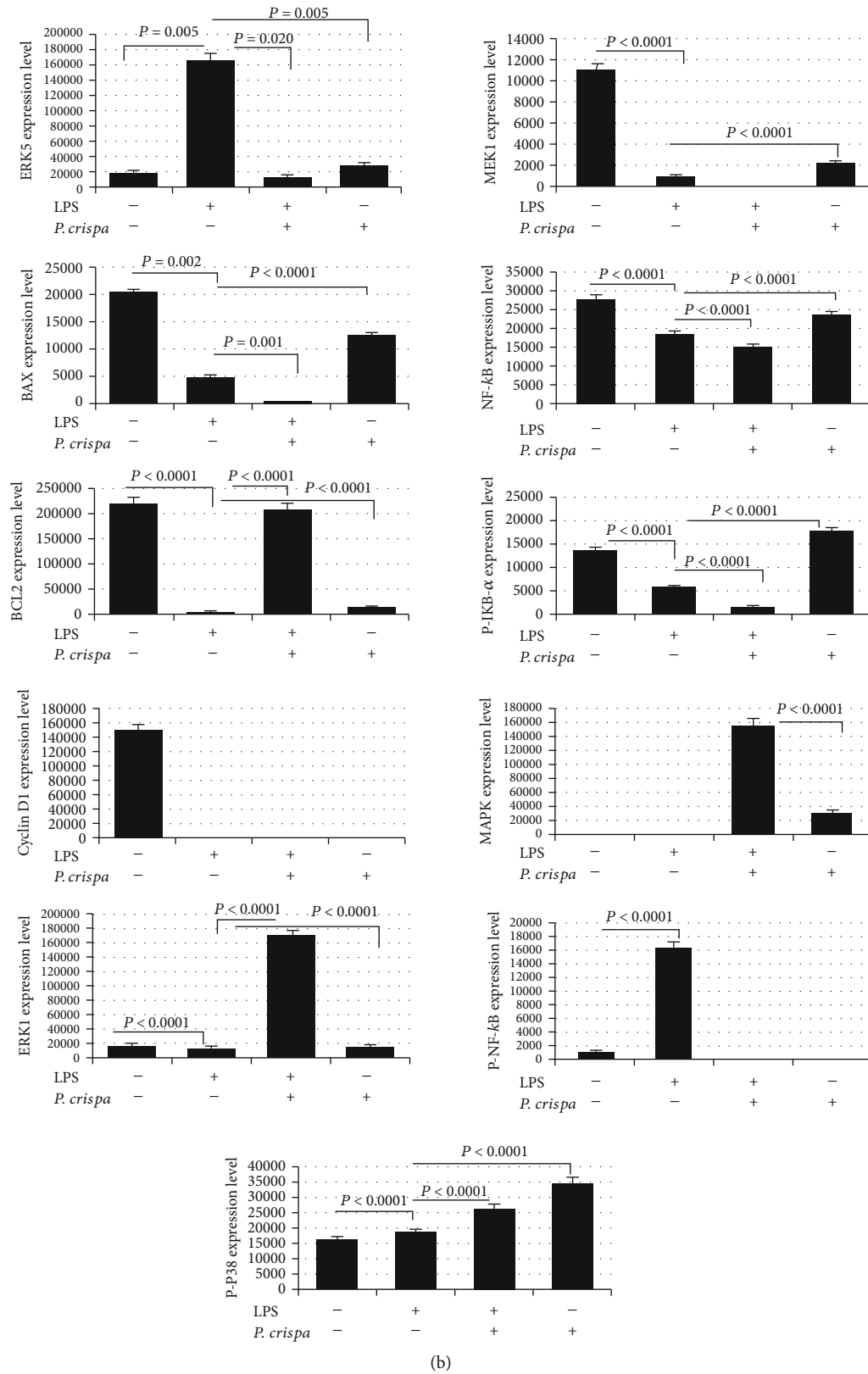


FIGURE 5: Expression analysis of proteins in THP-1 cells. (a) Western blot analysis and (b) densitometric analysis of the expression of ERK5, BAX, BCL2, Cyclin-D1, ERK1, MEK1, NF-κB, P-IKB-α, P-MAPK, P-NF-κB, and P-P38 proteins. Cells were either untreated (control), treated with 100 ng/ml of LPS, treated with 100 ng/ml of LPS + 100 μg/ml of *P. crispa* extract, or treated with 100 μg/ml of *P. crispa* extract alone. All data are expressed as mean ± SEM. All samples were processed in triplicate in three independent experiments. Statistical significance was established using the *t* test.

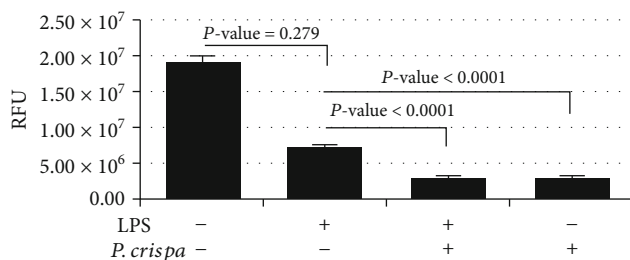


FIGURE 6: Migratory potential of THP-1 cells. Cells were treated with LPS (100 ng/ml) in the presence or absence of *P. crispa* extract (100 μ g/ml). Migration capability of cells was quantified by cell migration assay. Values represent the mean of triplicate experiments done in triplicate for each time point tested. Statistical significance was established using the *t* test. RFU: relative fluorescence units.

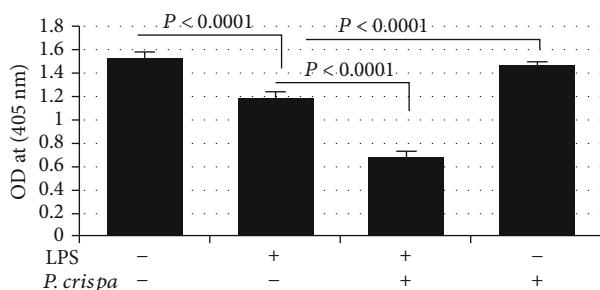


FIGURE 7: Phagocytosis assay using Zymosan particles. THP-1 cells were treated with LPS (100 ng/ml) and/or *P. crispa* extract (100 μ g/ml). Values represent the mean of triplicate experiments done in triplicate for each time point tested. Statistical significance was established using the *t* test

Several studies have documented that biochemical constituents, such as Alkaloid, Flavonoids, and Terpenoids, in the extract of *P. crispa* might be associated with antimicrobial and anti-inflammatory activity [20, 22]. Another study found that organic constituents from *P. undulata* significantly promoted apoptosis in hepatocellular carcinoma (HCC) HepG2 cells and elevated the expression of miR-34a. Furthermore, the extract enhanced the caspase 3/9 and proapoptotic p53 protein expression with plummeting of B-cell lymphoma-2 protein expression. Therefore, the antitumor activity of *P. crispa* through regulation of p53/B-cell lymphoma-2/caspases signaling pathway in the HCC HepG2 cells by overexpressing miR-34a is suggested. Such an antitumor effect might be attributed to the presence of triterpenoids and coumarins [42]. Also, Foudah et al. reported noticeable antioxidant and antimicrobial properties, and this could be owing to the presence of flavonoids, phenols, and tannins in the methanol extract of *P. crispa* plant [17].

Overall, this study showed that treatment of LPS-stimulated cells with 50 and 100 μ g/ml of *P. crispa* extract inhibited THP-1 cell proliferation, migration, and phagocytosis and altered the expression of several inflammatory- and cell survival/apoptosis-related proteins. To our knowl-

edge, this is the first *in vitro* study to evaluate the immunomodulatory and anti-inflammatory effects of *P. crispa* in LPS-stimulated human THP-1 cells.

First, results from the MTT assay showed that both concentrations of *P. crispa* extract inhibited THP-1 cell proliferation. In parallel, downregulation of ERK5 and lack of MEK1 and Cyclin-D expression were observed in treated cells. ERK5 is a member of the MAPK family that responds to extracellular stimuli, such as stress and growth factors, to regulate cell proliferation and differentiation via its downstream targets including AKT serine-threonine protein kinase and myocyte enhancer factor [43]. Downregulation of this MAPK protein may explain the observed proliferation inhibition. In addition, the lack of MEK1, another MAPK protein involved in cell growth and proliferation, [44] and Cyclin-D (a cell cycle regulator [45] expression in *P. crispa*-exposed cells could explain the ability of the extract's constituents to suppress the intracellular proliferation signaling pathways. However, flow cytometry plots showed a large increase in necrotic cells following treatment with extract, which is also a sign of potential toxicity of *P. crispa* extract.

Interestingly, we also observed the increased expression of prosurvival (ERK1, MAPK, and P-P38) and antiapoptotic (Bcl2) proteins in THP-1 cells, exposed to *P. crispa* extracts. Activated ERK-1 activates the MAPK signal transduction pathway, which regulates cell cycle progression and survival [46]. Moreover, previous studies have shown that phosphorylated-p38 (P-P38) expression is linked to enhanced cell survival in normal and malignant cells [47, 48]. In parallel, the Annexin V staining method showed that exposure to *P. crispa* extract alone reduces the frequency of THP-1 cell apoptosis yet increases the frequency of late apoptosis. This discrepancy may be caused by a shift in the expression pattern after exposure to the *P. crispa* extract.

Another interesting finding was the ability of *P. crispa* extract to inhibit the migration of stimulated THP-1 cells. Molecular investigations revealed supporting results, i.e., treatment with *P. crispa* extract significantly downregulated the expression of CCL1, CCL2, CCL5, CCL22, CXCL1, and CXCL10 (all are known chemoattractant proteins) [49] in human THP-1 cells. These chemokines are produced by macrophages, and their function is to recruit leukocytes to the inflammation site. Of interest, it has been shown that *P. crispa* extract ameliorates leucocytes infiltration [27]; however, the current study is the first to focus on the molecular mechanisms underlying these cellular changes. No significant effects were observed with regard to ICAM1 expression upon *P. crispa* extract exposure, which may indicate that the extract constituents may inhibit the cellular migration, but their effects on leukocyte adhesion and cell-to-cell interactions are not significant [50].

In addition, the *P. crispa* extract showed multiple anti-inflammatory effects in the present study. First, the significant reduction in NF- κ B and P-NF- κ B expression in LPS-stimulated cells occurred after treatment with 100 μ g/ml of the extract. Pereira and colleagues showed that inhibiting ERK5 suppresses the NF- κ B signaling pathway [51]. Another study by Kloster et al. reported that MEK signaling is important for activating NF- κ B signaling [52]. The observation that

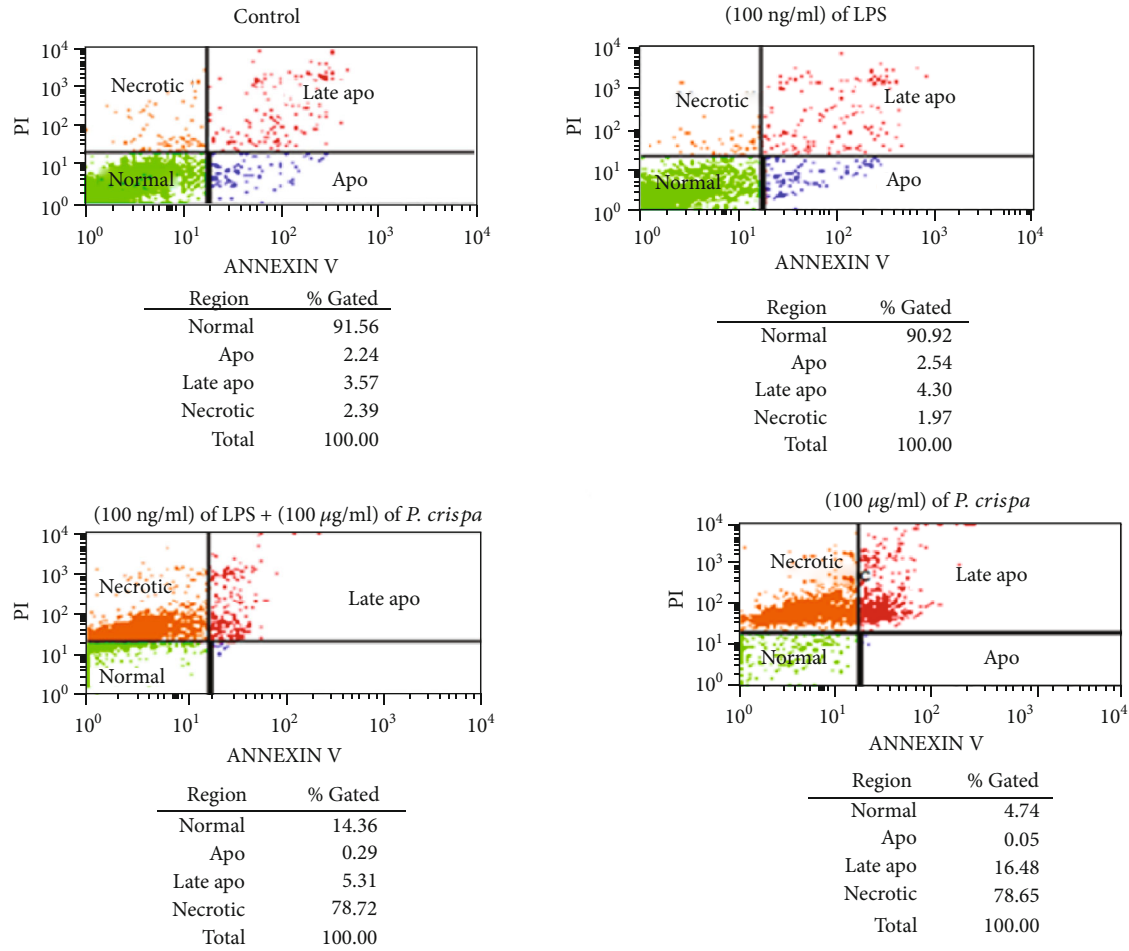


FIGURE 8: Flow cytometry using Annexin V staining method to analyze apoptosis in THP-1 cells. Analysis of apoptosis in the cells exposed to 100 ng/ml LPS and/or 100 µg/ml *P. crispa* extract. Cells that were propidium iodide (PI) negative and Annexin V negative are considered healthy, cells, PI negative and Annexin V positive cells are considered apoptotic, and cells that are positive to both PI and Annexin V considered necrotic. * indicates significance.

TABLE 1: Flow cytometry using Annexin V staining method to analyze apoptosis in THP-1 cells.

	Control	(100 ng/ml) of LPS	<i>p</i> value
Apoptosis	2.24	2.54	0.774
Late apoptosis	3.57	4.3	
	(100 ng/ml) of LPS	(100 ng/ml) of LPS + (100 µg/ml) of <i>P. crispa</i> extract	<i>p</i> value
Apoptosis	2.54	0.29	0.774
Late apoptosis	4.3	5.31	
	Control	(100 µg/ml) of <i>P. crispa</i> extract	<i>p</i> value
Apoptosis	2.24	0.05	0.015
Late apoptosis	3.57	16.48	

MEK expression was absent in LPS-stimulated cells after *P. crispa* extract exposure may explain the observed reduction in NF-κB signaling. Moreover, it has been shown that activation of NF-κB mainly occurs via IκB kinase-mediated phosphorylation of the inhibitory molecule IκB-α [53]. The

downregulated NF-κB expression may explain the observed underexpression of chemotactic factors in the current study [54]. However, to our surprise, *P. crispa* extract increased TNF-α expression in LPS-stimulated and unstimulated cells. Although this would need confirmation in future studies, it may indicate that *P. crispa* extract constituents target other regulatory factors that control the TNF-α expression.

Phagocytosis is a major function of macrophages in the innate immune response against foreign bodies. It is regulated by several cytokines including TNF-α and IL-1 [55]. However, it may be implicated in several chronic inflammatory diseases such as chronic infections, systemic lupus erythematosus, and autoimmune anemia [56]. The present study showed that *P. crispa* extract inhibited the phagocytic activity in LPS-stimulated cells. However, surprisingly, it enhanced phagocytosis in unstimulated THP-1 cells. This differential effect needs to be further confirmed in future studies.

In conclusion, treatment of THP-1 cells with *P. crispa* extract significantly reduced cell migration, proliferation, and phagocytosis in LPS-stimulated cells. Moreover, it significantly reduced the expression of various chemotactic and

cell survival-related proteins. These results highlight the anti-inflammatory and immunomodulatory effects of *P. crispa* extract in LPS-stimulated THP-1 cells. Future studies should investigate these mechanisms in animal models with chronic inflammatory diseases.

Abbreviations

CCL:	C-C motif chemokine ligand
CXCL:	C-X-C motif ligand 2
ERK:	Extracellular-signal regulated kinase
ICAM:	Intracellular adhesion molecule
I κ B- α :	Inhibitor kappa B- α
LPS:	Lipopolysaccharide,
MAPK:	Mitogen activated protein kinase
TNF:	Tumor necrosis factor
M Φ s:	Macrophages
IL:	Interleukin
DAMPs:	Damaged associated molecular patterns
MHC:	Major histocompatibility complex
ICAM-1:	Intracellular adhesion molecule
FBS:	Fetal bovine serum
qRT-PCR:	Quantitative reverse-transcriptase polymerase chain reaction
ELISA:	Enzyme-linked immunosorbent assay
TMB:	Tetramethylbenzidine
HRP:	Streptavidin-horseradish peroxidase
PVDF:	Polyvinylidene difluoride
HCC:	Hepatocellular carcinoma.

Data Availability

The data used to support the findings of this study are available from the corresponding author upon request.

Conflicts of Interest

The authors declare that there is no conflict of interest regarding the publication of this paper.

Authors' Contributions

AAA and SA conceived and designed the study. TA, MMA, and MRA were responsible for the performance of the experiments. MMA, MRA, and MDA analyzed the data, prepared the figures, and analyzed the data. AAA and SA interpreted the results. TA, MMA, MRA, and MDA helped in writing the preliminary draft of the manuscript. AAA and SA were responsible for revising and approval of the final version of the manuscript.

Acknowledgments

This research was funded by the Deanship of Scientific Research at Princess Nourah bint Abdulrahman University, through the Research Funding Program (Grant Number: FRP-1440-T).

References

- [1] S. Gordon and L. Martinez-Pomares, "Physiological roles of macrophages," *Pflügers Archiv - European Journal of Physiology*, vol. 469, no. 3-4, pp. 365-374, 2017.
- [2] S. Gordon, "Phagocytosis: the legacy of Metchnikoff," *Cell*, vol. 166, no. 5, pp. 1065-1068, 2016.
- [3] Z. Bar-Shavit, "The osteoclast: a multinucleated, hematopoietic-origin, bone-resorbing osteoimmune cell," *Journal of Cellular Biochemistry*, vol. 102, no. 5, pp. 1130-1139, 2007.
- [4] J. A. Chasis and N. Mohandas, "Erythroblastic islands: niches for erythropoiesis," *Blood*, vol. 112, no. 3, pp. 470-478, 2008.
- [5] R. C. Paolicelli, G. Bolasco, F. Pagani et al., "Synaptic pruning by microglia is necessary for normal brain development," *Science*, vol. 333, no. 6048, pp. 1456-1458, 2011.
- [6] T. Ganz, "Macrophages and systemic iron homeostasis," *Journal of Innate Immunity*, vol. 4, no. 5-6, pp. 446-453, 2012.
- [7] S. E. Headland and L. V. Norling, "The resolution of inflammation: principles and challenges," *Seminars in Immunology*, vol. 27, no. 3, pp. 149-160, 2015.
- [8] M. Hesketh, K. B. Sahin, Z. E. West, and R. Z. Murray, "Macrophage phenotypes regulate scar formation and chronic wound healing," *International Journal of Molecular Sciences*, vol. 18, no. 7, p. 1545, 2017.
- [9] A. Shapouri-Moghaddam, S. Mohammadian, H. Vazini et al., "Macrophage plasticity, polarization, and function in health and disease," *Journal of Cellular Physiology*, vol. 233, no. 9, pp. 6425-6440, 2018.
- [10] Y. Chen and X. Zhang, "Pivotal regulators of tissue homeostasis and cancer: macrophages," *Experimental Hematology & Oncology*, vol. 6, no. 1, 2017.
- [11] A. Das, M. Sinha, S. Datta et al., "Monocyte and macrophage plasticity in tissue repair and regeneration," *The American Journal of Pathology*, vol. 185, no. 10, pp. 2596-2606, 2015.
- [12] L. Arnold, A. Henry, F. Poron et al., "Inflammatory monocytes recruited after skeletal muscle injury switch into anti-inflammatory macrophages to support myogenesis," *Journal of Experimental Medicine*, vol. 204, no. 5, pp. 1057-1069, 2007.
- [13] S. Lee, S. Huen, H. Nishio et al., "Distinct macrophage phenotypes contribute to kidney injury and repair," *Journal of the American Society of Nephrology*, vol. 22, no. 2, pp. 317-326, 2011.
- [14] A. Parihar, T. D. Eubank, and A. I. Doseff, "Monocytes and macrophages regulate immunity through dynamic networks of survival and cell death," *Journal of Innate Immunity*, vol. 2, no. 3, pp. 204-215, 2010.
- [15] S. Deane, C. Selmi, S. S. Teuber, and M. E. Gershwin, "Macrophage activation syndrome in autoimmune disease," *International Archives of Allergy and Immunology*, vol. 153, no. 2, pp. 109-120, 2010.
- [16] D. Watts and A. H. Al-Nafie, *Vegetation and biogeography of the sand seas of Saudi Arabia*, Kegan Paul, 2003.
- [17] A. I. Foudah, A. Alam, G. A. Soliman, M. A. Salkini, E. O. Ibnouf Ahmed, and H. S. Yusufoglu, "Pharmacognostical, Antioxidant and Antimicrobial Studies of Aerial Part of *Pulicaria Crispa* (Family: Asteraceae)," *Bulletin of Environment, Pharmacology and Life Sciences*, vol. 4, no. 12, pp. 19-27, 2015.
- [18] A. A. Fahmi, M. Abdur-Rahman, A. F. Aboul Naser et al., "Chemical composition and protective role of *Pulicaria undulata* (L.) C.A. Mey. subsp. *undulata* against gastric ulcer

- induced by ethanol in rats,” *Heliyon*, vol. 5, no. 3, article e01359, 2019.
- [19] M. A. alo Yahya, A. M. el-Sayed, J. S. Mossa et al., “Potential cancer chemopreventive and cytotoxic agents from *Pulicaria crispa*,” *Journal of Natural Products*, vol. 51, no. 3, pp. 621–624, 1988.
- [20] Y. H. Elshiekh and M. A. AbdElMoniem, “Phytochemical, antibacterial screening and antioxidant activity of *Pulicaria crispa* extracts,” *The Pharma Innovation*, vol. 3, no. 12, pp. 12–15, 2015.
- [21] A. Adebisi, E. Bassey, R. Ayo, I. Bello, J. Habila, and G. Ishaku, “Anti-mycobacterial, antimicrobial and phytochemical evaluation of *Pulicaria crispa* and *Scoparia dulcis* plant extracts,” *Journal of Advances in Medical and Pharmaceutical Sciences*, vol. 7, no. 4, pp. 1–11, 2016.
- [22] Y. H. Elshiekh and A. Mona, “Gas chromatography–mass spectrometry analysis of *Pulicaria crispa* (whole plant) petroleum ether extracts,” *American Journal of Research Communication*, vol. 3, no. 3, pp. 58–67, 2015.
- [23] V. Kuete, B. Wiench, M. S. Alsaïd et al., “Cytotoxicity, mode of action and antibacterial activities of selected Saudi Arabian medicinal plants,” *BMC Complementary and Alternative Medicine*, vol. 13, no. 1, 2013.
- [24] A. S. Maghraby, N. Shalaby, H. I. Abd-Alla, S. A. Ahmed, H. M. Khaled, and M. M. Bahgat, “Immunostimulatory effects of extract of *Pulicaria crispa* before and after *Schistosoma mansoni* infection,” *Acta Poloniae Pharmaceutica*, vol. 67, no. 1, pp. 75–79, 2010.
- [25] M. M. A. MM, E. EH, W. SE, and M. SE, “*In vitro* antileishmanial activity of *Helianthus annuus* and *Pulicaria crispa* (Asteraceae),” *Natural Products Chemistry & Research*, vol. 5, no. 4, p. 2, 2017.
- [26] A. H. Arbab, M. K. Parvez, M. S. al-Dosari, and A. J. al-Rehaily, “*In vitro* evaluation of novel antiviral activities of 60 medicinal plants extracts against hepatitis B virus,” *Experimental and Therapeutic Medicine*, vol. 14, no. 1, pp. 626–634, 2017.
- [27] A. A. Alghaithy, H. A. el-Beshbishy, A. AbdelNaim, A. A. Nagy, and E. M. Abdel-Sattar, “Anti-inflammatory effects of the chloroform extract of *Pulicaria guestii* ameliorated the neutrophil infiltration and nitric oxide generation in rats,” *Toxicology and Industrial Health*, vol. 27, no. 10, pp. 899–910, 2011.
- [28] P. Hunter, “The inflammation theory of disease. The growing realization that chronic inflammation is crucial in many diseases opens new avenues for treatment,” *EMBO Reports*, vol. 13, no. 11, pp. 968–970, 2012.
- [29] Z. D. Hu, T. T. Wei, Q. Q. Tang et al., “Gene expression profile of THP-1 cells treated with heat-killed *Candida albicans*,” *Annals of Translational Medicine*, vol. 4, no. 9, 2016.
- [30] H. Bosshart and M. Heinzelmann, “THP-1 cells as a model for human monocytes,” *Annals of Translational Medicine*, vol. 4, no. 21, 2016.
- [31] S. Tedesco, F. de Majo, J. Kim et al., “Convenience versus biological significance: are PMA-differentiated THP-1 cells a reliable substitute for blood-derived macrophages when studying *in vitro* polarization?,” *Frontiers in Pharmacology*, vol. 9, no. 71, 2018.
- [32] P. Wangchuk, P. A. Keller, S. G. Pyne, and M. Taweechotipatr, “Inhibition of TNF- α production in LPS-activated THP-1 monocytic cells by the crude extracts of seven Bhutanese medicinal plants,” *Journal of Ethnopharmacology*, vol. 148, no. 3, pp. 1013–1017, 2013.
- [33] S. S. Choudhury, L. Bashyam, N. Manthapuram, P. Bitla, P. Kollipara, and S. D. Tetali, “*Ocimum sanctum* leaf extracts attenuate human monocytic (THP-1) cell activation,” *Journal of Ethnopharmacology*, vol. 154, no. 1, pp. 148–155, 2014.
- [34] L. Allen-Hall, P. Cano, J. T. Arnason, R. Rojas, O. Lock, and R. M. Lafrenie, “Treatment of THP-1 cells with *Uncaria tomentosa* extracts differentially regulates the expression of IL-1 β and TNF- α ,” *Journal of Ethnopharmacology*, vol. 109, no. 2, pp. 312–317, 2007.
- [35] J. Balsinde, B. Fernández, J. A. Solís-Herruzo, and E. Diez, “Pathways for arachidonic acid mobilization in zymosan-stimulated mouse peritoneal macrophages,” *Biochimica et Biophysica Acta (BBA) - Molecular Cell Research*, vol. 1136, no. 1, pp. 75–82, 1992.
- [36] L. Gil-de-Gómez, A. M. Astudillo, C. Meana et al., “A phosphatidylinositol species acutely generated by activated macrophages regulates innate immune responses,” *The Journal of Immunology*, vol. 190, no. 10, pp. 5169–5177, 2013.
- [37] D. M. Mosser and J. P. Edwards, “Exploring the full spectrum of macrophage activation,” *Nature Reviews. Immunology*, vol. 8, no. 12, pp. 958–969, 2008.
- [38] I. Tabas, “Macrophage death and defective inflammation resolution in atherosclerosis,” *Nature Reviews. Immunology*, vol. 10, no. 1, pp. 36–46, 2010.
- [39] M. G. Dorrington and I. D. Fraser, “NF- κ B signaling in macrophages: dynamics, crosstalk, and signal integration,” *Frontiers in Immunology*, vol. 10, 2019.
- [40] G. E. Jones, “Cellular signaling in macrophage migration and chemotaxis,” *Journal of Leukocyte Biology*, vol. 68, no. 5, pp. 593–602, 2000.
- [41] N. H. Bergman, K. D. Passalacqua, R. Gaspard, L. M. Shetron-Rama, J. Quackenbush, and P. C. Hanna, “Murine macrophage transcriptional responses to *Bacillus anthracis* infection and intoxication,” *Infection and Immunity*, vol. 73, no. 2, pp. 1069–1080, 2005.
- [42] M. A. Emam, H. I. Khattab, and M. G. Hegazy, “Assessment of anticancer activity of *Pulicaria undulata* on hepatocellular carcinoma HepG2 cell line,” *Tumour Biology*, vol. 41, no. 10, 2019.
- [43] G. N. Nithianandarajah-Jones, B. Wilm, C. E. P. Goldring, J. Müller, and M. J. Cross, “ERK5: structure, regulation and function,” *Cellular Signalling*, vol. 24, no. 11, pp. 2187–2196, 2012.
- [44] R. Aoidi, A. Maltais, and J. Charron, “Functional redundancy of the kinases MEK1 and MEK2: rescue of the Mek1 mutant phenotype by Mek2 knock-in reveals a protein threshold effect,” *Science Signaling*, vol. 9, no. 412, 2016.
- [45] M. Fu, C. Wang, Z. Li, T. Sakamaki, and R. G. Pestell, “Minireview: Cyclin D1: normal and abnormal functions,” *Endocrinology*, vol. 145, no. 12, pp. 5439–5447, 2004.
- [46] R. Roskoski Jr., “ERK1/2 MAP kinases: structure, function, and regulation,” *Pharmacological Research*, vol. 66, no. 2, pp. 105–143, 2012.
- [47] B. Wang, H. Jiang, N. Ma, and Y. Wang, “Phosphorylated-p38 mitogen-activated protein kinase expression is associated with clinical factors in invasive breast cancer,” *Springerplus*, vol. 5, no. 1, 2016.
- [48] T. M. Thornton and M. Rincon, “Non-classical p38 map kinase functions: cell cycle checkpoints and survival,”

- International Journal of Biological Sciences*, vol. 5, no. 1, pp. 44–52, 2009.
- [49] T. Jin, X. Xu, and D. Hereld, “Chemotaxis, chemokine receptors and human disease,” *Cytokine*, vol. 44, no. 1, pp. 1–8, 2008.
- [50] L. Yang, R. M. Froio, T. E. Sciuto, A. M. Dvorak, R. Alon, and F. W. Luscinskas, “ICAM-1 regulates neutrophil adhesion and transcellular migration of TNF- α -activated vascular endothelium under flow,” *Blood*, vol. 106, no. 2, pp. 584–592, 2005.
- [51] D. M. Pereira, S. E. Gomes, P. M. Borralho, and C. M. P. Rodrigues, “MEK5/ERK5 activation regulates colon cancer stem-like cell properties,” *Cell Death Discovery*, vol. 5, no. 1, 2019.
- [52] M. M. Kloster, E. H. Naderi, H. Carlsen, H. K. Blomhoff, and S. Naderi, “Hyperactivation of NF- κ B via the MEK signaling is indispensable for the inhibitory effect of cAMP on DNA damage-induced cell death,” *Molecular Cancer*, vol. 10, no. 1, 2011.
- [53] P. Viatour, M. P. Merville, V. Bours, and A. Chariot, “Phosphorylation of NF- κ B and I κ B proteins: implications in cancer and inflammation,” *Trends in Biochemical Sciences*, vol. 30, no. 1, pp. 43–52, 2005.
- [54] M. Penzo, D. M. Habel, M. Ramadass, R. R. Kew, and K. B. Marcu, “Cell migration to CXCL12 requires simultaneous IKK α and IKK β -dependent NF- κ B signaling,” *Cell Research*, vol. 1843, no. 9, pp. 1796–1804, 2014.
- [55] G. Arango Duque and A. Descoteaux, “Macrophage cytokines: involvement in immunity and infectious diseases,” *Frontiers in Immunology*, vol. 5, 2014.
- [56] D. Hirayama, T. Iida, and H. Nakase, “The phagocytic function of macrophage-enforcing innate immunity and tissue homeostasis,” *International Journal of Molecular Sciences*, vol. 19, no. 1, 2018.

Research Article

A Novel Oral Astaxanthin Nanoemulsion from *Haematococcus pluvialis* Induces Apoptosis in Lung Metastatic Melanoma

Hsing-Yu Haung,¹ Yi-Chen Wang,² Ying-Chen Cheng,¹ Wenyi Kang ,³ Shang-Hsiu Hu,⁴ Dengyong Liu ,⁵ Chaogeng Xiao,⁶ and Hui-Min David Wang ^{1,7,8,9}

¹Graduate Institute of Biomedical Engineering, National Chung Hsing University, Taichung City 402, Taiwan

²Division of Cardiology, Department of Internal Medicine, Kaohsiung Armed Forces General Hospital, Kaohsiung City 802, Taiwan

³National R&D Center for Edible Fungus Processing Technology, Henan University, Kaifeng 475004, China

⁴Department of Biomedical Engineering and Environmental Sciences, National Tsing Hua University, Hsinchu 30013, Taiwan

⁵College of Food Science and Technology, Bohai University, National & Local Joint Engineering Research Center of Storage, Processing and Safety Control Technology for Fresh Agricultural and Aquatic Products, Jinzhou 121013, China

⁶Food Science Institute, Zhejiang Academy of Agricultural Sciences, Hangzhou 310021, China

⁷Graduate Institute of Medicine, College of Medicine, Kaohsiung Medical University, Kaohsiung City 807, Taiwan

⁸Department of Medical Laboratory Science and Biotechnology, China Medical University, Taichung City 404, Taiwan

⁹College of Food and Biological Engineering, Jimei University, Xiamen 361021, China

Correspondence should be addressed to Hui-Min David Wang; davidw@dragon.nchu.edu.tw

Received 3 June 2020; Accepted 3 July 2020; Published 26 August 2020

Guest Editor: Daoud Ali

Copyright © 2020 Hsing-Yu Haung et al. This is an open access article distributed under the Creative Commons Attribution License, which permits unrestricted use, distribution, and reproduction in any medium, provided the original work is properly cited.

Astaxanthin (AST) is a naturally occurring xanthophyll carotenoid having the potential to be used as an anticancer agent; however, the human body has a low bioavailability of AST due to its poor solubility in the water phase. Therefore, we applied D- α -tocopheryl polyethylene glycol succinate (TPGS) as an emulsifier and natural edible peanut oil to form a steady oil-in-water (O/W) nanoemulsion loaded with AST (denoted as TAP-nanoemulsion). TAP-nanoemulsions were stable without the droplet coalescence against thermal treatments (30-90°C), pH value changes (over a range of 2.0-8.0), and ionic strength adjustments (at NaCl concentrations of 100-500 mM) measured by dynamic light scattering (DLS). AST within TAP-nanoemulsion was released up to 80% in a simulated intestinal enzymatic fluid *in vitro*, and the overall recovery rate was fairly consistent in the Caco-2 cellular model. In order to further evaluate *in vivo* melanoma inhibitory experiments, we injected the fluorescent-stained B16F10 cells into female C57BL/6 mouse tail veins and treated TAP-nanoemulsion in an oral gavage. qRT-PCR and Western blot demonstrated that TAP-nanoemulsion triggered effectively the apoptosis pathway, including enhancements of cleaved caspase-3 and caspase-9, ataxia-telangiectasia mutated kinase (ATM), and p21WAF1/CIP1 (p21) and decreases of B-cell lymphoma 2 (Bcl-2); cyclins D, D1, and E; mitogen-activated protein kinase (MEK); extracellular signal-regulated kinases (ERK); nuclear factor κ -light-chain-enhancer of activated B cells (NF- κ B); and matrix metalloproteinase-1 and metalloproteinase-9 (MMP-1 and MMP-9) in both gene and protein expressions. In conclusion, this study suggests that TAP-nanoemulsion with the oral treatment has a positive chemotherapy effect in melanoma with lung metastases *in vivo*. As far as we know, this is the first time to demonstrate that an antioxidant in nanoparticle administration cures lung metastatic melanoma.

1. Introduction

Haematococcus pluvialis is very famous for its excellent powerful antioxidative property and is one of the widespread freshwater Chlorophyta species from Haematococcaceae

family members [1]. *H. pluvialis* is composed of high proteins, low fat, necessary vitamins, and important minerals, including magnesium, iron, calcium, and zinc. Astaxanthin (AST) is a kind of xanthophyll carotenoid, which commonly occurs in natural seafood creatures, such as salmon, trout,

shrimp, lobster, and crab; microorganisms; and plants [2]. *H. pluvialis* is frequently observed in temperate climate regions around the world [3]. The high quantity of AST is produced in *H. pluvialis* resting cells, which are secreted and speedily accumulated while the ecological situations develop unfavorably for cell proliferation. This species yielded AST in low accessibility of nutrients, high salinity, and strong bright sunshine irradiation. AST has been reported with many functions like oxidative stress decrease, immune response enhancement, cardiovascular disease treatment, antibacterial property, macular degeneration improvement, anti-inflammatory activity, and certain cancer inhibition [4–6]. However, AST might be limited in aquaculture, medicine, cosmetics, and functional food ingredient business applications due to its low stability in storage and poor solubility in the water phase for the human body. An attractive solving approach is to encapsulate AST within the emulsion delivery system. The nanoemulsion diameter is less than 200 nm and made up of two immiscible liquid phases blended by surfactants and mechanical shear forces. In general, the benefit of nanoemulsion is not only having a higher surface area than the conventional emulsion but also having better bioavailability and physicochemical stability due to the smaller droplet size [7].

Surfactants reduce the interfacial tension of water and oil in the emulsion and combine the hydrophilic group to the aqueous phase and the hydrophobic domain toward the oil phase. The emulsifier forms a stable interface and prevents the oil/water droplet from aggregation [8], and in this study, we apply D- α -tocopheryl polyethylene glycol succinate (TPGS) as the emulsifier. TPGS is comprised of the esterification of vitamin E succinate with polyethylene glycol, having advantages of extending the drug half-life in plasma and enhancing cellular uptake capacity. TPGS inhibits ATP-dependent p-glycoprotein transporters, and this unique ability improves the poorly soluble anticancer drug bioavailability, such as paclitaxel. Nowadays, it is widely employed in the hydrophobic drug delivery systems and is a suitable emulsifier to prepare the nanoemulsion as it enlarges the drug encapsulation efficiency and bioavailability. The medium-chain triacylglycerols and hydrolyzed vegetable oil were suggested widely for use in nanoemulsions. We applied natural edible oil and noncytotoxic and stable peanut oil, to raise the embedding concentration of AST.

The gastrointestinal tract secretes lipases to degrade nanoemulsions into diglycerides, monoglycerides, and free fatty acids [9]. The small intestine absorbs lipid components, and the fat-soluble materials need to be broken down by the engulfing action. Small size droplets with high surface areas of nanoemulsions accelerate the degradation ratio and constitute the release rate. In other words, the active agent easily diffuses into the surrounding aqueous environment from an oil phase. After digestion, the chylomicron stimulates bile secretion and gastrointestinal motility. Bile decomposes nanoemulsions as endogenous surfactants and colloidal structures called mixed micelles, and bile with these micelles further dissolve and absorb the free components.

Melanoma is an invasive tumor to metastasize other organs, and its 5-year survival rate is less than 15% [10]. In general, microenvironments and blood flow patterns influence the primary tumor cell spread to target organs. The tight junction with the basement membrane and endothelial cells resists transendothelial cancer migration. Nevertheless, melanoma utilizes the leakage of the vessel wall to spread out [11]. At the present time, nanoemulsion products as anticancer drug vehicles develop the inhibitory efficacies, and we prepare TAP-nanoemulsion to suppress melanoma proliferation and facilitate the apoptosis reactions. This work's purpose is to embed a high concentration and poorly soluble AST in O/W nanoemulsion which is stable at various pH, temperature, and ionic strength surroundings. We test TAP-nanoemulsion cytotoxicity in foreskin fibroblasts and bioavailability in Caco-2 cells and suppression in metastatic melanoma of the lung *in vivo*.

2. Materials and Methods

2.1. Reagents and Samples. *H. pluvialis* AST extract was purchased from Tianbaoherb Biotech Co., Ltd. (Shanxi Province, China) and Trade Wind Biotech Co. Ltd. (Taiwan). Briefly, the environmentally friendly ethanol supercritical carbon dioxide fluid extraction method was applied to obtain AST extract. TPGS was bought from Wei Ming Pharmaceutical MFG. Co., Ltd. (Taiwan). Peanut oil was obtained from God Bene Enterprise Co., Ltd. (Taiwan). AST (purity > 97%) was used to prepare the standard curve; aprotinin, bile extract porcine, bromo-3-chloropropane (BCP), dimethyl sulfoxide (DMSO), ethylenediaminetetraacetic acid (EDTA), glycerol, hydrochloric acid, β -glycerophosphate, pancreatin from porcine pancreas, leupeptin, phenylmethylsulfonyl fluoride, protein assay kit, radioimmunoprecipitation assay buffer (RIPA), sodium chloride, sodium fluoride, sodium hydroxide, sodium orthovanadate, sodium pyrophosphate, Tris-HCl, 3-(4,5-dimethylthiazolyl-2)-2,5-diphenyltetrazolium bromide (MTT), and TRIzol were purchased commercially from Sigma-Aldrich Chemical Inc. (St Louis, MO, USA). Dulbecco's Modified Eagle's Medium (DMEM), fetal bovine serum (FBS), and penicillin-streptomycin-amphotericin (PSA) were obtained from Life Technologies Co., Ltd. (Gibco, Grand Island, NY, USA). All other chemicals within this work were analytical grade. Milli-Q (Merck Co. NJ, USA) water was prepared for all the solutions and nanoemulsions.

2.2. Preparation of TAP-Nanoemulsion. AST was dissolved in peanut oil to stir at room temperature by a magnet stirrer for a proper time period, and undissolvable AST was removed via a 0.45 μ m membrane filter. Before the preparation of the nanoemulsion, AST concentration in the oil phase was analyzed at the absorbance of 450 nm by a spectrophotometer. TPGS at 0.5% was dissolved in the oil phase at 45°C and uniformly mixed to a soluble status, and then 2.0 mL deionized water was added and shaken to nanosized scale in an ultrasonicator. In the stability assay, we produced different concentrations of TPGS (0.25–1.5%, w/w) of TAP-nanoemulsion using the same method.

2.3. Droplet Size Analysis. The droplet size and size distribution of TAP-nanoemulsion was measured by dynamic light scattering (DLS, Nano ZS90, Malvern Instruments Ltd., Worcestershire, UK). This equipment can analyze nanoemulsion droplet size ranging between 0.3 nm and 10 μm . Samples were diluted with a buffer solution (1:100) before the analysis to avoid multiple scattering effects. The evaluation of each sample was repeated in triplicate for each experimental condition.

2.4. Cryo-Field Emission Scanning Electron Microscopy (Cryo-FESEM). A drop of dispersion was filled into brass rivets to dive frozen within liquid nitrogen. Samples were stored in liquid nitrogen and transferred into the cryo-FESEM stage (Quorum Technologies, PP3010T, UK) of the microscope (JEOL, JSM-7800F, Japan). The sample was fractured on the cryo-SEM and coated with platinum. Images were acquired at a temperature of -140°C and a voltage of 10 kV.

2.5. TAP-Nanoemulsion Stability Assays: Temperature, pH, and Ionic Strength. Physical and chemical stabilities of TAP-nanoemulsions were examined in various experimental surroundings which may be encountered in preparations and storages [12]. Briefly, TAP-nanoemulsion was prepared in 0.5% TPGS, 10% AST, and 20% peanut oil. Fresh TAP-nanoemulsions were put in a water-bath tank at different temperatures (30, 60, and 90°C) for 1 hr, to wait for it to cool to the room temperature before analyzing the resulting samples via DLS. In pH stability assay, TAP-nanoemulsion samples were adjusted to designed pH values (pH 2.0–8.0, phosphate buffer, 5 mM) by adding 0.1 mol/L HCl or 0.1 mol/L NaOH solutions and continuously stirred and then analyzed. Finally, in the ionic strength stability test, we put samples in various salt concentrations (NaCl, 0, 100, 200, 300, 400, and 500 mM). The resulting samples were gently mixed for 30 s, and the samples were put at 5°C for 24 hrs to analyze.

2.6. Quantification of AST Amount in TAP-Nanoemulsion System. The concentration of AST in the nanoemulsion system was assayed by UV-visible spectroscopy (Bio-Tek Co., VT, USA) with minor modifications. AST was separated from the nanoemulsion droplet using solvent extraction and quantified from the UV-visible spectrophotometer. 9.8 mL of an organic solvent (methanol : dichloromethane = 1 : 2, v/v) was mixed with 0.2 mL of TAP-nanoemulsion, and the nanoemulsion was completely separated from the oil phase into an aqueous phase. The absorbance was measured at 470 nm and the dichloromethane/methanol solution as a blank control. A calibration curve ($R^2 = 0.9983$, data not shown) was calculated for the AST concentration generated from the above solution while the concentration was expressed in mg/mL. Calculating AST encapsulation efficiency in nanoemulsion follows

$$\text{Encapsulation efficiency (\%)} = \frac{C_t}{C_0} \times 100, \quad (1)$$

where C_0 is the initial concentration of AST in the nanoemulsion, while C_t is the concentration of AST at a specific time interval point.

2.7. Cell Culture. Human foreskin fibroblasts were gifts acquired from Kaohsiung Medical University (Dr. Su-Shin Lee), and all procedures were approved by the Institutional Review Board (IRB) (Figure S2; KMHIRB-2014-07-07 (I), Kaohsiung City, Taiwan), and the cells were added with 143 U/mL benzylpenicillin potassium, 10 mM 4-(2-hydroxyethyl)-1-piperazineethanesulfonic acid (HEPES), 1% antiseptic, 10% fetal bovine serum (FBS), 100 $\mu\text{g}/\text{mL}$ streptomycin sulfate, and DMEM medium (13.4 mg/mL) [13]. Human colon adenocarcinoma Caco-2 cells were kindly provided by Professor Ping-Shan Lai (National Chung Hsing University, Taichung City, Taiwan). Mouse skin melanoma B16F10 cells were acquired from Bioresource Collection and Research Center (BCRC#60031, Hsinchu, Taiwan). Caco-2 and B16F10 cells were incubated in medium including DMEM with amphotercine 25 $\mu\text{g}/\text{mL}$, 10% FBS, penicillin 100 U/mL, 2 mmol/L l-Glu, and streptomycin 30 $\mu\text{g}/\text{mL}$. Both cells are cultured at 37°C in a 5% CO_2 humidified atmosphere.

2.8. In Vitro Cytotoxicity Study for TAP-Nanoemulsion. Before the experiment, cells are washed with PBS and incubated with DMEM supplement [13, 14]. The cytotoxicity of TAP-nanoemulsion was determined by MTT assay. MTT is a yellow tetrazolium that is absorbed by living cells and changed to a purple color because mitochondrial dehydrogenase is in a less reducing state. Cells were cultured with a density of 8×10^3 cells per well in a 96-well plate. After one-day incubation, fresh DMEM and the nanoemulsion were added to the plate and recultured for 24 hrs. We changed the broth to a medium including 100 μL of MTT (0.5 mg/mL) and incubated at 37°C , 5% CO_2 , for 2 hrs. After that, we discard the medium and added 100 μL of DMSO to dissolve MTT formazan and then quantified the absorbance values (A) of the supernatants measured at 595 nm. To determine the cell viability following

$$\text{Cell viability (100\%)} = \frac{A_{\text{sample}} - A_{\text{blank}}}{A_{\text{control}} - A_{\text{blank}}} \times 100\%, \quad (2)$$

where A_{sample} is the OD of the sample, A_{blank} is the OD of the MTT solution but without cells, and A_{control} is the OD of the untreated group.

2.9. Measurement of Intracellular Reactive Oxygen Species (ROS) Level in Foreskin. ROS-sensitive fluorescent dye, 2',7'-dichlorofluorescein diacetate (DCFDA) was used to determine PMA upregulated intracellular oxidative stress level in cells [15]. DCFDA is nonfluorescent, but in ROS presence (when reagent is oxidized), it shows green fluorescence. In order to observe sample antioxidative property, cells were pretreated with and without TAP-nanoemulsion (0–26 $\mu\text{g}/\text{mL}$) for 24 hrs and stimulated by PMA (20 $\mu\text{g}/\text{mL}$) for another 24 hrs. Afterward, it was rinsed with warm phosphate-buffered saline (PBS) buffer, and incubated with 20 μM DCFDA containing PBS at 37°C , 5% CO_2 , for 30 min, to replace a fresh cell medium and to wash cells at least 3 times with PBS. Using trypsin/EDTA cuts away the focal adhesion anchored cell to the culture dish. The cellular

fluorescence intensity was analyzed with Guava® easyCyte Flow Cytometers (Merck KGaA, Darmstadt, Germany) at 485 nm excitation and 530 nm emission for 2,7-dichloro-fluorescein (DCF) detection.

2.10. In Vitro Mimic Digestion Model: Simulated Gastric and Intestinal Fluid. The simulated gastric fluid was made of 7.0 mL HCl and 2.0 g NaCl to set the working volume of 1.0 L to adjust the pH value to 1.2 [16]. The simulated intestinal fluid was dissolved in 2.5 mL of pancreatic lipase solution (60 mg in PBS), 3.5 mL of bile extract (187.5 mg in PBS), and 1.5 mL of calcium chloride (110 mg in water) at pH 7.0, 37°C. TAP-nanoemulsion (2.0 mL) was added to the dialysis bag and put into the simulated gastrointestinal fluid maintained at 37°C and stirred by a magnetic stirrer (RT-10, IKA, Germany) at 100 rpm. At the scheduled time, an aliquot (1.0 mL) was taken and immediately replaced with the same volume of prewarmed fresh PBS. The concentration of AST was analyzed by HPLC to measure three times, and the results are shown as a percentage of AST-released amount over time.

2.11. Cellular Uptake and Transepithelial Permeation of TAP-Nanoemulsion. Caco-2 cells (1×10^5 cells/2.4 cm² insert) were seeded in a transwell chamber (0.4 μm pore size, 24 mm diameter; Costar, Kennebunk, ME, USA). The cell culture media were changed every two days, and we evaluated the integrity of monolayers by a Millicell ERS-2 epithelial cell volt-ohm meter (Taiwan Instrument Co., Ltd, Taiwan) to determine the transepithelial electrical resistance (TEER) by [17]

$$\text{TEER } (\Omega \cdot \text{cm}^2) = (\text{ohm}^1 - \text{ohm}^2) \times A, \quad (3)$$

where A is the surface area of the insert (4.4 cm²), ohm¹ is the resistance of the insert with cells, and ohm² is the resistance of the insert with cell culture medium only.

After the incubation, the resistance of cells achieved above 500 Ω/cm² could be used for performing all the experiments. To analyze the cellular uptake of TAP-nanoemulsion in vitro, the medium was changed to fresh DMEM for 24 hrs before the infiltration experiment. The monolayer cells were washed twice with PBS (pH 7.4, 37°C), and it was cultured with TAP-nanoemulsion overnight at 37°C in 5% CO₂ atmosphere. TAP-nanoemulsion was gently removed after the incubation, and the resulting solution was loaded into a 6-well transwell plate. To analyze AST permeability, 0.5 mL aliquot was added to each test solution (1.66, 3.22, 6.64, 13.3, and 26.6 μg/mL AST in TAP-nanoemulsion) in the top side of the transwell plate (donor chamber). The receiving chamber obtained 0.5 mL of medium, and all samples were cultured in a 5% CO₂ incubator overnight. After the culture, the apical and receiving chamber solutions were gathered and analyzed by UV-visible spectroscopy.

2.12. Animal Model. In the research, the animals conformed to the guidelines of the American Society of Physiology for animal care and use, approved by the National Chung Hsing University and Institutional Animal Care and Use

Committee (Figure S3; IACUC number: 105-141). C57BL/6 female mice (6-7 weeks) were bought from BioLASCO Experimental Animal Center (Taiwan Co., Ltd.). All mice were kept in plexiglas cages in a temperature-controlled room (22 ± 1°C) with a light/dark (12/12 hrs) schedule and free to obtain food and water [18]. Fifteen C57BL/6 mice were randomly divided into 3 groups: vehicle control (n = 3), tumor only (n = 6), and TAP-nanoemulsion treatment (n = 6), after 7-day prebreeding.

2.13. Tumor Development and TAP-Nanoemulsion Regimen Administration. B16F10 cells were cultured in DMEM and stained with PKH26, and all experiments were carried out in cells cultured less than 15 passages. We injected the fluorescent stained cells (1×10^5 cells within 200 μL of PBS) into female mouse tail veins twice a week. Two weeks after tumor injection, the mice were treated with the following conditions: vehicle control group (without treatment), tumor-only group (0.2 mL normal saline per day), and TAP-nanoemulsion group: 10 mg TAP-nanoemulsion per every other day by an oral gavage. The body weights of all mice were recorded every twice a week to check that the mice are healthy. Tumor growth inhibition was measured by IVIS spectral imaging system (Caliper Life Sciences, Hopkinton, MA, USA). After the 35th day, all mice were sacrificed by cervical dislocation, and the lung, spleen, heart, kidney, and liver organs were gathered at the end of this study.

2.14. Quantitative Real-Time Reverse Transcription Polymerase Chain Reaction (qRT-PCR) Analysis. qRT-PCR consists of an exclusive primer probe to generate the fluorescence signal. It uses a fluorescent detection technique to sense each cycle by a StepOnePlus™ System (Thermo Fisher Scientific Inc., USA). It detects and records the fluorescent intensity per cycle and calculates achieving the real-time quantitative data. We applied TRIzol™ (Invitrogen Co., CA, USA) to extract RNA from the lung tissue, and subsequently, a reverse transcription kit (Takara, Japan) generated DNA. Primers for qRT-PCR are listed in Table S1. First, the sample was heated to form a single strand of DNA. Second, primers were bound to form a double-stranded DNA (dsDNA). Third, SYBR Green dsDNA were combined by SYBR green Plus reagent kit (Roche, Basel, Swiss), releasing the fluorescence. A detection of fluorescent signals during the elongation or annealing phase of each cycle was detected [4, 19]. The expression levels of target genes were normalized with α-tubulin levels using the 2^{-ΔΔC_t} method.

2.15. Western Blotting of Lung Organization. Lung tissues were homogenized with RIPA buffer and centrifugated of the lysate at 18,000 g for 30 min. The supernatant was analyzed by BCA (bicinchoninic acid) protein assay kit (Sigma-Aldrich Co., St. Louis, MO, USA) [20, 21]. The samples (20 ng) were qualified by Western blotting protein electrophoresis on sodium dodecyl sulfate (SDS). The 8-10% SDS gels were transferred to polyvinylidene fluoride (PVDF) membranes. Next, PVDF membranes were added into Bcl-2, cleaved caspase-3 and caspase-9, ataxia-telangiectasia mutated kinase (ATM), p21WAF1/CIP1 (p21), cyclins D

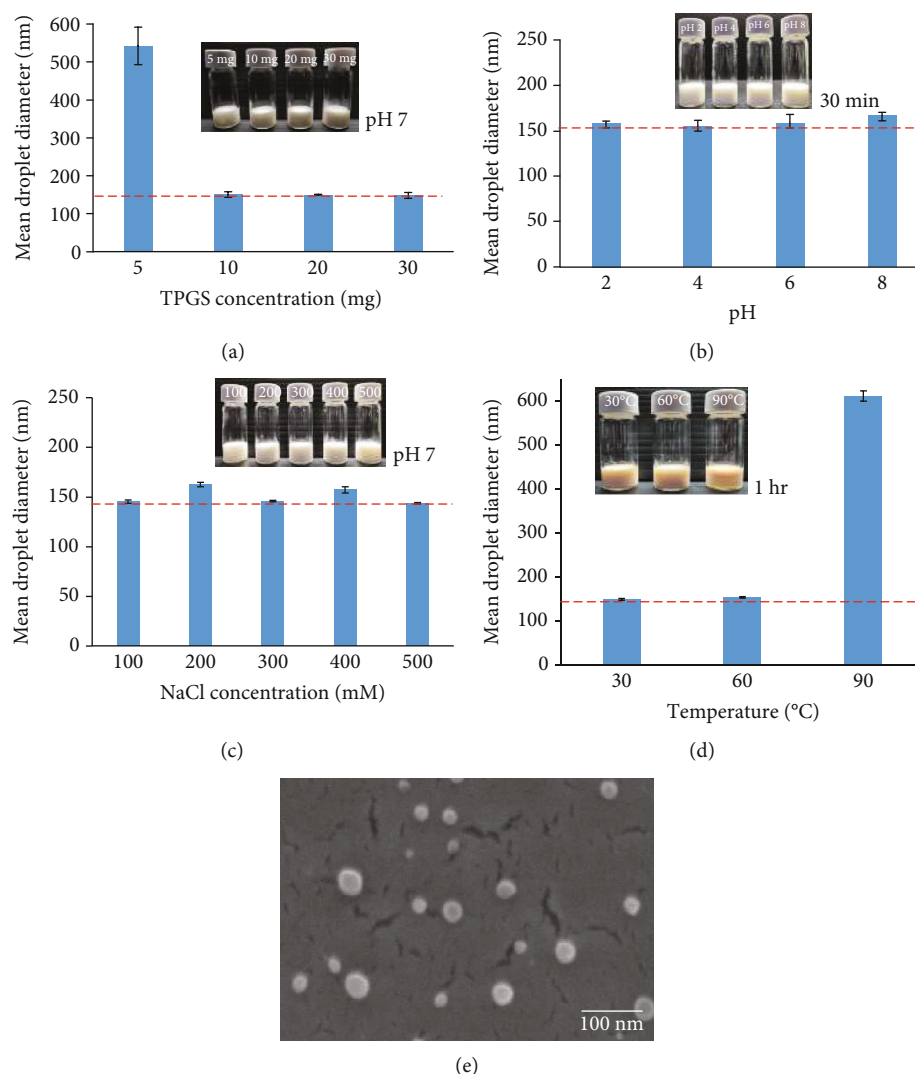


FIGURE 1: The influences on the physical stabilities of TAP-nanoemulsion. (a) Different TPGS concentrations, 2.5–15.0 mg/mL; (b) various pH values, pH 2.0–8.0; (c) diverse NaCl concentrations, 0–500 mM; and (d) various temperatures, 30–90°C. (e) Cryo-FESEM images of TAP-nanoemulsion.

and E, mitogen-activated protein kinase (MEK), extracellular signal-regulated kinases (ERK), nuclear factor kappa-light-chain-enhancer of activated B cells (NF- κ B), and matrix metalloproteinase-1 and metalloproteinase-9 (MMP-1 and MMP-9, respectively) antibodies at 4°C for 24 hrs. It was added into biotinylated secondary antibodies at 25°C for 1 hr. Finally, it was detected by enhanced chemiluminescence (ECL) detection reagent (PerkinElmer, USA; ECL1 : ECL2 = 1 : 1) exposing it to X-rays for a specific period of time to obtain the vision. Dyeing images can be visualized via a commercially available image system. We took α -tubulin as our experimental loading control.

2.16. Statistical Analysis. All results within each experiment were in triplicate and presented as a mean \pm standard deviation (SD). All data were compared multiple times by Student's t-test for statistical analysis. Significant difference (*) was defined as $p < 0.05$.

3. Results and Discussion

3.1. Characterization of TAP-Nanoemulsion in Different Surroundings

3.1.1. Effects of Various Emulsifier Concentrations on TAP-Nanoemulsion Droplet Diameters. It is well known that oil and water are immiscible because of polar properties, and the interfacial tension between two phases is fairly high. In order to successfully prepare emulsions, surfactants adsorbed at the boundary reduce the interfacial tension and droplet size [22]. We made nanoemulsions in different emulsifier concentrations and measured the particle size changes in Figure 1(a). TAP-nanoemulsion with 5 mg TPGS had the biggest size distribution and the mean particle radius was 542.1 ± 49.5 nm (polydispersity index, PDI: 0.251). Conversely, increasing TPGS concentration to 10 mg, the average droplet size decreased 3.5 times and the mean particle radius was 150.5 ± 7.32 nm (PDI: 0.239). The average droplet sizes

of the samples with treatments at 20 and 30 mg were 155.0 ± 40.8 and 145.6 ± 27.7 nm, respectively. It was insignificantly altered to compare with over 10 mg dosage, and the system was pretty stable at least six months better than 5 mg treatment. Therefore, as the emulsifier concentration increased from 0 to 10 mg TPGS, the globule size reduced to around 150 nm and the system stability was improved.

3.1.2. Effects of Various pH Values on TAP-Nanoemulsion Droplet Diameters. In beverage and food, the pH value of the aqueous phase is widely distributed, from acidic soft drinks to minor alkaline nutritional beverages. We investigated the pH value influence on TAP-nanoemulsion physical stability stored at 25°C for one day in Figure 1(b). The nanoemulsion with 10 mg TPGS was stable in different pH environments, and the droplet size remained constant (~150 nm), and there was no phase segmentation phenomenon and droplet aggregation. At pH 8.0, the droplet size showed only a little increase, indicating TAP-nanoemulsion was stable at pH 6.0. With pH at 2.0 and 4.0, TAP-nanoemulsion droplet size was 154.0 ± 8.6 and 155.3 ± 4.9 nm, respectively. The results indicated TAP-nanoemulsion was stable at a wide pH range from 2.0 to 6.0 because of the steric repulsion.

3.1.3. Effects of Various Ionic Strengths on TAP-Nanoemulsion Droplet Diameters. Analyzing TAP-nanoemulsion stability for ionic strength is important since many emulsified foods and beverages may contain some minerals that affect the final product stability and appearance. TAP-nanoemulsion permanence was investigated at different NaCl concentrations (0, 100, 200, 300, 400, and 500 mM) at pH 7, 25°C in Figure 1(c). The electrostatic repulsion was sufficient to ensure both hydrophobic attractiveness and Van Der Waals forces were low at all designed salt concentrations. We added NaCl to decrease the electrostatic repulsions between nanoparticles which led to the O/W droplet becoming unstable. As NaCl concentration increased to 500 mM, the droplet size did not significantly vary, and its average particle radius was 143.8 ± 0.7 nm (PDI: 0.144). The spatial repulsive force of TAP-nanoemulsion droplets was strong enough to keep droplets steady even at high NaCl solution dosage of our experimental conditions.

3.1.4. Effects of Various Temperatures on TAP-Nanoemulsion Droplet Diameters. We designed this nanoemulsion model to release AST after being attached to the digestive enzymes in the gastrointestinal system *in vivo*. As we know, the mammal creature temperature range is above 30°C (34–38°C), and we also consider the temperature changes at the manufacturing, shipping, and storage processes. Accordingly, we proposed the temperature stability between 30 and 90°C as the constancy assay (Figure 1(d)) to avoid the TAP-nanoemulsion quality lost during the whole process. After it was incubated at 30°C and 60°C for 1 hr, the particle size did not notably vary. The droplet size markedly increased at 90°C, and the inference of unstable nanoemulsion was due to the droplet coalescence and aggregation to weaken the interfacial tension compared to the same in recent studies. We observed the

solution color was a kind of orange-red due to AST separation from the oil phase at high temperature. Prior studies also found that carotenoid degrades quickly when stored at high temperatures [22], indicating carotenoids were unstable due to biochemical demotion. TAP-nanoemulsion was destructed at 90°C, showing temperature had a major effect on the short-term thermal stability of the nanoemulsion, and AST release increased when the temperature increased.

3.1.5. Cryo-FESEM Images of TAP-Nanoemulsion. The microstructure of TAP-nanoemulsion was observed by electron microscopy in Figure 1(e). One advantage of using cryo-FESEM was that the liquid dispersion could be frozen and viewed in the solid state. The micrograph of TAP-nanoemulsion revealed spherical droplets in the nanometer scale range which was in agreement with the size data determined by DLS as above.

3.2. Cytotoxicity Evaluations on TAP-Nanoemulsion System. Any latent chemoprotective substance should be first evaluated for its sensitivity and safety, and we assessed our raw materials via MTT assay on human primary foreskin fibroblasts [1, 4]. The cellular viability was less than 10% after treatments with TPGS over 1 mg/m in Figure 2(a), and the surfactant was cytotoxic to cells. It was a normal phenomenon that adding a surfactant directly to the culture medium will cause cell membrane lysis and cell death. In previous studies, TPGS was used as an anticancer agent to enhance cellular uptake. Fibroblasts had cell growths greater than 90% at peanut oil concentrations lower than 50% (v/v) in Figure 2(b), and the peanut oil was not toxic. To cultivate cells with all peanut oil (100%, v/v) forces cells to suffocate and die. Finally, cells were incubated with TAP-nanoemulsion at suitable concentrations in Figure 2(c). After AST dosage within the nanoemulsion reached to 53 µg/mL, the cell viability declined gradually. We believed high TPGS concentrations induce cell death due to the above reason. In order to avoid the experimental errors inflicted by undesired toxic effects, the highest dosage of TAP-nanoemulsion was set at 53 µg/mL.

3.3. Antioxidative Assay of TAP-Nanoemulsion System. Antioxidants are important agents for foods and cosmetics because of the core functions in reducing the radical-induced degradation and scavenging free radicals of living cells and tissues. We already published several papers to demonstrate that 3S, 3'S-astaxanthin is the most powerful antioxidant to scavenge ROS all over the world [1, 2, 6]. It has a powerful capacity to scavenge hurt-free radicals than vitamins and other natural pure compounds, especially in human healthy rejuvenation applications. For measuring the antioxidative properties on the testing samples of interest, the cellular experimental platform was carried out in practice. DCFDA staining is a typical quantitative method for the intracellular H₂O₂ amounts to survey oxidative stresses [1]. To determine whether TAP-nanoemulsion suppresses oxidations, we investigate ROS generations in cell-based foreskin fibroblasts. PMA is an inducer for endogenous superoxide secretions, and PMA-activated cells produced

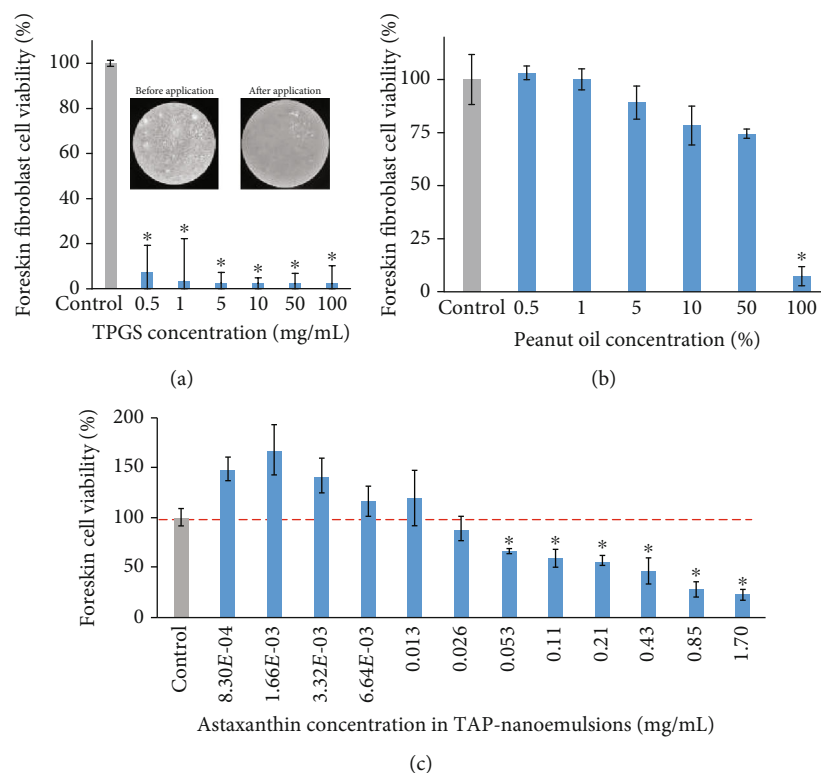


FIGURE 2: The cellular viability of foreskin fibroblasts was measured by MTT assay after (a) TPGS, (b) peanut oil, and (c) TAP-nanoemulsion treatments for 24 h. The data was represented with mean values \pm SD of three independent experiments performed. * $p < 0.05$ as compared with the vehicle control group.

ROS which emitted the fluorescent intensity to be detected [23]. In Figure 3, it was demonstrated that TAP-nanoemulsion gradually reduced oxidative stresses in a dose-dependent manner. The fluorescence potency of DCFDA was reduced from 159.35% to 101.00% (58.35% reduction) at 0 and 26.66 $\mu\text{g}/\text{mL}$ AST-nanoemulsion at 20 $\mu\text{m}/\text{mL}$ PMA presence. We discovered that TAP-nanoemulsion inhibited the production of cellular ROS successfully.

3.4. TAP-Nanoemulsion Bioaccessibility Measurement In Vitro. During the digestion process, TAP-nanoemulsion passed through three phases, including the oral, gastric, and small intestine stages. It should be noted that the size and interface characteristics of nanoemulsion might be changed during component assimilations [5, 6]. Our sample was in an aqueous gavage form (hence, the chewing procedure was irrelevant), and the oral residence time was ignored. Moreover, it did not contain starch, meaning the main enzyme did not work on amylase and saliva. The bioavailability of TAP-nanoemulsion was evaluated via incubating with the simulated digestive fluid environmental model, and AST kinetic release was monitored by the cumulative amount for 8 hrs in Figure 4(a). The gastrointestinal release profile exhibited two-stage drug discharge behaviors in the stomach and intestines. Initially, AST was released slightly and followed to speed up in the first phase. As for the gastric fluid digestion in vitro, we observed that the cumulative release sum of AST was less than 35% within 2 hrs. The small intestine

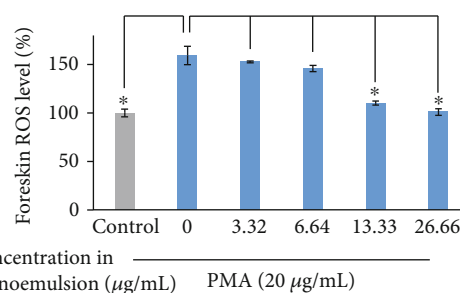


FIGURE 3: The ROS production percentage was enhanced by PMA (20 $\mu\text{g}/\text{mL}$) and reduced via TAP-nanoemulsion administration measured by flow cytometry.

tine is a digestive tract responsible for physiological activity and drug absorption. We found that AST was slowly released from simulated intestinal surroundings, and the released amount was higher over 80% after another 6 hrs in the second digestive phase. A reasonable explanation for this phenomenon was that lipases leisurely penetrated approaching the oil droplets to destroy the TAP-nanoemulsion conformational structure. In addition, bile adsorption took place in the oil/water interface contributing to the lipase attack on the lipid hydrolysis [24].

3.5. AST Uptake in Caco-2 Cell from TAP-Nanoemulsion. In our research, TEER calculated values were confirmed whether the Caco-2 confluent Transwell[®] monolayer culture

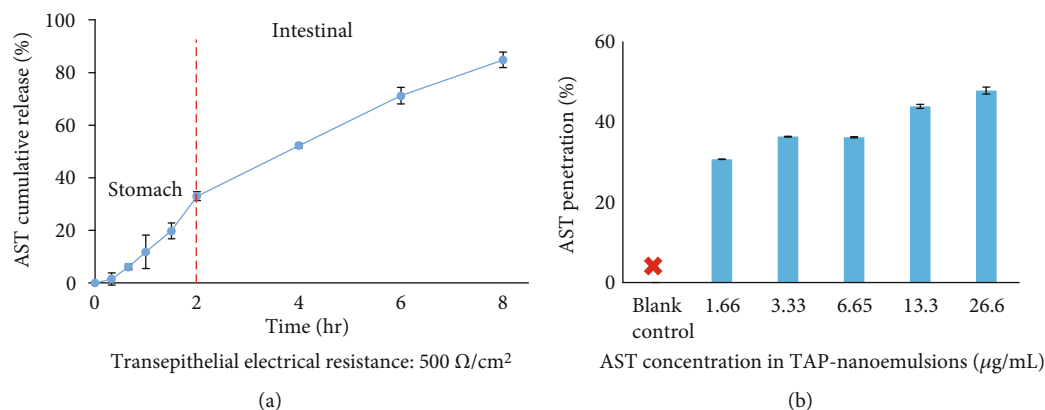


FIGURE 4: (a) Bioaccessibility of TAP-nanoemulsion after each step of an *in vitro* gastrointestinal mimic digestion. (b) Permeability of TAP-nanoemulsion across the Caco-2 monolayer with various concentrations (0–26.6 µg/mL). Each value was represented as the mean values ± SD (n = 3).

was suitable for the permeation experiments [25]. The values increased while the culture time was extended, and it reached over 500 Ω·cm² after the incubation, and the data is shown in Figure 4(b). AST was retrieved from the basolateral cell and top compartment after the Caco-2 cells were cultured for 24 hrs. The overall recovery rate of different AST-nanoemulsion concentrations raised fairly ranging from 30.7 ± 0.04% (1.6 µg/mL AST) to 47.9 ± 0.86% (26.6 µg/mL AST). AST imbalanced recovery loss might be due to AST metabolic conversion and chemical biodegradation occurrence during transepithelial infiltration. It was reported that the diameter of nanoemulsion less than 200 nm was delivered through the epithelial layer by the passive transport [26]. TAP-nanoemulsion with smaller particle size was able to penetrate the cell membrane efficiently compared to the conventional emulsion. Moreover, the smaller droplet had an extensive surface area to volume ratio resulting in an elevated cellular uptake. AST may have to be released from the capsule matrix by mechanical, chemical, and enzymatic processes that take place in the mouth, stomach, and small intestine. The released AST may be merged into droplets formed by coingested lipids within the mouth and stomach. Dietary lipids, such as triacylglycerols (TAG), undergo digestion within the stomach and small intestine due to the presence of gastric and pancreatic lipases leading to the formation of free fatty acids (FFA) and monoacylglycerols (MAG). These surface-active lipid digestion products interact with endogenous surface-active lipids (bile salts and phospholipids) to form mixed micelles, vesicles, and other colloidal structures [27]. These colloidal structures are capable of solubilizing lipophilic bioactive components (such as β-carotene) and transporting them to the epithelium cells where they are absorbed.

3.6. TAP-Nanoemulsion Inhibits Lung Metastatic Melanoma Proliferation *In Vivo*. The oral administration strategy is preferred over a variety of other administration routes of medicine delivery due to the many benefits it exhibits. The oral dosage forms include liquids, tablets, capsules, and granules. The advantages of the oral liquid form are the most conve-

nient way of drug administration. These advantages include good patient compliance, high versatility, prolonging the time of curative effect, reducing the fluctuation of the blood concentration, pain avoidance, ease of ingestion, improving the compliance of the medication, reducing the number of administrations, decreasing the side effects, and superior safety to accommodate different types of medicines. At first, we designed TAP-nanoemulsion as nutritional supplements. Nanoemulsions have shown the potentials to deliver various kind of drugs (hydrophilic, lipophilic, and amphiphilic agents) through many routes like oral, transdermal, ophthalmic, and parenteral modes. When the agent is directly injected to the site of intravenous (IV) injection, some medicines may cause local irritation. These pharmaceuticals, as well as certain cosolvents in aqueous solutions, induce the phlebitis, an inflammation of a vein leading to pain or redness. Considering the convenience, practicality, and safety, we planned the accumulation by oral administration. We assessed the anticancer potential of TAP-nanoemulsion in a metastatic melanoma C57BL/6 mouse model. Mice were anesthetized with 3.5% isoflurane (Abbott Scandinavia AB, Stockholm, Sweden) and injected with B16F10 cells (1 × 10⁵ cells within 200 µL PBS) through the tail vein at each concentration of 150 mg/g mouse body weight [7]. Anesthesia is kept by 2% isoflurane during bioluminescence scanning using an IVIS spectral imaging system to observe the red signal strength enhancement which corresponded with the tumor development. The result was quantified by the software Living Image 4.3, and images were obtained at 2 min intervals. The region of interest (ROI) is used to delineate the signal and made measurements. The signal intensity (radiation) was analyzed in photons/s/cm²/steradian (p/s/cm²/sr). The melanoma-only group showed a strong metastasis consequence of B16F10 in the thorax, especially in the lung organ. After one week, all mice presented melanoma invasion results in the melanoma-only group. Until about three weeks, the strong metastatic developments were observed, and all mice were dead in the no-treatment group. It is about two weeks from the beginning to start the oral administration after tumor injection, and the mice were

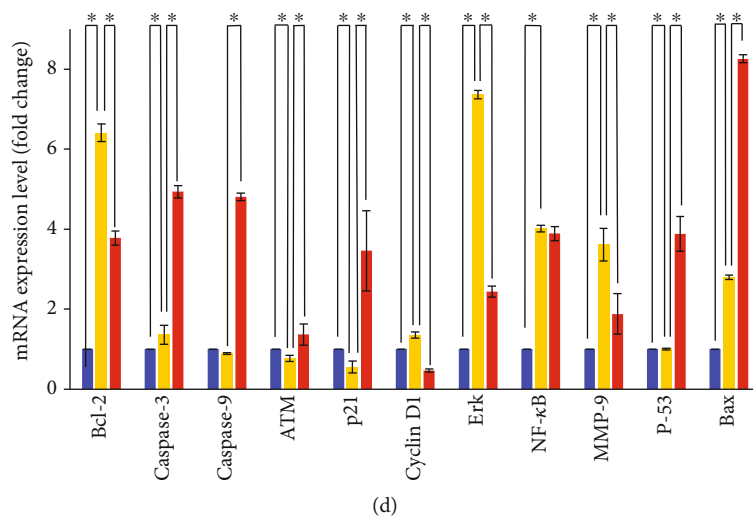
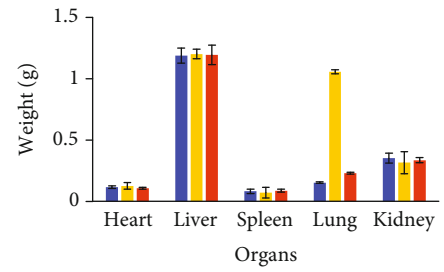
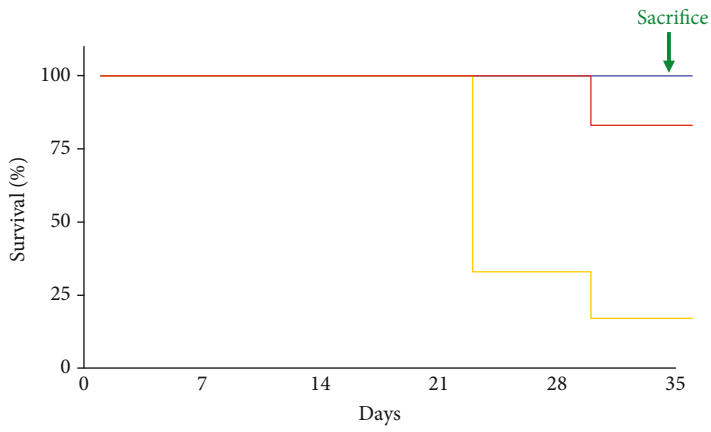
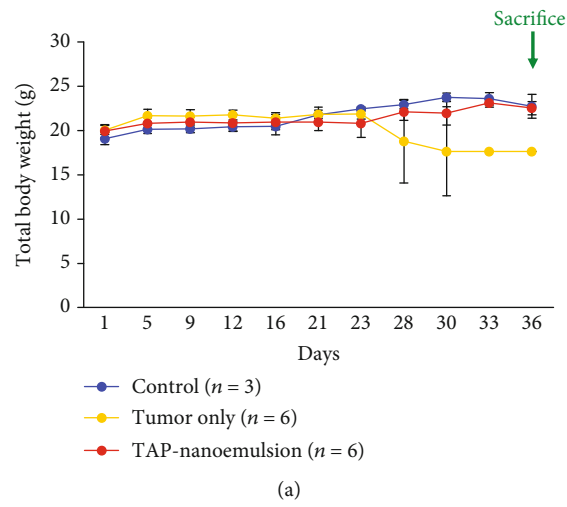


FIGURE 5: Continued.

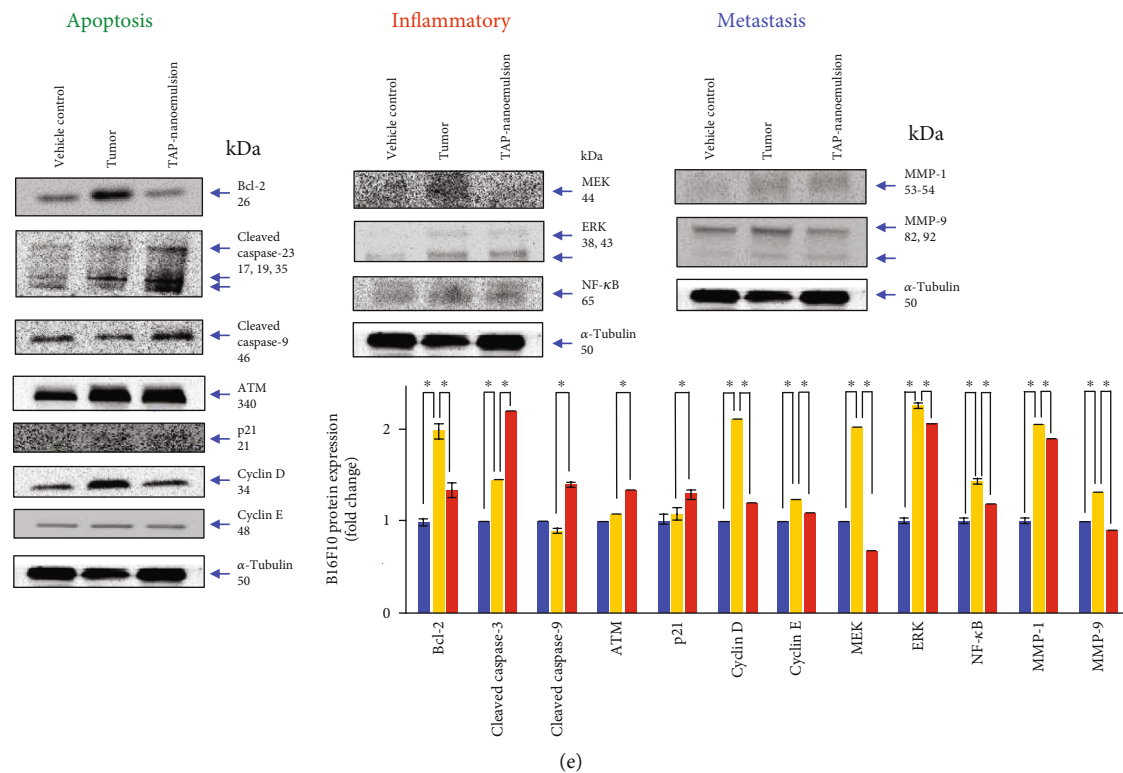


FIGURE 5: *In vivo* behavior, TAP-nanoemulsion administrated against metastatic melanoma in the lung of B16F10-bearing C57BL/6 mice. (a) Changes in mouse body weight after different treatments. (b) Mouse morbidity-free survival efficacy with different treatments following the vehicle control, tumor-only, and TAP-nanoemulsion groups. (c) The evaluations of organ weights observed from the three groups. (d) The mRNA expressions associated with the three groups in qRT-PCR assay. (e) TAP-nanoemulsion inhibited lung metastatic melanoma through induction of apoptosis-related proteins by Western blotting. We took α -tubulin as our experimental loading control. Data are representative of 3 experiments. Blue: blank control; yellow: tumor only; red: TAP-nanoemulsion treatment groups. * $p < 0.05$ as compared with the tumor-only group.

treated with the vehicle control or TAP-nanoemulsion. TAP-nanoemulsion was conducted to the experimental group at 10 mg/kg by the oral route and did not generate any significant changes and problems in normal defecation, posture, expression, respiration, skin shedding, and yellowing of the hair. The mice's body weight was measured every week during the experiment time period. As shown in Figure 5(a), the body weight of the TAP-nanoemulsion group was significantly enhanced over 30 days, and the volume of the mouse tumor was reduced compared to the 0 day between the three groups (Figure S1). Notably, the TAP-nanoemulsion group demonstrated longer survival periods, and only 1/4 of mice died within 35 days in Figure 5(b). The heart, liver, spleen, lung, and kidneys were cut from the sacrificed mice and weighed (Figure 5(c)). The weight of the lung from the tumor-only group compared with that from the vehicle control group was increased because the extra tissue of lung metastatic melanoma. On the other hand, after being treated with TAP-nanoemulsion in an oral form, the metastatic melanoma of the lung was reduced appreciably. In the tumor-only group, the average lung weight was 1.06 ± 0.06 g, whereas the TAP-nanoemulsion group suppressed the lung melanoma proliferation weights to 0.25 ± 0.05 g. There was no major difference in other organ weights

among the three groups, suggesting that TAP-nanoemulsion had no significant toxic effects on these parts. Our previous study confirmed that AST restrained the formation of melanoma [15], and in this case, we also inhibited B16F10 cellular melanoma with lung metastases successfully.

Based on our previous findings, we discovered AST suppressed melanoma proliferation via apoptotic mechanism *in vitro* and in a xenograft model [6, 7], and the lung metastatic melanoma inhibition by the oral TAP-nanoemulsion administration within this work was demonstrated. Bcl-2 family proteins are well known as major regulators of the mitochondrial apoptosis mechanism. We found that Bcl-2 decreased in the TAP-nanoemulsion treatment group in Figure 5(d), and it was assumed that TAP-nanoemulsion increased downstream representative apoptotic expressions of caspase-3 and caspase-9 which were proteolytic mRNA playing necessary roles in the programmed cell death. The ATM gene provides instructions for making a protein that is located in the nucleus, where it helps to control the cell growth and division rates. In particular, the nanoemulsion promoted the expression of ATM in the mouse lungs compared to the other two groups. The activities of cyclin-dependent kinases are positively regulated by cyclins and negatively adjusted by cyclin-dependent kinase inhibitors.

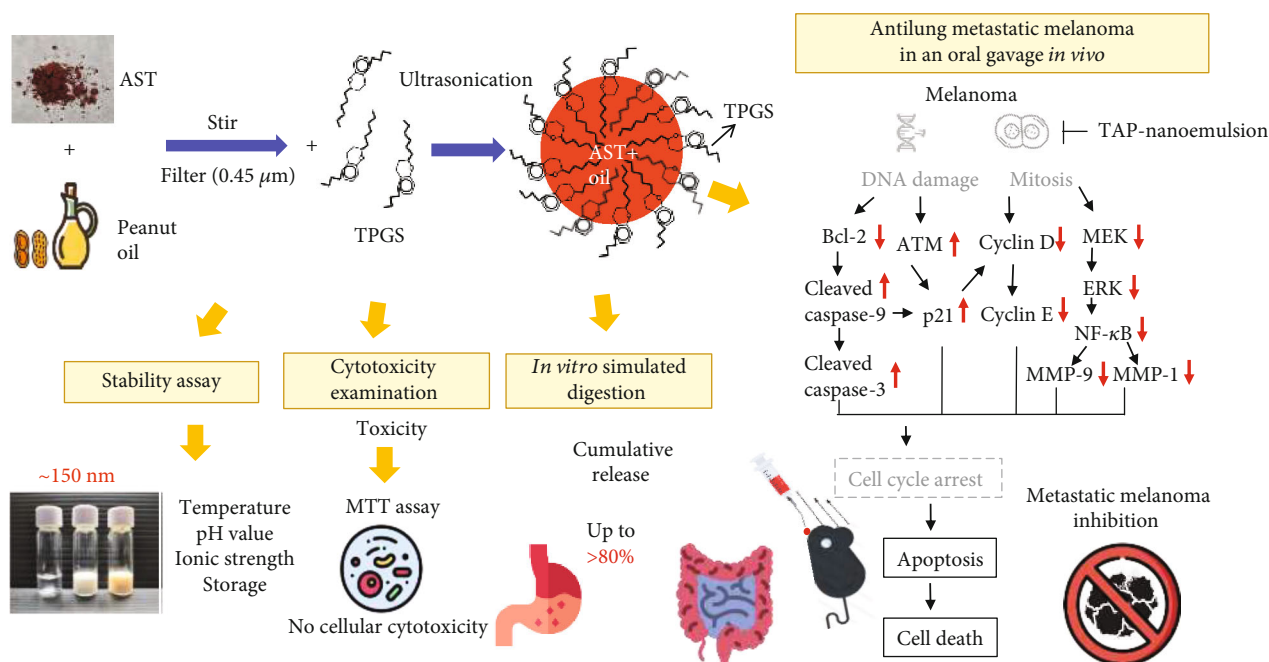


FIGURE 6: Proposed schematic diagram of TAP-nanoemulsion biofunction.

The cyclin-dependent kinase inhibitor p21 triggers cell cycle arrest to stop at the G1 phase in many stimulus responses [28]. It was important for the transition stage from G1 to S, and the suppression of *cyclin D1* reduced the hyperplasia of tumor cells. Extracellular signal-regulated protein kinase (ERK) signaling communicates to a neighboring protein by adding phosphate groups to play a switch position in the cancer process and is a required pace in the assistance of melanoma. Nuclear factor κ -light-chain-enhancer of activated B cell (NF- κ B) not only facilitates tumor initiation/proliferation/development, augments angiogenesis, inhibits apoptosis, and resists drugs but also causes epithelial-mesenchymal transition which assists distant metastasis. Most human cancers have a constitutive of NF- κ B because of the numerous oncogenic mutations and inflammatory microenvironments [29]. TAP-nanoemulsion inhibited mRNA expressions of ERK with significant difference and minor effect on NF- κ B. The famous migratory mRNA of matrix metalloproteinase-9 (MMP-9) was lower in the TAP-nanoemulsion treatment group than in the tumor-only group. The experimental data showed that it had a positive potential to suppress the invasion and metastasis of melanoma in the lung.

Following the gene expression analysis changes measured by qRT-PCR *in vivo*, we believed that our sample induced lung metastatic melanoma apoptosis due to the invasive suppression. To determine the involvements of signal transduction pathways in TAP-nanoemulsion cancer inhibition, further assays were shown to survey the protein expressions in Figures 5(e) and S4. Western blotting was used to measure the related protein expressions. TAP-nanoemulsion inhibited Bcl-2, cyclin D, ERK, NF- κ B, and MMP-9 that exhibited similar resultant trends as qRT-PCR consequences. Dysregulated cyclin E activity causes cell lineage-specific abnormali-

ties, such as impaired maturation, apoptosis, and senescence [30]. MEK is often overactive in some cancers. Once it is blocked, tumor growth is controlled and apoptosis is to take the field. The MMP family is related in the breakdown of all kinds of extracellular matrixes in the normal physiological processes. MMPs are recognized to be implicated with the tumor adhesion and dispersion, the cytokine and chemokine inactivation, the release of apoptotic ligands, the angiogenesis, and the cleavage of cell surface receptors [7]. In particular, the expressions of three proteins (cyclin E, MEK, and MMP-1) were reduced with the addition of TAP-nanoemulsion. Overall, we confirm that TAP-nanoemulsion effectively reduced the growth of melanoma and induced lung metastatic melanoma apoptosis in mRNA and proteins.

4. Conclusions

Based on the above results, we successfully manufactured a nanoemulsion loaded with AST and peanut oil, and TPGS as the emulsifier effectively stabilized the O/W nanoemulsion against various environment stresses. TAP-nanoemulsion had a good antioxidative stress in a dose-dependent manner to reduce the production of cellular ROS. In the physiologic mimic surrounding, TAP-nanoemulsion demonstrated a high-quality oral release characteristic and reasonable stability *in vitro*. TAP-nanoemulsion triggered apoptosis of human malignant melanoma in the lung by inhibiting Bcl-2, cyclins D1 and E, NF- κ B, ERK, MEK, and MMP-1 and MMP-9 and increasing cleaved caspase-9 and caspase-3, ATM, and p21. We are the first group to present that TAP-nanoemulsion had the potential clinical application for antioxidation and metastatic melanoma suppression *in vivo* in Figure 6.

Data Availability

The data used to support the findings of this study are available from the corresponding author upon request.

Conflicts of Interest

The authors have no competing financial interests to declare.

Authors' Contributions

H.-Y.H. and Y.-C.W. contributed equally to this work. H.-Y.H., Y.-C.W., Y.-C.C., W.K., D.L., C.X., and H.-M.D.W. conceived and designed the experiments; H.-Y. H. and Y.-C.C. performed the experiments and analyzed the data; W.K., D.L., C.X., Y.-C.W., and H.-M.D.W. contributed the reagents, materials, and analysis tools; H.-Y.H., Y.-C.W., W.K., Y.-C.C., D.L., C.X., and H.-M.D.W. wrote this manuscript.

Acknowledgments

This work is supported by the Ministry of Science and Technology (MOST 108-2221-E-005-044) and Kaohsiung Armed Forces General Hospital (KAFGH 108-01).

Supplementary Materials

Table S1: the primer sequences used in this study. Figure S1: tumor developments and TAP-nanoemulsion regimen administration *in vivo*. Figure S2: IRB certificate of human foreskin fibroblasts [KMUHIRB-2014-07-07 (I)]. Figure S3: IACUC certificate of animal examination (IACUC number: 105-141). Figure S4: TAP-nanoemulsion inhibited lung metastatic melanoma through induction of apoptosis-related proteins by Western blotting verification. (*Supplementary Materials*)

References

- [1] H.-Y. Chou, C. Lee, J.-L. Pan et al., "Enriched astaxanthin extract from *Haematococcus pluvialis* augments growth factor secretions to increase cell proliferation and induces MMP1 degradation to enhance collagen production in human dermal fibroblasts," *International Journal of Molecular Sciences*, vol. 17, no. 6, pp. 955–967, 2016.
- [2] Y. T. Chen, C. J. Kao, H. Y. Huang et al., "Astaxanthin reduces MMP expressions, suppresses cancer cell migrations, and triggers apoptotic caspases of *in vitro* and *in vivo* models in melanoma," *Journal of Functional Foods*, vol. 31, pp. 20–31, 2017.
- [3] J.-L. Pan, H.-M. Wang, C.-Y. Chen, and J.-S. Chang, "Extraction of astaxanthin from *Haematococcus pluvialis* by supercritical carbon dioxide fluid with ethanol modifier," *Engineering in Life Sciences*, vol. 12, no. 6, pp. 638–647, 2012.
- [4] H. M. D. Wang, C. C. Chen, P. Huynh, and J. S. Chang, "Exploring the potential of using algae in cosmetics," *Bioresource Technology*, vol. 184, pp. 355–362, 2015.
- [5] H. M. D. Wang, X. C. Li, D. J. Lee, and J. S. Chang, "Potential biomedical applications of marine algae," *Bioresource Technology*, vol. 244, no. 2, pp. 1407–1415, 2017.
- [6] C.-C. Tseng, Y.-J. Lin, W. Liu et al., "Metabolic engineering probiotic yeast produces 3S, 3'S-astaxanthin to inhibit B16F10 metastasis," *Food and Chemical Toxicology*, vol. 135, pp. 110993–1111001, 2020.
- [7] S. Kentish, T. J. Wooster, M. Ashokkumar, S. Balachandran, R. Mawson, and L. Simons, "The use of ultrasonics for nanoemulsion preparation," *Journal of Functional Foods*, vol. 9, no. 2, pp. 170–175, 2008.
- [8] E. M. Persson, R. G. Nilsson, G. I. Hansson et al., "A clinical single-pass perfusion investigation of the dynamic *in vivo* secretory response to a dietary meal in human proximal small intestine," *Pharmaceutical Research*, vol. 23, no. 4, pp. 742–751, 2006.
- [9] E. Dickinson, "Food Emulsions: Principles, Practices, and Techniques, Julian McClements, 2nd edition, CRC Press, Boca Raton, FL (2005), pp. 609, \$149.95," *Food Hydrocolloids*, vol. 20, no. 1, p. 137, 2006.
- [10] D. D'Arcangelo, C. Giampietri, M. Muscio, F. Scatozza, F. Facchiano, and A. Facchiano, "WIP1, BAG1, and PEX3 autophagy-related genes are relevant melanoma markers," *Oxidative Medicine and Cellular Longevity*, vol. 2018, Article ID 1471682, 12 pages, 2018.
- [11] M. Venza, M. Visalli, C. Beninati, G. V. De Gaetano, D. Teti, and I. Venza, "Cellular Mechanisms of Oxidative Stress and Action in Melanoma," *Oxidative Medicine and Cellular Longevity*, vol. 2015, Article ID 481782, 11 pages, 2015.
- [12] Z. Dou, C. Chen, and X. Fu, "Digestive Property and Bioactivity of Blackberry Polysaccharides with Different Molecular Weights," *Journal of Agricultural and Food Chemistry*, vol. 67, no. 45, pp. 12428–12440, 2019.
- [13] L. C. Lin, C. Y. Chen, C. H. Kuo et al., "36H: A novel potent inhibitor for antimelanogenesis," *Oxidative Medicine and Cellular Longevity*, vol. 2018, Article ID 6354972, 12 pages, 2018.
- [14] J. Li, Y. R. Lu, I. F. Lin et al., "Reversing UVB-induced photoaging with *Hibiscus sabdariffa* calyx aqueous extract," *Journal of the Science of Food and Agriculture*, vol. 100, no. 2, pp. 672–681, 2019.
- [15] E. S. Hwang, G. M. Bornhorst, P. I. Oteiza, and A. E. Mitchell, "Assessing the fate and bioavailability of glucosinolates in kale (*Brassica oleracea*) using simulated human digestion and Caco-2 cell uptake models," *Journal of Agricultural and Food Chemistry*, vol. 67, no. 34, pp. 9492–9500, 2019.
- [16] Y. C. Wang, X. Y. Huang, C. C. Chiu et al., "Inhibitions of melanogenesis via *Phyllanthus emblica* fruit extract powder in b16f10 cells," *Food Bioscience*, vol. 28, pp. 177–182, 2019.
- [17] I. Hubatsch, E. G. E. Ragnarsson, and P. Artursson, "Determination of drug permeability and prediction of drug absorption in Caco-2 monolayers," *Nature Protocols*, vol. 2, no. 9, pp. 2111–2119, 2007.
- [18] L. J. Liu, W. Wang, S. Y. Huang et al., "Inhibition of the Ras/Raf interaction and repression of renal cancer xenografts *in vivo* by an enantiomeric iridium (III) metal-based compound," *Chemical Science*, vol. 8, no. 7, pp. 4756–4763, 2017.
- [19] P.-H. Li, Y.-P. Chiu, C.-C. Shih et al., "Biofunctional activities of *Equisetum ramosissimum* extract: protective effects against oxidation, melanoma, and melanogenesis," *Oxidative Medicine and Cellular Longevity*, vol. 2016, Article ID 2853543, 9 pages, 2016.
- [20] H. M. Wang, C. Y. Chen, and Z. H. Wen, "Identifying melanogenesis inhibitors from *Cinnamomum subavenium* with *in vitro* and *in vivo* screening systems by targeting the human

- tyrosinase," *Experimental Dermatology*, vol. 20, no. 3, pp. 242–248, 2011.
- [21] P.-H. Li, L.-H. Liu, C.-C. Chang et al., "Silencing stem cell factor gene in fibroblasts to regulate paracrine factor productions and enhance c-kit expression in melanocytes on melanogenesis," *International Journal of Molecular Sciences*, vol. 19, no. 5, p. 1475, 2018.
- [22] H. S. Ribeiro, L. G. Rico, G. G. Badolato, and H. Schubert, "Production of O/W emulsions containing astaxanthin by repeated premix membrane emulsification," *Journal of Food Science*, vol. 70, no. 2, pp. E117–E123, 2005.
- [23] J. Li, S.-Y. Huang, Q. Deng et al., "Extraction and characterization of phenolic compounds with antioxidant and antimicrobial activities from pickled radish," *Food and Chemical Toxicology*, vol. 136, p. 111050, 2020.
- [24] M. Primozic, A. Duchek, M. Nickerson, and S. Ghosh, "Formation, stability and *in vitro* digestibility of nanoemulsions stabilized by high-pressure homogenized lentil proteins isolate," *Food Hydrocolloids*, vol. 77, pp. 126–141, 2018.
- [25] J. Wang, Y. Zhou, L. Ma et al., "CIAPIN1 targeted NHE1 and ERK1/2 to suppress NSCLC cells' metastasis and predicted good prognosis in NSCLC patients receiving pneumonectomy," *Oxidative Medicine and Cellular Longevity*, vol. 2019, Article ID 1970818, 15 pages, 2019.
- [26] D. J. McClements and H. Xiao, "Potential biological fate of ingested nanoemulsions: influence of particle characteristics," *Food & Function*, vol. 3, no. 3, pp. 202–220, 2012.
- [27] L. Yonekura and A. Nagao, "Intestinal absorption of dietary carotenoids," *Molecular Nutrition & Food Research*, vol. 51, no. 1, pp. 107–115, 2007.
- [28] X. Zhang, W. Zhao, L. Hu, L. Zhao, and J. Huang, "Carotenoids inhibit proliferation and regulate expression of peroxisome proliferators-activated receptor gamma (PPAR γ) in K562 cancer cells," *Archives of Biochemistry and Biophysics*, vol. 512, no. 1, pp. 96–106, 2011.
- [29] Y. Xia, S. Shen, and I. M. Verma, "NF- κ B, an active player in human cancers," *NIH Public Access*, vol. 2, no. 9, pp. 823–830, 2014.
- [30] A. C. Minella, K. R. Loeb, A. Knecht et al., "Cyclin E phosphorylation regulates cell proliferation in hematopoietic and epithelial lineages *in vivo*," *Genes & Development*, vol. 22, no. 12, pp. 1677–1689, 2008.

Clinical Study

Genetic Polymorphism of the Nrf2 Promoter Region (rs35652124) Is Associated with the Risk of Diabetic Foot Ulcers

Rajan Teena ¹, Umopathy Dhamodharan,¹ Daoud Ali,² Kesavan Rajesh,³ and Kunka Mohanram Ramkumar ¹

¹Department of Biotechnology and SRM Research Institute, SRM Institute of Science and Technology, Kattankulathur, Tamil Nadu, India

²Department of Zoology, College of Science, King Saud University, Riyadh, Saudi Arabia

³Department of Podiatry, Hycare Super Speciality Hospital, MMDA Colony, Arumbakkam, Chennai, Tamil Nadu, India

Correspondence should be addressed to Kunka Mohanram Ramkumar; ramkumak@srmist.edu.in

Received 20 June 2020; Accepted 28 July 2020; Published 17 August 2020

Academic Editor: Shane Thomas

Copyright © 2020 Rajan Teena et al. This is an open access article distributed under the Creative Commons Attribution License, which permits unrestricted use, distribution, and reproduction in any medium, provided the original work is properly cited.

The genetic polymorphism in the nuclear factor erythroid 2-related factor 2 (Nrf2) gene has been reported as one of the prognosis markers for various diseases, including cancer. Nrf2 is a key transcription factor involved in wound healing by regulating angiogenesis. We investigated the genetic association of *NRF2* single-nucleotide polymorphism rs35652124 with T2DM and DFU and assessed its functional impact. A total of 400 subjects were recruited for the study and categorized into three groups: infected DFU patients (DFU, $n = 100$), T2DM patients without complications (T2DM, $n = 150$), and healthy adults with normal glucose tolerance (NGT, $n = 150$). The subjects were genotyped by PCR-RFLP, and the polymorphism was identified by bidirectional Sanger sequencing. The expression of *NRF2*, *IL-10*, *TNF- α* , and *IL-6* was studied by qPCR to evaluate the functional impact of rs35652124. The “TT” genotype of rs35652124 was associated with a significant risk for T2DM [OR = 2.2 (1.2-4.2), $p = 0.01$] and DFU [OR = 7.9 (4-14.9), $p < 0.0001$]. A significant decrease in transcriptional levels of *NRF2* and *IL-10* and a remarkable increase in *TNF- α* and *IL-6* were observed in subjects with TT genotype. In conclusion, rs35652124 (TT) is a harmful genetic variant that predisposes to insulin resistance and impaired angiogenesis. Hence, it may serve as a diagnostic genetic marker for T2DM and DFU in combination with different inflammatory markers.

1. Introduction

Diabetic Foot Ulcer (DFU) is the fastest growing chronic complication of diabetes and a major cause of mortality in the diabetic population [1]. Amputation in subjects with diabetes is ten to twenty times higher than in subjects without diabetes [2]. The progression of DFU is often complicated by wide-ranging diabetic changes, such as neuropathy and vascular disease. Recent research is now focusing on the role of epigenetic factors, which by themselves and/or in combination with classical genetic factors, may be the major causative factor for the progression of DFU. Although genetic and epigenetic factors predispose an individual to diabetes and, these molecular mechanisms have not been completely elucidated.

Nuclear factor erythroid 2-related factor 2 (Nrf2), encoded by the gene *NRF2*, is a main redox homeostasis mediator. Nrf2 triggers an array of proteins such as glutathione-S-transferase (GST), glutathione peroxidase (GPx), UDP-glucuronosyltransferase (UGT), NAD(P)H:quinone oxidoreductase 1 (NQO1), multidrug resistance-associated protein (MRP), heme-oxygenase-1 (HO-1), peroxiredoxin (Prx), Sulfiredoxin 1 (SRXN1), and Thioredoxin reductase 1 (TXNRD1) involved in cytoprotection and detoxification [3]. However, recent research has demonstrated that Nrf2 is downregulated in various inflammatory disorders [4, 5]. Studies from our laboratory have reported that circulatory levels of Nrf2 and its downstream targets were significantly low in type 2 diabetes and DFU [6, 7]. Previous investigations have reported that *NRF2* expression is

regulated by genetic factors such as single-nucleotide polymorphisms (SNPs), epigenetic factors such as promoter methylation and posttranslational modifications of histones [8]. However, the molecular mechanisms that downregulate the *NRF2* expression in T2DM and DFU remain unresolved.

One of the most prevalent genetic variations that predispose an individual to diabetes and its complications is SNPs [9–12]. It induces nucleotide substitution at specific locations in a gene, causing variations in susceptibility to disease. Polymorphisms in the promoter region can regulate gene expression [13]. Epidemiological and genetic association studies have proven the association of *NRF2* promoter polymorphisms with diseases linked to oxidative stress, suggesting the genetic predisposition of *NRF2* polymorphisms to disease susceptibility [14]. Among the *NRF2* promoter polymorphisms, rs6721961, rs6706649, and rs35652124 are the most studied ones. We have chosen rs35652124 (g.178130073 C/T, c.-214 G>A) due to its involvement in regulating efficient binding of Nrf2 with promoter binding sites like antioxidant response element (ARE) [15]. Nrf2 autoregulates its activity through its ARE, and the consequence of a polymorphism in ARE could be the decline of transcriptional activity of Nrf2-dependent cytoprotective genes [16]. Previous studies have also demonstrated that rs6721961 and rs6706649 have low minor allele frequencies when compared to rs35652124 [17, 18].

The association of rs35652124 with a few diseases has been previously documented. The investigation by Córdova et al. demonstrated the association of rs35652124 with nephritis in childhood-onset systemic lupus erythematosus [19]. Zhu et al. analyzed three SNPs, namely, rs35652124, rs6706649, and rs6721961, in Hashimoto's thyroiditis and reported that the presence of one or more minor alleles was linked with a near-significant risk [20]. Collectively, these investigations demonstrated the genetic association of rs35652124 with diseases linked to autoimmunity, inflammation, and oxidative stress. However, the functional impact of rs35652124 on diabetes and DFU has never been explored. In the present study, we have analyzed the genetic association of rs35652124 with T2DM and DFU. Further, its functional impact was analyzed by measuring the expression of *NRF2*, interleukin-10 (*IL-10*), tumor necrosis factor- α (*TNF- α*), and interleukin-6 (*IL-6*) in the study subjects.

Our investigation demonstrated that the rs35652124 TT genotype was significantly associated with T2DM and DFU and found to have a significant decrease in transcriptional levels of *NRF2* and anti-inflammatory marker *IL-10* and a significant increase in pro-inflammatory markers *TNF- α* and *IL-6*, suggesting the inherent deleterious impacts of the polymorphism.

2. Patients and Methods

2.1. Study Population. A total of 400 participants were chosen for this cross-sectional study and grouped into three, i.e., group I: subjects with normal glucose tolerance ($n = 150$), group II: subjects with type 2 diabetes mellitus ($n = 150$), and group III: subjects with diabetic foot ulcers ($n = 100$). The research subjects were recruited from the Hycare Super

Speciality Hospital, Chennai, and the blood samples were collected in the fasting state. The ethics committee of the institute approved the study protocol (025-A/HYC/IEC/2018), and all the study subjects gave written informed consent. The investigation was conducted in accordance with the Declaration of Helsinki.

2.2. Inclusion and Exclusion Criteria. The participants in this investigation are of south Indian origin aged 50 to 55 years. Subjects with T2DM and DFU were chosen based on the World Health Organization criteria and IDSA (Infectious Diseases Society of America)-IWDF (International Working Group on the Diabetic Foot) classification, respectively. NGT included subjects with normal FPG (72 to 99 mg/dL), PPG (below 140 mg/dL), and HbA1c (below 6.0%). T2DM subjects were identified on the basis of FPG (>100 mg/dL), PPG (200 mg/dL or more), and HbA1c (6.5% or above). Duration of diabetes was not considered. Similarly, subjects with infected DFU were selected based on their symptoms of systemic inflammatory responses (WBC >12,000 or <4000 cells/ μ L) and wound size (≥ 2 cm).

Subjects with infectious diseases, peripheral vascular disease, autoimmune diseases, and haematological diseases and subjects with other reasons of harm to the peripheral nerves, such as vitamin B₁₂ insufficiency, use of neurotoxic drugs, and inherited neuropathy were not considered for this investigation.

2.3. Anthropometric Measurements and Biochemical Parameters. Anthropometric measurements of study subjects like height and weight were obtained using standard techniques. Body mass index (BMI) calculation was done according to the formula, i.e., dividing the weight in kilograms by the height in centimeters squared. The blood pressure was measured using INFI deluxe mercury sphygmomanometer. Biochemical analysis of fasting plasma glucose (FPG), postprandial plasma glucose (PPG), total serum cholesterol, HDL-cholesterol (HDL-c), and LDL-cholesterol (LDL-c) was performed in Hitachi-912 autoanalyzer using kits supplied by Roche Diagnostics (Germany). FPG and PPG were analyzed by the glucose oxidase-peroxidase method. Total serum cholesterol was analyzed by cholesterol oxidase-peroxidase-amidopyrine method. HDL-c was measured by the direct method with polyethylene glycol-pre-treated enzymes. LDL-c was calculated by Friedewald formula. Glycated haemoglobin A1c (HbA1c) levels were analyzed using HPLC. The total blood cell counts were analysed on a hematology analyzer (XN-1000; Sysmex, Kobe, Japan).

2.4. Genotyping of *NRF2* rs35652124 Polymorphism. Genomic DNA was isolated using QIAamp DNA Mini Kit (Qiagen) according to the manufacturer's instructions. The purity and concentration of isolated DNA were analyzed using Thermo Scientific™ NanoDrop™ 2000/2000c spectrophotometer. The samples with a purity of 1.8 (A260/280) was used for the study. The *NRF2* promoter region with the polymorphism rs35652124 was amplified by S1000 thermal cycler (Bio-Rad, USA), using the primers: Forward: 5'-CCTTGCCCTGCTTTTATCTC-3' and Reverse: 5'-CTTC

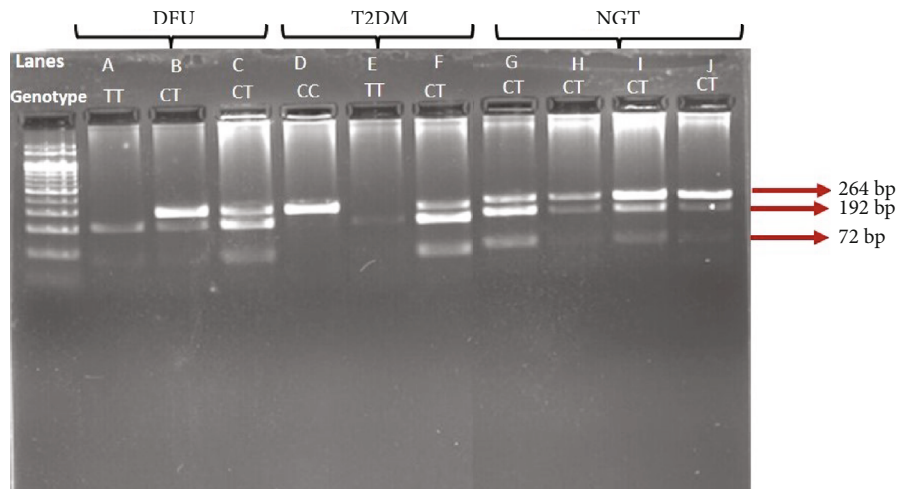


FIGURE 1: PCR-RFLP results of rs35652124. First lane shows 100 bp DNA ladder. Lanes A and E indicate the “TT” genotype with bands at 192 and 72 bp. Lane D represents CC genotype with a single band at 264 bp alone. Lanes B, C, F, G, H, I, and J indicate CT genotype with three bands at 264, 192, and 72 bps.

TCCGTTTGCCTTTGAC-3'. The PCR was done based on the following protocol: initial denaturation of 95°C for 5 min, followed by 30 cycles of denaturation at 95°C for 30 s, annealing at 57°C for 30 s, and extension at 72°C for 1 min, followed by a final extension at 72°C for 10 min. Following PCR, the amplicon of 264 base pairs (bps) was subjected to Restriction Fragment Length Polymorphism (RFLP) using the restriction enzyme BseRI (Neb enzyme, USA) as per the manufacturer's instructions. The restriction digested products were resolved on three percent agarose gel and visualised in Syngene G Box XR5 Chemiluminescence Imaging System (Syngene International Limited, India). The homozygous wild CC genotype was obtained as 1 band (264 bp), the heterozygous CT genotype as 3 bands (264, 192, and 72 bps), and the homozygous mutant genotype TT as two bands (192 and 72 bps) (Figure 1). Further, the PCR products were purified using the QIA quick gel extraction kit (Qiagen, USA) and sequenced on SeqStudio Genetic Analyzer (Applied Biosystems, USA). The chromatograms were visualised in CodonCode Aligner (CodonCode Aligner 9.0.1).

2.5. Analysis of NRF2 and Inflammatory Markers by qPCR. 5 mL of venous blood was obtained from the study subjects based on their rs35652124 genotypes. Further, peripheral blood mononuclear cells (PBMCs) were separated from the whole blood by a Ficoll-histopaque density gradient centrifugation method. mRNA was isolated using the RNeasy Mini Kit (Qiagen) according to the manufacturer's instructions. cDNA conversion was performed using Takara PrimeScript RT-reagent kit. The expression of *NRF2*, *IL-10*, *IL-6*, and *TNF- α* among the study subjects was analyzed by quantitative real-time PCR using CFX Connect Real-Time PCR Detection System (Bio-Rad, USA). The primers used are as follows: *NRF2* (F): 5'-TG TAGATGACAATGAGGTTTC-3', *NRF2* (R): 5'-ACTGAGCCTGATTAGTAGCAA-3', *IL-10* (F): 5'-ACATCAGGGTGGCGACTCTA-3', *IL-10* (R): 5'-AAGGTTTCTCAAGGGGCTGG-3', *IL-6* (F): 5'-GTCCAG

TTGCCTTCTCCCTG-3', *IL-6* (R): 5'-AGCACGACCACGACCTTG-3', *TNF- α* (F): 5'-TCTGGGCAGGTCTACTTTGG-3', *TNF- α* (R): 5'-GGTTGAGGGTGTCTGAAGGA-3', *GAPDH* (F): 5'-AAGAAGGTGGTGAAGCAGGC-3', and *GAPDH* (R): 5'-GTCAAAGGTGGAGGAGTGGG-3'.

2.6. Statistical Analysis. Statistical analysis was carried out using the SPSS version 20.0. The data of continuous variables are represented as mean \pm SD. For non-normally distributed variables, Mann-Whitney *U* tests were used to compare medians. The analysis of Hardy Weinberg equilibrium was performed by chi-square test. Determination of frequencies of alleles and genotype distribution were performed by chi-square test of independence with two by twofold contingency and *z*-score. Multivariate logistic regression analysis calculated the odds ratio (OR) with ninety-five percent confidence interval. *p* values of less than 0.05 were regarded as statistically significant.

3. Results

3.1. Biochemical Characteristics of the Study Subjects. The clinical and biochemical characteristics such as blood glucose, blood pressure, lipid profile, and HOMA index of the study subjects are depicted in Table 1. The NGT subjects were normoglycemic with BMI and biochemical parameters in the normal range. Reflecting the severity of the disease, SBP, DBP, FPG, PPG, HbA1c, HOMA-IR, LDL-c, total serum cholesterol, and WBC counts were significantly high among T2DM and DFU subjects when compared to NGT ($p < 0.001$), whereas HDL-c levels were significantly low in T2DM and DFU when compared to NGT ($p < 0.001$).

3.2. The nsSNP rs35652124 (g.178130073T>C) Is Associated with T2DM and DFU. Table 2 depicts the genetic interrelation of rs35652124 with T2DM and DFU. The frequency of TT genotype was significantly higher in DFU subjects (52%) when compared to T2DM (23.3%) and NGT subjects

TABLE 1: Clinical and biochemical characteristics of the study population.

Clinical parameters	NGT ($n = 150$)	T2DM ($n = 150$) ^a	DFU ($n = 100$) ^b
Gender (M/F)	77M/73F	79M/71F	48M/52F
Age (years)	51.6 ± 1.2	51.4 ± 1.4	52.8 ± 1.6
BMI (kg/m ²)	21.2 ± 1.6	27.6 ± 1.4 ^{****}	28.1 ± 1.7 ^{****}
SPG (mmHg)	102.2 ± 6.9	118.6 ± 7.8 ^{****}	128.5 ± 3.5 ^{****}
DBP (mmHg)	75.3 ± 4.1	81.1 ± 3.2 ^{****}	86.3 ± 2.5 ^{****}
FPG (mg/dL)	89.9 ± 7.2	136.6 ± 8.5 ^{****}	215.2 ± 11.4 ^{****}
PPG (mg/dL)	100.9 ± 11.2	234.5 ± 10.3 ^{****}	271.2 ± 39.7 ^{****}
HbA1c (%)	5 ± 0.6	9.4 ± 0.5 ^{****}	11 ± 0.9 ^{****}
Total serum cholesterol (mg/dL)	128.4 ± 22.4	139.9 ± 22.4 ^{****}	190 ± 5 ^{****}
HDL-cholesterol (mg/dL)	60.3 ± 4.1	47.6 ± 4.2 ^{****}	43.5 ± 1.9 ^{****}
LDL-cholesterol (mg/dL)	94.7 ± 7.6	108.8 ± 9.3 ^{****}	124.3 ± 4.5 ^{****}
HOMA-IR	1.3 ± 0.3	3.2 ± 1.1 ^{****}	7.4 ± 1 ^{****}
WBC count (10 ⁹ /L)	6.3 ± 1.5	8.1 ± 1.5 ^{****}	13.4 ± 2.5 ^{****}

All data are reported as mean ± SD for continuous variables; **** $p < 0.0001$; ^acomparison between T2DM and NGT; ^bcomparison between T2DM and DFU.

TABLE 2: Distribution of allele and genotype frequencies and genetic interrelation of rs35652124 SNP with T2DM and DFU: odds ratio (OR) for minor alleles and their homozygous and heterozygous genotypes.

rs35652124	Genotypes			Alleles	
	CC	CT	TT	C	T
NGT	27 (18%)	105(70%)	18 (12%)	159(53%)	141 (47%)
T2DM	22(14.7%)	93(62%)	35(23.3%)	137(46%)	163 (54%)
DFU	8(8%)	40(40%)	52(52%)	56(28%)	144(72%)
NGT vs. T2DM OR (95% CI)	0.8 (0.4-1.4) $p = 0.4$	0.7 (0.4-1.1) $p = 0.14$	2.2 (1.2-4.2) $p = 0.01$	0.5 (0.3-0.7) $p = 0.0001$	1.3 (1-1.8) $p = 0.07$
NGT vs. DFU OR (95% CI)	0.4 (0.2-0.9) $p = 0.03$	0.3 (0.2-0.5) $p < 0.0001$	7.9 (4-14.9) $p < 0.0001$	0.3 (0.2-0.5) $p < 0.0001$	2.9 (2-4.3) $p < 0.0001$
T2DM vs. DFU OR (95% CI)	0.5 (0.2-1.2) $p = 0.12$	0.4 (0.2-0.7) $p = 0.0007$	4 (2.1-6.1) $p < 0.0001$	0.5 (0.3-0.7) $p = 0.0005$	2.2 (1.5-3.2) $p = 0.0001$

Figures in bold are significant with $p < 0.05$ and has odds ratio greater than one, suggesting the pathogenicity.

(12%). Patients with TT genotype had a significant risk for the pathogenesis of T2DM and DFU when compared against NGT vs. T2DM (OR = 2.2 (1.2-4.2), $p = 0.01$) and NGT vs. DFU (OR = 7.9 (4-14.9), $p < 0.0001$), relative to subjects with CT and CC genotypes. The minor allele ‘T’ was significantly prevalent among the DFU subjects relative to T2DM (2.2 (1.5-3.2), $p = 0.0001$) and NGT subjects (2.9 (2-4.3), $p < 0.0001$). As depicted in Figure 2, bidirectional Sanger sequencing identified polymorphism in the study subjects. In forward sequencing, ‘T’ peak is indicative of mutant allele, and ‘C’ peak is indicative of wild allele. Similarly, in reverse sequencing, ‘A’ peak is indicative of mutant allele, and ‘G’ peak is indicative of wild allele.

3.3. Low NRF2 in T2DM and DFU Patients with rs35652124 (TT) Genotype. As depicted in Figure 3, NRF2 expression was significantly downregulated in DFU subjects when compared to T2DM and NGT subjects. But analysis of NRF2 expression based on patient’s genotype demonstrated that DFU (2-fold, $p < 0.0001$), T2DM (1.1-fold, $p < 0.0001$), and

NGT (1-fold, $p < 0.001$) subjects with the homozygous mutant TT genotype had a greater decline in NRF2 expression when compared to T2DM and DFU subjects with homozygous wild CC genotype. This is suggestive of the inhibitory effect of TT genotype in suppressing NRF2 expression.

3.4. Dysregulation in Transcriptional Levels of Pro-inflammatory and Anti-inflammatory Markers in T2DM and DFU Patients with rs35652124 (TT) Genotype. The transcriptional levels of anti-inflammatory cytokine IL-10 and pro-inflammatory cytokines IL-6 and TNF- α were analyzed in study subjects based on their genotype. As depicted in Figure 4, DFU subjects with the homozygous mutant TT genotype were observed to have a significant increase in IL-6 and TNF- α expression when compared to T2DM and DFU subjects with homozygous wild CC genotype, whereas IL-10 expression was significantly decreased in DFU subjects with the homozygous mutant TT genotype when compared to T2DM and DFU subjects with homozygous wild CC genotype.

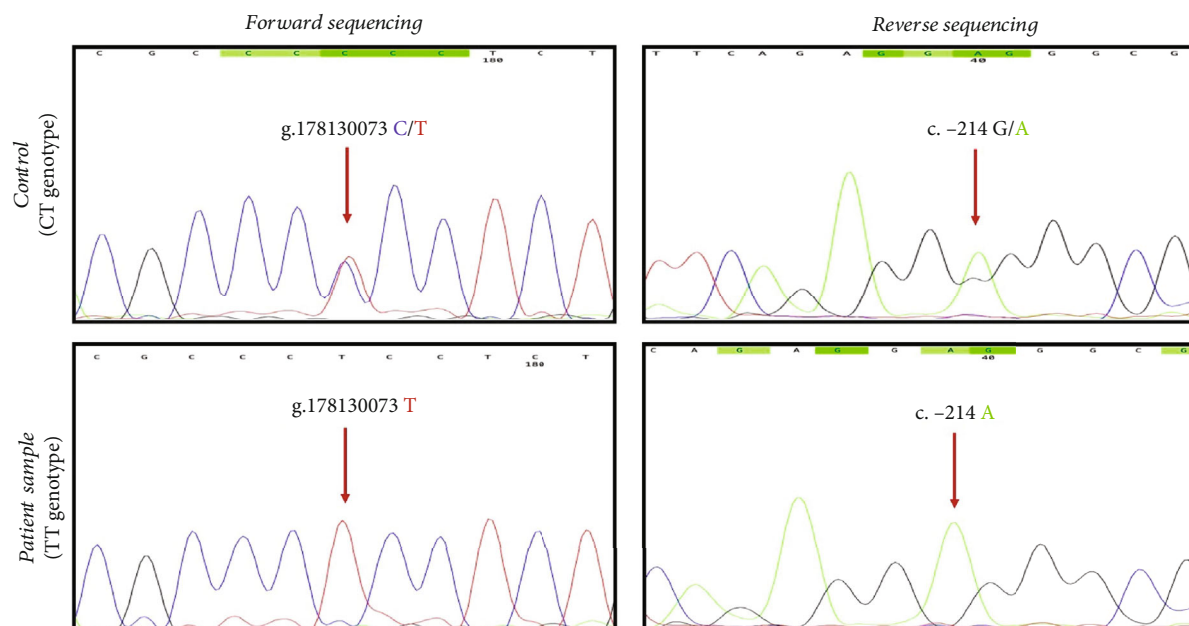


FIGURE 2: Bidirectional Sanger sequencing results of rs35652124. In forward sequencing, “C” peak is indicative of wild allele, and “T” peak is indicative of mutant allele. Similarly, in reverse sequencing, “G” peak is indicative of wild allele, and “A” peak is indicative of mutant allele.

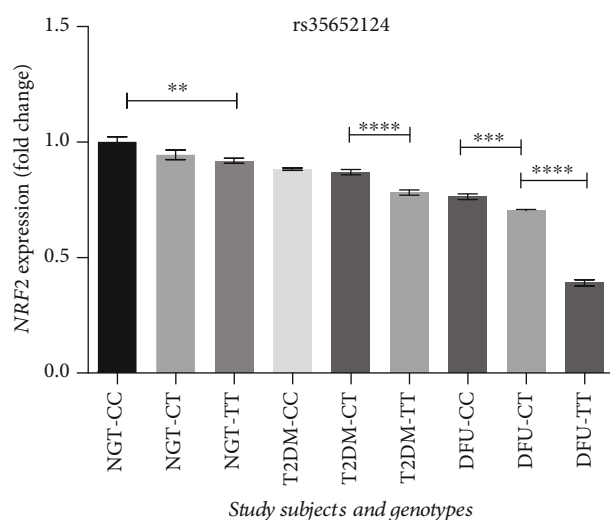


FIGURE 3: Relative gene expression of *NRF2* in PBMCs of study subjects based on their genotype. All data are reported as mean \pm SEM; **** $p < 0.0001$, *** $p < 0.001$, ** $p < 0.01$.

Further, to understand the influence of the other two well-known SNPs in *NRF2* promoter, namely, rs6721961 (G>T) and rs6706649 (C>T) on *NRF2* regulation, we performed bidirectional Sanger sequencing in NGT and DFU subjects. As represented in Figure 5, none of the analyzed subjects had homozygous mutant genotype at rs6721961 and rs6706649 loci. NGT subjects were observed to have homozygous wild genotype at rs6721961 and rs6706649 loci, whereas DFU subjects were observed to have heterozygous genotype. However, in-depth genetic association studies are required to gain more evidence.

4. Discussion

Prolonged hyperglycemia and cellular oxidative stress are the prime pathophysiological determinants of DFU [21]. In healthy subjects, the oxidative stress is counteracted by efficient cellular antioxidant machinery. But in diabetic subjects, prolonged hyperglycemia and oxidative stress result in the generation of excessive reactive oxygen species which causes endothelial dysfunction, vascular damage, and delayed wound healing [22]. Nrf2 is a transcription factor that maintains redox homeostasis in cells. It grants endogenous cellular security to cells by activating antioxidant and detoxifying genes that resist cellular stress [23]. Studies have confirmed the downregulation of Nrf2 in several diseases including diabetes [24, 25]. Extensive investigations indicate that the Nrf2-Keap1 cascade performs a pivotal role in redox homeostasis [26].

Under normal physiology, Nrf2 is subjected to proteasomal degradation by its negative regulator Keap1. However, during cellular stress, the Keap1 cysteine residues get covalently modified, and this enables Nrf2 to dissociate from Keap1 complex, moved to the nucleus, and transcribes an array of genes responsible for detoxification and antioxidant mechanism. Hence, the Nrf2-Keap1 complex acts as a sensor for redox status [27]. However, the genetic mechanisms behind the dysregulation of *NRF2* expression in T2DM and DFU remain unexplored.

Downregulation of Nrf2 is one of the significant factors that cause impaired angiogenesis in DFU subjects [28]. The dysfunction of the *NRF2* by SNPs is gradually becoming a milestone to discern disease development and progression in diabetes [29]. The presence of SNPs in the regulatory motifs of *NRF2* gene would affect the efficient binding of transcription factors to the gene and consequently repress

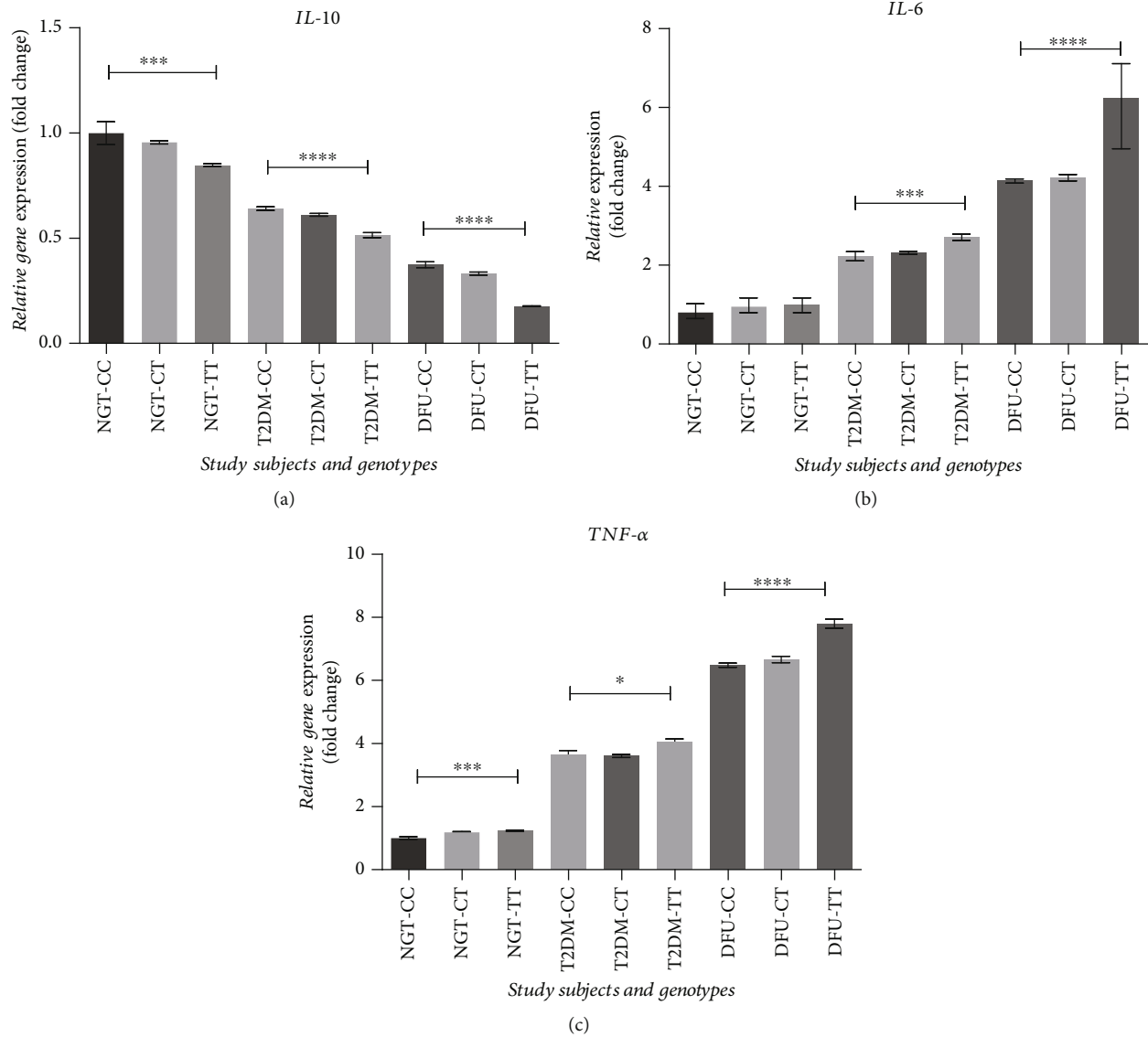


FIGURE 4: Relative gene expression of (a) *IL-10*, (b) *IL-6*, and (c) *TNF-α* in the study cohorts based on genotype. All data are reported as mean \pm SEM; **** $p < 0.0001$, *** $p < 0.001$, * $p < 0.05$.

transcription [30]. The present study analyzed the *NRF2* SNP rs35652124 (g.178130073 C/T, c.-214 G>A), in T2DM and DFU subjects. This polymorphism is located at position -214 of the *NRF2* promoter and adversely affects the binding of Nrf2 to antioxidant response element (ARE) like promoter binding sites [15].

The present study demonstrated that *NRF2* rs35652124 “TT” genotype was remarkably higher in T2DM and DFU subjects than in healthy control and conferred significant risk for the pathogenesis of T2DM and DFU. In addition, it demonstrated that *NRF2* expression was significantly decreased in DFU patients with TT genotype. These observations have coincided with the report of Santos et al., which demonstrated that rs35652124 was associated with a lower level of *NRF2* expression in a cohort of alcoholic liver disease subjects [31]. Besides, a few previous studies have also demonstrated that SNP rs35652124 (TT) decreases the binding of

Nrf2 to ARE and hence downregulates the transcriptional activity of Nrf2 [15, 32].

Investigations by Shimoyama et al. have shown that *NRF2* rs35652124 TT genotype is associated with increased risk for blood pressure in a Japanese cohort [33]. Shimoyama et al. have also demonstrated that TT genotype is a strong predisposing risk factor for cardiovascular mortality in Japanese hemodialysis patients [34]. Similarly, Song et al. have also demonstrated that *NRF2* rs35652124 TT SNP confers vitiligo risk in Han Chinese subjects [32]. All these previous investigations support our findings and confirm that *NRF2* rs35652124 TT is a harmful genetic variant of *NRF2*.

In contrast, there are a few investigations that suggested that *NRF2* rs35652124 TT genotype is not a harmful genetic variant, whereas *NRF2* rs35652124 CC genotype is harmful. For example, based on studies of Marczak et al. in African Americans, subjects with “C” variant allele had significantly

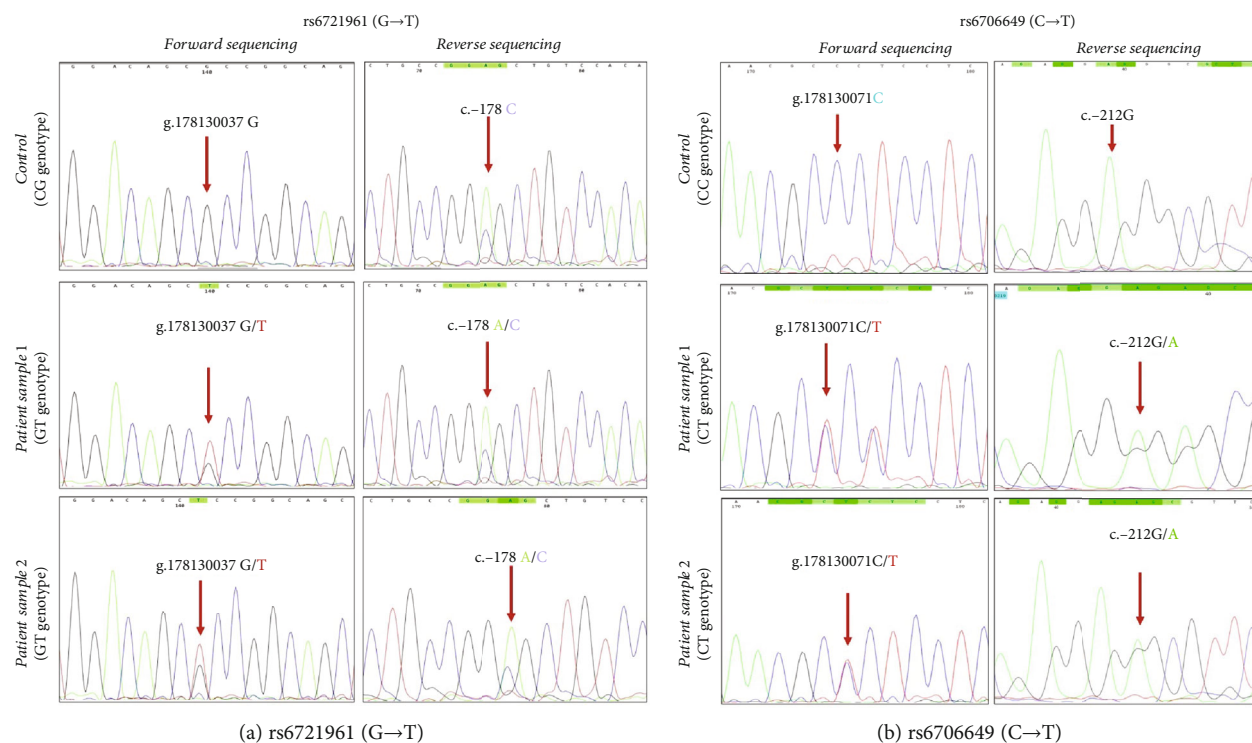


FIGURE 5: Bidirectional Sanger sequencing results of (a) rs6721961: in forward sequencing, “G” peak indicates the wild allele, and “T” peak indicates the mutant allele. Similarly, in reverse sequencing, “C” peak indicates wild allele, and “A” peak indicates mutant allele; (b) rs6706649: in forward sequencing, “C” peak indicates the wild allele, and “T” peak indicates the mutant allele. Similarly, in reverse sequencing, “G” peak indicates the wild allele, and “A” peak indicates the mutant allele.

lower forearm blood flow and higher forearm vascular resistance when compared to healthy control. Besides, following oxidative stress, the C allele exhibited reduced *NRF2* expression compared with the “T” allele. The disparity in these findings with the present study could be mainly due to differences in ethnicity [35]. The present study was conducted in the South Indian population, whereas the aforementioned study was conducted in African Americans. Likely, rs35652124 SNP acts differently in diverse ethnic population, and samples according to which transcription factors are regulated [17].

Further, to validate the functional impacts of the rs35652124 TT genotype on insulin resistance and wound healing process, we have studied the transcriptional profile of *IL-10*, *TNF- α* , and *IL-6* in the study cohort based on their genotype. The decline of *IL-10* and elevation of *TNF- α* and *IL-6* are reported to be important regulators underlying insulin resistance and a slow nonhealing chronic wound process [36, 37]. Consistent with these findings, we found a reduced expression of *IL-10* and a significant increase in *TNF- α* and *IL-6*, in T2DM and DFU subjects with TT genotype. In summary, these findings confirm that the *NRF2* rs35652124 TT genotype dysregulate key genes involved in redox homeostasis and wound healing, and hence, it is a predisposing risk factor in the pathogenesis of T2DM and DFU.

This work represents an advance in biomedical science as it demonstrates that *NRF2* SNP rs35652124 serves as a diagnostic genetic marker for T2DM and DFU in the South Indian population and is associated with decreased tran-

scriptional levels of *NRF2* in these subjects. There are no investigations, so far, representing the clinical significance of this polymorphism in T2DM and DFU. The strength of this case-control study is that it was confined to subjects with the same ethnicity. However, the shortcoming of the study is its cross-sectional nature, which implies that no cause and effect relationship can be conveyed. Further studies are required in a diverse ethnic population to gather more evidence.

Data Availability

The data used to support the findings of this study are available from the corresponding author upon request.

Conflicts of Interest

The authors declare no conflict of interest.

Authors' Contributions

KMR and RK are responsible for the conception and design of this paper; TR performed the experiments and drafted the manuscript; DU, DA, KMR, and RK are responsible for the analysis and interpretation; and KMR, DA, and RK are responsible for the critical revision of the article.

Acknowledgments

This work was funded by the SRM Institute of Science and Technology, Kattankulthur, India. The authors acknowledge “SRM-DBT Partnership Platform for Contemporary Research Services and Skill Development in Advanced Life Sciences Technologies” (No. BT/PR12987/INF/22/205/2015), Department of Biotechnology, Govt. of India. This work was funded by Researchers Supporting Project number RSP-2020/165, King Saud University, Riyadh, Saudi Arabia.

References

- [1] K. Jeyaraman, T. Berhane, M. Hamilton, A. P. Chandra, and H. Falhammar, “Mortality in patients with diabetic foot ulcer: a retrospective study of 513 cases from a single Centre in the Northern Territory of Australia,” *BMC Endocrine Disorders*, vol. 19, no. 1, p. 1, 2019.
- [2] R. S. Most and P. Sinnock, “The epidemiology of lower extremity amputations in diabetic individuals,” *Diabetes Care*, vol. 6, no. 1, pp. 87–91, 1983.
- [3] L. Xiong, J. Xie, C. Song et al., “The activation of Nrf2 and its downstream regulated genes mediates the antioxidative activities of xueshuan xinmaining tablet in human umbilical vein endothelial cells,” *Evidence-based Complementary and Alternative Medicine*, vol. 2015, Article ID 187265, 7 pages, 2015.
- [4] S. M. U. Ahmed, L. Luo, A. Namani, X. J. Wang, and X. Tang, “Nrf2 signaling pathway: pivotal roles in inflammation,” *Biochimica et Biophysica Acta (BBA) - Molecular Basis of Disease*, vol. 1863, no. 2, pp. 585–597, 2017.
- [5] D. Sugumar, J. Saravanan, R. Emdormi, and T. Praveen, “An update on the role of Nrf2 and its activators in diseases associated with oxidative stress,” *Indian Journal of Pharmaceutical Sciences*, vol. 82, no. 2, pp. 184–192, 2020.
- [6] D. Sireesh, U. Dhamodharan, K. Ezhilarasi, V. Vijay, and K. M. Ramkumar, “Association of NF-E2 related factor 2 (Nrf2) and inflammatory cytokines in recent onset type 2 diabetes mellitus,” *Scientific Reports*, vol. 8, no. 1, 2018.
- [7] U. Dhamodharan, A. Karan, D. Sireesh et al., “Tissue-specific role of Nrf2 in the treatment of diabetic foot ulcers during hyperbaric oxygen therapy,” *Free Radical Biology & Medicine*, vol. 138, pp. 53–62, 2019.
- [8] F. P. Fabrizio, A. Sparaneo, D. Trombetta, and L. A. Muscarrella, “Epigenetic versus genetic deregulation of the KEAP1/NRF2 axis in solid tumors: focus on methylation and noncoding RNAs,” *Oxidative Medicine and Cellular Longevity*, vol. 2018, Article ID 2492063, 21 pages, 2018.
- [9] D. Umopathy, P. Balashanmugam, P. Vanniya Subramanyam et al., “Association of SNP rs7181866 in the nuclear respiratory factor-2 beta subunit encoding GABPB1 gene with obesity and type-2 diabetes mellitus in South Indian population,” *International Journal of Biological Macromolecules*, vol. 132, pp. 606–614, 2019.
- [10] U. Juttada, S. Kumpatla, R. Parveen, and V. Viswanathan, “TCF7L2 polymorphism a prominent marker among subjects with type-2-diabetes with a positive family history of diabetes,” *International Journal of Biological Macromolecules*, vol. 159, pp. 402–405, 2020.
- [11] S. Pichu, J. Sathiyamoorthy, S. Vimalraj, V. Viswanathan, and S. Chatterjee, “Impact of lysyl oxidase (G473A) polymorphism on diabetic foot ulcers,” *International Journal of Biological Macromolecules*, vol. 103, pp. 242–247, 2017.
- [12] K. Ezhilarasi, U. Dhamodharan, and V. Vijay, “BSMI single nucleotide polymorphism in vitamin D receptor gene is associated with decreased circulatory levels of serum 25-hydroxyvitamin D among micro and macrovascular complications of type 2 diabetes mellitus,” *International Journal of Biological Macromolecules*, vol. 116, pp. 346–353, 2018.
- [13] D. Umopathy, E. Krishnamoorthy, V. Mariappanadar, V. Viswanathan, and K. M. Ramkumar, “Increased levels of circulating (TNF- α) is associated with (-308G/A) promoter polymorphism of TNF- α gene in Diabetic Nephropathy,” *International Journal of Biological Macromolecules*, vol. 107, Part B, pp. 2113–2121, 2018.
- [14] H. Y. Cho, “Genomic structure and variation of nuclear factor (erythroid-derived 2)-like 2,” *Oxidative Medicine and Cellular Longevity*, vol. 2013, Article ID 286524, 24 pages, 2013.
- [15] J. M. Marzec, J. D. Christie, S. P. Reddy et al., “Functional polymorphisms in the transcription factor NRF2 in humans increase the risk of acute lung injury,” *The FASEB Journal*, vol. 21, no. 9, pp. 2237–2246, 2007.
- [16] C. Tonelli, I. I. C. Chio, and D. A. Tuveson, “Transcriptional regulation by Nrf2,” *Antioxidants & Redox Signaling*, vol. 29, no. 17, pp. 1727–1745, 2018.
- [17] G. Scutt, A. Overall, P. Bakrania et al., “The association of a single-nucleotide polymorphism in the nuclear factor (erythroid-derived 2)-like 2 gene with adverse drug reactions, multimorbidity, and frailty in older people,” *The Journals of Gerontology: Series A*, vol. 75, no. 6, pp. 1050–1057, 2020.
- [18] G. F. Korytina, L. Z. Akhmadishina, Y. G. Aznabaeva et al., “Associations of the NRF2/KEAP1 pathway and antioxidant defense gene polymorphisms with chronic obstructive pulmonary disease,” *Gene*, vol. 692, pp. 102–112, 2019.
- [19] E. J. Cordova, R. Velazquez-Cruz, F. Centeno, V. Baca, and L. Orozco, “The NRF2 gene variant, -653G/A, is associated with nephritis in childhood-onset systemic lupus erythematosus,” *Lupus*, vol. 19, no. 10, pp. 1237–1242, 2010.
- [20] M. Zhu, T. Zhou, G. Zu, and Z. Liang, “The NFE2L2rs35652124 polymorphism and the risk of Parkinson’s disease: a systematic review and meta-analysis,” *Neuroreport*, vol. 27, no. 12, pp. 901–905, 2016.
- [21] S. B. Catrina and X. Zheng, “Disturbed hypoxic responses as a pathogenic mechanism of diabetic foot ulcers,” *Diabetes/Metabolism Research and Reviews*, vol. 32, Supplement 1, pp. 179–185, 2016.
- [22] M. Schafer and S. Werner, “Oxidative stress in normal and impaired wound repair,” *Pharmacological Research*, vol. 58, no. 2, pp. 165–171, 2008.
- [23] K. Itoh, T. Chiba, S. Takahashi et al., “An Nrf2/small Maf heterodimer mediates the induction of phase II detoxifying enzyme genes through antioxidant response elements,” *Biochemical and Biophysical Research Communications*, vol. 236, no. 2, pp. 313–322, 1997.
- [24] Y. Tan, T. Ichikawa, J. Li et al., “Diabetic downregulation of Nrf2 activity via ERK contributes to oxidative stress-induced insulin resistance in cardiac cells in vitro and in vivo,” *Diabetes*, vol. 60, no. 2, pp. 625–633, 2011.
- [25] X. Wu, J. Huang, C. Shen et al., “NRF2 deficiency increases obesity susceptibility in a mouse menopausal model,” *PLoS One*, V. Souza-Mello, Ed., vol. 15, no. 2, article e0228559, 2020.

- [26] J. A. David, W. J. Rifkin, P. S. Rabbani, and D. J. Ceradini, "The Nrf2/Keap1/ARE pathway and oxidative stress as a therapeutic target in type II diabetes mellitus," *Journal Diabetes Research*, vol. 2017, article 4826724, pp. 1–15, 2017.
- [27] P. Canning, F. J. Sorrell, and A. N. Bullock, "Structural basis of Keap1 interactions with Nrf2," *Free Radical Biology and Medicine*, vol. 88, Part B, pp. 101–107, 2015.
- [28] M. N. Valcarcel-Ares, T. Gautam, J. P. Warrington et al., "Disruption of Nrf2 signaling impairs angiogenic capacity of endothelial cells: implications for microvascular aging," *The Journals of Gerontology. Series A, Biological Sciences and Medical Sciences*, vol. 67, no. 8, pp. 821–829, 2012.
- [29] X. Wang, H. Chen, J. Liu et al., "Association between the NF-E2 related factor 2 gene polymorphism and oxidative stress, anti-oxidative status, and newly-diagnosed type 2 diabetes mellitus in a Chinese population," *International Journal of Molecular Sciences*, vol. 16, no. 7, pp. 16483–16496, 2015.
- [30] A. Matana, P. G. Ziros, D. V. Chartoumpakis et al., "Rare and common genetic variations in the Keap1/Nrf2 antioxidant response pathway impact thyroglobulin gene expression and circulating levels, respectively," *Biochemical Pharmacology*, vol. 173, article 113605, 2020.
- [31] K. N. dos Santos, R. M. Florentino, A. França et al., "Polymorphism in the promoter region of NFE2L2 gene is a genetic marker of susceptibility to cirrhosis associated with alcohol abuse," *International Journal of Molecular Sciences*, vol. 20, no. 14, p. 3589, 2019.
- [32] P. Song, K. Li, L. Liu et al., "Genetic polymorphism of the Nrf2 promoter region is associated with vitiligo risk in Han Chinese populations," *Journal of Cellular and Molecular Medicine*, vol. 20, no. 10, pp. 1840–1850, 2016.
- [33] Y. Shimoyama, Y. Mitsuda, N. Hamajima, and T. Niwa, "Polymorphisms of Nrf2, an antioxidative gene, are associated with blood pressure in Japanese," *Nagoya Journal of Medical Science*, vol. 76, no. 1-2, pp. 113–120, 2014.
- [34] Y. Shimoyama, Y. Mitsuda, Y. Tsuruta, N. Hamajima, and T. Niwa, "Polymorphism of Nrf2, an antioxidative gene, is associated with blood pressure and cardiovascular mortality in hemodialysis patients," *International Journal of Medical Sciences*, vol. 11, no. 7, pp. 726–731, 2014.
- [35] E. D. Marczak, J. Marzec, D. C. Zeldin et al., "Polymorphisms in the transcription factor NRF2 and forearm vasodilator responses in humans," *Pharmacogenetics and Genomics*, vol. 22, no. 8, pp. 620–628, 2012.
- [36] V. de Oliveira Leal and D. Mafra, "Adipokines in obesity," *Clinica Chimica Acta*, vol. 419, pp. 87–94, 2013.
- [37] K. O. Galstyan, L. V. Nedosugova, N. S. Martirosian et al., "Modification of tumor necrosis factor- α and C-C motif chemokine ligand 18 secretion by monocytes derived from patients with diabetic foot syndrome," *Biology*, vol. 9, no. 1, p. 3, 2020.

Research Article

Investigation of Cytotoxicity Apoptotic and Inflammatory Responses of Biosynthesized Zinc Oxide Nanoparticles from *Ocimum sanctum* Linn in Human Skin Keratinocyte (Hacat) and Human Lung Epithelial (A549) Cells

Bader Almutairi, Gadah Albahser , Rafa Almeer , Nouf M. Alyami, Hanouf Almukhlafi, Khadijah N. Yaseen, Saad Alkahtani , and Saud Alarifi 

Department of Zoology, College of Science, King Saud University, Riyadh, Saudi Arabia

Correspondence should be addressed to Saud Alarifi; salarifi@ksu.edu.sa

Received 19 June 2020; Accepted 15 July 2020; Published 14 August 2020

Guest Editor: Madhukar Saxena

Copyright © 2020 Bader Almutairi et al. This is an open access article distributed under the Creative Commons Attribution License, which permits unrestricted use, distribution, and reproduction in any medium, provided the original work is properly cited.

Pristine and engineered metal nanoparticles are widely applied in various fields of industry, and as consequences, they are useful as well as harmful to human health and environment. This study aimed at synthesizing the green zinc oxide nanoparticles (ZnNPs) using the leaf extract of *Ocimum sanctum* Linn and assessing its toxicity on human skin epidermal (HaCaT) and human lung epithelial (A549) cells. The synthesized green ZnNPs (gZnNPs) were characterized by using dynamic light scattering (DLS) and a high-resolution transmission electron microscope. The average size of gZnNPs obtained was 62 nm with a spherical shape. The effects of gZnNPs on the viability of HaCaT and A549 cells were investigated using tetrazolium salt (MTT) for 24 h. We have seen more reduction of cell viability of A549 cells in comparison to HaCaT cells. The induction of intracellular reactive oxygen species (ROS) was measured using DCFDA assay and showed a slightly high intensity of green fluorescence in A549 than HaCaT cells. The different oxidative stress biomarkers such as ROS generation and lipid peroxide were increased, and GSH was decreased in a dose-dependent manner. The apoptotic and necrotic effect of gZnNPs in both cells was carried out using Annexin-V-FITC and propidium iodide staining. More apoptotic and necrotic cells were found at a higher concentration of gZnNPs exposure. Also, we determined the effect of gZnNPs at the molecular level by evaluating the apoptotic and inflammatory markers, in which gZnNPs downregulated Bcl2 and upregulated Bax, caspase-3, and TNF- α in HaCaT and A549 cells. Ultimately, gZnNPs exerted toxicity and apoptosis in HaCaT and A549 cells.

1. Introduction

Engineered nanoparticles are an inventive class of materials. Due to this reason, development of nanotechnology is used in different interdisciplinary areas, e.g., medical purposes and industry. In this field, the improvement of nanotechnology headed to the productions of nanoparticles (NPs), as contrast agents or in targeted treatments. Recently, due to their more applications in clinical purposes, the NPs are intensively investigated, and more development was done on new techniques to biological synthesize eco-friendly nanomaterials and on assessing their biological effects on living organisms [1]. The manufacturing techniques of eco-friendly NPs are

a challenge that made nanotechnology one of the most studied and well-financed domains of the last decades. Metal or metal oxide NPs are progressively used in dermatology and cosmetology. For example, ZnO and TiO₂ NPs have been extensively used to sunscreens since the 1980s to confer better ultraviolet (UV) protection than traditional inorganic sunscreens [2]. Natural antioxidants are in high demand for application as nutraceuticals, biopharmaceuticals, as well as a food additive [3]. *Ocimum sanctum* Linn is commonly known as Tulsi and is applied for the curing of various health indications. However, *Ocimum sanctum* has medicinal properties and used as herbal tea. Chandrasekaran et al. [4] have reported its signs of toxicity for 14 days in Wistar rats. In

the current investigation, the leaf extracts of *Ocimum sanctum* were used to biologically synthesize ZnONPs and mediate its toxicity involved various mechanisms, in particular the production of excess ROS. As it is well known, mitochondrial dysfunction is the major source of ROS overload [5]. Oxidative stress, apoptotic, and inflammatory response are key molecular mechanisms to induce toxic effects of exogenous substances [6, 7]. Oxidative stress mainly results from the generation of intracellular ROS. Excessive ROS causes the imbalance of oxidation and antioxidant system in the body, which may induce lipid peroxidation and change various enzymatic activities [8]. Malondialdehyde is one of the most important products of lipid peroxidation, which can be measured to reflect cell oxidative damage. However, antioxidant enzyme superoxide dismutase (SOD) that catalyzes SOD could catalyze superoxide anion radicals to oxygen and hydrogen peroxide, and then, catalase (CAT) catalyzes hydrogen peroxide to oxygen and water, helps to scavenge ROS and free radicals, and prevents the cells from an injury effectively. Studies showed that oxidative stress is often associated with the germination of inflammation. ROS generated by ZnNPs not only induced oxidative damage but also increased the synthesis of proinflammatory cytokines in human epithelial cells. Few studies have confirmed the harmful effects of gZnNPs on human skin epidermal cell lines. So, in this study, we will investigate the toxic effects of gZnNPs on HaCaT and A549 cells.

2. Materials and Methods

2.1. Chemical and Reagents. Green zinc oxide nanoparticle (gZnNPs) was prepared by using leaves extracts of *Ocimum sanctum* Linn plant. MTT [3-(4, 5-dimethylthiazol-2-yl)-2, 5-diphenyltetrazolium bromide], DCFH-DA, dimethyl sulfide, Annexin-V-FITC, and propidium iodide were purchased from Sigma-Aldrich (St. Louis, Missouri, United States). Dulbecco's modified Eagle's medium (DMEM), fetal bovine serum (FBS), and antibiotics were purchased from Gibco, USA.

2.2. Preparation of Leaves of *Ocimum sanctum* Extracts. The fresh leaves of *Ocimum sanctum* Linn were collected from the local area and washed with running tap water. Leaves were cut in small pieces, ground, and filtered using mesh (22 μm) and stored in the refrigerator for further use.

2.3. Green Synthesis of ZnNPs and Physical Characterization. The leaves extracts (50 g/l) were mixed to 5 g/l of zinc acetate in a conical flask and very well shaken. After 30 min, the reaction mixture was heated overnight at 60°C, and the ZnO NPs powder is obtained.

A measurement of synthesized gZnNPs was done by using a high-resolution transmission electron microscope (JEOL Inc., Tokyo, Japan) at an accelerating voltage 120 kV. The size of gZnNPs in water and culture medium were determined by DLS (Nano-Zeta Sizer-HT, Malvern, UK) as described by Alarifi et al. [9]. We have used 35 $\mu\text{g}/\text{ml}$ for DLS measurement because this is the maximum treatment concentration used to evaluate cell viability.

2.4. Establishment of Cell Lines and Exposure of gZnNPs. HaCaT and A549 cells were brought from American Type Culture Collection (ATCC), USA. These cells were cultured in DMEM with 10% FBS and 10000 U/ml antibiotics at 5% CO₂ incubator at 37°C. The cells at 80% confluence were subculture into 96 well plates, 6 well plates, and 25 cm² flasks according to designed experiments.

HaCaT and A549 cells were subcultured for one day before treatment to gZnNPs. The standard solution of gZnNPs was prepared in Milli-Q water at 1 $\mu\text{g}/\mu\text{l}$ and diluted according to the experimental dosage (0-35 $\mu\text{g}/\text{ml}$). Control cells were not exposed to NPs and considered as controls with each experiment.

2.5. Cell Viability Detection. The cell survival rates were measured by methylthiazol tetrazolium (MTT) assay after 24 hours of exposure. Briefly, HaCaT and A549 cells in good growth conditions were collected and seeded into 96-well plates at 5×10^3 cells/well. Four multiple wells were prepared for each concentration. After adhesion, the cells were exposed to various concentrations of gZnNPs (0, 2, 6, 12, 25, and 35 $\mu\text{g}/\text{ml}$). Meanwhile, an equal volume of the medium was used as a blank control, and cell suspension alone as controls. After exposure for 24 h, 10 μl MTT (5 mg/ml) was added into each well and cultured for another 4 hours. Then, 100 μl SDS-isopropanol-HCL (triple solution) was added to each well and placed overnight at 37°C. The absorbance at 570 nm was detected by a microplate reader (BioTek, USA) to calculate cell viability.

2.6. Estimation of Intracellular ROS Production. Formation of ROS in HaCaT and A549 cell lines due to gZnNPs (0, 6, 12, 25, and 35 $\mu\text{g}/\text{ml}$) treatment for 24 h was determined according to the method [10]. Briefly, 1×10^4 HaCaT and A549 cells were grown in 96-well black culture plates and incubated in a CO₂ incubator at 37°C for 24 h for attachment. Different concentrations of gZnNPs were added to the culture plates of HaCaT and A549 cells for 24 h. After exposure, the culture plates were washed with PBS, and 10 μM DCFH-DA was mixed per well at 37°C for 60 minutes. After incubation, the plate was washed and the fluorescence intensity was read at 485 nm excitation and 520 nm emissions using the microplate reader (Synergy-H1; BioTek). Data were represented as obtained fluorescence intensity of exposed and control wells.

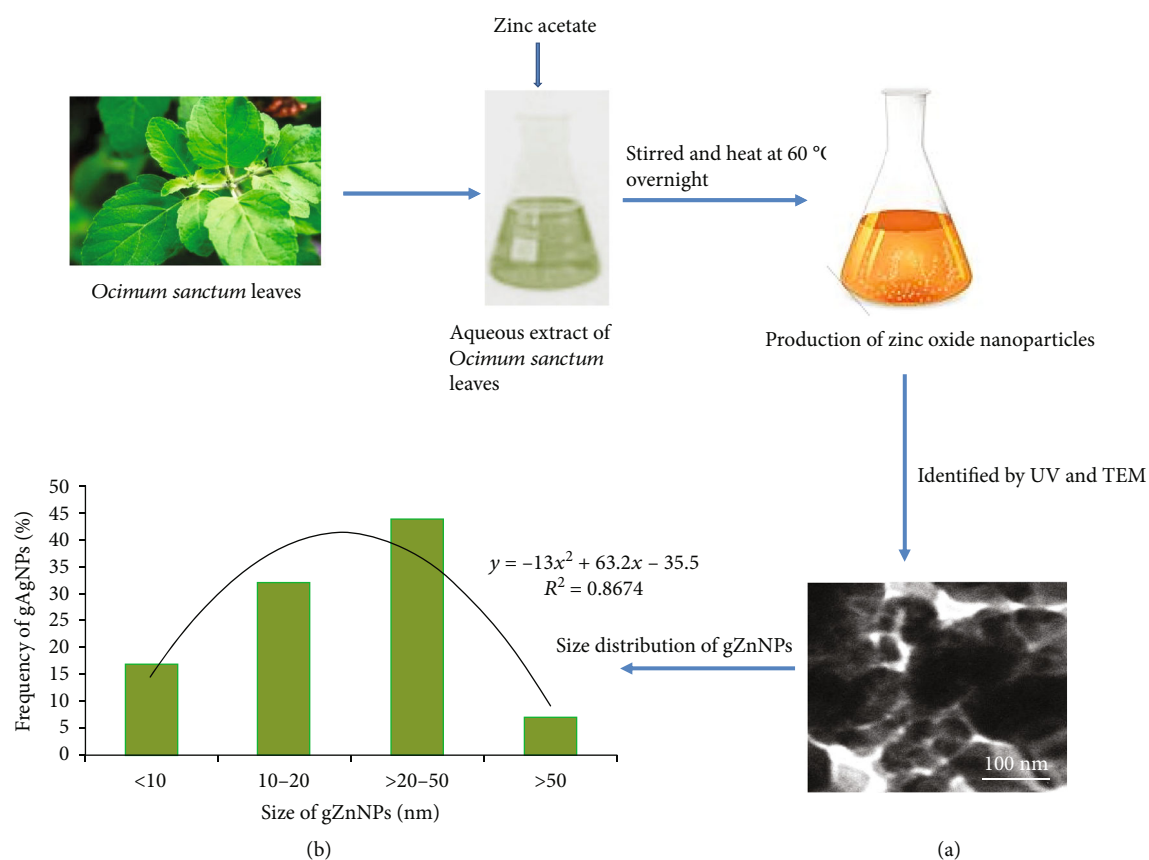
A parallel set of experiments was carried out in a 6-well culture plate, and DCF fluorescence images of cells were captured by using a fluorescence microscope (Olympus CKX 41; Olympus: Center Valley, Pennsylvania, USA).

2.7. Detection of MDA Content and GSH Activities. After treatment with gZnNPs (0, 6, 12, 25, and 35 $\mu\text{g}/\text{ml}$) for 24 h, the cells were collected by 0.25% trypsin and split by ultrasonic crushing. After that, the cell samples were used for the next detection. The content of GSH and the MDA was measured according to the instruction of Cayman Chemical kits.

2.8. Caspase-3 Activity. Caspase-3 enzymes play a significant role in cell death. Caspase-3 enzymes were determined in gZnNPs (0, 6, 25, and 35 $\mu\text{g}/\text{ml}$) exposed and control cells by using the BioVision colorimetric assay kits.

TABLE 1: Primer sequences and theoretical amplification length.

Genes	Orientation primer	Sequences (5' to 3')
Bcl-2	Forward-	ATGTGTGTGGAGACCGTCAA
	Reverse-	GCCGTACAGTTCCACAAAGG
BAX	Forward-	ATGTTTTCTGACGGCAACTTC
	Reverse-	AGTCCAATGTCCCAGCCCAT
Caspase-3	Forward-	TGTTTTGTGTGCTTCTGAGCC
	Reverse-	CACGCCATGTCATCATCAAC
TNF- α	Forward-	AAGGACACCATGAGCACTGAAAGC
	Reverse-	AGGAAGGAGAAGAGGCTGAGGAAC
β -Actin	Forward-	CCTGGCACCCAGCACAAAT
	Reverse-	GGCCCGGACTCGTCGCATAC

FIGURE 1: Schematic diagram of green synthesis of zinc oxide nanoparticles (gZnNPs) using zinc acetate salt and *Ocimum sanctum* leaf extract. (a) TEM image of gZnNPs. (b) Size distribution of gZnNPs (%).TABLE 2: Hydrodynamic size and zeta potential of gZnNPs in different dispersion medium. Data represent the mean \pm SE of three independent experiments.

Nanopowder	Dispersion media	DLS mean \pm SE (nm)	Zeta potential \pm SE (mV)
gZnNPs	d-H ₂ O	140 \pm 1.0	~ 10.2 \pm 0.8
	DMEM/supplemented media	155 \pm 2	~ 9.0 \pm 1.6

2.9. Analysis of Apoptosis Using FCM. The apoptotic and necrotic HaCaT and A549 cells due to gZnNP (0, 6, 25, and 35 μ g/ml) exposure were detected using Annexin-V-FITC/PI staining through flow cytometer (Becton-Dickinson Immu-

nocytometry Systems, Sunnyvale, CA, USA). The cells were collected by trypsin enzyme and washed with PBS and resuspended in binding buffer. Annexin-V-FITC (5 μ l) and PI (5 μ l) were mixed to cell suspension (500 μ l) and put in the

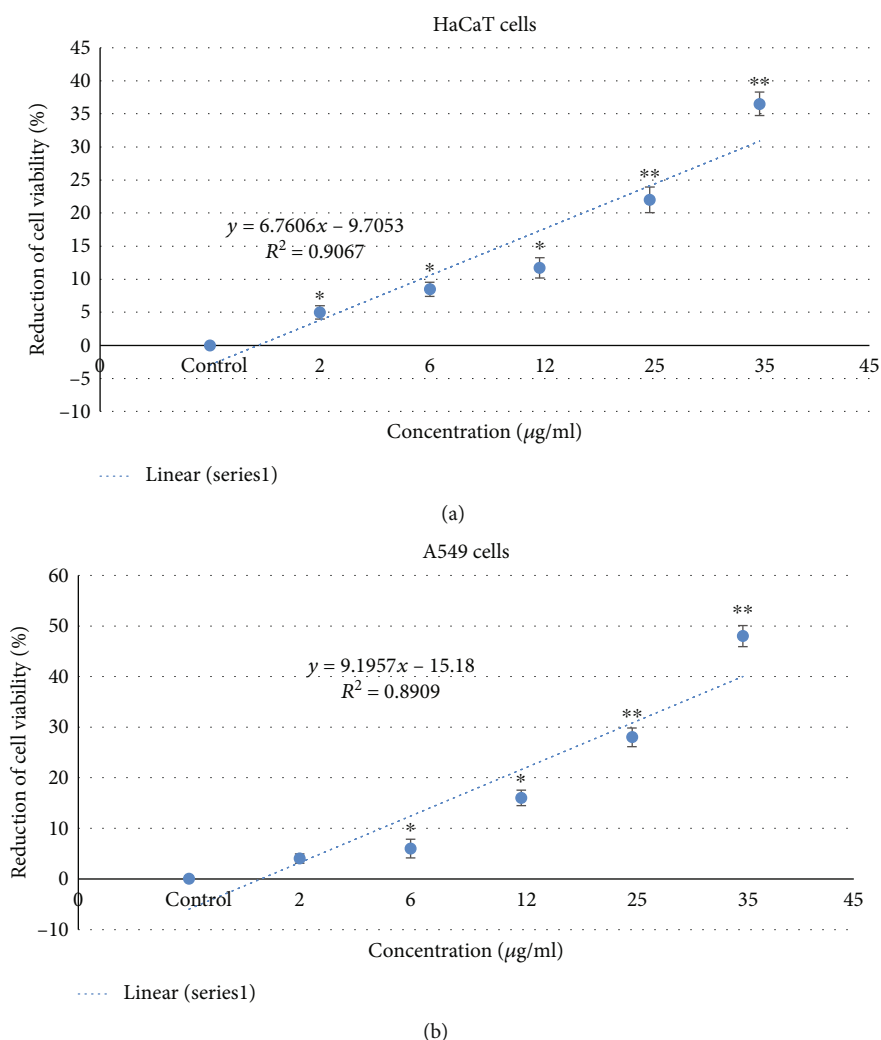


FIGURE 2: Cytotoxicity of gZnNPs on HaCaT and A549 cells for 24 h, as measured by MTT assay. Each value represents the mean \pm SE of three experiments. $n = 3$, * $p < 0.05$, ** $p < 0.01$ vs. control.

dark for 30 minutes at room temperature. Fluorescence emitted by Annexin-V-FITC and DNA-bound propidium iodide in each event were detected as red fluorescence, respectively. Results were analyzed by the FACS Diva 6.1.2 software.

2.10. RNA Isolation and RT qPCR. The total RNA was extracted from gZnNP- (0, 6, 25, and 35 $\mu\text{g/ml}$) treated HaCaT and A549 cells using the RNAiso Plus reagent (Takara, China) after treatment for 24 h, and the concentration was measured at the absorbance of 260 nm by NanoDrop 2000C spectrophotometer (Thermo Scientific, Waltham, Massachusetts). Then, the total RNA was reverse-transcribed into single-strand cDNA using the PrimeScript RT reagent kit (Takara, China). The gene expression levels were quantified using a SYBR Premix Ex Tap II Kit in the IQ5 Real-Time PCR Detection System (Bio-Rad, USA) under the conditions of heating at 95°C for 30 s, 40 cycles of denaturing at 95°C for 5 s, annealing at 55–60°C for 30 s, and extension at 72°C for 30 s. The primer sequences are shown in Table 1, β -actin was used as the internal reference, and

the relative mRNA expression was calculated by using the $2^{-\Delta\Delta C_t}$ method.

2.11. Western Blot Assay. HaCaT and A549 cells were treated with gZnNPs (0, 25, and 35 $\mu\text{g/ml}$) for 24 h, and after exposure, the cell lysate was prepared in RIPA buffer (ab156034). The cell lysate was centrifuged at 13000 rpm, 4°C for 30 min, and the supernatant was used for protein expressions. The concentration of protein was evaluated by the Bradford method [11]. Protein (20 μg) was migrated on the gel and transferred to a PVDF membrane (Bio-Rad, Laboratories Inc., Berkeley, CA, USA). The PVDF membrane was incubated with different mouse monoclonal antibody against β -actin (1:12000 dilutions, Abcam, Cambridge, UK), Bcl2 (1:500 dilutions, Santa Cruz), Bax (1:1000 dilutions, Antibodies-online), Caspase-3 (1:500 dilutions, Cayman), and TNF- α (1:500 dilutions, Santa Cruz) for 24 h at 4°C.

Secondary antibody HRP-conjugated goat anti-mouse IgG (H + L) antibody (1:2000 dilutions Bio-Rad) was used.

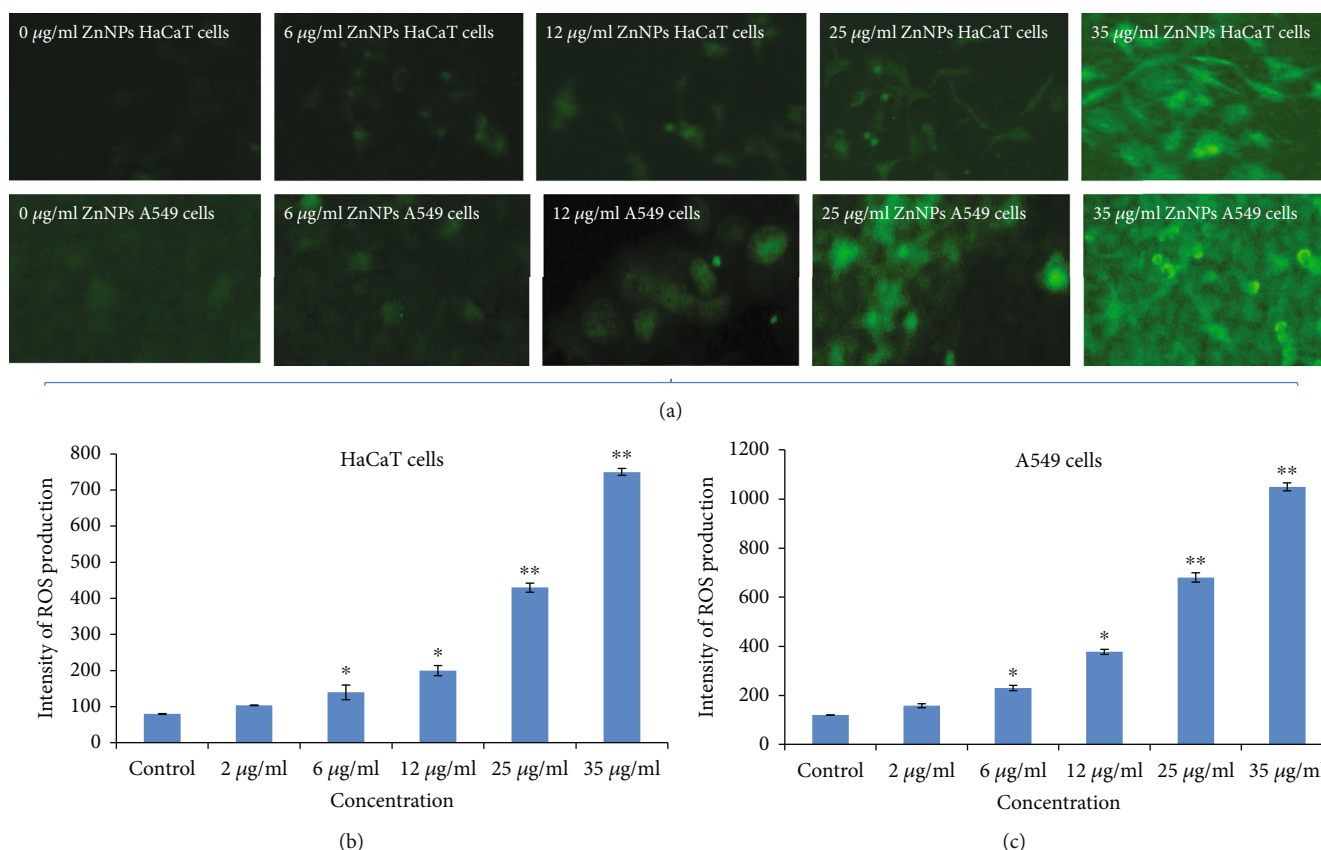


FIGURE 3: (a) Photomicrograph of green fluorescence (DCF intensity) in HaCaT and A549 cells after exposure to gZnNPs for 24 h. (b) Intracellular intensity of ROS production in HaCaT cells (c). Intracellular intensity of ROS production in A549 cells. Each value represents the mean \pm SE of three experiments. * $p < 0.05$ and ** $p < 0.01$ vs. control.

Immunoreactive bands were detected using an EZ west Lumi plus (ATTO Corporation, Tokyo, Japan), which is a chemiluminescent substrate to detect HRP on the western blotting membrane. The luminescence intensity (optical density) of the target protein bands was quantified using Lumino Graph 2 (ATTO Corporation). All protein expression levels were normalized to the levels of β -actin protein expression in each band.

2.12. Statistical Analysis. The data were analyzed by the SPSS 24.0 software (IBM) and expressed as mean \pm standard deviation (SD). Differences between the groups were determined by a one-way ANOVA test with the least-significant difference test. Values of $p < 0.05$ were considered statistically significant.

3. Results

3.1. Characterization of gZnNPs. Biosynthesized gZnNPs were characterized using HR-TEM and DLS (Figure 1). The TEM image of gZnNPs was presented in Figure 1(a). The average diameter of gZnNPs with spherical shape was 58.5 ± 2.5 nm (Figure 1(b)). The size of gZnNPs in dH_2O and culture media was 140 ± 1.0 nm and 155 ± 2 nm. The zeta potential of NPs in dH_2O and culture media were $\sim 10.2 \pm 0.8$ mV and $\sim 9.0 \pm 1.6$ mV (Table 2).

3.2. Cytotoxicity. Cell viability of HaCaT and A549 cells were determined by the MTT test, and the results are presented in Figures 2(a) and 2(b). We have observed the reduction of cell viability in both cells in concentration in a dependent manner, and the A549 cell viability is more reduced than HaCaT cells Figures 2(a) and 2(b). We have found the reduction of cell viability as 0.02, 5%, 8.5%, 11.72%, 22%, and 36.5% in HaCaT cells (Figure 2(a)) and 0.03, 4%, 6%, 16%, 28%, and 48% in A549 cells (Figure 2(b)) at 0, 2, 6, 12, 25, and 35 $\mu\text{g/ml}$ gZnNPs, respectively.

3.3. Oxidative Stress. ROS production in HaCaT and A549 cells due to gZnNPs exposure was determined, and its generation depends on the concentration of NPs. The generation of ROS was measured by using DCFDA, and it was oxidized in cells and formed DCF fluorescent compound. High intensity of green fluorescence demonstrates more generation of ROS in cells. We have seen more generation of ROS in A549 cells than HaCaT cells (Figures 3(a)–3(c)). The generation of ROS was as DCF intensity was more in A549 cells (Figure 3(b)) than HaCaT cells (Figure 3(c)).

Meanwhile, LPO and GSH were determined and compared with the control group, the activities of LPO was significantly increased in HaCaT (Figure 4(a)) and A549 cells (Figure 4(b)), and the GSH level was decreased in HaCaT (Figure 4(c)) and A549 cells (Figure 4(d)) at 35 $\mu\text{g/ml}$ after exposing ZnNPs.

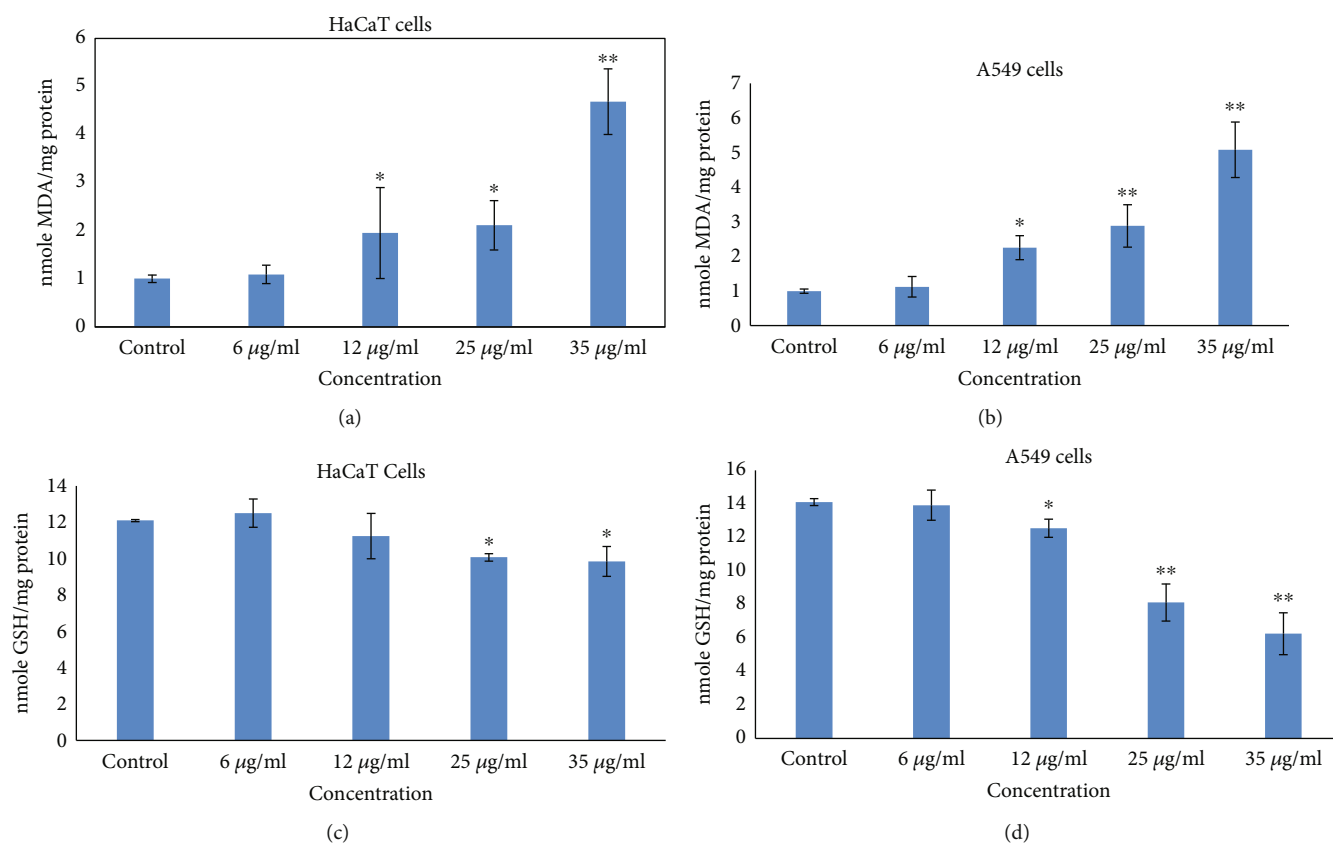


FIGURE 4: Oxidative stress biomarkers after exposure to gZnNPs on HaCaT and A549 cells for 24 h. (a) LPO in HaCaT. (b) LPO in A549 cells (c). GSH in HaCaT cells. (d) GSH in A549 cells. Each value represents the mean \pm SE of three experiments. * $p < 0.05$ and ** $p < 0.01$ vs. control.

3.4. Detection of Apoptotic. The activity of caspase-3 was calculated in HaCaT and A549 cells. Activities of caspase-3 were increased according to concentration dependence, and its level was more in A549 cell than HaCaT cells (Figure 5(h)). We have confirmed the apoptotic effect of NPs on both cells using Annexin-V-FITC and PI staining, and the cell scatter diagram of cell distribution is shown in Figures 5(a)–5(g). Analysis of the percentage of early and late apoptotic cells was determined by (FACS) as shown in Figure 5(g). The early and late apoptosis rates were 44.65 in A549 cells and 29.84% in HaCaT cells at gZnNPs (35 µg/ml) exposure, respectively, compared with the control group (Figure 5(g)).

3.5. mRNA Expressions in HaCaT and A549 Cells. The mRNA expressions of Bax, Bcl2, caspase-3, and TNF- α were identified to confirm apoptotic and inflammatory effects of gZnNPs (Figure 6). Compared with the control group, the mRNA expressions of Bax, caspase-3, and TNF- α were increased while expression of Bcl2 was decreased at 35 µg/ml gZnNPs group in HaCaT (Figure 7(a)) and A549 cells (Figure 7(b)).

3.6. Western Blot Analysis. The expression of apoptotic and inflammatory proteins in HaCaT and A549 cells after gZnNPs exposure was determined using western blot analysis. In HaCaT cells, gZnNPs reduced in Bcl2 protein expression (Figures 6(a) and 6(b)) and increased expres-

sion of Bax, caspase-3, TNF- α , and IL-6 as the compared control group (Figures 6(a) and 6(b)). Also, similar effects of gZnNPs on the expression of apoptotic and inflammatory proteins were observed in A549 cells (Figures 6(a) and 6(b)). The results indicated higher expressions of apoptotic and inflammatory protein in A549 cells than HaCaT cells (Figures 6(a) and 6(b)).

4. Discussion

Nanosize particles and dust are key risk factors for respiratory diseases and distribute in ambient air at significant levels. Nanotechnology is an inventive area of science with more application of new materials. In this study, ZnNPs was synthesized using the extract of *Ocimum* leaves and used to explore the potential influence of exposure to ZnNPs on the skin and pulmonary inflammation in HaCaT and A549 cells, respectively. TEM analysis explored that the average size of synthesized ZnONPs was 58.5 ± 2.5 nm with a face-centered cubic structure with a spherical shape (Figure 1). Moosa et al. [12] and Ahmed et al. [13] reported that the size of synthesized nanoparticles depends upon the plant extract volume. No cytotoxicity was observed at a lower concentration, while exerting clear cytotoxic effects at higher concentration of gZnNPs (at 35 µg/ml) for 24 h in HaCaT and A549 cells. These results suggested the cytotoxic effects of gZnNPs to some extent. Alarifi et al. [14] reported zinc oxide

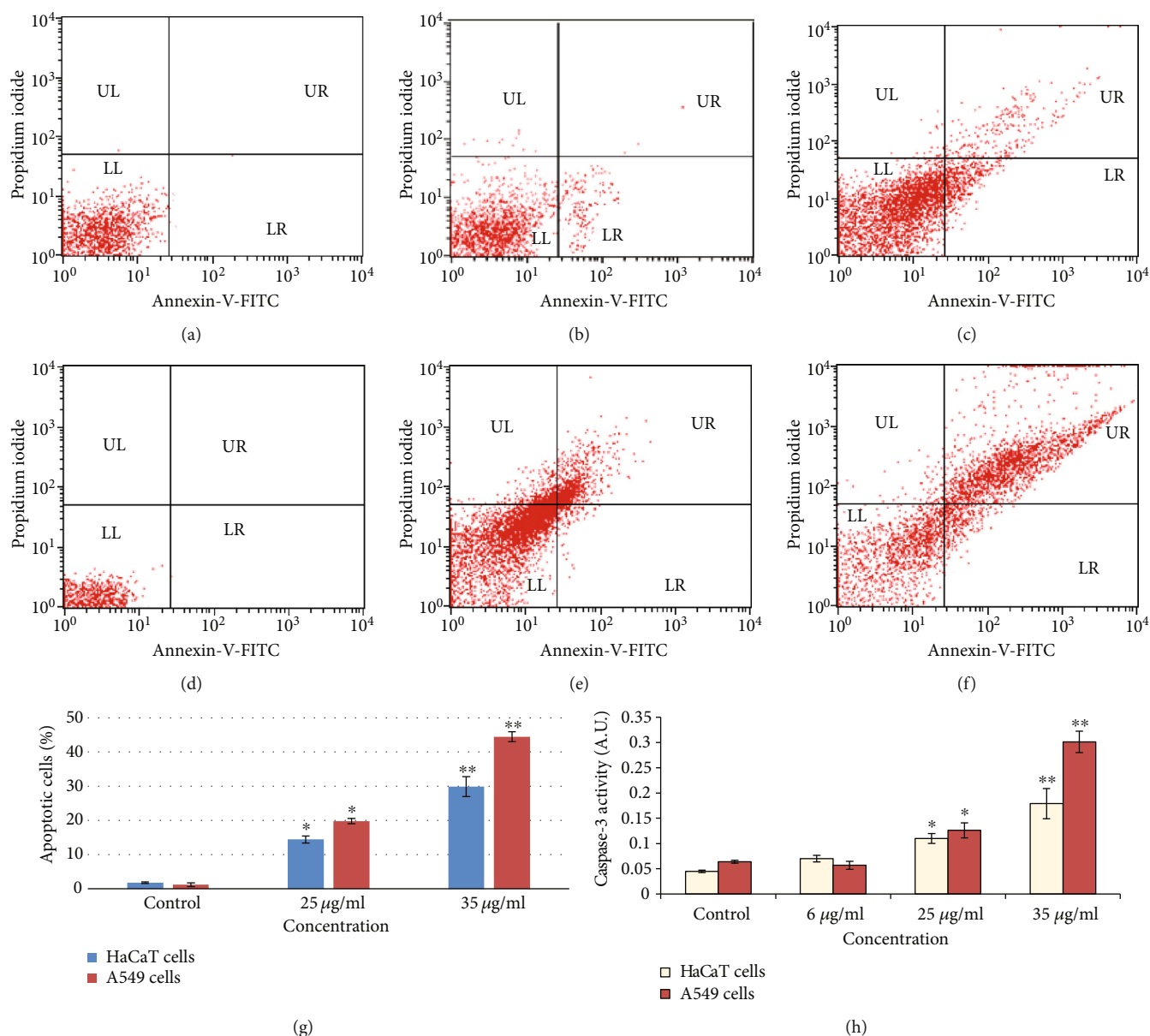


FIGURE 5: Scatter diagram after treatments of gZnNPs to HaCaT and A549 cells for 24 h. (a) HaCaT cells at 0 $\mu\text{g/ml}$. (b) HaCaT cells at 25 $\mu\text{g/ml}$. (c) HaCaT cells at 35 $\mu\text{g/ml}$. (d) A549 cells at 0 $\mu\text{g/ml}$. (e) A549 cells at 25 $\mu\text{g/ml}$. (f) A549 cells at 35 $\mu\text{g/ml}$. (g) Percentage of early and late apoptotic cells after treatment of ZnNPs (0, 25, and 35 $\mu\text{g/ml}$) for 24 h. (h) Caspase-3 activity after treatment of ZnNPs (0, 6, 25, and 35 $\mu\text{g/ml}$) for 24 h. Data represents the mean \pm SE of three experiments. * $p < 0.05$ and ** $p < 0.01$ vs. control.

nanoparticle (at 20 $\mu\text{g/ml}$) induced cytotoxicity, oxidative stress, and apoptosis in malignant human skin melanoma cell line. Also, this study showed that gZnNPs inhibited cell viability more in A549 cells than HaCaT cells. Furthermore, gZnNPs showed a low reduction of cell viability in HaCaT and A549 cells than the reduction of cell viability in A375 cells due to ZnONP exposure. This might occur in the presence of an extract of *Ocimum sanctum*. Gautam and Goel [15] reported that 50% ethanol extract of *Ocimum sanctum* leaves was nontoxic after its acute and subacute oral administrations mice. Nowadays, biosynthesized metallic nanoparticles using plant extract have received more attention due to simple and viable alternative against chemical and physical methods with their potential applications in nanomedicine.

Zinc oxide nanoparticles were synthesized using *Laurus nobilis* L leaf aqueous extract and two different zinc salts [16] and showed antibacterial activity [17]. In this experiment, we have investigated the generation of intracellular reactive oxygen species, and its levels increase in a dose-dependent manner; subsequently, ROS induction was more in A549 cell than HaCaT cells. Conformably, the current results showed significant generations of ROS and MDA by ZnNPs in A549 and HaCaT cells. Nanoparticles induced free radicals which may damage the cells through oxidative stress mechanism. The generation of intracellular ROS deteriorates the lipid membrane of target cells by the formation of malondialdehyde molecule, and this is known as lipid peroxidation [18]. In this study, LPO activity was observed more in A549

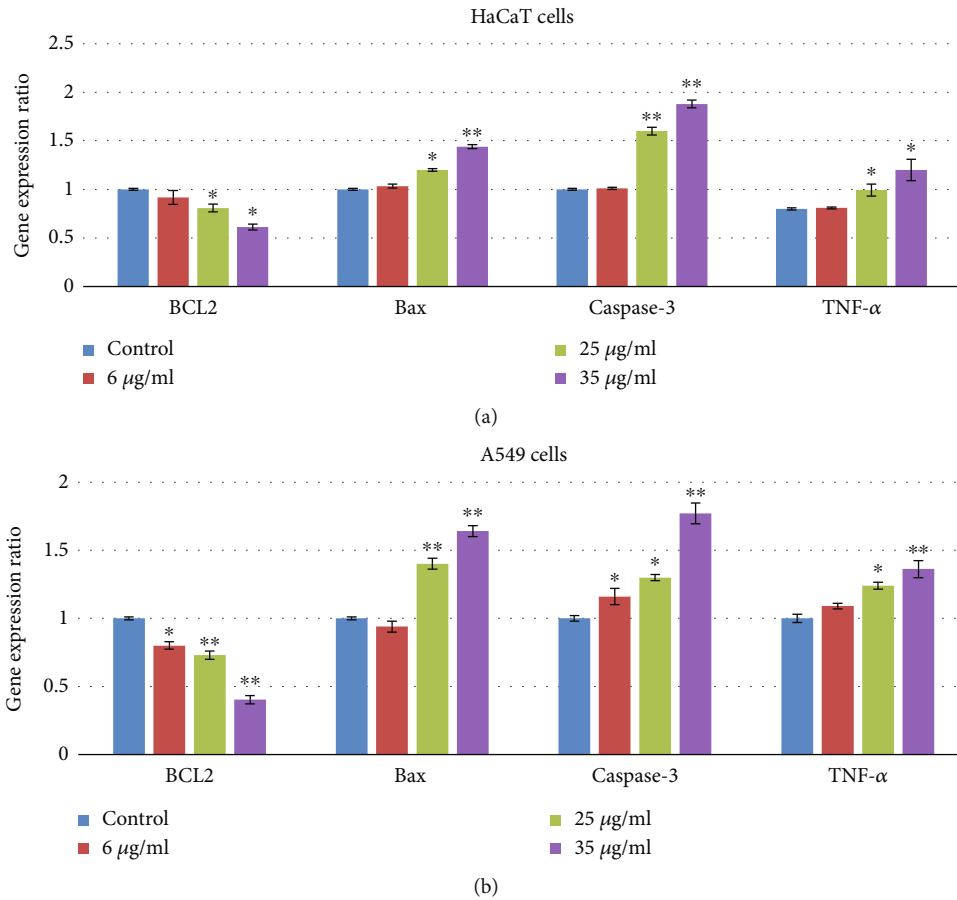


FIGURE 6: ZnNPs induce apoptosis and inflammatory response of HaCaT and A549 cells. Western blot analysis was carried out to assess apoptosis and inflammatory response-related protein expression in HaCaT and A549 cells. β -Actin was used as an internal reference. ZnNPs significantly increased the expression of Bax, caspase-3, and TNF- α and decreased the expression of Bcl-2 at a concentration 35 $\mu\text{g/ml}$ (a, b). Data represents the mean \pm SE of three experiments. * $p < 0.05$ and ** $p < 0.01$ vs. control.

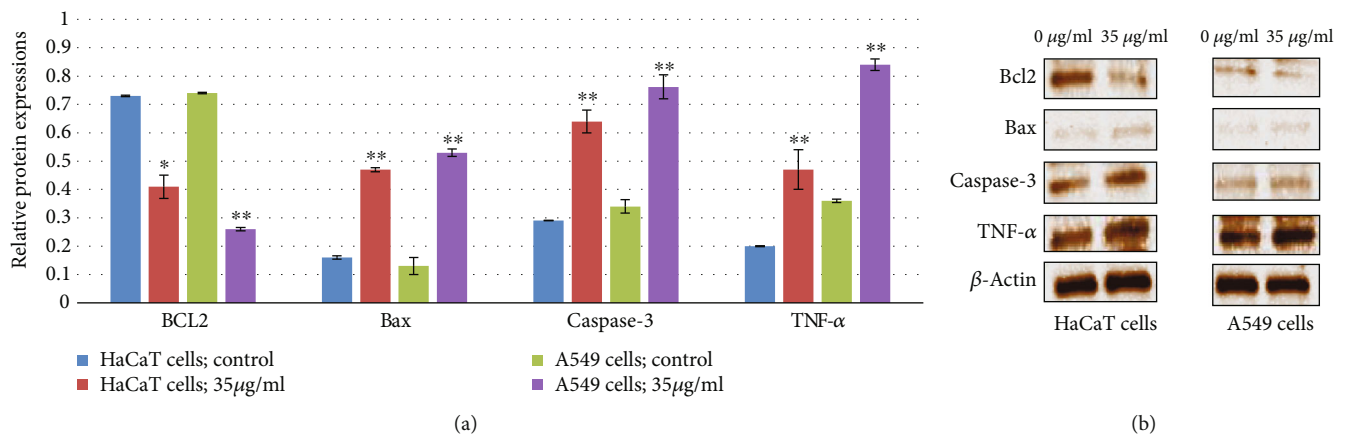


FIGURE 7: ZnNPs induce apoptosis and inflammatory response of HaCaT and A549 cells. mRNA expression analysis was carried out to assess apoptosis and inflammatory response-related gene expression in HaCaT cells (a) and A549 cells (b). β -Actin was used as an internal reference. ZnNPs significantly increased the gene expression of Bax, caspase-3, and TNF- α and decreased the expression of Bcl-2 in a concentration-dependent manner (a, b). Data represents the mean \pm SE of three experiments. * $p < 0.05$ and ** $p < 0.01$ vs. control.

than in HaCaT cells. ROS has been linked in different mechanisms, viz. damaging of nuclear components (DNA and RNA), protein, interference of cellular signaling pathways, and alteration in gene expression, and ultimately, the mech-

anism of cell growth was stopped [18]. Interestingly, among these two cell types, A549 cells were more sensitive than HaCaT cells. Liu et al. [19] found that particulate matters increased intracellular ROS level and induced oxidative stress

via the activation of IL-6/AKT/STAT3/NF- κ B signaling pathway in lung epithelial cells. To confirm whether proliferation of cell was inhibited by the apoptotic response, we have determined apoptotic cells by using Annexin-V-FITC and PI staining after exposure to gZnNPs. The gZnNP-induced apoptosis was led by the activation of caspase-3, which is observed at 35 μ g/ml nanoparticle exposure by evaluation of caspase-3 activity by the enzyme-linked immunosorbent assay (ELISA) and immunoblotting. Activation of caspase-3 was accompanied by downregulation of bcl2 and upregulation of Bax proteins. All these events indicated the signs of apoptosis, which were observed more in A549 cells after exposure to NPs.

It is a more important finding that A549 cells are more susceptible to gZnNPs than HaCaT cells. In the future, we will do investigations about the mechanism of toxicity due to gZnNPs in in vivo experiments.

Data Availability

All data generated or analyzed during this study are included in the article.

Conflicts of Interest

The authors declare that they have no conflicts of interest.

Acknowledgments

The authors extend their appreciation to the Deanship of Scientific Research at King Saud University for funding this work through research group project RGP-180.

References

- [1] S. Hajebi, M. H. Tabrizi, M. N. Moghaddam, F. Shahraki, and S. Yadamani, "Rapeseed flower pollen biogreen synthesized silver nanoparticles: a promising antioxidant, anticancer and antiangiogenic compound," *JBIC Journal of Biological Inorganic Chemistry*, vol. 24, no. 3, pp. 395–404, 2019.
- [2] S. Q. Wang and I. R. Tooley, "Photoprotection in the era of nanotechnology," *Seminars in Cutaneous Medicine and Surgery*, vol. 30, no. 4, pp. 210–213, 2011.
- [3] W. J. Craig, "Health-promoting properties of common herbs," *The American Journal of Clinical Nutrition*, vol. 70, no. 3, pp. 491S–499S, 1999.
- [4] C. V. Chandrasekaran, H. S. Srikanth, M. S. Anand, J. J. Allan, M. M. H. Viji, and A. Amit, "Evaluation of the mutagenic potential and acute oral toxicity of standardized extract of *Ocimum sanctum*," *Human & Experimental Toxicology*, vol. 32, no. 9, pp. 992–1004, 2013.
- [5] P. T. Schumacker, M. N. Gillespie, K. Nakahira et al., "Mitochondria in lung biology and pathology: more than just a powerhouse," *American Journal of Physiology. Lung Cellular and Molecular Physiology*, vol. 306, no. 11, pp. L962–L974, 2014.
- [6] S. De Prins, E. Dons, M. Van Poppel et al., "Airway oxidative stress and inflammation markers in exhaled breath from children are linked with exposure to black carbon," *Environment International*, vol. 73, pp. 440–446, 2014.
- [7] I. H. El-Sayed, X. Huang, and M. A. El-Sayed, "Surface plasmon resonance scattering and absorption of anti-EGFR antibody conjugated gold nanoparticles in cancer diagnostics: applications in oral cancer," *Nano Letters*, vol. 5, no. 5, pp. 829–834, 2005.
- [8] C. Zhuang, Y. Wang, Y. Zhang, and N. Xu, "Oxidative stress in osteoarthritis and antioxidant effect of polysaccharide from *Angelica sinensis*," *International Journal of Biological Macromolecules*, vol. 115, pp. 281–286, 2018.
- [9] S. Alarifi, D. Ali, and S. Alkahtani, "Oxidative stress-induced DNA damage by manganese dioxide nanoparticles in human neuronal cells," *BioMed Research International*, vol. 2017, Article ID 5478790, 10 pages, 2017.
- [10] F. Alzahrani, M. Khadijah, D. Ali, and S. Alarifi, "Apoptotic and DNA-damaging effects of yttria-stabilized zirconia nanoparticles on human skin epithelial cells," *International Journal of Nanomedicine*, vol. 14, pp. 7003–7016, 2019.
- [11] M. M. Bradford, "A rapid and sensitive method for the quantitation of microgram quantities of protein utilizing the principle of protein dye binding," *Analytical Biochemistry*, vol. 72, no. 1-2, pp. 248–254, 1976.
- [12] A. A. Moosa, A. M. Ridha, and M. Al-Kaser, "Process parameters for green synthesis of silver nanoparticles using leaves extract of Aloe vera plant," *International Journal of Multidisciplinary and Current Research*, vol. 3, pp. 966–975, 2015.
- [13] S. Ahmed, M. Ahmad, B. L. Swami, and S. Ikram, "A review on plants extract mediated synthesis of silver nanoparticles for antimicrobial applications: a green expertise," *Journal of Advanced Research*, vol. 7, no. 1, pp. 17–28, 2016.
- [14] S. Alarifi, D. Ali, S. Alkahtani et al., "Induction of oxidative stress, DNA damage, and apoptosis in a malignant human skin melanoma cell line after exposure to zinc oxide nanoparticles," *International Journal of Nanomedicine*, vol. 8, pp. 983–993, 2013.
- [15] M. K. Gautam and R. K. Goel, "Toxicological study of *Ocimum sanctum* Linn leaves: hematological, biochemical, and histopathological studies," *Journal of Toxicology*, vol. 2014, Article ID 135654, 9 pages, 2014.
- [16] S. Fakhari, M. Jamzad, and H. K. Fard, "Greensynthesis of zinc oxide nanoparticles: a comparison," *Green Chemistry Letters and Reviews*, vol. 12, no. 1, pp. 19–24, 2019.
- [17] M. M. Chikkanna, S. E. Neelagund, and K. K. Rajashekarappa, "Green synthesis of zinc oxide nanoparticles (ZnO NPs) and their biological activity," *SN Applied Sciences*, vol. 1, no. 1, p. 117, 2019.
- [18] T.-Y. Wang, M. D. J. Libardo, A. M. Angeles-Boza, and J.-P. Pellois, "Membrane oxidation in cell delivery and cell killing applications," *ACS Chemical Biology*, vol. 12, no. 5, pp. 1170–1182, 2017.
- [19] C.-W. Liu, T.-L. Lee, Y.-C. Chen et al., "PM2.5-induced oxidative stress increases intercellular adhesion molecule-1 expression in lung epithelial cells through the IL-6/AKT/STAT3/NF- κ B-dependent pathway," *Particle and Fibre Toxicology*, vol. 15, no. 1, p. 4, 2018.

Research Article

Exploration of Cadmium Dioxide Nanoparticles on Bioaccumulation, Oxidative Stress, and Carcinogenic Potential in *Oreochromis mossambicus* L.

Monera A. Al-Abdan,¹ May N. Bin-Jumah,¹ and Saud Alarifi ²

¹Department of Biology, College of Science, Princess Nourah Bint Abdulrahman University, Riyadh, Saudi Arabia

²Department of Zoology, College of Science, King Saud University, Riyadh, Saudi Arabia

Correspondence should be addressed to Saud Alarifi; salarifi@ksu.edu.sa

Received 2 June 2020; Accepted 29 June 2020; Published 26 July 2020

Guest Editor: Khuram Ahmad

Copyright © 2020 Monera A. Al-Abdan et al. This is an open access article distributed under the Creative Commons Attribution License, which permits unrestricted use, distribution, and reproduction in any medium, provided the original work is properly cited.

The field of nanotechnology is rapidly expanding with the advancement of novel nanopesticide and nanofertilizers that have the potential for revolutionizing applications in the agricultural industry. Here, we have done chronic toxicity of cadmium dioxide nanoparticles (CdONPs) on fish *Oreochromis mossambicus* (*O. mossambicus*) using oxidative stress and genotoxic biomarkers. In this current study, the value of LC₅₀-96 hr of CdONPs has observed 40 µg/ml for *O. mossambicus*. The three sublethal concentrations, e.g., 4, 10, and 20 µg/ml were selected based on the LC₅₀ value. The fishes were treated to the above concentration of CdONPs for 21 days and were harvested at 1, 7, 14, and 21 days for evaluation of clastogenicity, mutagenicity, and genotoxicity of NPs. Generally, significant effects ($p < 0.01$) were observed as a dose and duration of exposure. It was observed that lipid peroxidation (LPO) was increased and glutathione was decreased in both tissues. Micronuclei (MNi) were produced significantly in peripheral blood on 21 days at maximum concentration. A similar trend was seen in the damage of DNA with the same manner in terms of the percentage of tail DNA in the lymphocyte, gills, and kidney cells. This study explored the application oxidative stress, comet assay, and micronucleus assay for in situ aquatic laboratory studies using fish *O. mossambicus* for screening the ecomutagenic and genotoxic potential of environmental pollutants.

1. Introduction

Engineered nanoparticles are parts of daily life. The application of heavy metals nanoparticles is increasing all over the world. They are incorporated into a wide array of products including sunscreens, clothing, electronics, paints, and automobiles. The continued development and expansion of industrial applications for nanoparticles ensure that they will enter the aquatic environment through the manufacture, use, and disposal of nanoplastics [1]. The effect of metal nanoparticles is still considered to be a big risk for the health of aquatic animals due to accumulation in different tissues of aquatic animals [2]. Due to anthropogenic activity such as manufacturing, agriculture, sewage, and motor vehicle emissions caused metal pollution in especially developing countries [3], metals are nonbiodegradable. Some researchers

documented that heavy metals, e.g., Cd, Cr, Hg, and Fe, affected cellular organelles and enzymes involved in metabolism in aquatic animals [4]. These heavy metals release metal ions and interact with nuclear materials and protein and alter the conformational which initiates apoptosis, carcinogenesis, and modulation of the cell cycle [5]. Many researchers have found the generation of reactive oxygen species as well as oxidative stress works as a key role in mutagenicity and ecotoxicity of metals [6–8]. This is a major risk to aquatic flora and fauna especially to fish, which contribute one of the important sources of protein-rich food for animals and humans. Heavy metallic nanoparticles discharge in the wastewaters from various sources and settle down in the sediments of ponds, lakes, and rivers. The nanoparticles adhere to the surface of plankton and get in the food web. Due to the increase of genotoxic in the aquatic ecosystem,

the development of specific biomarkers to find out the genotoxic effects on aquatic organisms has gained importance [9, 10]. However, comet assay is now more important in comparison to other assays due to high sensitivity to find out a little level of DNA damage [11]. The data regarding the oxidative stress and mutagenic and genotoxic nature of CdONPs in aquatic animals is meager, especially the data about the chronic genotoxic effect of CdONPs in *O. mossambicus*. Therefore, the current study investigates the underlying mechanism of mutagenic and genotoxic properties of CdONPs in fish *O. mossambicus*.

2. Materials and Methods

2.1. Experimental Specimens. The experimental specimen fish *Oreochromis mossambicus* belongs to family Cichlidae, and order Cichliformes were bought from fish markets. The fish had a mean length of 18 ± 2.0 cm and an average weight of 260 ± 10.0 g. The fishes were treated with a potassium permanganate solution (0.05%) for 3 min to escape any dermal infections. The fishes were accustomed for 15 days in the aquarium before CdONP treatments. The fishes were fed goat liver and poultry waste material. Every work as reported by Ali et al. [12] was done to maintain optimal conditions during adaptation.

2.2. Chemicals. For this experiment, cadmium dioxide nanoparticles (CdONPs) (average particle size ≥ 100 nm ± 4 nm) were purchased from American Elements 10884 Weyburn Avenue Los Angeles, CA, USA. All other chemicals were purchased from local markets.

2.3. Characterization of CdONPs

2.3.1. Transmission Electron Microscopy (TEM). CdONPs (10 mg) were suspended in Milli-Q water (10 ml). The carbon-coated copper grid was immersed into the suspension (40 μ g/ml) of CdONPs, and the grid was dried in the incubator for 24 hr. After drying the grid, the image of nanoparticles was captured by using a transmission electron microscope (JEOL Inc., Tokyo, Japan) at 120 kV. We have captured images of 10 areas of the TEM grid.

2.3.2. Determination of the Hydrodynamic Size of CdONPs. The size and zeta potential of CdONPs in aqueous solution were measured by using dynamical light scattering (DLS, Nano-Zeta Sizer-HT, Malvern, UK) as described by Alarifi and Alkahtani [13]. CdONPs were suspended (40 μ g/ml) in double-distilled water. The nanoparticle suspension was sonicated at 40 W for 10 min by a sonicator.

2.4. Experimental Design and Evaluation of Sublethal Concentrations. The fishes were put in an experimental glass tank (dimensions 40.30 \times 50.10 \times 40.30 cm) for 4 days in a semistatic system. Ten fishes were put in each tank. The suspension of CdONPs (10 mg) was prepared in 10 ml ultrapure water and sonicated at 40 mV for 15 minutes using a sonicator (Q-Sonica). The different concentrations of CdONPs (0, 1, 10, 20, 40, 80, and 150 mg/L) were exposed to *Oreochromis mossambicus* for 4 days.

During exposure, fishes were not fed to avoid the adherent of CdONPs to food materials. The experimental water (20 liters) was exchanged every day before the exposure of NPs. After 4 days, the LC₅₀ value of CdONPs was determined as 40.0 μ g/ml, applying the probit analysis method as reported by Finney [14]. Based on LC₅₀ value (4 days), the three test doses of CdONPs, viz., sublethal I (1/10 of LC₅₀ ~ 4 μ g/ml), sublethal II (1/4 of LC₅₀ ~ 10 μ g/ml), and sublethal III (1/2 of LC₅₀ ~ 20 μ g/ml) were determined.

The fish *Oreochromis mossambicus* were treated to the three sublethal doses of CdONPs for 21 days in a semistatic system. The exposure was continued up to 21 days, and tissue sampling was done at intervals of 1, 7, 14, and 21 days at the rate of 5 fishes per duration. An additional set for the positive control (cyclophosphamide 20 mg/kg body weight) was separately maintained.

The fishes were sacrificed on each sampling day, and blood, gills, and kidney tissues were collected for the study of oxidative stress and genotoxicity. The muscle tissue was collected to analyze the bioaccumulation of Cd²⁺ ion in fish. For histological analysis, the tissues were fixed in Bouin's fixative in small glass tubes. The physicochemical properties of test water, such as temperature, pH, total conductivity, dissolved oxygen, and total hardness, were analyzed by standard methods [15].

2.5. Preparation of Sample for ICP-MS. The freeze muscle tissue (5 mg) was mixed with concentrated nitric acid (HNO₃, 10 ml) and perchloric acid (HClO₄, 2 ml) in the flask. The flask was heated on a hot plate up to 100°C in fume hood till the yellow color was disappeared. Then, hydrogen peroxide (50 μ l) was added. The digested sample was vaporized up to 1.5 ml and diluted with dH₂O to 50 ml and filtered with a Whatman filter paper. The samples were analyzed using inductively coupled plasma mass spectrometry (ICP-MS) [15].

2.6. Oxidative Stress

2.6.1. Preparation of Tissue Lysate. The gills and kidney of CdONPs exposed to fish were washed with cold phosphate-buffered saline and collected in a small tube and minced in small pieces in lysis buffer through the homogenizer and centrifuged at 13000 rpm for 15 min at 4°C, and the supernatant (cell lysate) was put on ice for further tests for reduced glutathione (GSH), lipid peroxide (LPO), catalase (CAT), and glutathione-S-transferase (GST). The quantity of total protein in cell lysate was evaluated by the Bradford method [16] using bovine serum albumin as the standard.

2.6.2. GSH Test. The content of GSH was evaluated according to Ellman's [17] method. 100 μ l cell lysate was added with TCA (5%, TCA 900 μ l) and centrifuged at 3000 g for 10 min at 4°C. Again, 500 μ l supernatant was added with DTNB (0.01%, 1.5 ml), and OD of the mixture was taken at 412 nm. The quantity of glutathione was represented in mU/mg protein.

2.6.3. LPO Test. LPO was evaluated according to Ohkawa et al., [18] method. Cell lysate (100 μ l) was added with sodium phosphate buffer (1.9 ml, 0.1 M, pH 7.4) and

incubated for 60 min 37°C. Later incubation TCA (5%) was mixed and centrifuged at 3000 g for 10 min at 25°C to collect the supernatant. Then the supernatant was added with 1 ml TBA (1%) and boiled at 100°C for 30 min in a water bath. OD of the mixture was taken at 532 nm and was converted to MDA and expressed in terms of mU/mg protein.

2.6.4. Catalase (CAT). CAT enzyme was evaluated according to Ali et al. [19].

2.6.5. Glutathione-S-transferase. The activity of glutathione-S-transferase was evaluated by assessing the alteration of absorbance induced by the presence of glutathione dinitrobenzene complex as a product of the reaction between GSH and CDNB [20]. The working solution (0.1 M phosphate buffer, 10 mM GSH, and 60 mM EDTA), CDNB (10 mM), and enzyme source were mixed in a cuvette. The change in absorbance was measured every 30 s for 5 min at 340 nm. The GST level was presented as mU/mg protein.

2.7. MN Assay. After sampling the blood, the blood smear was made on the frosted glass slides. The smeared slides were dried at RT and fixed in the method for 10 minutes, and after air drying, the slide was stained with 6% Giemsa in the buffer (pH 6.8) for 30 min. Scoring of micronuclei (MNi) was done using a light microscope (Leitz Wetzlar Germany, 100X with oil). A total of 10000 erythrocytes were examined for each concentration. The micronucleus body was identified according to as described by Ali et al. [12].

MN frequency was calculated as follows:

$$\text{MN}\% = \frac{\text{Number of cells containing micronucleus}}{\text{Total number of cells counted}} \times 100. \quad (1)$$

2.8. Comet Assay. The DNA damaging potential of CdONPs on different tissues of *O. mossambicus* was assessed using the single-cell gel assay [21]. The gills and kidney tissues (about 50 mg each) were washed two times with chilled phosphate-buffered saline (Ca²⁺ Mg²⁺ free) to remove blood cells and transferred to ice-cold homogenization buffer (1-X Hanks' balanced salt solution, 20 mM EDTA, 10% dimethyl sulphoxide (DMSO), pH 7.0-7.5). The tissue was cut into small pieces using scissors and finally homogenized to obtain a single-cell suspension. The suspension of the cell was centrifuged at 3000 rpm at 4°C for five min, and the cell pellet was finally suspended in chilled phosphate-buffered saline for SCGE assay. Lymphocyte cells were isolated from the blood histopaque density gradient centrifugation method, and the cells were diluted 10-fold for the single-cell gel assay. The two slides were prepared from each fish (25 cells per slide) (250 cells per dose), and the slides were randomly scored using an image analysis system (Komet-5.5, Kinetic Imaging, United Kingdom) attached to a fluorescent microscope (Leica) equipped with appropriate filters. The parameter selected for quantification of DNA damage was percent tail DNA (i.e., %tail DNA = 100 - %head DNA) as determined by the software.

TABLE 1: Physiochemical characteristics of test water.

Parameters	Values
Temperature	23-24.8°C
pH	5.88-7.40
Dissolved oxygen (mg/l)	6.32-8.00
Total hardness (as CaCo ₃) (µg/ml)	154.0-190
Chloride (µg/ml)	45.06-53.0
Conductivity (µM/cm)	241.2-289

2.9. Statistical Analysis. Data were expressed as the mean (±SE) and analyzed by one-way analysis of variance (ANOVA). A *p* value of less than 0.05 and 0.01 was considered statistically significant. Minimum three independent experiments were done in duplicate for each treatment.

3. Results

3.1. Experimental Water Quality. Table 1 shows the properties of test water quality. During the experiment, the water quality parameters such as pH of water (5.88-7.40), temperature (from 23 to 24.8°C), and dissolved oxygen (DO) (6.32-8.0 mg/l) are found (Table 1). The total hardness of test water was found to be 154.0-190 µg/ml as CaCO₃. The chloride ion level and conductivity of test water were 45.06 to 53.0 µg/ml and 241.2-289 µM/cm, respectively (Table 1).

3.2. Characterization of CdONPs. The CdONPs have specific properties relative to CdO bulk particle counterparts which impart them beneficial characteristics; they may also bestow them with unique mechanisms of toxicity. We have characterized the size of CdONPs, and their average size was 45.20 ± 3.80 nm (Figures 1(a)–1(b)). Figure 1(a) shows the TEM image of nanoparticle, and most of the particles are round. The hydrodynamic size of CdONPs was 84.50 nm, and zeta potential was -9.3 mV.

3.3. Behavioral Response of Fish and Median Lethal Concentration. After exposure to CdONPs (1, 5, 10, 20, 40, 80, and 150 µg/ml), the freshwater fish showed abnormal behavior and we have observed 1%, 10.5%, 14%, 56%, 73%, and 100% mortality in 96 h, respectively (Figure 2). LC₅₀-96 h value with 95% confidence of CdONPs to fish was 40 µg/ml (Figure 2). Behavioral alterations of fish were noticed up to 4 days, and this might be due to intoxication of CdONPs. Due to these toxicities, fish was lost of swimming equilibrium, calmed down to the bottom of the tank, restless, and died without showing any movement and feeding activities at a maximum concentration of CdONPs.

3.4. Bioaccumulation of CdONPs. The Cd accumulation in various tissues such as the muscles, gills, and kidney of exposed fish was determined using ICP-MS, and the concentration of Cd metal increases according to the concentration-dependent manner (Table 2). The highest cadmium from CdONPs was found in the gills as compared to the muscles and kidneys (Table 2). The Cd bioaccumulation in different tissues of fish was gills > muscles > kidney (Table 2).

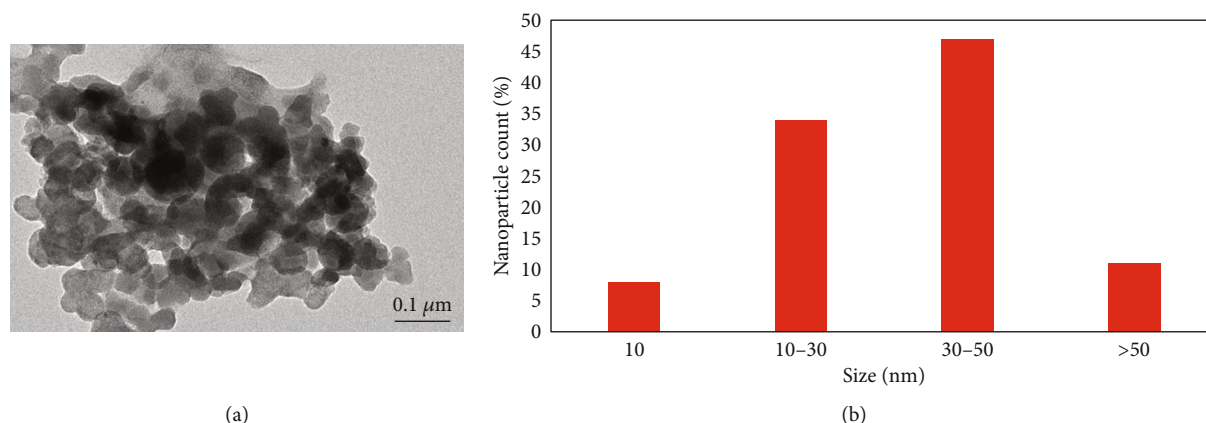


FIGURE 1: (a) TEM image of CdONPs. (b) Percentage of CdONP size.

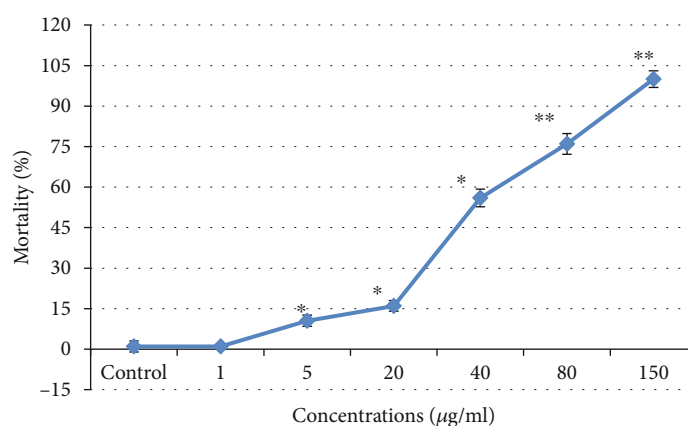


FIGURE 2: Acute toxicity of CdONPs on fresh water fish *Oreochromis mossambicus*. $n = 3$; * $p < 0.05$ and ** $p < 0.01$ vs. control.

TABLE 2: Bioaccumulation of Cd in gill, kidney, and muscles of fish.

Tissues	Control	Sublethal I	Exposure concentrations	
			Sublethal II	Sublethal III
Gill	0.062 ± 0.013	0.09 ± 0.01	0.102 ± 0.01	0.119 ± 0.01
Kidney	0.065 ± 0.012	0.063 ± 0.03	0.087 ± 0.016	0.098 ± 0.02
Muscles	0.088 ± 0.002	0.109 ± 0.002	0.116 ± 0.002	0.124 ± 0.001

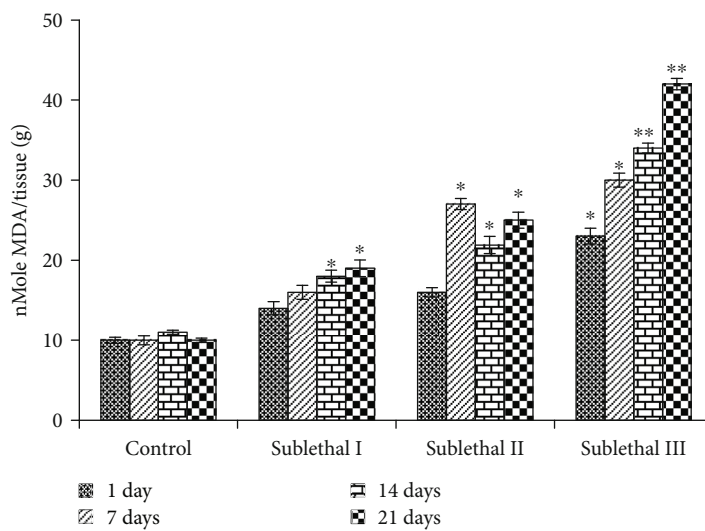
All values are the mean ± SE.

3.5. Induction of Oxidative Stress. The lipid peroxide (LPO) level was measured by measuring the formation of MDA in the gills and kidney tissue of fish. The LPO level was significantly increased at sublethal III dose (21 days) (Figures 3(a) and 3(b)). Exposure of NPs at sublethal I, II, and III for 21 days significantly reduced the GSH level in both tissues of fish (Figures 3(c) and 3(d)). The effect of CdONPs on the GST level in both tissues of fish significantly increased the concentration and time-dependent manner (Figures 4(a) and 4(b)).

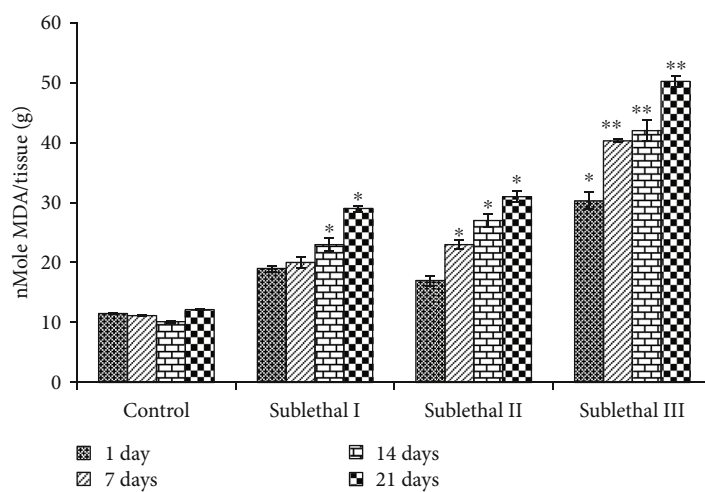
Catalase activity in both tissues is significantly induced at sublethal I for the 7th and 21st day, but on the other hand, catalase activity was reduced at sublethal III for the 21st day (Figures 4(c) and 4(d)).

3.6. Induction of Micronuclei (MNi). The mutagenic effect of CdONPs on fish was observed (Figures 5(b)–5(d)). The data showed the significant formation of micronuclei at sublethal II and III CdONPs exposure at the 21st day (Figures 5(b)–5(d)). Also, we have observed that the formation of MNi was in a concentration and time-dependent manner, and on the 21st day, there were 1.5-fold increases from lower to maximum concentrations. The negative control was unable to induce nonsignificant MNi frequency fish.

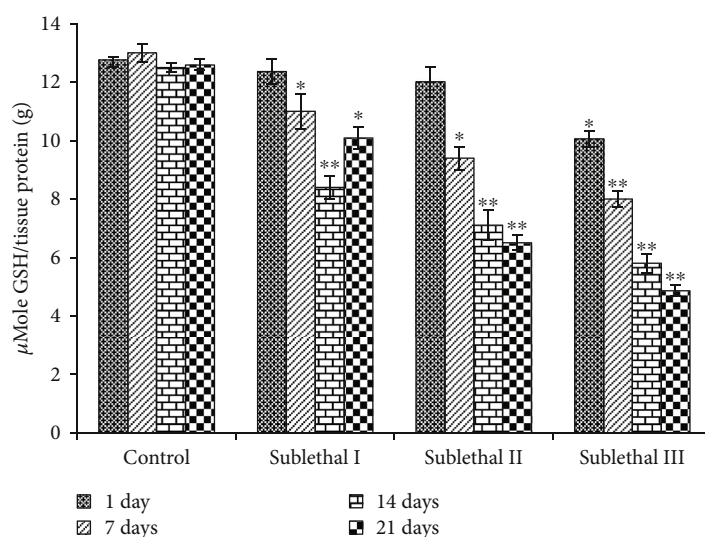
3.7. DNA Damage. The genotoxicity of CdONPs on freshwater fish was determined using single gel electrophoresis and DNA damage as measured in % tail DNA in lymphocyte, gills, and kidney tissue. During electrophoresis, the DNA of



(a)



(b)



(c)

FIGURE 3: Continued.

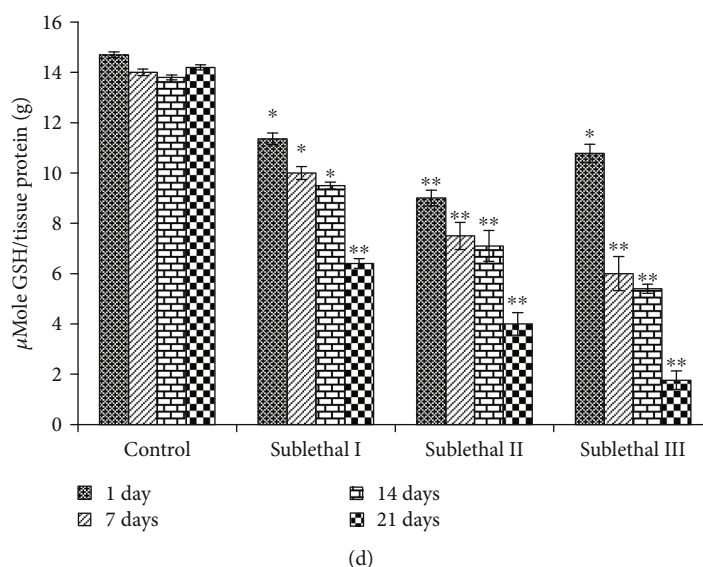


FIGURE 3: (a) Level of LPO in gill tissue. (b) Level of LPO in kidney tissue. (c) Level of GSH in gill tissue. (d) Level of GSH in kidney tissue. Each value represents the mean \pm SE of three experiments. * $p < 0.05$ and ** $p < 0.01$ vs. control.

all tissues was migrated faster towards the anode at sublethal III concentration than the sublethal I concentration exposure (Figures 6(c)–6(h)). The order of DNA damage in different tissues of fish was gills > lymphocyte > kidney (Figures 6(a) and 6(b)).

4. Discussion

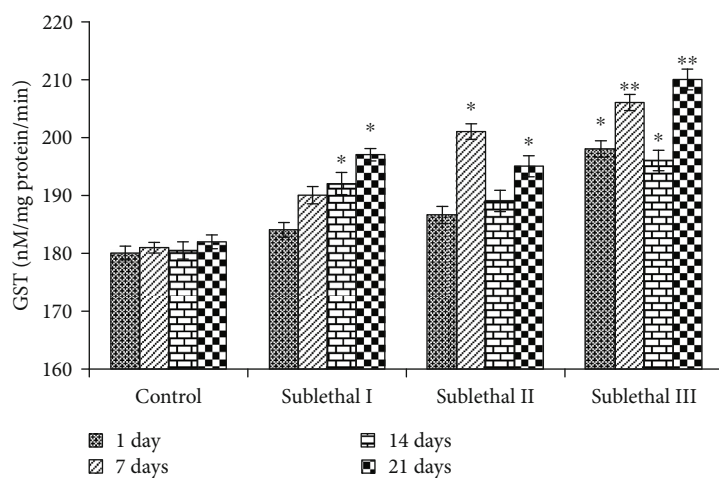
Cadmium dioxide nanoparticles (CdONPs) are found naturally in environments and parts of many commercial products, but little is known about their potential hazard on the freshwater organism. Several studies have been carried out about the accumulation of Cd CdONPs [22]. Shaw and Handy [23] reported that copper metal bio accumulated more in the liver in comparison to other organs such as the gills and intestine of fish. The distribution of Cd²⁺ during the study and distribution of CdONPs in *Oreochromis mossambicus* has been observed in the gills than in the kidney. The alteration of behavior is the result of adaptations to the exchange environment. Behavioral changes are a sensitive parameter of an animal's response to stress. Any change in the behavior of freshwater fish indicates a drop in water quality. We have observed the immediate reaction of fish after exposure to the acute concentration of nanoparticles. Fish moved to surface, and erect fins and secreted mucous were seen after exposure to CdONPs. The behavioral changes of this study were following the findings of Khunyakari et al. [24] for *C. carpio* and *Poecilia reticulata* under the effect of copper.

Maintaining the stress to it is the minimum stage, and applying their energy to acclimatize the changing water quality afore for activities may be the reason for behavioral changes in fish under the effect of CdONPs. Bioaccumulation of Cd²⁺ in different tissues after exposure to CdONPs depends upon the physiochemical nature of nanoparticles and water. Nussey et al. [25] have reported that metal

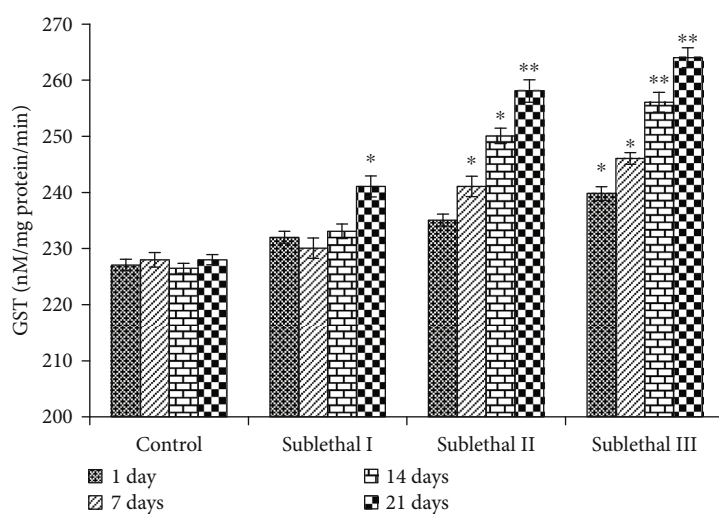
(e.g., Cd and Zn) toxicity is affected by the physical-chemical characteristic of test water. The acclimatized dose of Cd was 2 and 0.25 $\mu\text{g/l}$ in surface freshwater bodies in the United States or acute and chronic exposure [26]. In the current study, the physical-chemical characteristics of test water were maintained constant to reduce their effect on metal nanoparticle toxicity. The accumulation of metals indicates pollution of the metal and detects their route of intake and excretion [3, 27]. Some researchers advocated that heavy metals accumulated in tissues such as the gills, kidney, spleen, and liver in chronic exposure [28]. Exposure to heavy metals increases mucus secretion in fish to prevent gill uptake; hence, high levels of metals found in this tissue might be due to mucus-bonded metals. Lipid peroxidation occurred due to the reaction of ROS and membrane lipids [29]. MDA is an important by-product of polyunsaturated fatty acids. Lipid peroxidation by-product MDA level has been measured in the gills and kidney tissues of freshwater fish after exposure to CdONPs. LPO levels were significantly increased among controls and treatment groups in both tissues. Ali et al. [30] have reported that oxidative stress is a major mechanism of ecotoxicity. GSH and LPO (Figure 3) were increased, and GST and catalase (Figure 4) were increased at lower concentrations and increased higher concentration, indicating that toxic effects were related to oxidative stress.

In this study, we have used alkaline single-cell gel electrophoresis to detect the genotoxic potential of CdONPs in different tissues of freshwater fish because at higher pH > 13, the expression of alkali labile sites and single-strand breaks was increased. We have seen that fragments of DNA and loosed DNA loop were migrated towards the anode and forming the tail of a comet as seen in Figure 6. The percentage of tail DNA is an important parameter to express the genotoxicity.

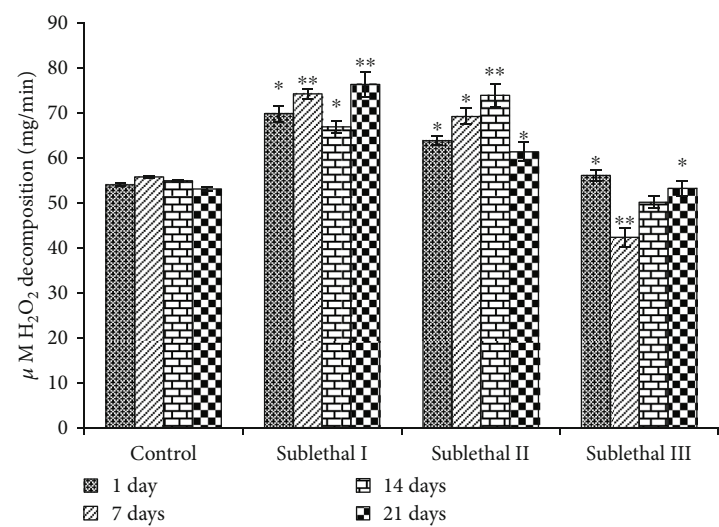
On the basis of the current study, the bioaccumulation of Cd ion was more in the muscle tissue than in the gills and



(a)



(b)



(c)

FIGURE 4: Continued.

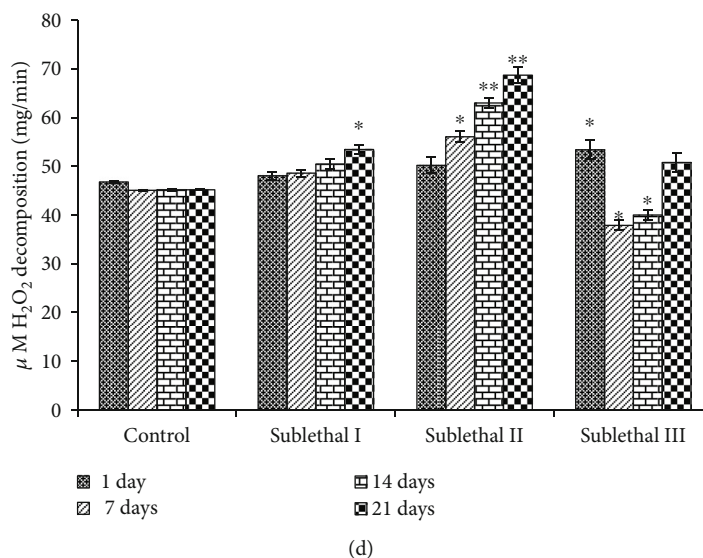


FIGURE 4: (a) Level of glutathione-S-transferase (GST) in gill tissue. (b) Level of glutathione-S-transferase (GST) in kidney tissue. (c) Level of catalase in gill tissue. (d) Level of catalase in kidney tissue. Each value represents the mean \pm SE of three experiments. * $p < 0.05$ and ** $p < 0.01$ vs. control.

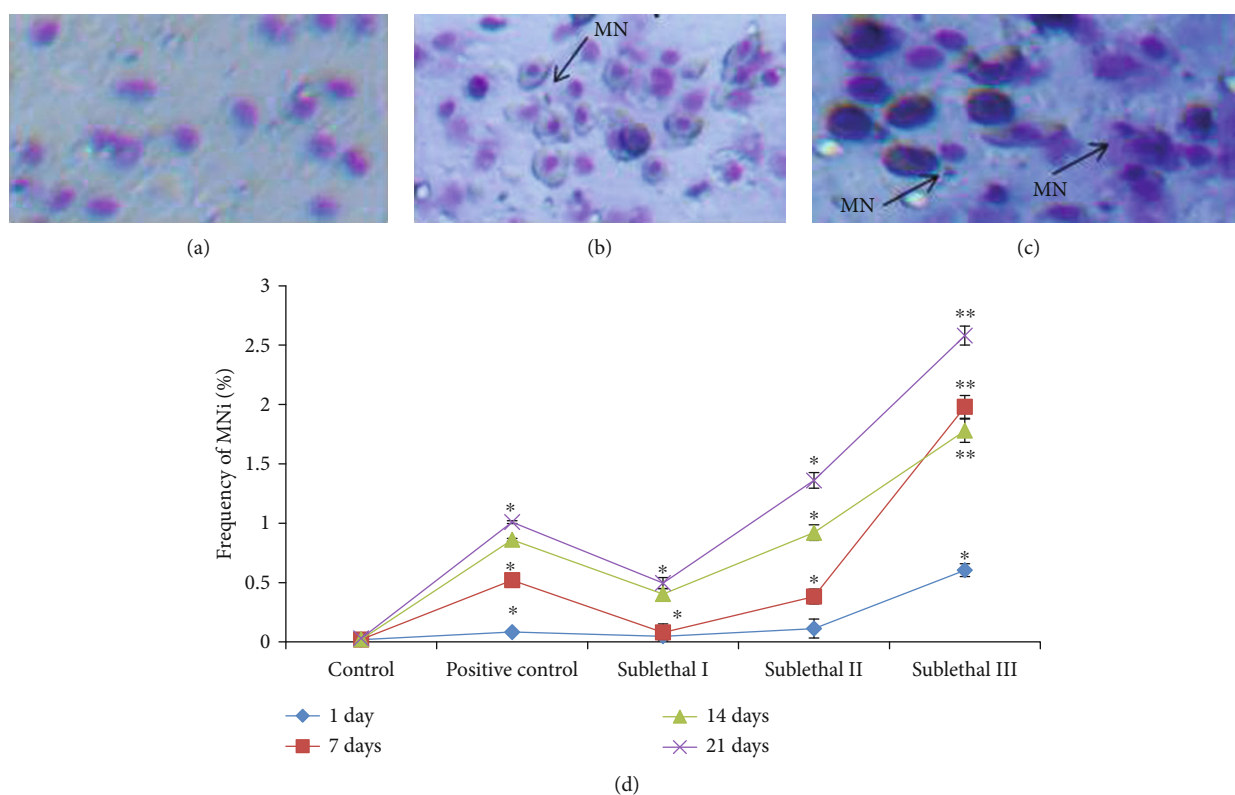


FIGURE 5: Induction of micronucleus (MN) in erythrocytes of *O. mossambicus* after exposure of different concentrations of CdONPs for 1, 7, 14, and 21 days. (a) Erythrocytes of control *O. mossambicus*. (b) MN in erythrocytes of *O. mossambicus* at sublethal II for 21 days. (c) MN in erythrocytes of *O. mossambicus* at sublethal III for 21 days. (d) Percentage of MN in erythrocytes of *O. mossambicus*. Each value represents the mean \pm SE of three experiments. * $p < 0.05$ and ** $p < 0.01$ vs. control.

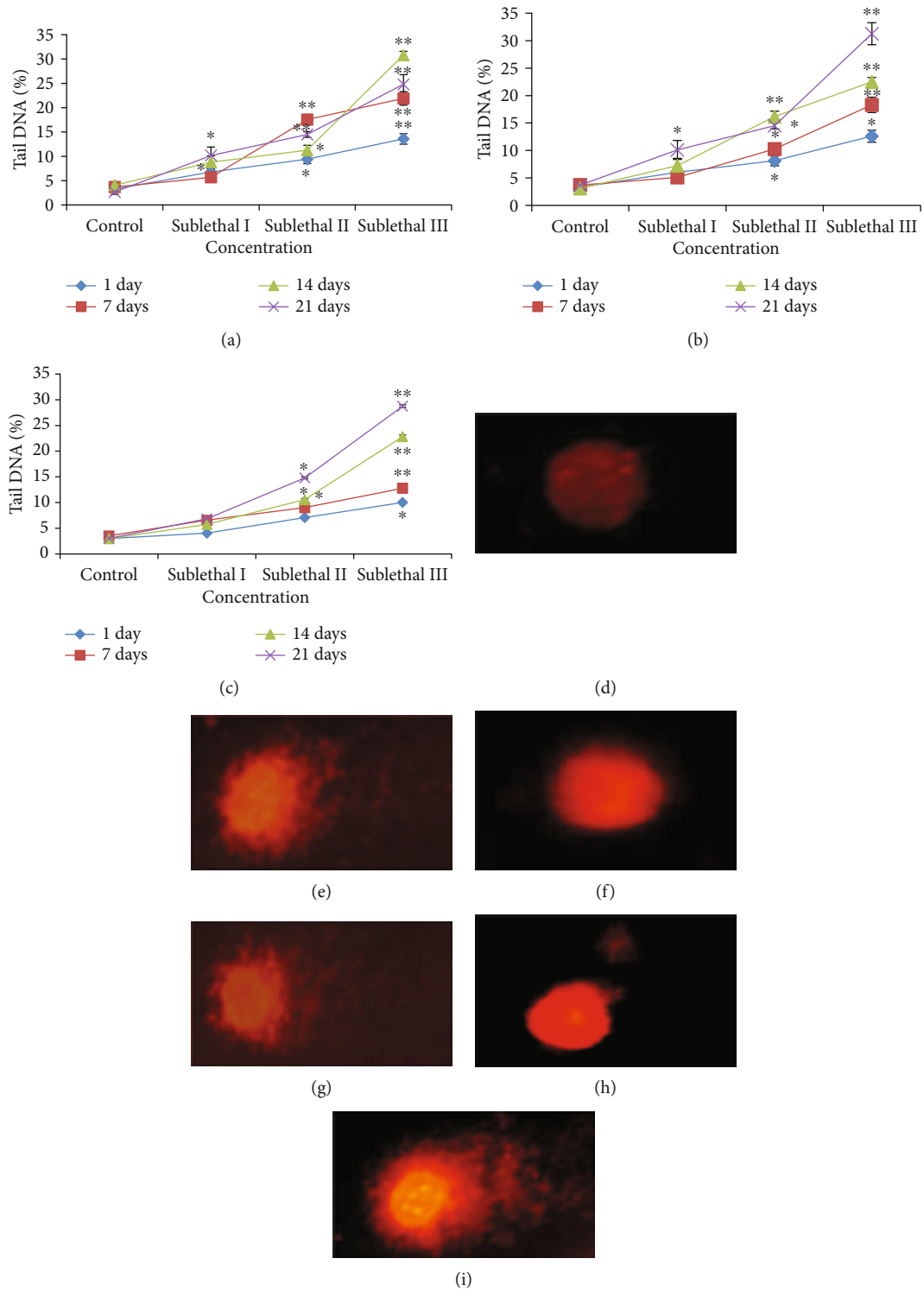


FIGURE 6: DNA damage in different tissues of *O. mossambicus* after exposure of different concentrations of CdONPs for 1, 7, 14, and 21 days. (a) Tail DNA (%) in lymphocytes. (b) Tail DNA (%) in gill tissue. (c) Tail DNA (%) in kidney tissue. (d) Control lymphocytes. (e) Lymphocyte cells at sublethal III exposure for 21 days. (f) Control gill cells. (g) Gill cells at sublethal III exposure for 21 days. (h) Control kidney cells. (i) Kidney cells at sublethal III exposure for 21 days. Each value represents the mean \pm SE of three experiments. * $p < 0.05$ and ** $p < 0.01$ vs. control.

kidney tissues after exposure to CdONPs for the 21st day. However, the genotoxicity effects of CdONPs were more in lymphocyte cells in comparison to the gill and kidney. This can be confirmed that CdONPs were eco-genotoxic and carcinogenic to aquatic organisms.

Data Availability

All data generated or analyzed during this study are included in the article.

Conflicts of Interest

There are no conflicts of interest.

Acknowledgments

This research was funded by the Deanship of Scientific Research at Princess Nourah Bint Abdulrahman University, through the Research Funding Program (Grant No. #FRP-1440-20).

References

- [1] K. Mattsson, L.-A. Hansson, and T. Cedervall, "Nano-plastics in the aquatic environment," *Environmental Science: Processes & Impacts*, vol. 17, no. 10, pp. 1712–1721, 2015.
- [2] R. Gupta and H. Xie, "Nanoparticles in daily life: applications, toxicity and regulations," *Journal of Environmental Pathology, Toxicology and Oncology*, vol. 37, no. 3, pp. 209–230, 2018.
- [3] P. B. Tchounwou, C. G. Yedjou, A. K. Patlolla, and D. J. Sutton, "Heavy metal toxicity and the environment," *EXS*, vol. 101, pp. 133–164, 2012.
- [4] S. Wang and X. Shi, "Molecular mechanisms of metal toxicity and carcinogenesis," *Molecular and Cellular Biochemistry*, vol. 222, no. 1/2, pp. 3–9, 2001.
- [5] L. W. Chang, L. Magos, and T. Suzuki, *Toxicology of Metals*, CRC Press, Boca Raton, FL, USA, 1996.
- [6] C. G. Yedjou and P. B. Tchounwou, "Oxidative stress in human leukemia cells (HL-60), human liver carcinoma cells (HepG2) and human Jerkat-Tcells exposed to arsenic trioxide," in *Metal Ions in Biology and Medicine*, vol. 9, pp. 298–303, NIH Public Access, 2006.
- [7] P. B. Tchounwou, A. Ishaque, and J. Schneider, "Cytotoxicity and transcriptional activation of stress genes in human liver carcinoma cells (HepG2) exposed to cadmium chloride," *Molecular and Cellular Biochemistry*, vol. 222, no. 1/2, pp. 21–28, 2001.
- [8] D. J. Sutton and P. B. Tchounwou, "Mercury induces the externalization of phosphatidyl-serine in human renal proximal tubule (HK-2) cells," *International Journal of Environmental Research and Public Health*, vol. 4, no. 2, pp. 138–144, 2007.
- [9] M. Hayashi, T. Ueda, K. Uyeno et al., "Development of genotoxicity assay systems that use aquatic organisms," *Mutation Research/Fundamental and Molecular Mechanisms of Mutagenesis*, vol. 399, no. 2, pp. 125–133, 1998.
- [10] T. Cedervall, L.-A. Hansson, M. Lard, B. Frohm, and S. Linse, "Food chain transport of nanoparticles affects behaviour and fat metabolism in fish," *PLoS One*, vol. 7, no. 2, article e32254, 2012.
- [11] P. Sykora, K. L. Witt, P. Revanna et al., "Next generation high throughput DNA damage detection platform for genotoxic compound screening," *Scientific Reports*, vol. 8, no. 1, p. 2771, 2018.
- [12] D. Ali, N. S. Nagpure, S. Kumar, R. Kumar, and B. Kushwaha, "Genotoxicity assessment of acute exposure of chlorpyrifos to freshwater fish *Channa punctatus* (Bloch) using micronucleus assay and alkaline single-cell gel electrophoresis," *Chemosphere*, vol. 71, no. 10, pp. 1823–1831, 2008.
- [13] S. Alarifi, D. Ali, and S. Alkahtani, "Nanoalumina induces apoptosis by impairing antioxidant enzyme systems in human hepatocarcinoma cells," *International Journal of Nanomedicine*, vol. 10, pp. 3751–3760, 2015.
- [14] D. J. Finney, *Probit Analysis*, Cambridge University Press, Cambridge, 1971.
- [15] APHA, AWWA, WPCF, *Standard Methods for Examination of Water and Wastewater*, American Public Health Association, New York, 21st edition, 2005.
- [16] M. M. Bradford, "A rapid and sensitive method for the quantitation of microgram quantities of protein utilizing the principle of protein-dye binding," *Analytical Biochemistry*, vol. 72, no. 1-2, pp. 248–254, 1976.
- [17] G. L. Ellman, "Tissue sulfhydryl groups," *Archives of Biochemistry and Biophysics*, vol. 82, no. 1, pp. 70–77, 1959.
- [18] H. Ohkawa, N. Ohishi, and K. Yagi, "Assay for lipid peroxides in animal tissues by thiobarbituric acid reaction," *Analytical Biochemistry*, vol. 95, no. 2, pp. 351–358, 1979.
- [19] D. Ali, P. G. Yadav, S. Kumar, H. Ali, S. Alarifi, and A. H. Harrath, "Sensitivity of freshwater pulmonate snail *Lymnaea luteola* L., to silver nanoparticles," *Chemosphere*, vol. 104, pp. 134–140, 2014.
- [20] W. H. Habig, M. J. Pabst, and W. B. Jakoby, "Glutathione S-transferases. The first enzymatic step in mercapturic acid formation," *The Journal of Biological Chemistry*, vol. 249, no. 22, pp. 7130–7139, 1974.
- [21] N. P. Singh, M. T. McCoy, R. R. Tice, and E. L. Schneider, "A simple technique for quantitation of low levels of DNA damage in individual cells," *Experimental Cell Research*, vol. 175, no. 1, pp. 184–191, 1988.
- [22] J. L. Blum, J. Q. Xiong, C. Hoffman, and J. T. Zelikoff, "Cadmium associated with inhaled cadmium oxide nanoparticles impacts fetal and neonatal development and growth," *Toxicological Sciences*, vol. 126, no. 2, pp. 478–486, 2012.
- [23] B. J. Shaw and R. D. Handy, "Physiological effects of nanoparticles on fish: a comparison of nano-metals versus metal ions," *Environment International*, vol. 37, no. 6, pp. 1083–1097, 2011.
- [24] R. P. Khunyakari, V. Tare, and R. N. Sharma, "Effects of some trace heavy metals on *Poecilia reticulata* (Peters)," *Journal of Environmental Biology*, vol. 22, no. 2, pp. 141–144, 2001.
- [25] G. Nussey, J. H. J. Van Vuren, and H. H. du Preez, "Effect of copper on the haematology and osmoregulation of the Mozambique tilapia, *Oreochromis mossambicus* (Cichlidae)," *Comparative Biochemistry and Physiology Part C: Pharmacology, Toxicology and Endocrinology*, vol. 111, no. 3, pp. 369–380, 1995.
- [26] USEPA, *National Recommended Water Quality Criteria*, United States Environmental Protection Agency (US EPA), Washington, DC, USA, 2002, EPA822-R-02-047.
- [27] A. Wicklund, P. Runn, and L. Norrgren, "Cadmium and zinc interactions in fish: effects of zinc on the uptake, organ distribution, and elimination of ¹⁰⁹Cd in the zebrafish, *Brachydanio*

- erio,” *Archives of Environmental Contamination and Toxicology*, vol. 17, no. 3, pp. 345–354, 1988.
- [28] S. Rajeshkumar and X. Li, “Bioaccumulation of heavy metals in fish species from the Meiliang Bay, Taihu Lake, China,” *Toxicology Reports*, vol. 5, pp. 288–295, 2018.
- [29] M. Hampel, J. Blasco, and M. L. M. Díaz, *Chapter 5 - Biomarkers and Effects, Marine Ecotoxicology Current Knowledge and Future Issues*, pp. 121–165, Academic Press, Cambridge UK, 2016.
- [30] D. Ali, M. Ahmed, S. Alarifi, and H. Ali, “Ecotoxicity of single-wall carbon nanotubes to freshwater snail *Lymnaea luteola* L.: impacts on oxidative stress and genotoxicity,” *Environmental Toxicology*, vol. 30, no. 6, pp. 674–682, 2015.

Research Article

Crystal Growth and Kinetic Behaviour of *Pseudoalteromonas espejiana* Assisted Biosynthesized Gold Nanoparticles

Rashmi Gupta,¹ Gourav Kumar,¹ Sabya Sachi Das,² Saad Alkahtani ,³ Abdullah Alkahtane,³ Badr Aldahmash,³ Saud Alarifi ,³ Bader Almutairi,³ Gadah Albasher ,³ Amit Kumar Nayak,⁴ and Md Saquib Hasnain ⁵

¹Department of Bio-Engineering, Birla Institute of Technology, Mesra, Ranchi, 835215 Jharkhand, India

²Department of Pharmaceutical Sciences and Technology, Birla Institute of Technology, Mesra, Ranchi, 835215 Jharkhand, India

³Department of Zoology, College of Science, King Saud University, P.O. Box 2455, Riyadh 11451, Saudi Arabia

⁴Department of Pharmaceutics, Seemanta Institute of Pharmaceutical Sciences, Mayurbhanj, Odisha, India

⁵Department of Pharmacy, ShriVenkateshwara University, NH-24, Rajabpur, Gajraula, Amroha – 244236, U.P., India

Correspondence should be addressed to Saad Alkahtani; salkahtani@ksu.edu.sa
and Md Saquib Hasnain; msaquibhasnain@gmail.com

Received 24 April 2020; Accepted 2 June 2020; Published 22 July 2020

Guest Editor: Khuram Ahmad

Copyright © 2020 Rashmi Gupta et al. This is an open access article distributed under the Creative Commons Attribution License, which permits unrestricted use, distribution, and reproduction in any medium, provided the original work is properly cited.

Pseudoalteromonas espejiana (*P. espejiana*) is a marine bacterium known for its high resistance to alkalinity. The ability of *P. espejiana* to reduce Au (III) and biosynthesize gold nanoparticles (AuNPs) is found positive and was confirmed using UV-VIS, EDS, SEM, and TEM studies. Previously, many studies have been reported regarding the crystalline nature of AuNPs; therefore, this research aims at studying the crystal growth behaviour of AuNPs through DLS and TEM studies. Spherically shaped and monodispersed, AuNPs ranging between 5 to 160 nm were obtained with an average particle size of 62 nm. Also, to achieve maximum production of AuNPs, the reaction kinetic study was performed using an ICP-OES method and the effect of various parameters including pH, temperature, rpm, and concentration of substrate was analyzed. During the biosynthesis process, an appropriate phase of nucleation, crystal growth, and saturation was observed and this helped to determine the rate constants and order of reaction. The parameters such as pH profile (pH 9), temperature (30°C), agitation speed (150 rpm), and enzyme substrate ratio (2:3) were found to be the best fits for maximum production of low size AuNPs. This demonstrates that in initial few hours, a quick conversion of the ionic gold precursor takes place into metallic gold nuclei, trailed by crystal growth via coalescence of small nuclei. Subsequently, it can be concluded that coalescence processes drive the crystal growth process of AuNPs over a time interval and finally leads to saturation and no newer particle formation in the solution.

1. Introduction

In the field of material science, nanotechnology is unremittingly carving its own zone as an emerging field of research. Applicability of nanoparticles (NPs) and nanomaterials is evolving rapidly; specially on the biomedical front from cell imaging, targeted drug delivery and cancer diagnostics to therapeutic applications [1–8]. Both the physical and chemical methods, or either of any, can be significantly applied for

the synthesis of NPs [9–11]. Since the last one decade, biological sources like microbes, plant, and plant parts along with various biomolecules are being used to biosynthesize NPs both intra and extracellularly giving rise to the new field “Nanobiotechnology”. The biological methods involves living organisms like bacteria, fungi, actinomycetes, yeast, algae, and plants [12–16] and exploiting them both intracellularly and extracellularly to synthesize and produce NPs of desired shape, size, and morphology [17]. Biogenic synthesis also

produces more stable NPs because microbes and plant extracts contain enzymes, phenols, and flavonoids, which act as a capping agent [18]. Marine microbes exhibit a very exploitable potential for biosynthesis of metal NPs especially gold, silver, iron, and copper. [19, 20].

One of the first reports by Singaravelu et al. [21] demonstrated the synthesis of monodispersed AuNPs using *Sargassum wightii* (*S. wightii*) marine algae. Venkatesan et al. [22] reported an interesting study involving marine brown alga *Ecklonia cava* (*E. cava*) wherein AuNPs biosynthesis occurred within 1 minute at a high temperature of 80°C [22]. Bacteria *Rhodospseudomonas capsulate* (*R. capsulate*) was also monitored for its potential in the biosynthesis of AuNPs. It showed successful synthesis using enzyme NADPH-dependent nitrate reductase [23]. Since marine flora and fauna can easily adjust to biotic and abiotic stress and also to the extreme environmental conditions; thus, an emphasis to explore marine microbes is trending since the last decade. Also, the lipid and polymer-based metallic systems have showed significant activities for eradicating various cancer-associated disorders and diseases [24, 25]. However, the noble metals such as gold and silver are expensive, and, thus, it is very important to use these materials as per need, which could be efficiently achieved through reducing their particle size and forming NPs through biosynthesis approach. This approach also regulates the cost and reduces the waste disposal, thus exhibits high biodegradability and biocompatibility [19].

Earlier studies have demonstrated that the synthesis of NPs involves a key mechanism of a precipitation reaction, followed by nucleation, crystal growth, and accumulation [26]. As per the reports, the process of nucleation is found to be an initial one and also appears very fast followed by the particle growth, which is the slowest step and also the rate-determining step. After nucleation, the particles having the size more than the critical size show a particle growth by coalesce whereas particles with size less than critical size dissolve back in the solution [27]. Also, the surface charge and polydispersity index (PDI) of the particles play crucial roles for regulating the processes of nucleation, crystal growth, and accumulation. It has been observed that the lesser the PDI value, the more would be the formation of monodispersed particles, thus lesser would be the size of the particles [28]. An extensive study focusing on kinetics involved in the biochemical process of metal NPs synthesis will suffice the lack of understanding of reaction complexity and will minimize the trial-and-error approaches. Biogenic synthesis still needs understanding and validation of the formation mechanism of NPs so as to scale up its bulk production.

The present research focuses on the biosynthesis of AuNPs using cell lysate supernatant (CLS) of marine bacteria, *P. espejiana*, and deduces the best possible culture conditions for AuNPs production. Temperature, pH, agitation speed, and concentration of chloroauric acid (precursor agent) were the four physico-chemical parameters, which were varied and tested to observe their effect on the biosynthesis of AuNPs using one-factor-at-a-time (OFAT) method. Colloidal AuNPs solutions were examined using UV-VIS

spectroscopy (UV-1800, Shimadzu, Japan); the obtained spectra presented an absorption band around 540 nm, which confirmed the successful production of AuNPs. Further, AuNPs were subjected to DLS, TEM, FE-SEM, and ICP-OES analysis to deduce out more results in order to establish an understanding of both the crystal growth kinetics and reaction kinetics.

2. Materials and Methods

2.1. Chemicals. Chloroauric acid ($\text{HAuCl}_4 \cdot 3\text{H}_2\text{O}$), and other pure chemicals and biochemicals, were purchased from Sigma-Aldrich, India. Zobell Marine broth was purchased from Himedia, India. Freshly prepared aqueous solution of HAuCl_4 (1 mM), prepared using double-distilled (DD) water, was used in the experimental work. All the glassware used was sterilized and thoroughly washed with pure water. All other chemicals and reagents were of analytical grade.

2.2. Method of AuNPs Biosynthesis Using *P. espejiana*. The authors have followed the protocol of AuNP synthesis as reported previously with some modifications [19]. The marine bacterial strains of *P. espejiana* were collected from Dr. Rajib Bandopadhyay, Associate Professor, The University of Burdwan, West Bengal. Both the bacterial component version, i.e., cell biomass and cell lysate supernatant (CLS) were tested for their ability to convert precursor HAuCl_4 to gold nanoparticles. Various steps involved in the biosynthesis of AuNPs are summarized in Figure 1. Visual observation of aliquot's color change from yellow to pinkish-purple was the preliminary indication for successful AuNP production. The AuNPs produced were further confirmed using UV-Vis spectroscopy by observing the SPR peak at 540 nm. Thereafter, the characterization of AuNPs was done using TEM, SEM, EDX, and DLS studies to access the shape, size, and morphology.

2.3. Determination of Enzyme-Substrate Ratio. Different combinations of enzyme-substrate ratios were analyzed, $[\text{E}] : [\text{C}_\text{A}] = 1 : 1, 1 : 2, 2 : 1, 2 : 3,$ and $3 : 2$, in order to determine the best enzyme-substrate ratio for significant AuNPs synthesis. Moreover, to observe the crystal growth and reaction kinetics of AuNPs, the optimum ratio of $[\text{E}] : [\text{C}_\text{A}]$ and alterations in the physico-chemical parameters were assessed.

2.4. Size Optimization of AuNPs. In order to optimize the size and observe the phenomenon of crystal growth of AuNPs, the synthesis was carried out at four different temperatures (25°C, 30°C, 35°C, and 37°C) and simultaneously at different pH ranging from 5 to 9 for a period of 24 hours. This study helped in deducing the influence of temperature and pH over the size of synthesized NPs. After obtaining results of the optimum pH and temperature, the samples were subjected to access various sizes of the synthesized NPs using DLS (Nano ZS Zetasizer Malvern Instrument, UK), so as to plot a graph showing the increase in the size of NPs with respect to time (time vs. size). Further, the AuNPs samples were drawn at regular time interval up to 48 hrs and analysis of morphological characters using FE-SEM (ZEISS Sigma 300), TEM (JEOL, JEM1400, USA).

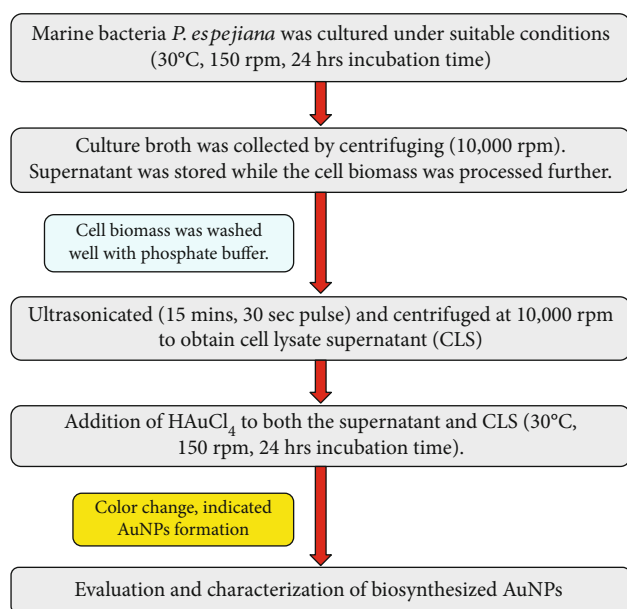


FIGURE 1: Schematic flow chart indicating various steps involved in AuNPs biosynthesis using *P. espejiana* testing for both intracellular synthesis and extracellular synthesis of gold nanoparticles.

2.5. Study of Reaction Kinetics. The effect of varying temperatures (25°C–40°C), pH (5–9), agitation speed (50–250 rpm), and HAuCl₄ concentration (1–10 mg/L) over the reaction kinetics involved in the biosynthesis of AuNPs was attempted to comprehend in this study. Multiple sets of experiments were carried out by varying one factor at a time (OFAT) while keeping the other factors constant over a period of reaction time (0–48 h) intervals. The enzyme substrate ratio was kept constant i.e., [E]: [C_A] = 2 : 3. All experiments were subjected to ICP-OES analysis over a period of 48 hours by altering different parameters and drawing samples at regular time interval. The concentrations of formed AuNPs were measured at regular time intervals to determine the effect of physical parameters. ICP-OES analysis was done on Perkin Elmer, USA; Optical 2100DV ICP-OES at CIF, BIT MESRA. The data and results helped in predicting the best combination of physical parameters for the most reliable and economically viable process for the AuNP production.

2.6. Study of Order of Reaction. The order of reaction was obtained from the experimental data which was expressed in the form of graphs. It is the sum of the exponents of the concentration terms in the rate expression.

3. Results and Discussion

3.1. AuNPs Screening and Characterization Studies. The successful synthesis of AuNP formation was confirmed by the SPR peak at 540 nm in U Visible spectroscopy. It was further characterized by DLS which gave an average particle size of 62 nm with net particle charge of -25.6 analyzed by zeta potential analyzer hence approving the stability of the

AuNPs. EDX results confirmed AuNPs production by accessing elemental composition.

3.2. Optimized Enzyme to Substrate Ratio. The best enzyme to substrate relation comes out to be [E]: [C_A] = 2 : 3 since maximum UV-VIS absorbance was observed as illustrated in Figure 2, which demonstrated that 2 units of enzymes is able to reduce 3 fractions of substrate successfully to synthesize the AuNPs. The second best was 3 : 2 which implied the amount of substrate is less than the enzyme. The use of less amount of enzymes at [E]: [C_A] = 2 : 3 produced more amount of AuNPs, hence, makes the process economically viable.

3.3. Size Optimization of Crystal NPs. Different temperatures (25°C–40°C) and pH (5–9) were selected for the experimental setup in order to optimize the best pH and temperature for the smallest homogeneous bulk production of AuNPs. While varying the factors, the enzyme substrate ratio was kept constant [E]: [C_A] = 2 : 3 along with keeping pH constant at 9 and temperature at 30°C. At the optimum pH and temperature, the crystal growth was keenly observed through TEM and FE-SEM images. It was also confirmed by DLS observations that the size of NPs increased with time, so the study was performed to comprehend the development of NPs and their growth behaviour. Also, the process parameters of the reaction were preserved till the reaction reached equilibrium. Figure 3 shows the AuNPs of largest size, around 250 nm, among other AuNPs synthesized at the other four temperatures. It could be mainly because of agglomeration and fusion of small NPs to give rise to larger ones. Further, TEM analysis confirmed the presence of the smallest AuNPs, around 5 nm, at 30°C during the time interval of 2–12 hrs.

After the 24th hour, the average particle size was 166 nm at 30°C. At 37°C, the particle size increased, probably because of high stability effects at high temperature, thus, the NPs size increases with the increase of reaction time.

On the basis of DLS results, it was concluded that at pH 9, maximum AuNPs of small spherical size around 160 nm were obtained. High alkalinity happens to increase OH⁻ concentration in the solution mixture, which affects the surface charge of NPs, subsequently resulting in an increase in the repulsive electrostatic/electrosteric interactions.

This causes an increase in the stability of cluster groups and colloid formation in the medium with a decreased affinity for agglomeration of the NPs. At alkaline pH, monodispersed and small-sized spherical AuNPs were produced, with the greater amount. At acidic pH like 5 and 6, the size of AuNPs produced was in the range of 450–550 nm as represented by the graph in Figure 4.

TEM and FE-SEM micrographs (Figures 5 and 6) clearly showed that, initially the NPs were mostly spherical but with an increase in time, the fusion of AuNPs led to the development of NPs of various geometrical shapes. The particle size analysis of AuNPs with varying time duration is tabulated in Table 1. The values showed that the AuNPs were the range of 5–160 nm over a period of 48 hours. It was observed that with increasing of time, the AuNPs agglomerate and fuse to

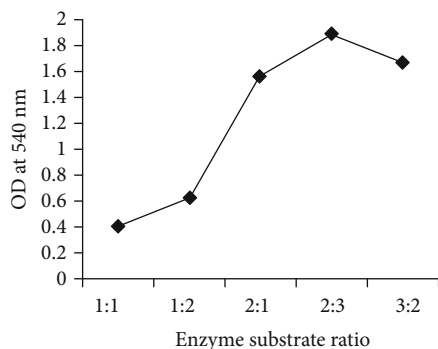


FIGURE 2: Different enzyme substrate ratio at 540 nm for AuNP production; 2:3 being the best optimum ratio followed by 3:2 and 2:1.

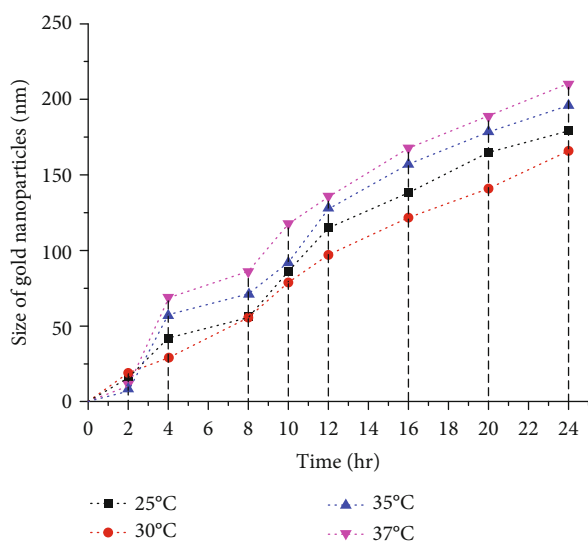


FIGURE 3: Influence of different temperatures on the size of AuNPs biosynthesis based on DLS analysis. The graph shows the smallest size AuNPs are biosynthesized at 30°C followed by second best optimum temperature at 25°C.

develop into larger crystals, and thus large-sized AuNPs are produced if the reaction is left for more than 12 hours.

3.4. Reaction Kinetics. This study was done to understand the influence of temperature, pH, agitation speed, and substrate (HAuCl_4) concentration on the kinetics of the biosynthesis of AuNPs. Various sets of experiments were done by changing the abovementioned 4 physical parameters whilst keeping the other parameters constant.

3.5. Effect of Temperature on the Production of AuNPs. The different temperatures selected were 25°C–40°C, and it was observed from the ICP-OES data that the concentration of NPs increased till the 12th hour of the reaction, and as the reaction reached equilibrium, it was observed that from the 24th hour to 48th hour, there was no significant increase in the amount of product. It was seen that with the increase in temperature, the concentration of the NPs also increased and the rate of synthesis of the reaction changed.

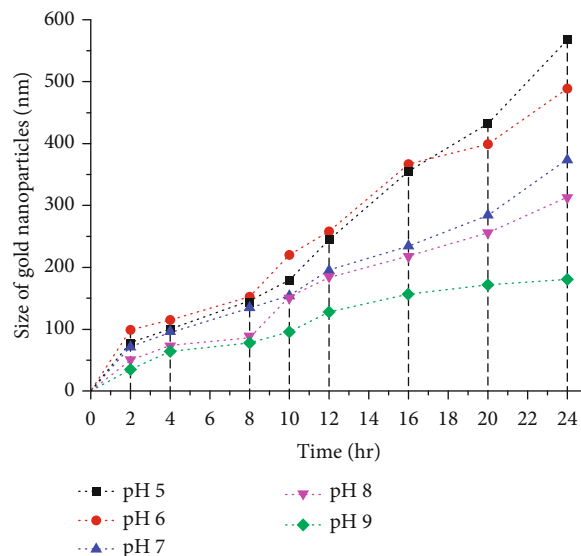


FIGURE 4: Influence of different pH(s) on the size of AuNPs biosynthesis based on DLS analysis. The graph shows the smallest size AuNPs are biosynthesized at pH 9 followed by second best optimum temperature at pH 8.

Temperature acts as one of the most crucial physical parameter in the biosynthesis of AuNPs. Figure 7 displays the ICP-OES analysis of the effect of temperature in the biosynthesis of AuNPs. It was observed that with the increase in the reaction temperature, from room temperature to 30°C, the biosynthesis of AuNPs also increased. As the temperature was increased further, the rate of reduction of HAuCl_4 decreased, the minimum being at 40°C perhaps because, at higher temperature, the enzymes tend to get denatured and loses its activity [29].

The observed mechanism shows that most of the gold ions were utilized in the formation of nuclei which leads to the secondary reduction. Once all the active sites of the enzyme get completely occupied, the reaction halts since there is no more scope of reduction to AuNPs. The movement of atoms in the solution (Brownian movement) increases with the increase in temperature and directly affects the reaction kinetics, leading to the aggregation of the NPs during synthesis and hence enhances the rate of production [30]. In this specific case, the results of ICP-OES showed the highest amount of AuNPs, synthesized at 30°C. The results when compared at 6 different temperatures, led to the conclusion that 30°C, were optimum for the biosynthesis of AuNPs. Further, the formation of AuNPs at other reported temperatures have been summarized in Figure 7. The ICP-OES results clearly showed that with every 1 mg/L of HAuCl_4 , the AuNPs biosynthesized is 0.961 mg/L, which means up to 96% conversion.

3.6. Effect of pH on the Production of AuNPs. The influence of pH in the production of AuNPs was evaluated at 5 different pH values (5, 6, 7, 8, and 9), and the results were demonstrated through ICP-OES analysis (Figure 8). It was observed that with the increase in pH, the concentration of the AuNPs increased. The pH of medium plays an integral role in the

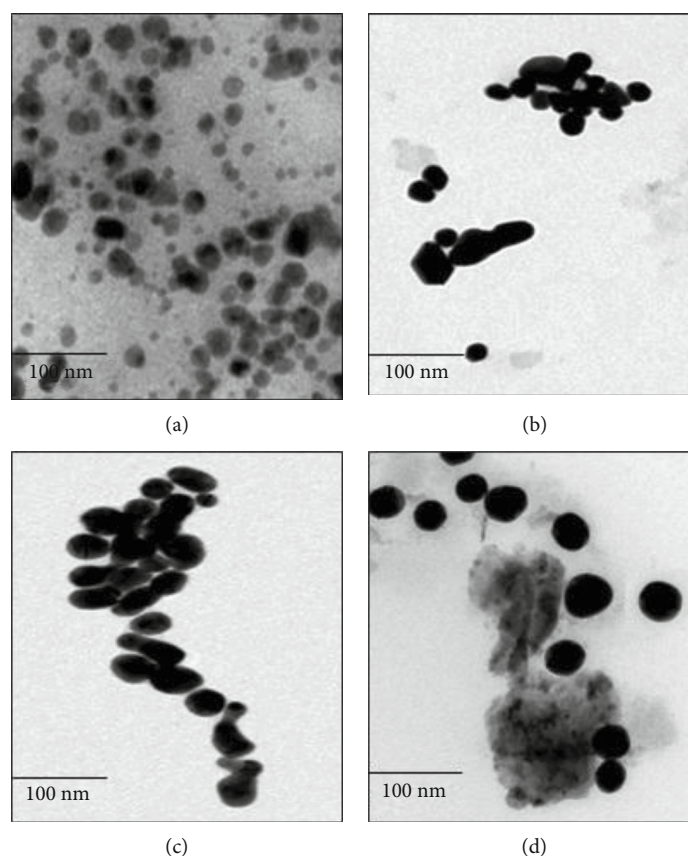


FIGURE 5: TEM images of AuNPs growth behaviour at varying time intervals: 0-2 h (a), 2-12 h (b), 12-24 (c), and 24-48 h (d) are depicted. The AuNPs size showed an increment at successive time interval due to fusion of smaller nuclei leading to a bigger particle due to crystal growth. All AuNPs in the images were synthesized with HAuCl_4 as a precursor ion. In the images, the scale on the bottom left corner represents 100 nm.

biosynthesis of NPs, since it encourages and determines the reactivity of the enzyme present in the bacterial CLS with gold ions.

As per the ICP-OES estimation, the maximum gold ions were converted to AuNPs at an alkaline pH of 9. One of the convincing reasons was that since the bacterial source used was of marine origin, so the enzyme was more effective at alkaline pH. Fast reduction of gold occurred in the basic medium. The rate at which NADPH-dependent nitrate reductase releases H^+ ions and donates the electrons is pH driven, which in turn determines the sensitivity of biosynthesis of AuNPs.

When the pH is basic, the concentration of H^+ ions in solution is very low, initiating fast dissociation of NADPH-dependent nitrate reductase and instantaneous reduction of a large amount of gold atoms, leading to the formation of many nuclei, which in turn leads to a higher rate of AuNPs production at pH9. Because of this, the concentration of reduced atoms decreases and the accelerated growth of the nuclei takes place to form nanospheres, avoiding the growth of anisotropic structures [31]. Hence, more spherical AuNPs are formed at basic pH9.

In the case of neutral to acidic pH, the rate at which NADPH-dependent nitrate reductase dissociates is slower because there are enough H^+ ions already present in the solution at pH5 and 6. Furthermore, due to the unavailabil-

ity of requisite electrons, the reduction of gold ions into AuNPs also lowers. Similar results were reported in *Coleus aromaticus* (*C. aromaticus*) leaf-mediated NPs synthesis where alkaline pH8.2 showed a narrow peak at 460 nm with maximum production [29]. Similarly, [32] used an aqueous extract of *Momordica charantia* (*M. charantia*) for AuNPs synthesis, and it exhibited maximum stability at pH10. Several reported results prove that pH plays an important role in the shape and size and also controls the activity of synthesized AuNPs. The current study specified that the alkaline pH was more appropriate for the biosynthesis of AuNPs.

3.7. Effect of Substrate (HAuCl_4) Concentration on the Production of AuNPs. Different concentrations, i.e., 1, 2, 3, 4, 5, and 10 mg/L of substrate (HAuCl_4) when added to bacterial CLS also resulted in the varying amounts of AuNPs production. ICP-OES results indicated that the production of AuNPs is directly proportional to the substrate concentration. The rate of reaction and amount of AuNPs production in a 48 hrs time period was majorly dependent on the initial metal ion concentration and reaction time. The more the concentration of gold ion available for reduction, the more was the AuNPs product at the end of the reaction. The substrate to product ratio was estimated via ICP-OES, and the results confirmed the formation of AuNPs, with a

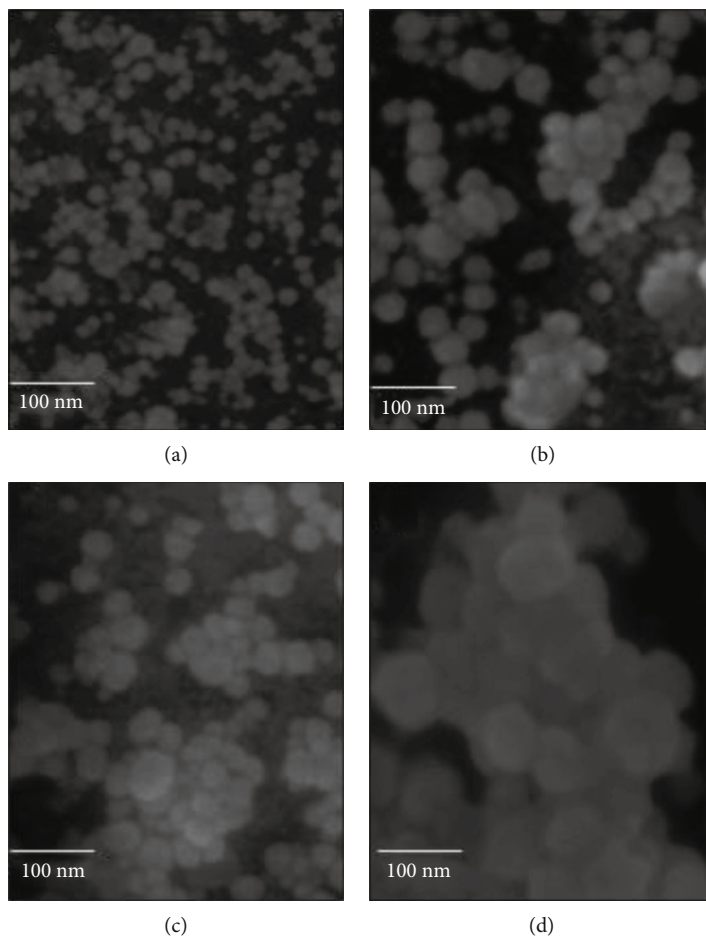


FIGURE 6: FE-SEM images depicts growth behaviour of AuNPs at varying time intervals: 0-2 h (a), 2-12 h (b), 12-24 (c), and 24-48 h (d). Owing to phenomenon of nuclei fusion and crystal growth, a successive increase in the size of AuNPs was observed as the time increased. The scale of 100 nm is present at left bottom corner of each of the four images.

TABLE 1: Particle size analysis of AuNPs at varying time through DLS studies.

S. no.	Time interval (hrs)	Average particle size (nm)
1	0-2	11 ± 6.36
2	2-12	66 ± 9.76
3	12-24	119 ± 11.57
4	24-48	148 ± 17.81

yield of 92% at a HAuCl_4 concentration of 10 mg/L. Further, the effect of different substrate (HAuCl_4) concentration on the production of AuNPs has been summarized in Figure 9.

3.8. Effect of Agitation Speed on the Production of AuNPs. The various agitation speeds selected were 50, 100, 150, 200, and 250 rpm. The observations made from the ICP-OES data and graphs were plotted over a period of 48 hrs which clearly supports the effective influence of agitation speed over nucleation and crystal growth. The highest production of AuNPs was obtained at 150 rpm followed by 200 rpm and 100 rpm (Figure 10). Agitation causes continuous stirring that causes

an overall homogenizing effect on the solution and hinders the localization of gold ions. Owing to this effect, an effective distribution of both gold ions and enzymes occur in the solution results in less agglomeration and production of AuNPs. An optimum agitation speed of 150 rpm increased the chances of exposure of gold ions to the enzymes which remarkably enhanced the overall production of AuNPs. Interestingly, a high agitation speed of 250 rpm had a comparatively negative effect on the rate of production of AuNPs because it causes disruption of a stable interactive system being formed between the gold ions and the enzymes. Very low agitation speed of 50 rpm did not show any considerable effect on the conversion of precursor gold to AuNPs due to an on-homogeneous mixture and improper mixing. The agitation speed significantly affected the crystallization behaviour, growth, and size of the AuNPs.

3.9. Determination of Order of Reaction. Evident facts from all the 4 graphs (Figures 7, 8, 9, and 10), where the effect of pH, temperature, substrate concentration, and agitation speed is studied up to 2 hours indicates the reaction order to be the first order as the variation of concentration is linear with the time course of the reaction. The phase up to 2 hours

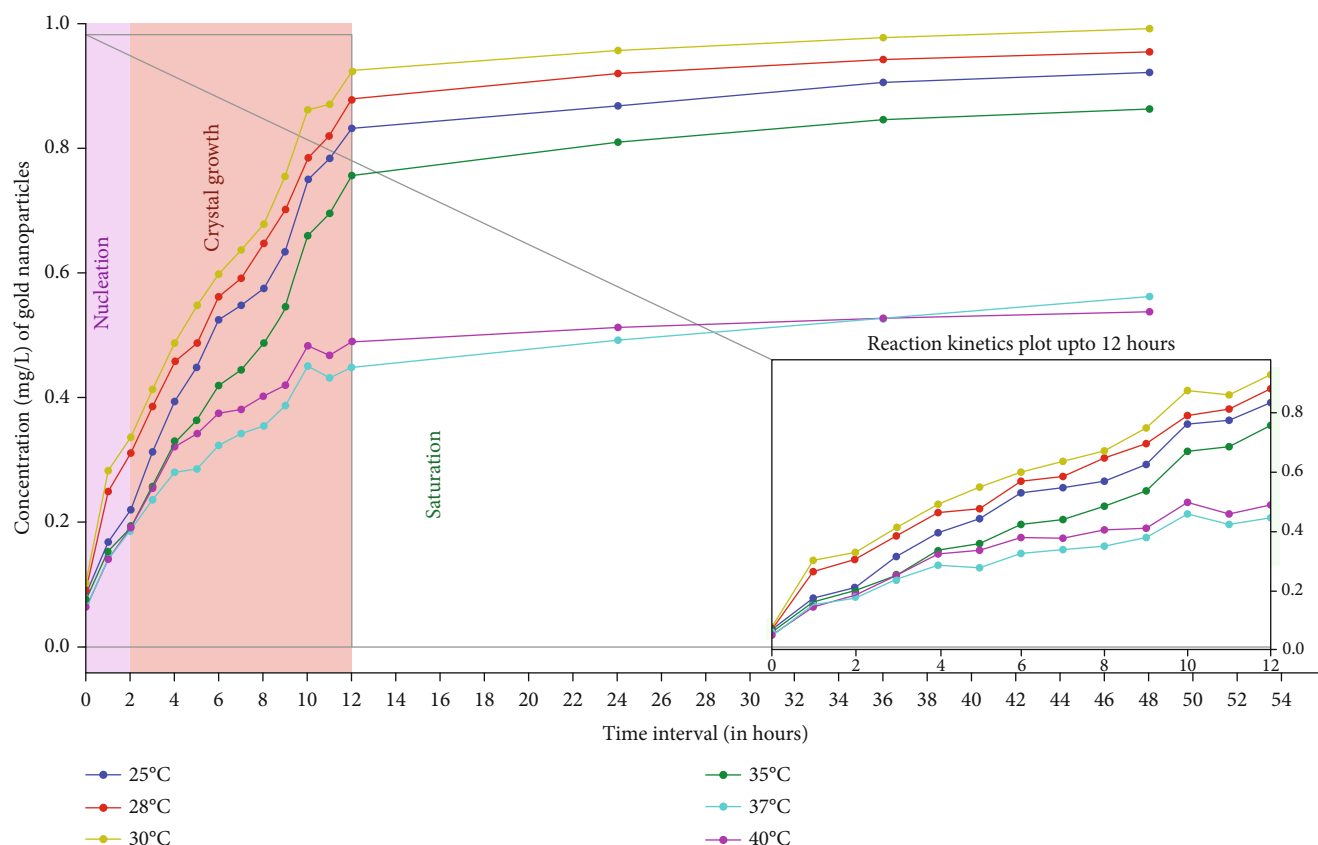


FIGURE 7: Influence of different temperatures on AuNPs biosynthesis kinetics based on ICP-OES analysis. Maximum AuNPs production was achieved at 30°C because the enzyme activity is supposedly the maximum at that temperature followed by 28°C enzyme was least active at 40°C thus lowest conversion rate of precursor gold to AuNPs. The enzyme substrate ratio was kept constant, $[E]: [C_A] = 2 : 3$, the pH was maintained at 9 with substrate concentration of 1 mg/L and agitation speed of 150 rpm throughout the reaction.

marks the nucleation zone, i.e., the initiation regime. From the 2nd hour onwards, up to the 12th hour, is the propagation regime, wherein more crystals are formed and AuNP size increased due to agglomeration as observed through DLS studies. From the observations, it was proposed that this phase of the reaction was autocatalytic in nature signifying the synthesized small-sized AuNPs acting as a catalyst for the further propagation of the reaction. The characteristic feature of an autocatalytic reaction is that the rate of the reaction escalates gradually as the reaction proceeds with the increased amount of catalyst and again decelerates down as the reactant concentration reduces (Frenklach et al. 1983; [33]). A similar trend was observed from the results of all the experiments performed and the graphs validate it effectively. The biosynthesis of AuNPs reaction followed first-order kinetics at the initiative phase, due to the best activity performed by enzyme and ample amount of substrate.

For a first-order reaction, the rate of the reaction is directly proportional to the concentration of the reactant. Proper crystal growth occurs up to the 12th hour. There was a minor increase in the production of AuNPs after the 12th hour up to the 24th hour owing to the start of the saturation phase, yet the crystal growth phase occurred. After the 24th hour, the reaction begins to reach its saturation phase, lowering the production of AuNPs. A flat line with a slight increase

to upwards was observed from 24th hour onwards up to the 48th hour, which can be said to follow zero-order kinetics wherein the reaction is independent of the reactant concentration. From 24 hours onwards up to 48 hrs was the third regime or the saturation of crystals regime wherein no new crystal formation was observed but the existing crystals just grow more in size. This phase, where the crystals grow in size is not a function of time, indicated zero-order kinetics. Overall from our preliminary study, it was concluded that the entire study exhibited a mixed reaction kinetics comprising of (i) first-order reaction, (ii) autocatalytic reaction, and (iii) zero-order reaction.

3.10. Determination of Rate Constant. In chemical kinetics, a reaction rate constant or reaction rate coefficient (k) quantifies the rate of a chemical reaction.

For a general reaction:



$$\text{Rate of reaction } (r_A) = k_A [A]^x \cdot [B]^y \quad (2)$$

$$x + y = n ; \text{ order of the reaction } (n) \quad (3)$$

$$\text{Rate constant } (k_A) = \text{Rate of reaction } k_A [A]^x \cdot [B]^y \quad (4)$$

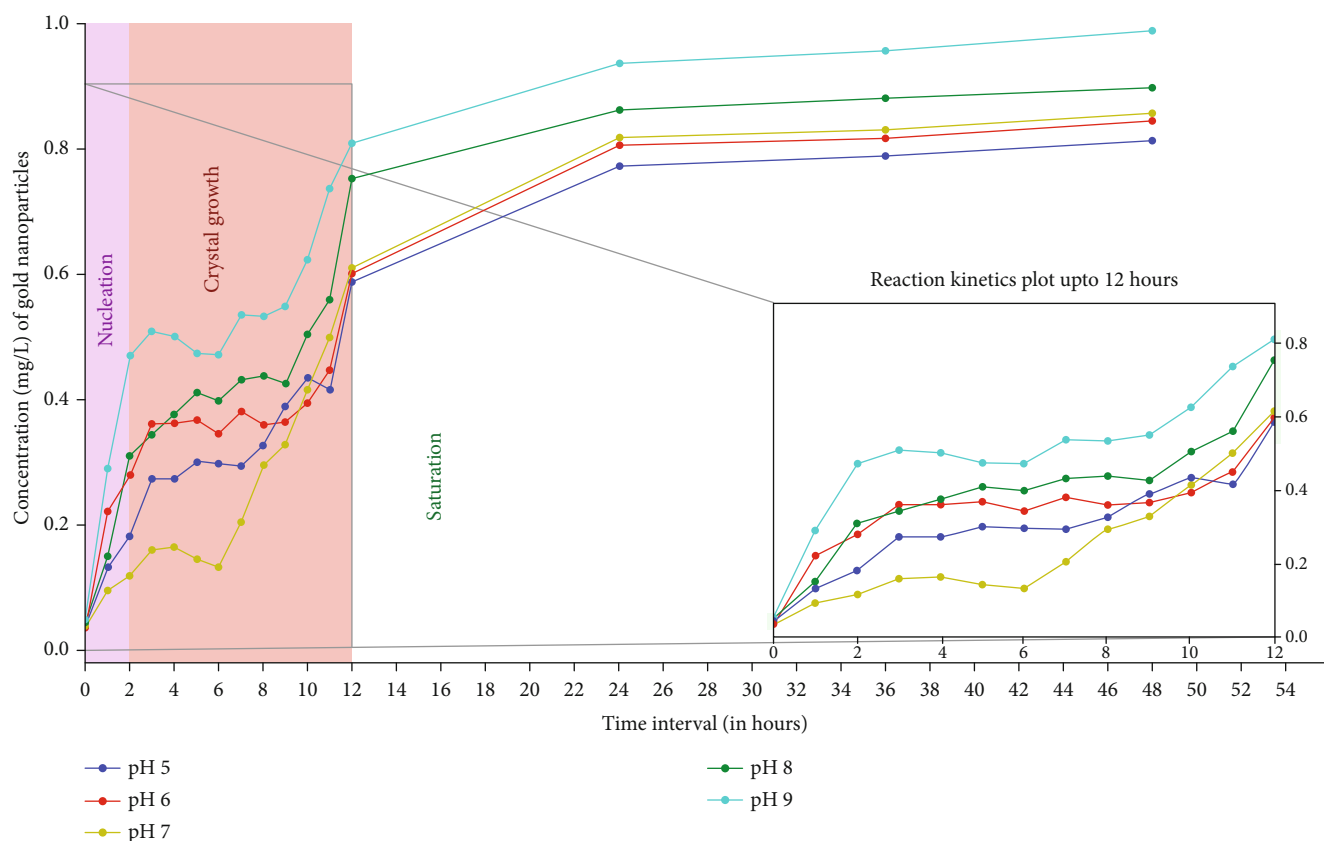


FIGURE 8: Influence of different pH(s) on AuNPs biosynthesis kinetics based on ICP-OES analysis. Maximum AuNPs production was achieved at pH 9 because the concentration of H^+ ions in solution is very low, causing fast dissociation of enzyme leading to higher AuNPs production. Enzyme was least reactive at pH 5 thus lowest conversion rate of precursor gold to AuNPs. The enzyme substrate ratio was kept constant, $[E]:[C_A] = 2:3$, the temperature at $30^\circ C$ throughout the reaction with substrate concentration of 1 mg/L along with agitation speed of 150 rpm.

The substrate ($HAuCl_4$) concentration is represented by A (r_A and k_A). The rate constant provides the relation between the r_A and the reactants concentration of a reaction. Here, the k_A was estimated via integral method of analysis [34]. The effect of each parameter (pH, temperature, substrate concentration, and agitation speed) over k_A and r_A was determined, rather keeping other parameters constant.

3.11. Effect of Physico-Chemical Parameters on r_A and k_A . Physico-chemical parameters that were taken into consideration were temperature, pH, substrate concentration, and agitation speed. The experimental design involved varying one factor at a time while keeping others constant. The constant values kept were temperature at $30^\circ C$, pH 9, substrate concentration at 1 mg/L, and agitation speed at 150 rpm while choosing to vary 1 factor at a time. The enzyme substrate ratio $[E]:[C_A]$ was kept 2:3 in all the experimental reactions. Since first-order kinetics was observed up to the first 2 hours, i.e., initiation phase, the r_A and k_A values were calculated for them only.

The different temperatures at which the biosynthesis of AuNPs were carried out were $25^\circ C$, $28^\circ C$, $30^\circ C$, $35^\circ C$, $37^\circ C$, and $40^\circ C$. The highest rate constant (k_A) of $0.0703 h^{-1}$ was

observed at $30^\circ C$ (Table 2). The pH was varied in the range of 5 to 9. The highest rate constant (k_A) of $0.0930 h^{-1}$ was observed at pH 9 (Table 3). Six different substrate concentrations, i.e., 1, 2, 3, 4, 5, and 10 mg/L of precursor ($HAuCl_4$) when added to bacterial CLS also resulted in the production of different amounts of AuNPs. The highest rate constant (k_A) of $0.46388 h^{-1}$ was observed at a substrate concentration of 10 mg/L (Table 4). The various agitation speeds selected were 50, 100, 150, 200, and 250 rpm. The highest rate constant (k_A) of $0.04796 h^{-1}$ was observed at agitation speed of 150 rpm (Table 5).

3.12. Optimum Process Conditions for AuNPs Biosynthesis. Optimum process conditions for AuNPs biosynthesis were tabulated with experimental data. The initial substrate concentration of $HAuCl_4$ was kept at 1 mg/L at the start of biosynthesis of AuNPs while varying various physico-chemical parameters [35]. Optimum process conditions are tabulated in Table 6. Comparative results of r_A showed that synthesis at pH 9 produced the highest r_A values of $0.0930 h^{-1}$, which apparently showed that the biosynthesis of AuNPs was based on biochemical reactions and the H^+ ions significantly affected the k_A values and subsequently the r_A values.

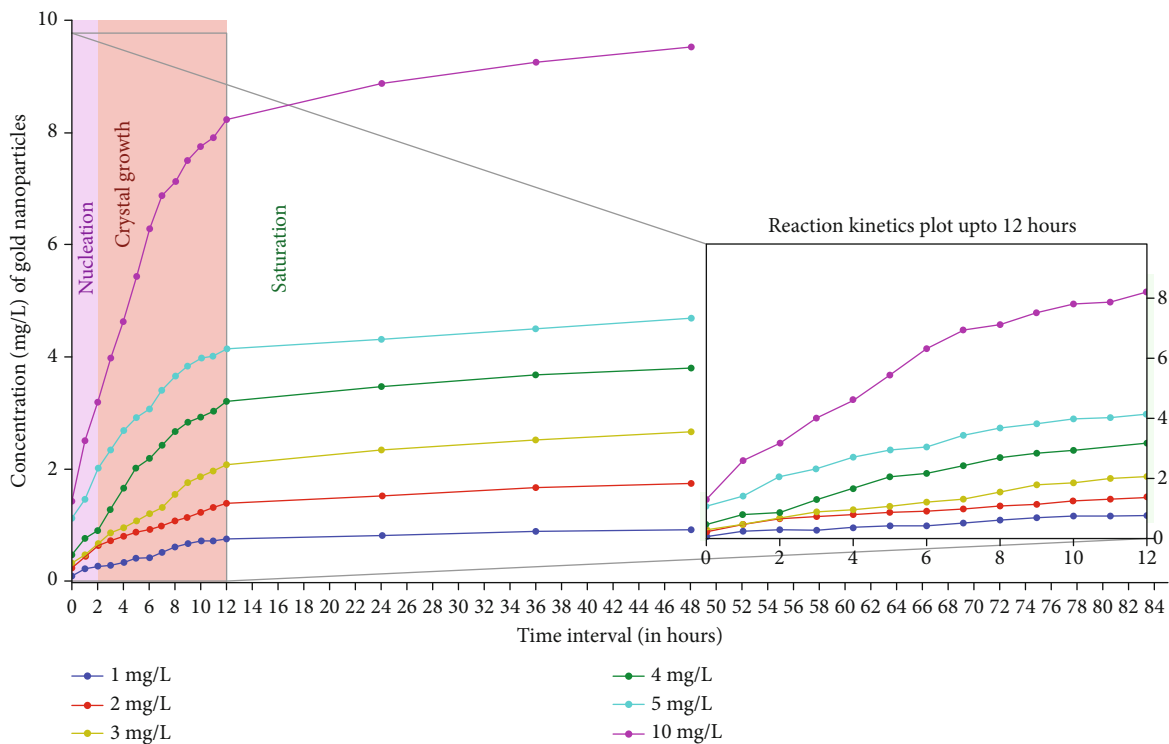


FIGURE 9: Influence of various substrate concentration (HAuCl₄) on AuNPs biosynthesis kinetics based on ICP-OES analysis. It was observed that the production of AuNPs is directly proportional to the substrate concentration hence the highest production occurred at 10 mg/L. The enzyme: substrate ratio was 2 : 3, the pH was kept at 9 and temperature at 30°C throughout the reaction with 150 rpm agitation.

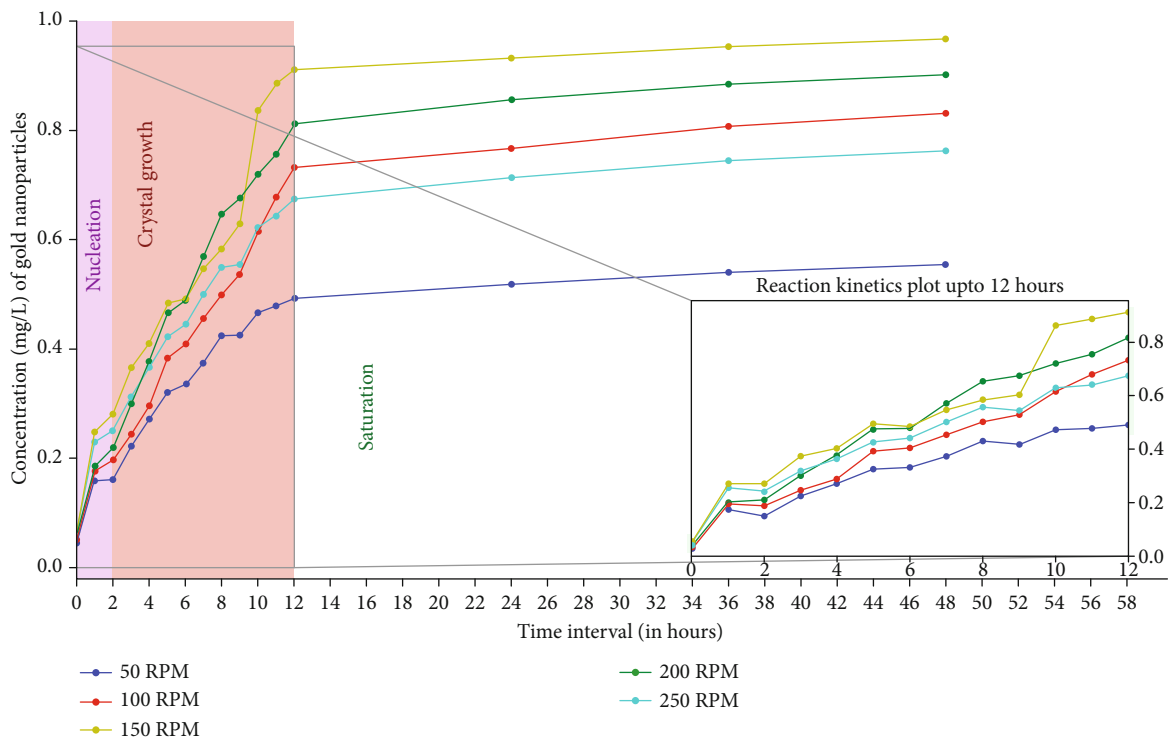


FIGURE 10: Influence of different agitation speeds on AuNPs biosynthesis kinetics based on ICP-OES analysis. Highest AuNPs production was recorded at 150 rpm because optimum agitation increases the chances of exposure of gold ions to the enzymes resulting in higher production. The enzyme: substrate ratio was 2 : 3, the pH was kept at 9 and temperature at 30°C throughout the reaction with substrate concentration of 1 mg/L.

TABLE 2: Determination of r_A and k_A with varying temperatures.

Temperature ($^{\circ}\text{C}$)	r_A up to 2 hrs (mg/hr)	k_A up to 2 hrs (h^{-1})
25	0.0791	0.038
28	0.1315	0.0636
30	0.1392	0.0703
35	0.076	0.038
37	0.073	0.032
40	0.0751	0.0369

TABLE 3: Determination of r_A and k_A with varying pH(s).

pH	r_A up to 2 hrs (mg/hr)	k_A up to 2 hrs (h^{-1})
5	0.049	0.0240
6	0.095	0.0491
7	0.0148	0.00732
8	0.1081	0.05372
9	0.1867	0.0930

TABLE 4: Determination of r_A and k_A with varying substrate concentrations.

Substrate concentration (mg/L)	r_A up to 2 hr (mg/hr)	k_A up to 2 hr (h^{-1})
1	0.083	0.047
2	0.2223	0.1119
3	0.1819	0.09084
4	0.2072	0.10333
5	0.4829	0.2425
10	0.9268	0.46388

TABLE 5: Determination of r_A and k_A with varying agitation speeds.

Agitation speed (rpm)	r_A up to 2 hr (mg/hr)	k_A up to 2 hr (h^{-1})
50	0.0431	0.0219
100	0.0599	0.02988
150	0.0961	0.04796
200	0.0634	0.0346
250	0.0827	0.0487

TABLE 6: Effect of various parameters on optimum process conditions.

Optimum process conditions	Product (AuNPs) produced mass/vol—in total reaction time (at 48 hrs)	% yield of AuNPs	Highest r_A and k_A
pH (9)	0.914 mg/L	91.4	$r_A = 0.1867$ $k_A = 0.0930$
Temperature (30°C)	0.961 mg/L	96.1	$r_A = 0.1392$ $k_A = 0.0703$
Agitation speed (150 rpm)	0.947 mg/L	94.7	$r_A = 0.0961$ $k_A = 0.04796$

4. Conclusions

The results of AuNPs synthesized using *P. espejiana* strongly indicate that particle size increases with the time and the rate of formation of AuNPs is dependent on the variation of parameters like temperature, pH, agitation speed (rpm), and the concentration of substrate (HAuCl_4). The increase in the rate of the reaction is due to an increase in the kinetic energy and the collision frequency between the molecules. A proper cycle of nucleation, crystal growth, and final saturation is observed in the AuNP biosynthesis. The measured rates support the fact that the process is chemically-controlled since pH has the highest rate of constant value. This research opens up further avenues to explore in the fields of kinetics, thermodynamics, and mass transfer involved in AuNP biosynthesis. Also, this study was a biochemical reaction and is enzyme-driven, so a different kinetic order was observed during the different phases of the reaction and thus makes it an interesting topic for further in-depth research.

Data Availability

The data generated or analyzed in this article are online publicly available without request.

Conflicts of Interest

The authors declare no conflicts of interest associated with this manuscript.

Authors' Contributions

Rashmi Gupta, Gourav Kumar, and Sabya Sachi Das contributed equally to this work.

Acknowledgments

This work was funded by the Researchers Supporting Project number (RSP-2020/26), King Saud University, Riyadh, Saudi Arabia.

References

- [1] J. Bejarano, M. Navarro-Marquez, F. Morales-Zavala et al., "Nanoparticles for diagnosis and therapy of atherosclerosis and myocardial infarction: evolution toward prospective therapeutic approaches," *Theranostics*, vol. 8, no. 17, pp. 4710–4732, 2018.
- [2] S. S. Das, A. Hussain, P. R. P. Verma et al., "Recent advances in liposomal drug delivery system of quercetin for cancer targeting: a mechanistic approach," *Current Drug Delivery*, vol. 17, 2020.
- [3] M. S. Hasnain, S. A. Ahmad, N. Chaudhary, M. N. Hoda, and A. K. Nayak, "Biodegradable polymer matrix nanocomposites for bone tissue engineering," in *Applications of Nanocomposite Materials in Orthopedics*, Inamuddin, A. M. Asiri, and A. Mohammad, Eds., pp. 1–37, Woodhead Publishing, 2019.
- [4] M. S. Hasnain, S. A. Ahmad, M. N. Hoda, S. Rishishwar, P. Rishishwar, and A. K. Nayak, "Stimuli-responsive carbon nanotubes for targeted drug delivery," in *Stimuli Responsive*

- Polymeric Nanocarriers for Drug Delivery Applications: Vol. 2: Advanced Nanocarriers for Therapeutics*, A. S. M. Makhoulouf and N. Y. Abu-Thabit, Eds., pp. 321–344, Woodhead Publishing, 2019.
- [5] M. S. Hasnain, S. A. Ahmad, M. A. Minhaj, T. J. Ara, and A. K. Nayak, “Nanocomposite materials for prosthetic devices,” in *Applications of Nanocomposite Materials in Orthopedics*, Inamuddin, A. M. Asiri, and A. Mohammad, Eds., pp. 127–144, Woodhead Publishing, 2019.
- [6] M. S. Hasnain and A. K. Nayak, “Nanocomposites for improved orthopedic and bone tissue engineering applications,” in *Applications of Nanocomposite Materials in Orthopedics*, Inamuddin, A. M. Asiri, and A. Mohammad, Eds., pp. 145–177, Woodhead Publishing, Elsevier Inc, 2019.
- [7] P. Rani, D. Pal, M. N. Hoda et al., “Dental pulp capping nanocomposites,” in *Applications of Nanocomposite Materials in Dentistry*, Inamuddin, A. M. Asiri, and A. Mohammad, Eds., pp. 65–91, Woodhead Publishing, Elsevier Inc., 2019.
- [8] T. Waghule, V. K. Rapalli, G. Singhvi et al., “Voriconazole loaded nanostructured lipid carriers based topical delivery system: QbD based designing, characterization, in-vitro and ex-vivo evaluation,” *Journal of Drug Delivery Science and Technology*, vol. 52, pp. 303–315, 2019.
- [9] S. Beg, A. Jain, S. Saini et al., “Metal–organic frameworks as expanding hybrid carriers with diverse therapeutic applications,” in *Organic Materials as Smart Nanocarriers for Drug Delivery*, Pp. 1–34, E. M. Grumezescu, Ed., William Andrew Publishing, 2018.
- [10] M. S. Hasnain, M. N. Javed, M. S. Alam et al., “Purple heart plant leaves extract-mediated silver nanoparticle synthesis: optimization by Box–Behnken design,” *Materials Science and Engineering: C*, vol. 99, pp. 1105–1114, 2019.
- [11] M. S. Hasnain, A. K. Nayak, M. Singh, M. Tabish, M. T. Ansari, and T. J. Ara, “Alginate-based bipolymeric-nanobioceramic composite matrices for sustained drug release,” *International Journal of Biological Macromolecules*, vol. 83, pp. 71–77, 2016.
- [12] M. S. Alam, M. N. Javed, F. H. Pottoo et al., “QbD approached comparison of reaction mechanism in microwave synthesized gold nanoparticles and their superior catalytic role against hazardous nirto-dye,” *Applied Organometallic Chemistry*, vol. 33, no. 9, article e5071, 2019.
- [13] P. Mohanpuria, N. K. Rana, and S. K. Yadav, “Biosynthesis of nanoparticles: technological concepts and future applications,” *Journal of Nanoparticle Research*, vol. 10, no. 3, pp. 507–517, 2008.
- [14] A. K. Nayak, T. J. Ara, M. S. Hasnain, and N. Hoda, “Okra gum–alginate composites for controlled releasing drug delivery,” in *Applications of Nanocomposite Materials in Drug Delivery*, Inamuddin, A. M. Asiri, and A. Mohammad, Eds., pp. 761–785, Woodhead Publishing, Elsevier Inc, 2019.
- [15] A. K. Nayak, M. S. Hasnain, S. S. Nanda, and D. K. Yi, “Hydroxyapatite-alginate based matrices for drug delivery,” *Current Pharmaceutical Design*, vol. 25, no. 31, pp. 3406–3416, 2019.
- [16] K. N. Thakkar, S. S. Mhatre, and R. Y. Parikh, “Biological synthesis of metallic nanoparticles,” *Nanomedicine: Nanotechnology, Biology and Medicine*, vol. 6, no. 2, pp. 257–262, 2010.
- [17] S. S. Das, P. R. P. Verma, and S. K. Singh, “Quercetin-loaded nanomedicine as nutritional application,” in *Nanomedicine for Bioactives*, M. Rahman, S. Beg, V. Kumar, and F. Ahmad, Eds., pp. 259–301, Springer, Singapore, 2020.
- [18] S. Majeed, E. L. Joel, and M. S. Hasnain, “Novel green approach for synthesis of metallic nanoparticles and its biomedical application,” *Current Nanomedicine*, vol. 8, pp. 177–183, 2019.
- [19] R. Gupta and P. Padmanabhan, “Biogenic synthesis and characterization of gold nanoparticles by a novel marine bacteria MARINOBACTER ALGICOLA: progression from nanospheres to various geometrical shapes,” *Journal of Microbiology, Biotechnology and Food Sciences*, vol. 8, no. 1, pp. 732–737, 2018.
- [20] A. Hussain, S. Singh, S. S. Das, K. Anjireddy, S. Karpagam, and F. Shakeel, “Nanomedicines as drug delivery carriers of anti-tubercular drugs: from pathogenesis to infection control,” *Current Drug Delivery*, vol. 16, no. 5, pp. 400–429, 2019.
- [21] G. Singaravelu, J. S. Arockiamary, V. G. Kumar, and K. Govindaraju, “A novel extracellular synthesis of monodisperse gold nanoparticles using marine alga, *Sargassum wightii* Greville,” *Colloids and Surfaces B: Biointerfaces*, vol. 57, no. 1, pp. 97–101, 2007.
- [22] J. Venkatesan, P. Manivasagan, S. K. Kim, A. V. Kirthi, S. Marimuthu, and A. A. Rahuman, “Marine algae-mediated synthesis of gold nanoparticles using a novel *Ecklonia cava*,” *Bioprocess and Biosystems Engineering*, vol. 37, no. 8, pp. 1591–1597, 2014.
- [23] S. He, Z. Guo, Y. Zhang, S. Zhang, J. Wang, and N. Gu, “Biosynthesis of gold nanoparticles using the bacteria *Rhodospseudomonas capsulata*,” *Materials Letters*, vol. 61, no. 18, pp. 3984–3987, 2007.
- [24] Harshita, M. A. Barkat, S. S. Das, F. H. Pottoo, S. Beg, and Z. Rahman, “Lipid-based nanosystem as intelligent carriers for versatile drug delivery applications,” *Current Pharmaceutical Design*, vol. 26, no. 11, pp. 1167–1180, 2020.
- [25] M. S. Hasnain and A. K. Nayak, “Recent progress in responsive polymer-based drug delivery systems,” in *Stimuli Responsive Polymeric Nanocarriers for Drug Delivery Applications*, A. S. M. Makhoulouf and N. Y. Abu-Thabit, Eds., pp. 569–595, Woodhead Publishing, Elsevier Ltd, 2019.
- [26] C. Tojo, F. Barroso, and M. de Dios, “Critical nucleus size effects on nanoparticle formation in microemulsions: a comparison study between experimental and simulation results,” *Journal of Colloid and Interface Science*, vol. 296, no. 2, pp. 591–598, 2006.
- [27] V. K. LaMer and A. S. Kenyon, “Kinetics of the formation of monodispersed sulfur sols from thiosulfate and acid,” *Journal of Colloid and Interface Science*, vol. 2, no. 2, pp. 257–264, 1947.
- [28] S. S. Das, P. R. P. Verma, and S. K. Singh, “Screening and preparation of quercetin doped nanoemulsion: characterizations, antioxidant and anti-bacterial activities,” *LWT*, vol. 124, p. 109141, 2020.
- [29] M. Vanaja, S. Rajeshkumar, K. Paulkumar, G. Gnanajobitha, C. Malarkodi, and G. Annadurai, “Kinetic study on green synthesis of silver nanoparticles using *Coleus aromaticus* leaf extract,” *Advances in Applied Science Research*, vol. 4, pp. 50–55, 2013.
- [30] S. Piñero, S. Camero, and S. Blanco, “Silver nanoparticles: influence of the temperature synthesis on the particles’ morphology,” *Journal of Physics: Conference Series*, vol. 786, article 012020, 2017.
- [31] G. R. C. Rodríguez, G. H. Gauthier, L. O. Ladeira, J. A. S. Cala, and D. L. Cataño, “Effect of pH and chloroauric acid concentration on the geometry of gold nanoparticles obtained

- by photochemical synthesis,” *Journal of Physics: Conference Series*, vol. 935, article 012027, 2017.
- [32] S. Pandey, G. Oza, A. Mewada, and M. Sharon, “Green synthesis of highly stable gold nanoparticles using *Momordica charantia* as nano fabricator,” *Archives of Applied Science Research*, vol. 4, pp. 1135–1141, 2012.
- [33] F. Mata-Perez and J. F. Perez-Benito, “The kinetic rate law for autocatalytic reactions,” *Journal of Chemical Education*, vol. 64, no. 11, p. 925, 1987.
- [34] O. Levenspiel, “Chemical reaction engineering,” *Industrial and Engineering Chemistry Research*, vol. 38, no. 11, pp. 4140–4143, 1999.
- [35] M. S. Nejad, G. H. Bonjar, and N. Khaleghi, “Biosynthesis of gold nanoparticles using *Streptomyces fulvissimus* isolate,” *Nanomedicine Journal*, vol. 2, pp. 153–159, 2015.